Alessandro Leone
Angiola Forleo
Luca Francioso
Simona Capone
Pietro Siciliano
Corrado Di Natale
Editors

Sensors and Microsystems

Proceedings of the 19th AISEM 2017
National Conference

Springer

Lecture Notes in Electrical Engineering

Volume 457

"Lecture Notes in Electrical Engineering (LNEE)" is a book series which reports the latest research and developments in Electrical Engineering, namely:

- Communication, Networks, and Information Theory
- Computer Engineering
- Signal, Image, Speech and Information Processing
- Circuits and Systems
- Bioengineering

LNEE publishes authored monographs and contributed volumes which present cutting edge research information as well as new perspectives on classical fields, while maintaining Springer's high standards of academic excellence. Also considered for publication are lecture materials, proceedings, and other related materials of exceptionally high quality and interest. The subject matter should be original and timely, reporting the latest research and developments in all areas of electrical engineering.

The audience for the books in LNEE consists of advanced level students, researchers, and industry professionals working at the forefront of their fields. Much like Springer's other Lecture Notes series, LNEE will be distributed through Springer's print and electronic publishing channels.

More information about this series at http://www.springer.com/series/7818

Alessandro Leone · Angiola Forleo
Luca Francioso · Simona Capone
Pietro Siciliano · Corrado Di Natale
Editors

Sensors and Microsystems

Proceedings of the 19th AISEM 2017
National Conference

Springer

Editors

Alessandro Leone
IMM-CNR
Lecce
Italy

Angiola Forleo
IMM-CNR
Lecce
Italy

Luca Francioso
IMM-CNR
Lecce
Italy

Simona Capone
IMM-CNR
Lecce
Italy

Pietro Siciliano
IMM-CNR
Lecce
Italy

Corrado Di Natale
University of Rome Tor Vergata
Roma
Italy

Preface

This book contains a selection of the papers presented at the 19th AISEM ("Associazione Italiana Sensori e Microsistemi") National Conference on *Sensors and Microsystems*, held in Lecce, 21–23 February 2017. The conference has been organized by the Institute for Microelectronics and Microsystems (IMM) of the National Research Council of Italy with the support of InnovAAL (Public–Private Partnership operating in the field of technologies for Ambient Assisted Living, Independent Living, Healthy Living and related services). The conference, as in the past editions, has been designed to emphasize the scientific talent of young researchers. The conference highlighted state-of-the-art results from both theoretical and applied research in the field of sensors and related technologies. This book presents material in an interdisciplinary approach, covering many aspects of the disciplines related to sensors, including physics, chemistry, materials science, biology and applications.

The editors would like to thank the numerous participants and the Local Organizing Committee for the organization of the event.

Lecce, Italy   Alessandro Leone
Lecce, Italy   Angiola Forleo
Lecce, Italy   Luca Francioso
Lecce, Italy   Simona Capone
Lecce, Italy   Pietro Siciliano
Roma, Italy   Corrado Di Natale

Contents

Part II   Chemical Sensors

Part III   Biosensors

Part I
Physical Sensors

Integrable Sensor System for Live Monitoring of Loudspeaker Performances

**Gianluca Barile, Giuseppe Ferri, Alfiero Leoni, Mirco Muttillo,
Vincenzo Stornelli, Marco Caldari, Marco Palombini
and Franco Ripa**

Abstract We here present a dedicated system capable of compensating loudspeaker distortion due to driver working condition or apparatus aging. The proposed monitoring system is formed by a reduced number of sensors that monitor the loudspeaker by a digital signal processing architecture (DSP) which performs a feedback to the loudspeaker amplifier so balancing its gain. All the sensors are designed to not interfere with output sound quality.

Keywords Loudspeaker · Signal distortion · Aging

1 Introduction

One of the worst issues that has to be taken into account when designing or using a moving-coil loudspeaker is the so called "thermal compression" (or "power compression"). This phenomenon consists of the uneven reduction of the radiated sound power level across signal spectrum due to the temperature increase of the main loudspeaker components, hence distorting output sound quality.

As commonly known, these drivers have an extremely low efficiency (from 3 to 7%), so that the most part of incoming power, which flows in the voice-coil (the moving part of the speaker), is converted into heat. Since the latter has to be dissipated in some way, this involves the increase of not only coil temperature, but also air gap as well as magnet temperatures. This increment leads to numerous downsides: demagnetization of driver magnet in either reversible or permanent way (see neodymium material); alteration of driver physical properties, for example the melting of the glue that links the coil to the cylinder or to the spider; in the worst

G. Barile · G. Ferri · A. Leoni · M. Muttillo · V. Stornelli (✉)
Department of Industrial and Information Engineering and Economics,
University of L'Aquila, L'Aquila, Italy
e-mail: vincenzo.stornelli@univaq.it

M. Caldari · M. Palombini · F. Ripa
Korg Italy Srl, Via Cagiata, 85, 60027 Osimo (AN), Italy

case scenario, the speaker breaking. These effects combined together can be considered as a partial origin of sound distortion. However, the largest worsening of sound quality arises from the increase in the coil input resistance as its temperature raises, being:

$$p(t, T) = \frac{v^2(t)}{R(T)} \tag{1}$$

where R(T) is given by the well known relation:

$$R(T) = R(T_0)\left[1 + \alpha_0(T - T_0) + \beta_0(T - T_0)^2\right] \tag{2}$$

In the literature some possible solutions have been proposed to overcome this issue. In [1] the problem has been faced by replacing the "voltage mode" amplifier that drives the speaker with a "current mode" [2–5] amplifier: since it is the current flowing into the coil that determines its magnetic field, fixing the current allows to overcome the thermal compression. The drawback in this solution is that commonly used loudspeakers have to be driven in voltage mode, so it is not applicable. Another solution is based on analog/digital compensation of the input voltage signal [6]. This system, as well as other similar, in different ways, manages to compensate input signal by means of "temperature estimation" based on thermal models of the loudspeaker and dedicated sensors interfaces [7, 8]. The issue here resides in these models: even if accurate, they are based upon parameters extracted measuring the driver through a testbench (i.e., once in their lifetime) [9]. They take into account what happens neither to the loudspeaker parameters during its aging, nor when the driver has to work at different environmental pressures. This means that when the driver reaches a certain amount of years, or when the driver experiences different environmental parameters, temperature estimations used to compensate input signal might be wrong, thus giving rise to a wrong compensation. One of the most used sound-compensation techniques consists of measuring the loudspeaker magnitude response (or frequency response) right after its fabrication, at different temperatures. In this case, once characterized the amount of distortion given by the loudspeaker, a so called "smart amplifier" is calibrated to pre-distort the signal in the opposite way so to compensate driver distortion. This method needs a continuous temperature monitoring so that the smart amp's DSP knows exactly what kind of pre-distortion has to be applied to the input signal. However, aging still represents source of errors. Moreover, since speaker tends to decrease radiated sound power level as temperature increases, the "pre-distortion" technique consists of an increase of the input power. This means that some kind of loudspeaker protection systems have to be designed, hence increasing the overall system complexity.

In this work we present a system capable of compensating loudspeaker distortion regardless of driver working condition or aging.

2 Proposed Systems Architecture

As shown in Fig. 1, the proposed monitoring system consists of a number of sensors that send driver parameters to a DSP which performs a feedback to the amplifier so balancing its gain (i.e., output signal amplitude). All the sensors are designed to not interfere with loudspeaker output sound quality.

In particular, the current sensor performs measurements through Hall effect, so to avoid input series resistances that would have modified driver input impedance.

The same approach has been used with the IR thermal sensor device, which is an infrared sensor able to send to the DSP a thermal image (32 × 8 pixels), as reported in Fig. 2 where an example of temperature measurements of the loudspeaker membrane and magnet is depicted. Thanks to that, it is possible to measure, at the same time, the temperatures of the magnet, of the membrane and of the coil, whose heat can be detected even if it is physically hidden. The digital signal processor has to work at a much higher frequency than the sampling one, so to perform all the needed calculations and to offer an output signal "instantaneously" with respect to the sound. The most critical part though is the amplifier, because even if the DSP offers a very fast output analogue signal, the amplifier has to respond to the aforementioned signal fast enough. Preliminary results obtained applying the proposed system on a commercial loudspeaker are shown in Fig. 3. In this figure, two traces are plotted: the blue one, related to the uncompensated loudspeaker working condition, depicting RMS input power decreases with time (i.e., with temperature increments). On the contrary, the red one refers to the actively-compensated loudspeaker: it is evident that the proposed system is able to cope with the device delivered power during the operation time when a reduction occurs due to thermal phenomena shown in Fig. 2.
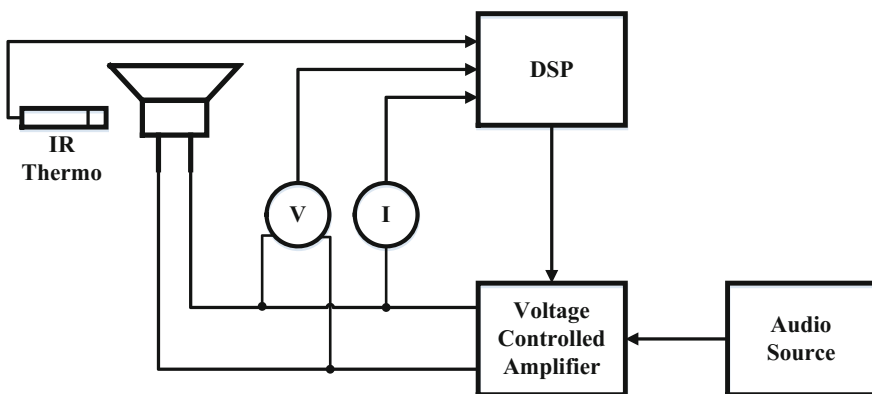
Fig. 1 System block diagram
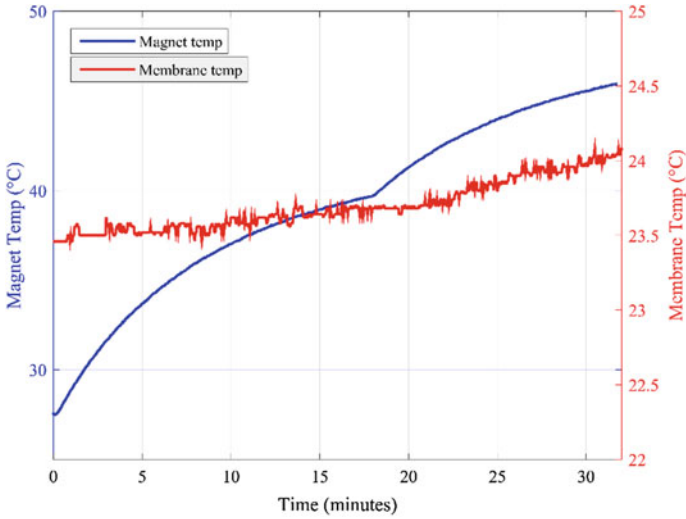
Fig. 2 Example of temperature measurements of the loudspeaker membrane and magnet
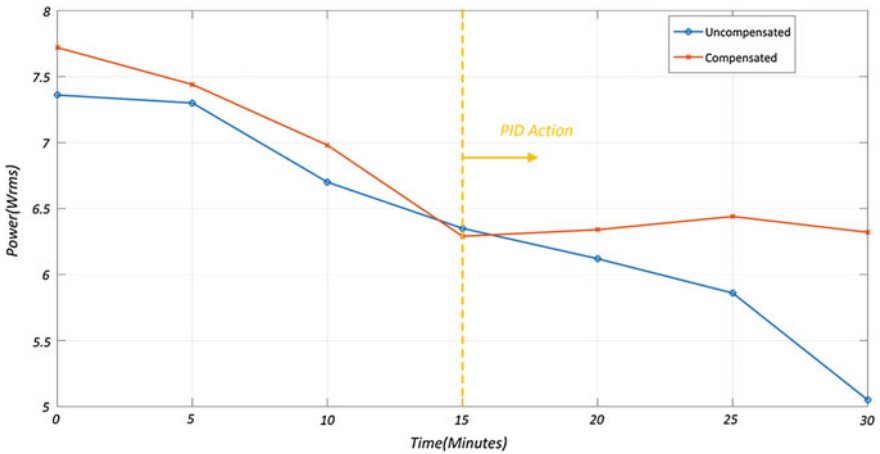
Fig. 3 Power versus time results on a 8 W commercial loudspeaker

3   Conclusion

The proposed system allows a reliable loudspeaker compensation which is independent both from working conditions and from the aging of the device. Moreover, its circuit simplicity and compactness allows to place it directly into loudspeakers cabinets, in particular the keyboards, which this application has been initially thought for.

References

1. Bellini, A., Boni, A., Morandi, C.: Mixed high level and circuital simulation of current driven loudspeaker systems, in International Midwest symposium on circuits and systems (1998)
2. Ferri, G., Stornelli, V., Di Simone, A.: A CCII-based high impedance input stage for biomedical applications. J. Circ. Syst. Comput. **20**(8), 1441–1447 (2011)
3. Ferri, G., Stornelli, V., Fragnoli, M.: An integrated improved CCII topology for resistive sensor application. Analog Integrated Circ. Signal Process. J. **48**(3), 247–250 (2006)
4. Stornelli, V.: Low voltage low power fully differential buffer. J. Circ. Syst. Comput. **18**(3), 497–502 (2009)
5. Stornelli, V., Ferri, G.: A 0.18 μm CMOS DDCCII for portable LV-LP filters. Radioengineering **22**(2), 434–439 (2013)
6. Poornima, K.A., Hsu, T.S.: Moving magnet loudspeaker system with electronic compensation". IEEE Proc-Circ. Devices Syst. **148**(4), 211–216 (2001)
7. Ferri, G., Stornelli, V., De Marcellis, A., Flammini, A., Depari, A.: Novel CMOS fully integrated interface for wide-range resistive sensor arrays with parasitic capacitance estimation. Sens. Actuators B **130**, 207–215 (2008)
8. Baschirotto, A., Capone, S., D'Amico, A., Natale, C., Ferragina, V., Ferri, G., Francioso, L., Grassi, M., Guerrini, N., Malcovati, P., Martinelli, E., Siciliano, P.: A portable integrated wide-range gas sensing system with smart A/D front-end. Sens. Actuators B **130**(1), 164–174 (2008)
9. Chapman, P.J.: Thermal simulation of loudspeakers. J. Audio Eng. Soc. **104**, 4667 (1998)

Re-configurable Switched Capacitor Sigma-Delta Modulator for MEMS Microphones in Mobiles

M. Grassi, F. Conso, G. Rocca, P. Malcovati and A. Baschirotto

Abstract This paper presents a reconfigurable discrete-time audio Sigma-Delta modulator implemented in 0.18-μm CMOS technology. The 600 μm × 400 μm core area SD modulator is based on a 2 + 2 MASH architecture, and features several different operating modes in which noise-shaping order, number of output word bits, sampling rate, and bandwidth can be programmed ad hoc. By design, the power consumption is minimized for the selected operating mode. The achieved performance ranges from 99-dB DR with 4th-order noise shaping and full standard audio bandwidth, while consuming 0.97 mW down to 85-dB DR with second order noise shaping over reduced bandwidth for vocal control operation, while consuming 100 μW. The developed device can be used either to read-out different sources (microphones) or to operate in different modes within the same system (i.e. with the same microphone in different scenarios). The trade-off between performance and re-configurability is the key element of this work.

Keywords MASH · Sigma-Delta · Data converter · Microphones
Re-configurable · MEMS

1 Introduction

Audio modules are key elements in most portable devices such as mobile phones, tablets or music players and recorders. For instance, in the latest generation of mobiles, simple processing of the audio signal for calls is not enough anymore:

M. Grassi (✉) · P. Malcovati
Dept. of Electrical, Computer, and Biomedical Engineering,
University of Pavia, Pavia, Italy
e-mail: marco.grassi@unipv.it

F. Conso · G. Rocca
Epcos-Europe-TDK, Copenhagen, Denmark

A. Baschirotto
Dept. of Physics, University of Milano-Bicocca, Milan, Italy

more demanding features such as high-fidelity audio recording, voice commands execution or dictation of text must be available on the device. These new functionalities lead to an enhanced scenario which must deal with an intrinsic trade-off between performance and power consumption. For example, in devices that support voice commands, the audio module must always be active with an extremely low power consumption and a dynamic range (DR) that can be relatively small [1–4]. However, when an input signal is detected, the DR and, therefore, the power consumption can be increased in order to perform the required functions. For example, when the audio acquisition module must be always active to detect voice commands, the bandwidth and DR specifications are of the order of 4 kHz and 70 dB, respectively, accompanied by an extremely limited power consumption (around 100 μW). On the other hand, in Hi-Fidelity applications the required bandwidth is the standard one (20 kHz) and the DR must be larger than 90 dB, accepting a power consumption of the order of mW. [5–7]. This paper reports a reconfigurable Sigma-Delta (SD) modulator, whose performance can be adapted in real time to the function to be performed. In particular, the noise-shaping order can be programmed (second or fourth order), as well as the bandwidth of the signal (4 or 20 kHz), the sampling frequency (780 kHz, 2.4 MHz, or 3.6 MHz), the bias current (50, 75, or 100% of the nominal value) and the number of bits of the digital output word (single-bit, 2-bit).

2   Reconfigurable Sigma-Delta Modulator

The proposed SD modulator [8] is based on a multi-stage noise shaping architecture (MASH), whose block diagram is illustrated in Fig. 1, and consists of two cascaded second-order stages followed by a digital recombination. The DR and the power consumption obtained in the configurations are summarized in Table 1. It is possible to identify three main modes, defined as "low power" (LP), "standard" (ST) and "high resolution" (HR). When second order noise shaping is selected, only the second stage of the MASH structure is active, while the first stage is turned off. The two switched-capacitor SD modulators of the MASH structure are topologically identical, but in the second stage the values of the capacitors and of the bias currents are reduced. The modulator has been fabricated in 0.18-μm technology supporting a variable voltage supply from 1.6 to 3.6 V, typical of battery operated systems thanks to a suitable on-chip linear low dropout voltage regulator.

3   Measurements Results

The chip prototype, whose photo is shown in Fig. 2, features a core area of 0.24 mm^2, including voltage references buffers, which consume 0.29 mW in HR, 0.21 mW in ST, and 30 μW in LP, and the voltage supply regulator (LDO), which
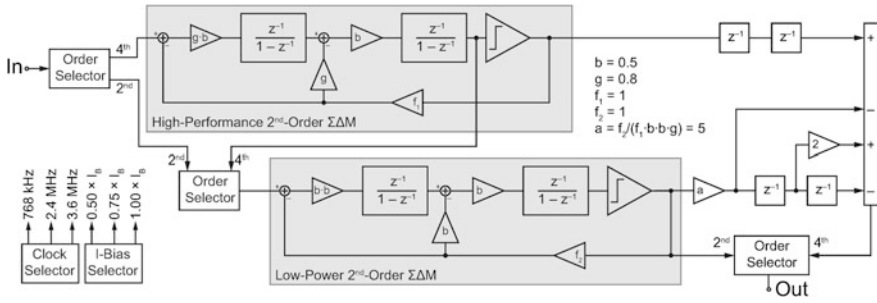
Fig. 1 SD modulator block diagram

Table 1 SD modulator operating configurations and performance

fs[MHz]	B[kHz]	2nd-Order		4th-Order	
		Single-bit DR[dB]	Output P[mW]	Multi-bit DR[dB]	Output P[mW]
0.768	4	**85(LP)**	0.10	99	0.48
	20	59		97	
2.4	4	95	0.15	98	0.73
	20	77		**96(ST)**	
3.6	4	96	0.20	102	0.97
	20	85		**99(HR)**	

consumes 40 µW in HR, ST and 20 µW in LP. The reference voltages $V_{ref,+}$ and $V_{ref,-}$ are set to 500 mV around the common-mode voltage $V_{cm} = 900$ mV (the full-scale voltage of the SD modulator is thus 2 V_{pp}).

The spectra of the SD modulator output signal in HR and LP, obtained with an input signal to 1-kHz are shown in Figs. 3 and 4 respectively.

Fig. 2 Chip microphotograph (core + padring)
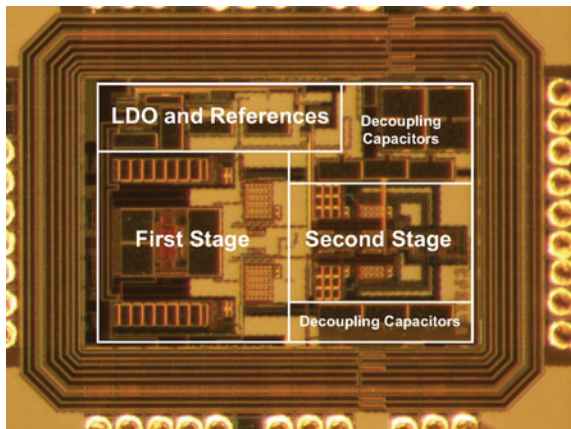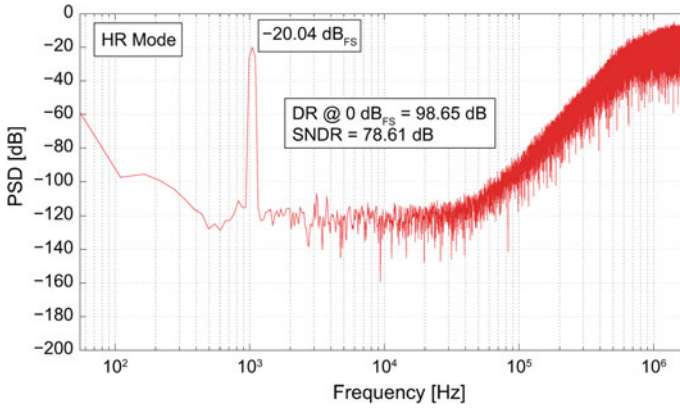
Fig. 3 SD digital output spectrum (HR)
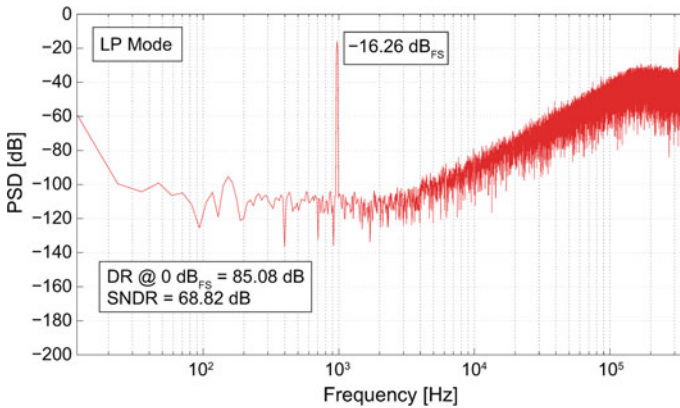
Fig. 4 SD digital output spectrum (LP)

The circuit exhibits a noise shaping of the fourth order in the HR measurement and of the second order in the LP measurement, as expected. The noise floor in HR is about 12 dB lower than in LP due to the reduction of sampling and DAC capacitor values and bias current. Figure 5 shows the signal-to-noise and distortion ratio (SNDR) of the SD modulator as a function of the amplitude of a 1 kHz input signal in HR, ST, and LP configuration.

The circuit achieves a DR of 99 dB in HR, of 96 dB in ST, and of 85 dB in LP configuration respectively. The peak SNDR for large signals is limited in all configurations to about 80 dB due to the harmonic distortion of the source available for the measurements (in the application, considered, the SNDR for audio signals with amplitude larger than 100 dB SPL would be limited in any case to about 75 dB by the harmonic distortion of the MEMS microphone). The optimal SNDR characterization of a SC input SD could be carried out thanks to the availability of an ad
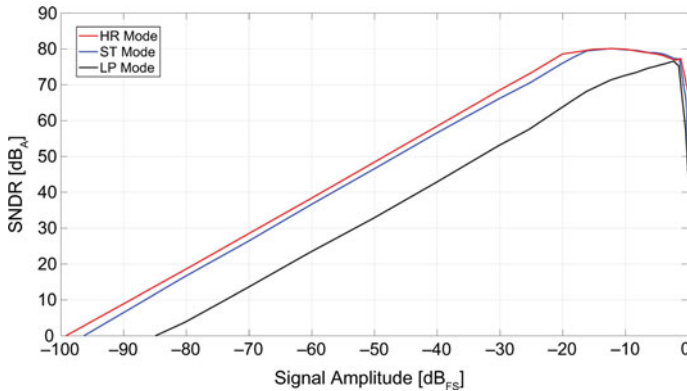
Fig. 5 SD SNDR versus signal amplitude

hoc on-chip pre-amplifier with noise and distortion contributions negligible with respect to the modulator features. Table 1 also summarizes the performances of SD modulator in the three main configurations.

References

1. Badami, K.M.H., et al.: A 90-nm CMOS, 6-mW power-proportional acoustic sensing frontend for voice activity detection. IEEE J. Solid-State Circ. **51**(1), 291–302 (Jan. 2016)
2. Park, H., et al.: A 0.7-V 870-mW digital-audio CMOS sigma-delta modulator. IEEE J. Solid-State Circ. **44**(4), 1078–1088 (Apr. 2009)
3. Yang, Z., et al.: A 0.5-V 35-mW 85-dB DR double-sampled DS modulator for audio applications. IEEE J. Solid-State Circ. **47**(3), 722–735 (Mar. 2012)
4. Christen, T.: A 15-bit 140-mW scalable-bandwidth inverter-based DS modulator for a MEMS microphone with digital output. IEEE J. Solid-State Circ. **48**(7), 1605–1614 (July 2013)
5. Yang, Y.Q., et al.: A 114-dB 68-mW chopper-stabilized stereo multibit audio ADC in 5.62 mm2. IEEE J. Solid-State Circ. **38**(12), 2061–2068 (Dec. 2003)
6. Luo, H., et al.: A 0.8-V 230-mW 98-dB DR inverter-based SD modulator for audio applications. IEEE J. Solid-State Circ. **48**(10), 2430–2441 (Oct. 2013)
7. De Berti, C., et al.: A 106.7-dB DR, 390-mW CT 3rd-order SD modulator for MEMS microphones. In: Proc. ESSCIRC, 209–212 (Sep. 2015)
8. Grassi, M., Conso, F., Rocca, G., Malcovati, P., Baschirotto, A.: A multi-mode SC audio Sigma-Delta Modulator for MEMS microphones with reconfigurable power consumption, noise-shaping order, and DR. In: 42nd European Solid State Conference Proceedings - ESSCIRC 2016, Lausanne, 12–15 September 2016, pp. 245–248, IEEE (2016)

A Low Cost Inclinometer with InkJet-Printed Resistive Readout Strategy

Bruno Andò, Salvatore Baglio, Vincenzo Marletta and Antonio Pistorio

Abstract This paper deals with the prototyping and a preliminary characterization of an InkJet-Printed inclinometer. The developed sensor consists of a thin flexible beam, clamped to a rigid support, with a printed strain gauge to exploit the resistive readout strategy. The voltage at the output of a Wheatstone bridge circuit, where the printed strain gauge is connected, reflects the tilt to be measured. Advantages of the proposed approach are mainly related to the adopted low cost direct printing technology, which allows for the realization of cheap and customizable devices.

Keywords Inclinometer · Inkjet printing · Rapid prototyping

1 Introduction

Inclinometers with high performances are required in a high number of applications including the automotive safety system and many automatic control/sensing systems to improve the life quality of people. The structures of conventional inclinometers can be classified into three categories: solid pendulum, liquid pendulum and gas pendulum [1, 2].

Specifications of reliability, robustness, wide operating range, high sensitivity, and high resolutions are strongly fixed by physical and mechanical parameters. In this sense, printed sensors could be a good solution also to meet the market needs in terms of low costs and small dimensions. Moreover, printed sensors would be strategic for specific contexts where short developing times and low cost features of printing equipment are mandatory.

Compared to traditional silicon electronics, printed sensors are really cheap and can address a wide set of applications requiring low cost and disposable devices [3]. Main techniques for the realization of printed sensors are Screen Printing and InkJet Printing. Screen Printing is based on deposition on a substrate of thick film of

B. Andò (✉) · S. Baglio · V. Marletta · A. Pistorio
DIEEI, Università Di Catania, V.Le a. Doria 6, 95125 Catania, Italy
e-mail: bruno.ando@unict.it

material by the use of masks and a roller pressure mechanism. Many different materials, like conductive, insulating and other functional layers, are available to be deposited on the surface of the substrate and many different typologies of sensors realized by Screen Printing are available in [4–6].

Main drawbacks of Screen Printing are related to the use of masks and waste of materials. Conversely, InkJet Printing is a contactless technique which allows for the real rapid prototyping of electronic component with particular regards to sensors. Interesting advantages of InkJet technologies reside in the direct printing feature, high spatial resolution and compatibility with many substrates. Among materials compatible with InkJet Printing technology, polymers like PEDOT-PSS (3, 4-ethylen dioxythiophene) and PANI (Polyaniline) and conductive silver nanoparticles are widely used.

The possibility to print both conductors and functional layers by low cost printers is a great advancement in terms of effective solutions for the rapid prototyping of sensors [7, 8]. Examples of devices developed by low cost InkJet printers are available in [9–17].

This paper focuses on the development of an InkJet-Printed inclinometer. The device consists of a thin flexible beam clamped to a rigid support along a short edge. A strain gauge has been printed between the beam and the rigid support in order to implement the resistive readout strategy of the developed sensor. In correspondence of the second short edge of the beam, a proof-mass has been placed to enhance the strain along the vertical axis due to the action of the gravity force. When the device is tilted, the inclination measured from the sensor is a function of the resistance variation of the printed strain gauge. The latter is detected with a Wheatstone bridge circuit.

In the following sections are described some details about the working principle, the conditioning electronics and the theoretical aspects of the inclinometer developed. The results of the static characterization and the dynamic behavior are also included.

2 An Overview of the System Developed

The layout designed with a CAD tool and a real view of the developed InkJet-Printed sensor is shown in Fig. 1a, b, respectively. The sensor consists of a strain gauge printed in correspondence of a short edge of a flexible beam of PET (polyethylene terephthalate). The beam thickness is 140 µm. The coil in the upper part of the beam has been printed for future applications of the sensor.

The PET beam is 70 mm long and 19 mm wide. The device dimensions have been fixed on the basis of the technology and application driven constraints. In particular, the printed strain gauge is 10 mm long and 10 mm wide; the spacing and the track width are 300 µm. The resistance of the printed strain gauge, R_s, measured by a digital multimeter is 186.3 Ω.

The printing process adopted to realize both the strain gauge and the coil on the PET substrate uses a low cost Stylus Office BX535WD piezo inkjet printer (Epson,
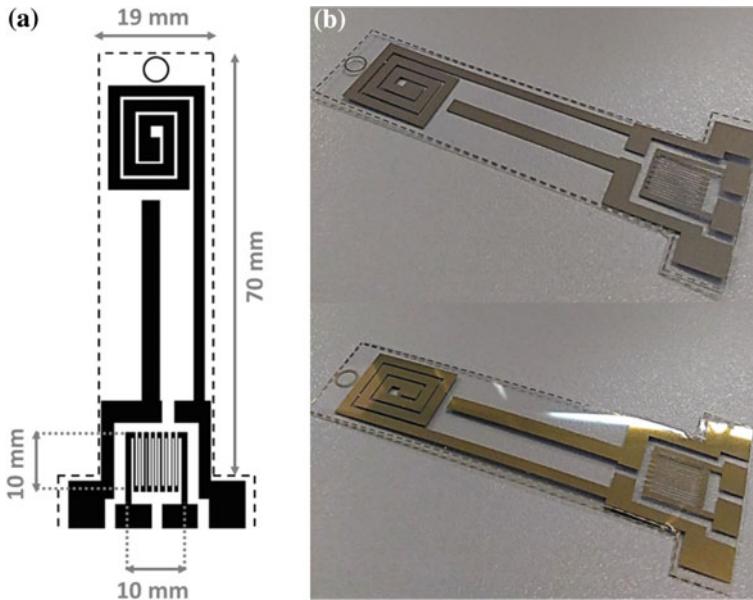
Fig. 1 The developed InkJet-Printed sensor: **a** layout; **b** top and bottom real views

Suwa, Japan) and a metal ink for the realization of conductive patterns. The latter is the silver nano-particles solution "Metalon® JS-B15P" by Novacentrix (Austin, TX, USA). The adopted PET substrate is the Novele™ IJ-220 Printed Electronics Substrate by Novacentrix, suited to low-cost and low-temperature applications and specifically engineered for inkjet-compatible conductive inks. The thickness of the silver layer on the PET substrate is 200 nm.

In order to implement the electric contact between the beam components and the conditioning electronic, a clamping system has been developed. It consists of a sandwich structure clamping the PET substrate and a patterned contacting support realized by Printed Circuit Board (PCB) technology. The clamping system blocks the printed strain gauge to about half of its length. Moreover, for the sake of convenience, a commercial strain gauge has been bonded on the printed sensor.

The inclinometer has been finalized as shown in Fig. 2. The beam has been blocked on a rigid support in correspondence of the clamping system and the InkJet-Printed strain gauge. On the second edge of the beam has been placed a proof-mass which magnifies the flection of the beam even at equilibrium position (tilt angle 0°) for the gravity force perpendicular to the beam. When the inclinometer is tilted, which means that the device is rotated clockwise or counterclockwise along the sensing axis, the measured inclination is a function of the strain of the beam. The latter causes a negative/positive variation of the resistance of the printed strain gauge depending on the rotation clockwise/counterclockwise of the device. Essentially, the printed strain gauge implements a resistive readout strategy through the monitoring of the beam strain.
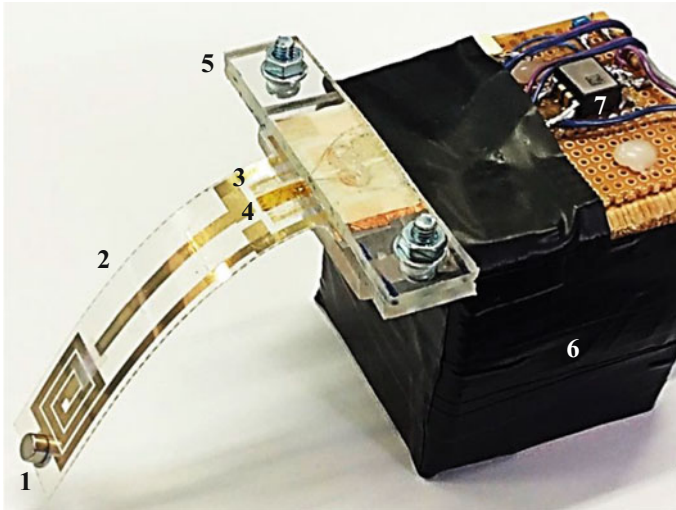
Fig. 2 The final assembly of the inkjet-printed inclinometer: *1* proof-mass; *2* beam of PET; *3* printed strain gauge; *4* commercial strain gauge; *5* clamping system; *6* rigid support; *7* reference inclinometer

A dedicated conditioning electronics has been implemented. It consists of a Wheatstone bridge circuit and an instrumentation amplifier. The electrical scheme of the conditioning electronics is shown in Fig. 3. Referring to this figure, R_s is the resistance of the developed sensor. The values of the other resistors have been chosen as follows: $R_1 = R_2 = R_d = 180 \, \Omega$. A first trimmer, $TR_1 = 200 \, \Omega$, has been included to easily compensate the bridge balance for the effect of tolerance in all the resistor values, including the sensors. The supply voltage of the Wheatstone bridge has been fixed to 2.5 V to cope with the maximum current value allowable for the printed sensors (in the order of few mA). In a future release of the device a dummy gauge will be included to compensate for the effect of the temperature fluctuations. In the present version an independent measurement of the temperature has been performed by a dedicated temperature sensor. The instrumentation amplifier INA111 amplifies the output voltage of the Wheatstone bridge. A second trimmer, $TR_G = 50 \, \Omega$, adjusts the gain of the amplifier. The supply voltage of the INA111 has been fixed to ± 15 V.

3 Theoretical Expectations and Device Characterization

Starting from the equilibrium position ($\theta = 0°$), when the InkJet-Printed inclinometer rotates clockwise or counterclockwise along the sensing axis (which means that an inclination occurs) the vertical component of the gravity force which acts on the beam through the proof-mass is reduced by a geometrical factor corresponding
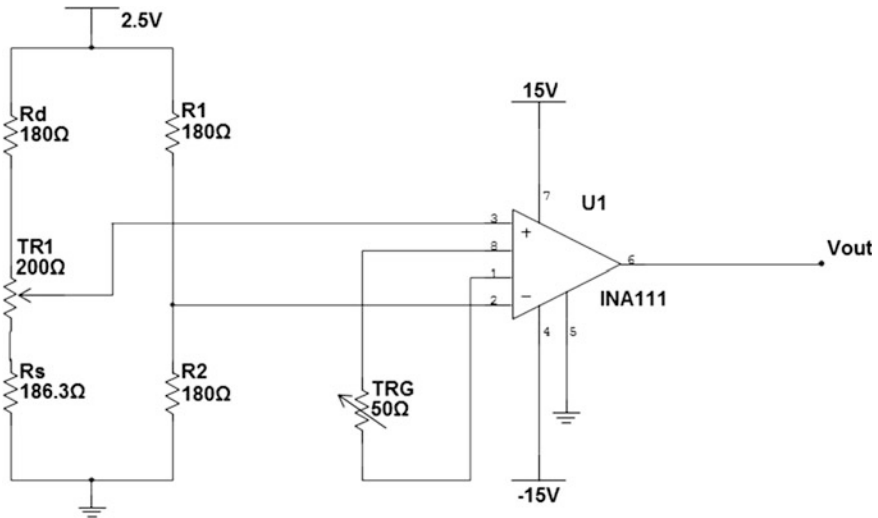
Fig. 3 Electrical scheme of the conditioning electronics

to the contribution of the projection of the gravity force. The predicted trend of the resistance variation of the printed strain gauge due to the strain of the beam can be expressed as follows:

$$\frac{\Delta R}{R_s} = k_1\theta + k_2 \tag{1}$$

where ΔR is the resistance variation of the printed strain gauge with respect to R_s, θ is the tilt occurred, k_1 is the gain factor and k_2 is the offset.

$\Delta R/R_s$ derives from the output voltage of the conditioning electronics. The parameters k_1 and k_2 have been estimated with a fitting algorithm described in the following.

The InkJet-Printed inclinometer has been characterized by fixing the device on a movable platform. The used movable platform is able to provide the target tilt through a step motor with a resolution of 0.06°. The reference inclinometer SCA61T-FA1H1G by Murata Electronics Oy (see Fig. 2) has been used to achieve an independent measurement of the target tilt. This sensor is a MEMS-based single axis inclinometer characterized by a resolution of 0.0025° in the operating range of ± 90°. The analog output voltages of the conditioning electronics and of the reference sensor, the digital signals to drive the step motor and the signal processing tasks have been managed through the NI USB-6002 data acquisition device by National Instruments and a dedicated LabVIEW™ interface.

The InkJet-Printed inclinometer has been characterized for a proof-mass of 0.873×10^{-3} kg placed at 3 mm from the upper edge of the beam.

The InkJet-Printed inclinometer has been tilted from 0° to 90°. For each tilt step, five consecutive measurements at the sampling frequency of 10 kHz have been acquired from the output of the conditioning electronics. With the aim to fit the experimental data to the predicted trend (Eq. 1), the Nelder-Mead optimization algorithm has been used. The following functional J, computing the root mean square of residuals between the observed output voltage, $V_{out}^{imp,obs}$, and the predicted one, $V_{out}^{imp,pred}$, was used by the minimization algorithm:

$$J = \frac{\sqrt{\sum_i^N (V_{out}^{imp,obs} - V_{out}^{imp,pred})^2}}{N} \tag{2}$$

The following values of k_1 and k_2 have been estimated: $k_1 = 1.87 \times 10^{-5}(°)^{-1}$, $k_2 = 7.46 \cdot 10^{-6}$. The fitting of the predicted trend (Eq. 1) to the experimental data is shown in Fig. 4a. The calibration diagram is shown in Fig. 4b; the uncertainty band

Fig. 4 a fitting of the predicted trend (Eq. 1) to the experimental data; **b** inclinometer calibration diagram
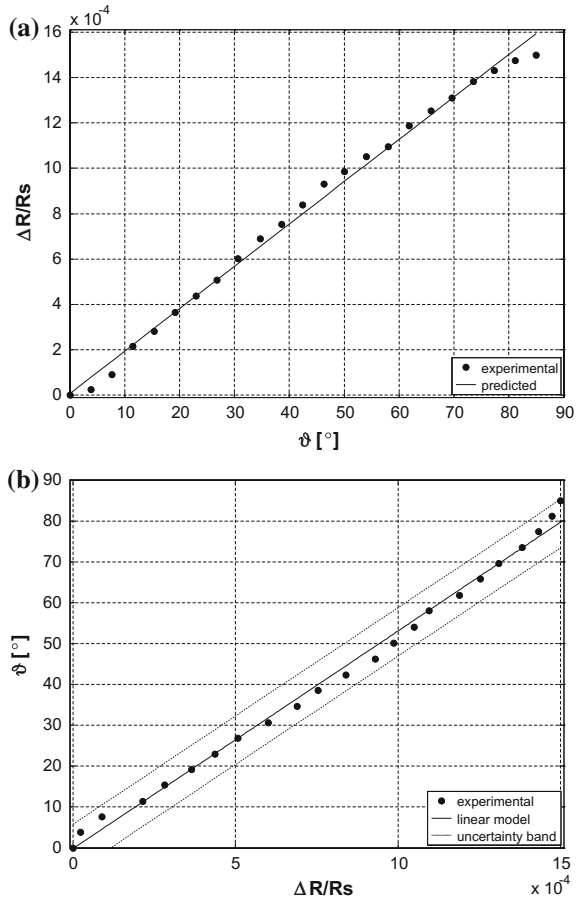
Fig. 5 Experimentally observed output voltage of the readout electronics to an impulsive stimulus
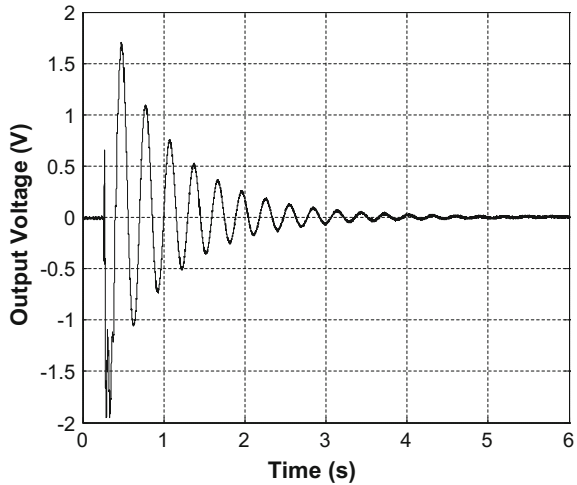
has been estimated in the 3σ level (where σ is the standard deviation of the residuals between the linear model and the experimental data).

The device responsivity is $1.9 \times 10^{-5}(\Delta R/R_s)\cdot(°)^{-1}$. The device resolution, estimated as the ratio between the standard deviation of the sensor response and the responsivity in case of a null stimulus, is $0.5°$.

The obtained operating range is $(0°-85°)$.

The impulse response of the sensor has been experimentally detected. The experimental response provided by the conditioning electronics to an impulse stimulus is shown in Fig. 5. The mean value of the observed natural frequency is $f_n = 3.38$ Hz. According to the value predicted during the design phase, a spring mass constant of 0.394 N/m has been estimated.

The predicted trend for the impulse response is given by

$$V_{out}^{imp,pred} = A \frac{e^{-\xi\omega_n t}}{\sqrt{1 - \xi^2}} \sin(\omega_n t) \tag{3}$$

where A is the measured signal amplitude, $\omega_n = 2\pi f_n$, ξ is the damping factor.

By fitting the experimental response of Fig. 5 to the predicted trend (Eq. 3), with the abovementioned Nelder-Mead optimization algorithm a damping factor of 0.056 has been estimated.

4   Conclusion

In this paper a InkJet-Printed inclinometer with resistive readout strategy has been presented. The working principle, the conditioning electronics, the theoretical aspects, the static characterization and the dynamic behavior have been discussed.

The observed performances of the developed device, taking into account the proof-of-concept nature of the lab-scale prototype, are encouraging in view of further developments.

Advantages of the sensor architecture proposed are related to the embedded strain sensing feature, the layout flexibility and ease with which it adapts to application requirements and the low cost technology and materials adopted.

References

1. Lin, C.H., Kuo, S.M.: High-performance inclinometer with wide-angle measurement capability without damping effect., In: Proceedings of the 20th IEEE International Conference on Micro Electro Mechanical Systems, Kobe, Japan, 21–25 January 2007, pp. 585–588
2. Mescheder, U., Majer, S.: Micromechanical inclinometer. Sens. Actuators **A60**, 134–138 (1997)
3. Mäntysalo, M., Pekkanen, V., Kaija, K., Niittynen, J., Koskinen, S., Halonen, E., Mansikkamäki, P., Hämeenoja, O.: Capability of Inkjet technology in electronics manufacturing. In: Electronic Components and Technology Conference, San Diego, CA, US, 26–29 May 2009, pp. 1330–1336
4. Unander, T., Nilsson, H.E.: Characterization of printed moisture sensors in packaging surveillance applications. IEEE Sens. J. **9**(8), 922–928 (2009)
5. Lakhmi, R., Debeda, H., Dufour, I., Lucat, C.: Force sensors based on screen-printed cantilevers. IEEE Sens. J. **10**(6), 1133–1137 (2010)
6. Jacq, C., Lüthi, B., Maeder, T., Lambercy, O., Gassert, R., Ryser, P.: Thick-film multi-DOF force/torque sensor for wrist rehabilitation. Sens. Actuators A Phys. **162**, 361–366 (2010)
7. Andò, B., Baglio, S.: Inkjet-printed sensors: a useful approach for low cost, rapid prototyping. IEEE Instrum. Meas. Mag. **14**(5), 36–40 (2011)
8. Andò, B., Baglio, S., Bulsara, A.R., Emery, T., Marletta, V., Pistorio, A.: Low-cost inkjet printing technology for the rapid prototyping of transducers. Sensors **17**(4) (April 2017), Article number 748
9. Crowley, K., Morrin, A., Hernandez, A., O'Malley, E., Whitten, P.G., Wallace, G.G., Smyth, M.R., Killard, A.J.: Fabrication of an ammonia gas sensor using inkjet-printed polyaniline nanoparticles. Int. J. Pure Appl. Anal. Chem. **77**(2), 710–717 (2008)
10. Andersson, H., Manuilskiy, A., Unander, T., Lidenmark, C., Forsberg, S., Nilsson, H.-E.: Inkjet printed silver nanoparticle humidity sensor with memory effect on paper. IEEE Sens. J. **12**(6), 1901–1905 (2012)
11. Andò, B., Baglio, S.: All-Inkjet printed strain sensors. IEEE Sens. J. **13**(12), 4874–4879 (2013)
12. Lorwongtragool, P., Sowade, E., Watthanawisuth, N., Baumann, R.R., Kerdcharoen, T.: A novel wearable electronic nose for healthcare based on flexible printed chemical sensor array. Sensors **14**, 19700–19712 (2014)

13. Andò, B., Baglio, S., Marletta, V., Pistorio, A.: A contactless InkJet printed passive touch sensor. In: Instrumentation and Measurement Technology Conference (I2MTC 2014) Proceedings, 2014 IEEE International, Montevideo, Uruguay, 12–15 May 2014
14. Andò, B., Baglio, S., Lombardo, C.O., Marletta, V., Pistorio, A.: A low-cost accelerometer developed by Inkjet printing technology. IEEE Trans. Instrum. Meas. **65**(5), 1242–1248 (2015)
15. Andò, B., Baglio, S., Di Pasquale, G., Pollicino, A., D'Agata, S., Gugliuzzo, C., Lombardo, C.O., Re, G.: An Inkjet Printed CO_2 Gas Sensor. In: XXIX Eurosensors 2015 Proceedings, Freiburg, Germany, 6–9 September 2015
16. Andò, B., Baglio, S., Marletta, V., Pistorio, A.: "All Inkjet-Printed B Field Sensor," accepted for oral presentation in XXXI Eurosensors 2017, Paris, France, 3–6 September 2017
17. Andò, B., Baglio, S., Bulsara, A.R., Marletta, V., Ferrari, V., Ferrari, M.: A Low-cost snap-through buckling Inkjet printed device for vibrational energy harvesting. IEEE Sens. J. **15**(6), 3209–3220 (2015)

Dual Wavelength Botda
for Strain/Temperature Discrimination

A. Minardo, E. Catalano, A. Coscetta and L. Zeni

Abstract The sensitivity of Brillouin Frequency Shift (BFS) to strain and temperature has been studied in a bending-loss insensitive fiber (BIF), at two different wavelengths (850 and 1550 nm). The results show that the ratio between strain sensitivity at the two wavelengths is different from the ratio between temperature sensitivity, which can be conveniently used for simultaneous and distributed measurement of the two parameters using a single sensing element. Experimental results, carried out at 1-m spatial resolution, demonstrate the feasibility of the proposed method.

Keywords Fiber optic sensors · Strain measurement · Temperature measurement

1 Introduction

Optical fiber sensors based on Brillouin scattering are traditionally operated at 1.32 or 1.55 μm wavelength [1, 2], in order to leverage the very low propagation loss of silica fibers at these wavelengths. Recently, we have demonstrated the feasibility of Brillouin Optical Time-Domain Analysis (BOTDA) at 850 nm wavelength [3]. The investigation of the 850-nm window may open new perspectives in Brillouin sensing. For example, single-mode optical fibers exhibit a larger power Brillouin gain coefficient at 850 nm, compared to single-mode optical fibers operated at 1550 nm. Furthermore, both temperature and strain sensitivity of the BFS increase, as they roughly scale with the inverse of the wavelength. Finally, it has been suggested that measuring the BFS along the same fiber at two widely separated wavelengths, may provide a mechanism for separating the effects of temperature and strain [3]. In this work, we make use of a bending-loss insensitive fiber (BIF) for simultaneous measurement of strain and temperature.

A. Minardo (✉) · E. Catalano · A. Coscetta · L. Zeni
Department of Industrial & Information Engineering, Università Degli Studi Della
Campania "Luigi Vanvitelli", Via Roma 29, Aversa, Italy
e-mail: Aldo.Minardo@unicampania.it

2 Experimental Results

A G657-B3 BIF has been characterized in terms of BFS sensitivity to temperature
and strain, using two different Brillouin Optical Time-Domain Analysis (BOTDA)
equipment, a conventional one operating at 1550 nm, and the other one operating at
850 nm [3]. Figure 1 shows the set-up used for the experiments. Two 850/1550
WDM (wavelength-division-multiplexers) couplers (Haphit Ltd) were used in order
to combine (and separate) the pump and probe signals interacting along the sensing
fiber. In particular, each WDM coupler combines the pump (or probe) beams
provided by the two BOTDA units, in order to launch them simultaneously into the
sensing fiber. In addition, the upper WDM coupler re-directs the back-scattered
signal at each wavelength towards the corresponding BOTDA unit. This scheme
allows us to acquire the BFS distribution simultaneously at the two wavelengths.
This is important because, in case of sequential measurements at the two wave-
lengths, possible variations of the temperature (or strain) conditions of the fiber may
result in errors in the determination of these two parameters.

At 1550 nm wavelength, the measured sensitivities of the BFS to temperature
and strain are 1.056 MHz/°C and 47 kHz/με, respectively. Vice versa, at 850 nm
wavelength the retrieved sensitivities are 2.296 MHz/°C and 85 kHz/με, respec-
tively. Note that, the ratio between strain sensitivities is ≈1.81, i.e. very close to the
wavelength ratio (≈1.82). In other words, the different strain sensitivities can be
fully explained in terms of wavelength diversity. Vice versa, the ratio between
temperature sensitivities is 2.17, thus quite larger than the wavelength ratio (note
that strain/temperature discrimination is actually possible in virtue of this diversity).
The "boost" of temperature sensitivity at shorter wavelength can be explained, by
considering that the 850 nm light is more concentrated around the core axis, so it is
less influenced by the regions of depressed index around the core of the BIF, which
reduce the temperature sensitivity of the BFS at 1550 nm [4].

We have carried out a proof-of-concept experiment over the BIF fiber. A 1.40 m
portion of the fiber was subjected to ≈3000 με tensile strain, while another 2.5 m
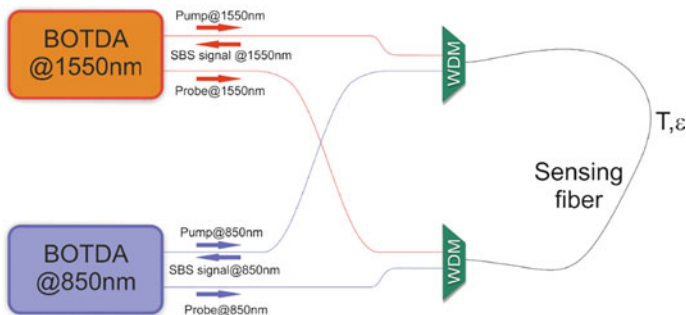
Fig. 1 Experimental set-up used for dual wavelength BOTDA measurements

piece was heated at T $\approx$62 °C by immersion in a water bath. Room temperature was $\approx$25 °C. The BFS profiles measured at 1550 and 850 nm and a spatial resolution of 1 m for both systems are shown in Fig. 2a. Solving the system of linear equations expressing the BFS changes as a function of strain and temperature [5], we obtain the temperature and strain changes shown in Fig. 2b, c, respectively. The results demonstrate that the system is capable of strain/temperature separation.
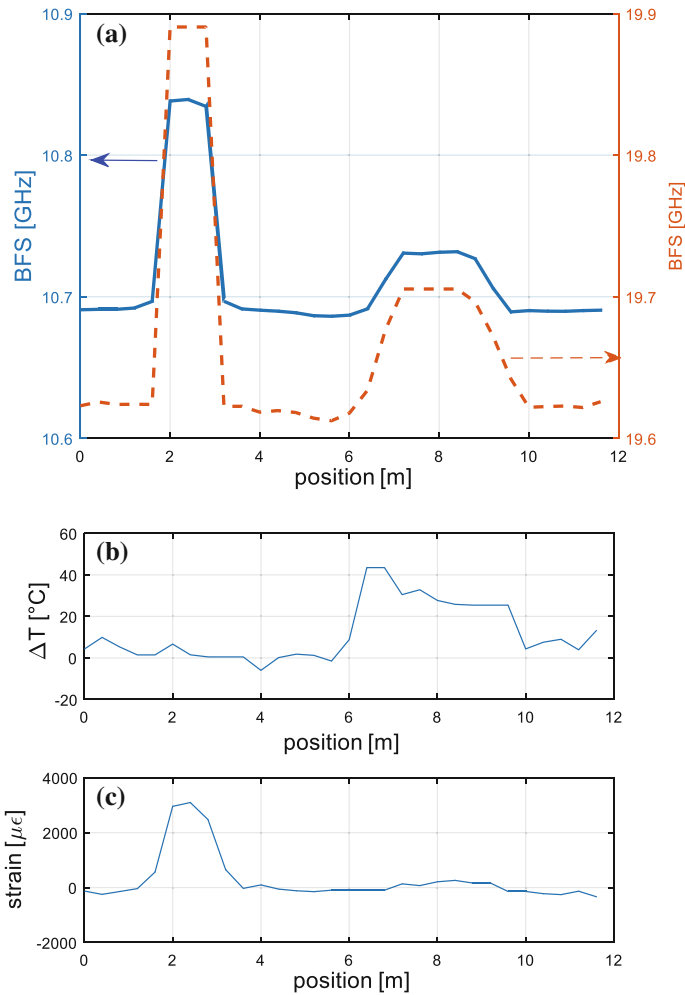
Fig. 2 a BFS measured at 1550 nm (*blue solid line*) and 850 nm (*red dashed line*); **b** temperature profile and **c** strain profile reconstructed using the two BFS profiles shown in (**a**) (color figure online)

3   Conclusions

A dual wavelength BOTDA scheme has been proposed and demonstrated for simultaneous strain and temperature measurements using a bending-loss insensitive fiber, at 1-m spatial resolution. Better accuracy may be achieved by improving the SNR of BOTDA measurements at the two wavelengths and/or by selecting a fiber with a higher wavelength-based discriminative BFS sensitivity.

References

1. Bao, X., Chen, L.: Recent progress in Brillouin scattering based fiber sensors. Sensors **11**(4), 4152–4187 (2011)
2. Thévenaz, L.: Brillouin distributed time-domain sensing in optical fibers: state of the art and perspectives. Frontiers of Optoelectronics in China **3**(1), 13–21 (2010)
3. Minardo, A., Coscetta, A., Bernini, R., Zeni, L.: Brillouin optical time domain analysis in Silica fibers at 850-nm wavelength. IEEE Photon. Technol. Lett. **28**(22), 2577–2580 (2016)
4. Zou, W., He, Z., Hotate, K.: Investigation of strain- and temperature-dependences of Brillouin frequency shifts in GeO_2 -doped optical fibers. J. of Lightw. Technol. **26**(13), 1854–1861 (2008)
5. Zou, W., He, Z., Hotate, K.: Complete discrimination of strain and temperature using Brillouin frequency shift and birefringence in a polarization-maintaining fiber. Opt. Express **17**, 1248–1255 (2009)

Electrical Characterization of Microstrip Resonators Based on Nanostructured Sensing Materials

**G. Gugliandolo, A. Mirzaei, M. Bonyani, G. Neri,
M. Latino and N. Donato**

Abstract In this paper is reported the development of microstrip resonators working in the frequency range of 3–6 GHz and their employment in the investigation of the sensing properties of nanostructured materials towards gas. The materials are deposited as films on the gap of the resonators by drop coating aqueous solutions of Ag@α-Fe$_2$O$_3$ nanocomposite having a core–shell structure. Here are reported sensing data about humidity monitoring in the range from 0 to 70%. The increase of humidity value brings to a large frequency shift of the resonance one. The good characteristics of the fabricated device suggest its promising use as humidity sensor.

Keywords Microwave sensors · Ag@α-Fe$_2$O$_3$ nanocomposite · Humidity sensors

1 Introduction

The research of new typologies of sensors with low power consumption features is today one of the areas of greatest interest in the market. Low power sensors can be easily connected in sensors networks, with the right balance between sensor performance and battery lifetime [1]. In such a frame, a relatively new category of sensors can be represented by microwave devices with interesting properties in terms of fast response, low power, fully compatibility with wireless technologies and room temperature working [2].

G. Gugliandolo
Department of Electronics and Telecommunications, Politecnico di Torino, Turin, Italy

A. Mirzaei · M. Bonyani
Department of Materials Science and Engineering, Shiraz University, Shiraz, Iran

G. Neri (✉) · M. Latino · N. Donato
Department of Engineering, University of Messina, Messina, Italy
e-mail: gneri@unime.it

Microwave sensor devices can be included in conductometric transducers category, with a slightly different mechanism of transduction than traditional ones, because in these sensors typology the change of permittivity of sensitive layer is involved in the transduction process. The possibility to balance between the sensing material properties and the resonator configuration for design of the sensor make them very versatile for different applications. Microstrip technology is widely employed in the design of microwave resonators and filters and can be successfully used in the development of such sensors.

In this work, we investigate a resonant microstrip structure with a circular disk geometry and coated by a nanostructured sensing layer. In such a context, microstrip resonators are designed and realized in a frequency range spanning from 3 to 6 GHz, then sensing films are deposited on the resonator's surface. Accordingly with the geometry ensuring the motion of an electromagnetic wave in the microwave range through the sensing layer, the reflected wave on the material should be modified, namely attenuated and/or out of phase.

Here, we investigate a resonant microstrip structure with a circular disk geometry by coating it with a humidity sensitive layer. Humidity monitoring is of outmost importance in many technological fields. For this reason, there is still a substantial interest in the development of new simple humidity sensors with high performances. In this investigation, Ag@α-Fe$_2$O$_3$ nanocomposite, synthesized by a simple two-step reduction-sol gel approach [3], was used as humidity sensing layer. The high porosity of the nanostructure is a beneficial factor for enhancing the interaction with water vapor and this would lead to a higher sensitivity of the microstrip resonator towards humidity.

2 Experimental

2.1 Sensing Material Synthesis

Ag@α-Fe$_2$O$_3$ composite nanostructure was synthesized by a two-step reduction-sol gel approach [3]. First, Ag nanoparticles were synthesized as follows. The solutions of PVP and AgNO$_3$ were prepared by dissolving appropriate amounts of PVP (about 20 wt%) and AgNO$_3$ in redistilled water in separate well-cleaned dry beakers at room temperature and ice-bath temperature respectively. PVP solution and AgNO$_3$ solution were subsequently mixed and magnetically stirred for 30 min. Ice bath was used to slow down the reaction and give better control over final particle size/shape. Then, 20 mM (10 ml) NaBH$_4$ was added drop wise (about 1 drop/second, until it is all used up) under vigorous stirring and the solution stirred for another 30 min. Upon sodium borohydride addition, the color of the solution slowly turned into pale yellow, indicating the reduction of the Ag + ions. The above solution was purified by washing it with water and separating the Ag/PVP

solid phase obtained by centrifugation and successive drying. The silver nanoparticles were separated from the remaining part of above solution after adding a large amount of acetone ($\sim 5 \times$ the total solution volume) followed by centrifugation at 4000 rpm for 60 min and then washed three times with distilled water and acetone to remove organic species. Successively, the silver nanoparticles were ultrasonically re-dispersed in water. Then, the pH of the Ag colloid solution was firstly adjusted to 10.5 by adding 0.1 M NaOH solution. The solution was maintained at 70 °C for 30 min and 25 mL (100 mM) of fresh iron sulphate at the rate of 0.1 ml/min was added and the resulting solution was stirred for 30 min. Finally, the mixture was refluxed for 2 h under moderate stirring at 70 °C. The composite Ag@iron oxide so formed was separated by centrifugation.

2.2 Microwave Sensor Fabrication

The resonator was realized with the LPKF Protomat S103 rapid prototyping system on an FR4 substrate, with a relative dielectric constant ε_r of 4.3, a thickness of 3.2 mm, and two copper layers of 35 μm. The prototype was equipped with a SMA connector to provide the connection with the VNA Agilent 8753ES. Two resonant frequency values at 3.729 and 5.505 GHz, respectively, were observed. A schematic view of the microwave resonator and its main parameter values, is reported in Fig. 1.

The resonator was coated by drop coating on the gap with an aqueous solution of Ag@α-Fe$_2$O$_3$ nanocomposite. The MW sensor prototype was tested in the monitoring of relative humidity (RH), in a range spanning from 0 to 70%, in a test chamber with controlled atmosphere provided with an RF feed-through for the VNA connection.

Parameter	Value (mm)
W	67.2
L	49.26
d_1	2.0
d_2	30.22
g_1	0.2
g_2	2.1
l_m	15.86
2r	6.0
s	2.1
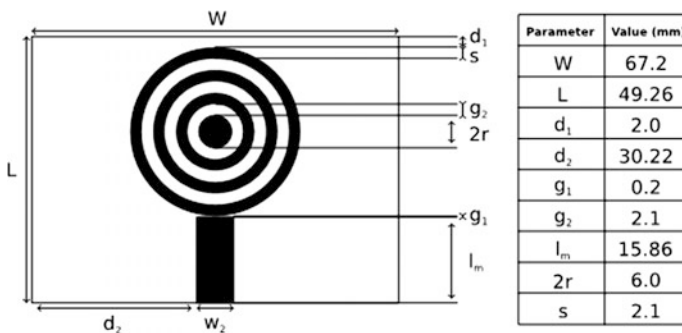
Fig. 1 Resonator topology

3   Results and Discussion

In Fig. 2a is reported a picture of the microstrip resonator transducer, consisting of a resonant disk with external rings coupled to a microstrip line through a small gap (approximatively 200 μm), with a characteristic impedance of 50 Ω.

Figure 2b shows a SEM image of the synthesized Ag@iron oxide surface. The nanostructure of the material can be easily observed; furthermore, an elevated fraction of the material is characterized by the presence of voids. The elemental analysis of the sample by EDX (see inset) shows the presence of Ag, Fe and O as the main elements.

S_{11} parameter measurement have been carried out in the 3–6 GHz frequency range, through the setup in Fig. 3. In the graph is reported the shift of the resonant frequency values at 3.729 and 5.505 GHz, respectively, before and after the deposition of the sensing layer.

The MW sensor was then characterized towards relative humidity at several concentration values in the range spanning from 0 to 70%. The presence of humidity brings to a decreasing of the resonance frequency value of the device with a corresponding frequency shift in magnitude and phase. In Fig. 4a is reported the phase of S_{11} towards humidity values.

In Fig. 4b is reported the resonance frequency shift for both resonance values. It is noteworthy the high sensitivity observed at low relative humidity value, where many humidity sensors based on metal oxide fails. Furthermore, by comparing the two data sets, it can be noted as the higher resonance peak brings to a larger frequency shift.

In summary, we reported here results achieved in the development of a microstrip resonator with nanostructured sensing materials and its employment as resonant transducer for relative humidity sensing. The increase of humidity value brings to a frequency shift of the resonance one, allowing to measure relative humidity in a large range of concentration. Further activities are in progress to evaluate the response to different gas targets.
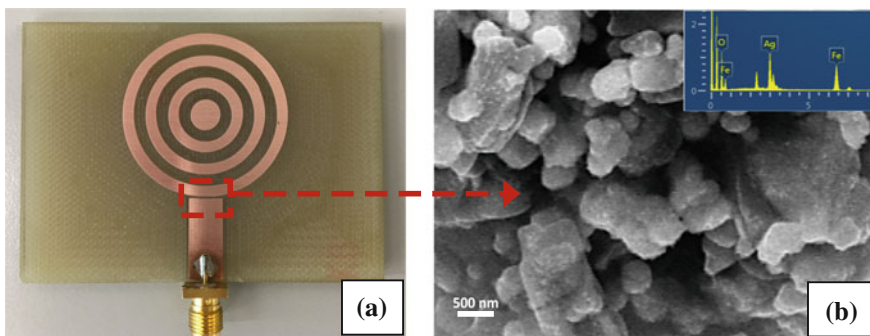
Fig. 2 **a** Picture of the microstrip resonator transducer; **b** SEM image of the surface of the sensing layer. In the inset is reported the EDX analysis
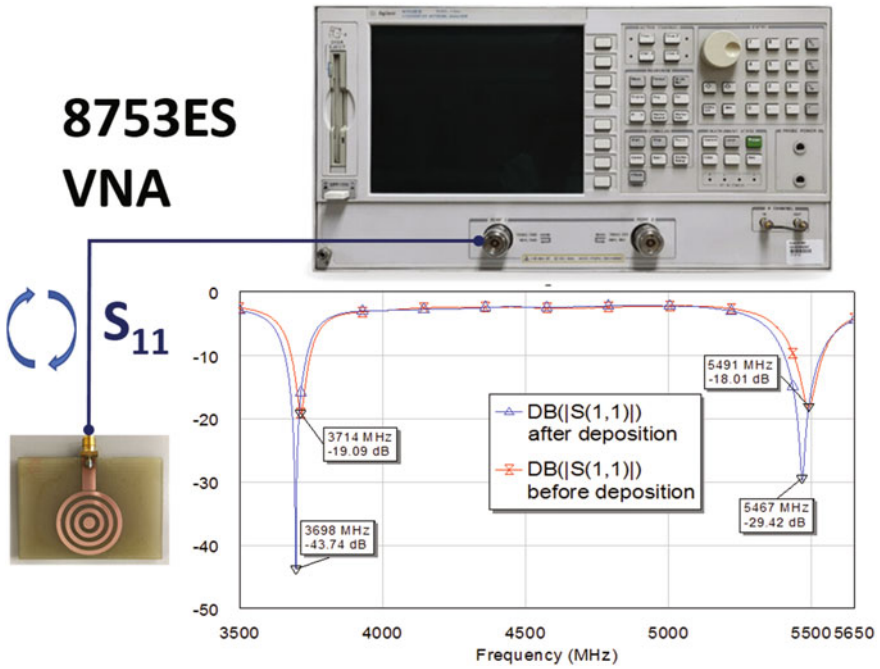
Fig. 3 Measurement setup. S_{11} measurement in the 3–6 GHz frequency range, for both uncoated and coated device, is also shown
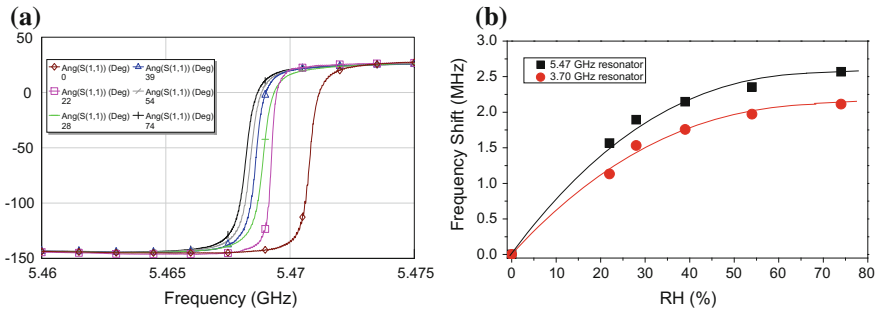
Fig. 4 **a** S_{11} phase of 5.47 GHz resonator versus relative humidity; **b** Frequency shift versus relative humidity for 3.70 and 5.47 GHz resonance values

References

1. Zhang, J., Liu, X., Neri, G., Pinna, N.: Nanostructured materials for room-temperature gas sensors. Adv. Mater. **28**, 795–831 (2016)
2. Barochi, G., Rossignol, J., Bouvet, M.: Development of microwave gas sensors. Sens. Actuators, B **157**, 374–379 (2011)
3. Mirzaei, A., Janghorban, K., Hashemi, B., Bonavita, A., Bonyani, M., Leonardi, S.G., Neri, G.: Synthesis, characterization and gas sensing properties of Ag@α-Fe2O3 core-shell nanocomposites. Nanomaterials **5**, 737–749 (2015)

Graphene Decoration for Gas Detection

**Brigida Alfano, Ettore Massera, Maria Lucia Miglietta,
Tiziana Polichetti, Chiara Schiattarella and Girolamo Di Francia**

Abstract A comparison among the gas sensing properties of pristine graphene and graphene decorated with noble metal nanoparticles is herein investigated. Pristine graphene sheets are realized using the Liquid Phase Exfoliation method; noble metal decoration (namely platinum and palladium) is performed by a facile one-step chemical procedure which relies on the reduction of metal precursor salts directly onto graphene surface. All the materials have been employed as chemical sensing layer in a conductometric structure and tested towards some key analytes of interest for environmental monitoring, namely NO_2, NH_3 and H_2. The device based on pristine graphene exhibits a specific response to NO_2, whereas the device based on palladium-decorated graphene is more sensitive towards hydrogen. The third typology of device, based on graphene functionalized with platinum, shows a poorly selective behaviour. Unexpectedly, thanks to the remarkable stability of the material, this apparent drawback can be profitably exploited and overcome by integrating the sensing devices into an array, which enables to discriminate hydrogen from ammonia.

Keywords Metal decoration · Graphene functionalization
Room temperature device

1 Introduction

Graphene attracts a great interest in gas sensor field due to its exceptional electric properties. Most of the literature confirms that pristine graphene is able to "sense" several compounds with a peculiar sensitivity to nitrogen dioxide [1, 2]. In this

B. Alfano (✉) · E. Massera · M.L. Miglietta · T. Polichetti · G. Di Francia
ENEA, P. le E. Fermi 1, I-80055 Portici (Naples), Italy
e-mail: brigida.alfano@enea.it

C. Schiattarella
University of Naples Federico II, Via Cinthia 26, 80126 Naples, Italy

regard, the functionalization of graphene with metal nanoparticles proves to be an effective way to extend the range of analytes to which the material is sensitive [3–9].

In view of this premise, a comparison among chemical devices based on pristine graphene (GR) and graphene decorated with platinum nanoparticles (PtNPs-GR) or palladium nanoparticles (PdNPs-GR) has been performed in order to study the effect of metallic nanoparticles on the gas sensing properties.

The composites have been morphologically characterized by atomic force microscopy (AFM) and scanning electron microscopy (SEM) coupled with Energy Dispersive X-Ray Analyser (EDX) to provide elemental identification and quantitative compositional information. Moreover, the sensing behaviour of graphene/metal nanoparticles hybrids has been compared to those of pristine graphene. Data confirm the functionalization-induced modulation of the sensing properties: after graphene decoration with both PdNPs and PtNPs, a loss of specificity towards nitrogen dioxide and an increased sensitivity to hydrogen is observed. Although the device based on Pt shows to be poorly able to distinguish between ammonia and hydrogen, a combination of all the devices can be profitably employed into an array of sensors, by exploiting the different adsorption kinetics to discriminate the two analytes thanks to the remarkable stability of all the investigated materials.

2 Materials and Method

A colloidal suspension of graphene has been prepared by liquid phase exfoliation (LPE) [10]. The process consists of a sonication-assisted exfoliation of natural graphite flakes in a hydro-alcoholic solution. The process yield is ~ 10 wt% with respect to the initial graphite powders.

Palladium decoration of graphene is described in detail in our previous works [11, 12]: briefly, a mixture of 1 ml of graphene suspension (0.1 mg/ml) with 2 ml of sodium dodecyl sulfate (SDS) in water (1 mg/ml) and 1 mg of palladium acetate (Pd(OAc)2) has been prepared and subjected to cyclic microwave exposures at 700 W for a total of 4500 s.

The decoration with PtNPs has been performed through a slightly modified procedure: graphene suspension and SDS have been mixed with $PtCl_2$ (with the same quantities) and stirred at 100 °C for 2 h.

3 Results and Discussion

A morphological characterization through SEM was carried out on samples drop casted onto Si substrate and dried at ambient conditions.

Both morphological characterizations and elemental microanalysis, performed on the hybrid materials, confirm the effective functionalization of graphene sheets.

Pd-functionalization of graphene resulted in an effective presence of nanoparticles (NPs) of ~ 50 nm diameter, possibly arranged in clusters of variable dimensions (Fig. 1a).

Also, PtNPs densely cover the graphene surface with nanoparticles of ~ 40 nm diameter (Fig. 1b).

AFM images confirm the formation of metal nanoparticles directly anchored onto graphene surface, as shown in Fig. 2.

The graphene and decorated graphene-based gas sensing devices have been prepared by drop casting onto gold interdigitated electrodes on alumina substrate and dried on hot plate, realizing three different series of chemiresistors. The achievement of the ohmic contact between GR-metal NPs films and gold electrodes is proven by the linear response of I–V measurements (Fig. 3).

The As-fabricated devices have been exposed to 1% of H_2, 300 ppb of NO_2 and 50 ppm of NH_3 in N_2 carrier at room temperature and 50% of relative humidity; their response has been quantified via the absolute value of the percentage conductance change.

The decoration of graphene sheet tunes the sensing performance of the devices.

In fact, Fig. 4 shows pristine graphene with a specific response towards NO_2 (Fig. 4a), whereas the device based on palladium nanoparticles exhibits a marked specificity towards hydrogen due to Pd hydride formation (Fig. 4b). On the contrary, the device based on Pt-decorated graphene does not show a particular specificity, since the functionalization has increased the response towards both the reducing gases, hydrogen and ammonia, without removing the sensitivity towards NO_2 (Fig. 4c). Being the sensing mechanism of Pt analogous to that of the Pd, the lack of a specificity of this material is expected.

In particular, ammonia is a possible interfering gas of hydrogen, being they both reducing analytes and showing a similar behaviour when adsorbed on graphene. In a previous paper, our group tested a variety of metal NPs to modulate the selectivity of graphene [11]. In that work, Ag was identified as a metal suitable for the detection of ammonia; unfortunately, this material is affected by a strong instability, due to the quick oxidation of silver NPs. On the contrary, Platinum is highly stable
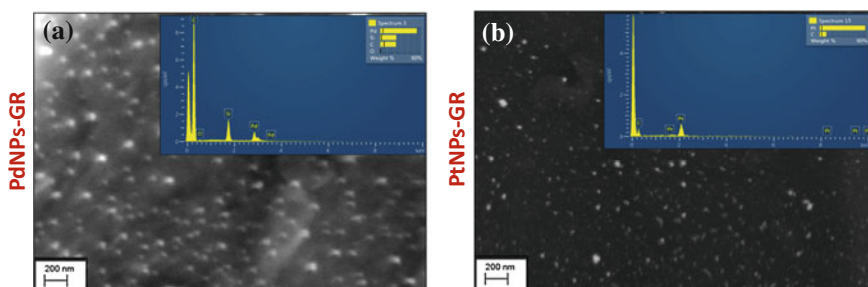
Fig. 1 SEM micrographs of graphene after decoration: **a** graphene/palladium nanoparticles, **b** graphene/platinum nanoparticles. In the inset, the EDX spectrum collected during the SEM analysis, confirms that a relevant amount of Pd and Pt can be found in the investigated area
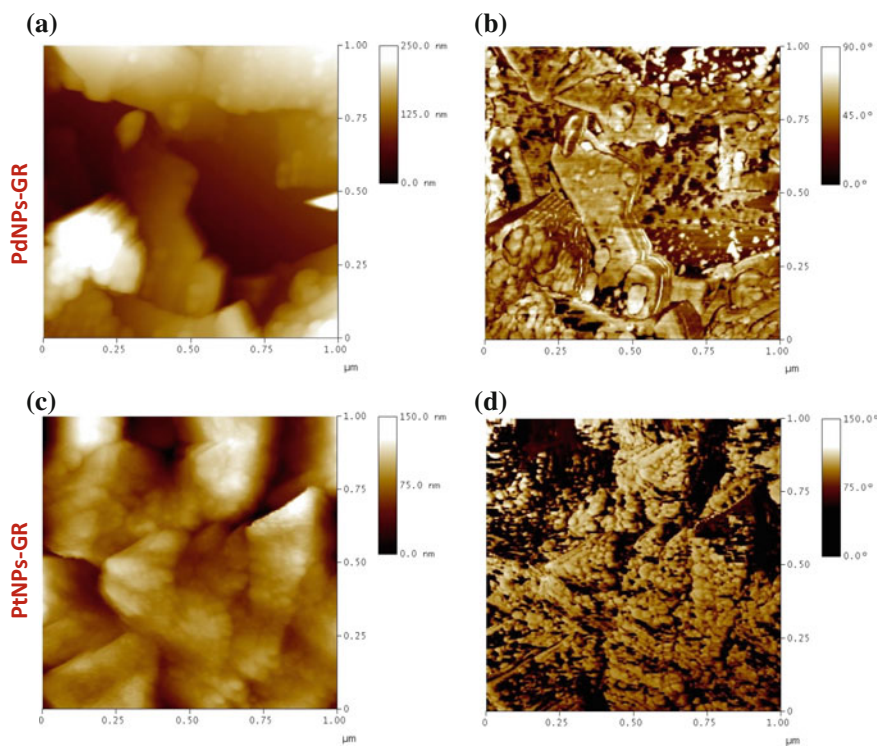
Fig. 2 AFM topography and phase images of graphene decorated with Pd nanoparticles (**a** and **b**) and Pt nanoparticles (**c** and **d**)
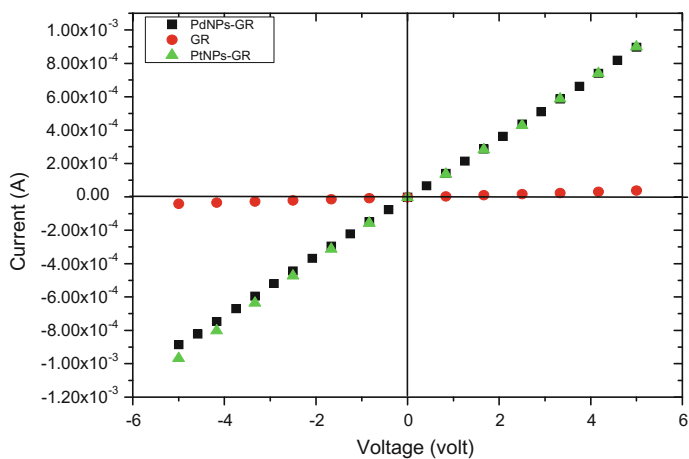
Fig. 3 I–V curves of pristine graphene (*red* spots), PdNPs/GR films (*black* spots) and PtNPs/GR films (*green* spots). Data were collected in the range [−5, 5 V] (Color figure online)
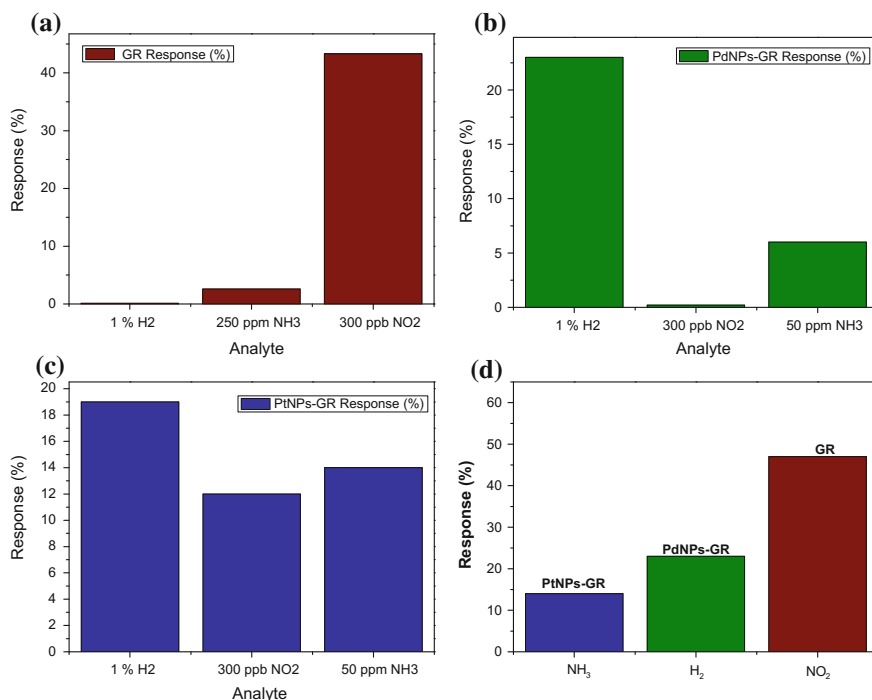
Fig. 4 Comparison of the conductance percentage responses, in absolute values to different analytes of the GR, PdNPs-GR and PtNPs-GR based devices

and its response kinetics to ammonia and hydrogen, different from those of Pd, can be employed in the detection of these analytes despite the lower specificity. Nevertheless, this apparent drawback can play in our favour: the use of an array of sensors, able to perform the comparison of the different adsorption kinetics, can dramatically reduce the uncertainty on the identification of a particular analyte [13]. Indeed, all of these peculiarities can pave the route in the use of Pt-based devices in combination with the other two materials to effectively discriminate between these two interferents.

4 Conclusions

In summary, we have compared the sensing performance of graphene decorated with different metal nanoparticles. The sensing properties of graphene can be tuned by changing the metal nanoparticles: indeed, after the decoration of graphene with both PdNPs and PtNPs, a loss of specificity towards nitrogen dioxide and an increased sensitivity to hydrogen is observed. Although the device based on the Pt

has a poor ability to distinguish between ammonia and hydrogen, its stability allows to assemble a combination of all the devices that can be profitably employed into an array of sensors. Henceforth, future perspective will be focused on the development of an array of devices capable of discerning the two analytes, by exploiting the different adsorption kinetics as discriminating factor.

References

1. Novoselov, K.S., Geim, A.K., Morozov, S.V., Jiang, D., Dubonos, S.V., Grigorieva, I.V., Firsov, A.A.: Science **306**, 666 (2004)
2. Novoselov, K.S., Geim, A.K.: Nat. Mater. **6**, 183 (2007)
3. Lu, G., Li, H., Liusman, C., Yin, Z., Wu, S., Zhang, H.: Chem. Sci. **2**, 1817 (2011)
4. Cui, S., Mao, S., Wen, Z., Chang, J., Zhang, Y., Chen, J.: Analyst **138**, 2877 (2013)
5. Tran, Q.T., Hoa, H.T.M., Yoo, D.H., Cuong, T.V., Hur, S.H., Chung, J.S., Kim, E.J., Kohl, P.A.: Sensors and Actuators B **194**, 45 (2014)
6. Kaniyoor, A., Jafri, R.I., Arockiadoss, T., Ramaprabhu, S.: Nanoscale **1**, 382 (2009)
7. Gautam, M., Jayatissa, A.H.: Solid-State Electron. **78**, 159 (2012)
8. Chu, B.H., Lo, C.F., Nicolosi, J., Chang, C.Y., Chen, V., Strupinski, W., Pearton, S.J., Ren, F.: Sens. Actuators B **157**, 500 (2011)
9. Pasricha, R., Gupta, S., Srivastava, A.K.: Small **5**, 2253 (2009)
10. Fedi, F., Ricciardella, F., Miglietta, M.L., Polichetti, T., Massera, E., Di Francia, G.: J. Sens. Sens. Syst. **3**, 241–244 (2014)
11. Alfano, B., Polichetti, T., Mauriello, M., Miglietta, M.L., Ricciardella, F., Massera, E., Di Francia, G.: Sen. Actuators B: Chem. **222**, 1032–1042 (2016)
12. Alfano, B., Polichetti, T., Miglietta, M.L., Massera, E., Schiattarella, C., Ricciardella, F., Di Francia, G.: G. Sens. Actuators B: Chem. **239**, 1144–1152 (2017)
13. De Vito, S., Miglietta, M.L., Massera, E., Fattoruso, G., Formisano, F., Polichetti, T., Salvato, M., Alfano, B., Esposito, E., Di Francia, G.: Sensors **17**(4), 754 (2017)

(002)-Oriented AlN Thin Films Sputtered on Ti Bottom Electrode for Flexible Electronics: Structural and Morphological Characterization

A. Taurino, M.A. Signore, M. Catalano, M. Masieri, F. Quaranta and P. Siciliano

Abstract Aluminum nitride (AlN) thin films were deposited by sputtering on Ti bottom electrodes and integrated on a kapton substrate for flexible and stretchable electronics. The aim of this work was to find the best combination of Ti underlayer sputtering conditions and AlN over-growth to obtain the (002) nitride orientation, fundamental requirement for the piezoelectric response of the material in piezoelectric devices. Flexible electronics represent today's cutting-edge electronic technologies thanks to their low cost and easy fabrication scalability.

Keywords Aluminum nitride · Magnetron sputtering · Piezoelectricity
Flexible electronics

1   Introduction

The deposition of piezoelectric thin films on polymeric substrates is a very desirable technological challenge for the development of piezoelectric flexible electronics, especially for biomedical applications [1]. The possibility to realize conformable piezoelectric devices which match the shape and the mechanical properties of soft tissues opens the opportunity to transform the available mechanical energy from internal organ movements (i.e. cardiac and respiratory motions) into electric energy to power medical devices. This specific application requires piezoelectric materials to be biocompatible. In this regard, AlN has emerged as an attractive alternative to others, such as lead zirconate titanate (PZT) that contains lead [2]. Moreover, AlN exhibits many interesting properties which make it compatible with CMOS technology processes [3]. Many attempts have been made to deposit AlN onto commercial polyimide

A. Taurino (✉) · M.A. Signore · M. Catalano · F. Quaranta · P. Siciliano
CNR, Institute for Microelectronics and Microsystems, Via Monteroni, 73100 Lecce, Italy
e-mail: Antonietta.Taurino@cnr.it

M. Masieri
CNR, Institute of Archeological Heritage-Monuments and Sites, Via Monteroni,
73100 Lecce, Italy

films by using different metal underlayers and tuning different sputtering parameters [4–6] with the aim to obtain nitride films with a strong (002) orientation, fundamental requirement for a significant piezoelectric response [7]. Therefore, the investigation of the structural and morphological properties of piezoelectric films is an important preliminary step before their integration into piezoelectric device. X-ray diffraction (XRD) analysis and transmission electron microscopy (TEM) represent two suitable characterization techniques to determine the degree of c-axis orientation and to investigate the columnar microstructure of the films [8]. Here, the evolution of morphology and structure of Ti films and of the AlN grown on Ti underlayer was characterized by XRD and TEM analyses. Highly oriented AlN film was obtained on flexible substrate when the underneath Ti layer was mainly (002)-oriented. The successful deposition of AlN/Ti on kapton represents a promising result for the integration of this material in flexible piezoelectric electronics.

2   Experimental Details

Aluminum nitride (AlN) thin films were deposited by RF magnetron sputtering on Ti bottom electrodes which in turn were sputtered on kapton polyimide 100H (Dupont-Toray Inc., thickness 25 μm) substrate. Kapton was chosen as flexible substrate owing to its excellent mechanical and electrical properties, chemical stability, and wide operating temperature range (−269 to +400 °C). The polymeric foil was fixed on a silicon wafer by silicone (Polydimethylsiloxane, PDMS Sylgard 184) and removed after the deposition process for the characterization.

500 nm thick AlN films were fabricated in a sputtering system by using a 99.999% pure Al target, in pure Ar and N_2 gas mixture, which was introduced into the chamber by two separate mass flow controllers. The N_2 flux percentage in the reactive mixture was fixed at 60%, the RF power applied to Al target at 150 W and the total pressure at 4×10^{-3} mbar. Before the deposition of the AlN layer, a 100 nm-thick Ti bottom electrode was deposited on kapton substrate by tuning the process pressure and the RF power applied to the Ti target. The chamber was evacuated down to 2×10^{-7} mbar and then the gases were introduced for the depositions of Ti and AlN layers. The target-substrate distance was fixed at 80 mm for both Ti and Al targets. All depositions were performed keeping the substrate at room temperature. The influence of Ti underlayer structure and morphology on the structural arrangement of AlN thin film has been investigated. Table 1 summarizes the sputtering conditions used for the deposition of the Ti layers.

Table 1 Sputtering parameters of Ti bottom electrode depositions

Sample K	Total pressure (mbar)	RF power (W)
Ti1	1.6×10^{-2}	200
Ti2	2.5×10^{-2}	200
Ti3	1.6×10^{-2}	150
Ti4	2.5×10^{-2}	150

The crystalline structure and crystal orientation of both Ti and AlN films were analyzed by X-ray diffraction using Cu-Kα radiation and scanned angle of 2θ = 30°–60°.

Transmission Electron Microscopy (TEM) analysis was performed on cross-sectional TEM lamellas prepared by Focused Ion Beam (FIB). The investigations were carried out by using a JEM-ARM200F TEM/STEM instrument, operating at 200 kV, with a resolution 78 pm.

Scanning electron microscopy (SEM) was used to investigate the evolution of the morphology of the specimens produced by a change in the growth parameters, A Zeiss NVISION 40 dual beam FIB machine, equipped with a high resolution SEM Gemini column was used for SEM experiments.

3 Results and Discussion

Figures 1 and 2 summarize the main results on the structural and morphological properties of Ti and AlN films, respectively, according to the tuned sputtering parameter, as reported and extensively discussed by the same authors in [9].

In particular, at lower pressure the films Ti1 K and Ti3 K appear almost amorphous with a porous surface, suggesting a low adatom mobility. When the pressure is increased, the structure quality is enhanced and the Ti(002) peak appears, having a higher intensity at lower RF power, where the Ti(100) peak is also detected. Their surfaces exhibit larger grains, whose size and structural quality decrease with the increase of the power (Ti2 K).

An AlN film was sputtered on the four analyzed metal layers, under the deposition conditions reported in the experimental section. The structure and morphology of the Ti underlayer guide the growth of AlN film demonstrating the strong influence of the seed layer properties for the nitride orientation. AlN grows

Fig. 1 XRD spectra and SEM surface images of Ti bottom electrode deposited on kapton substrate at different RF power applied to the target and Ar flux in the sputtering chamber
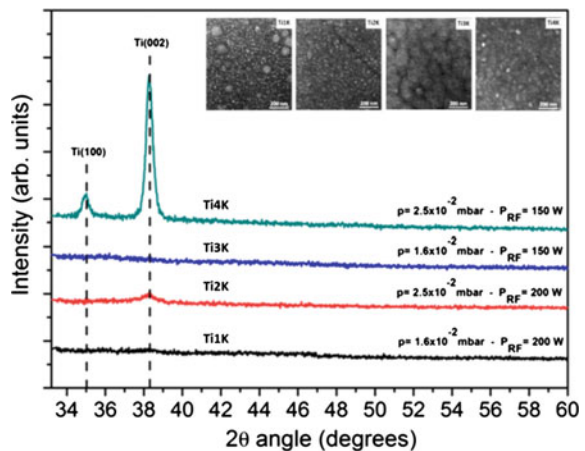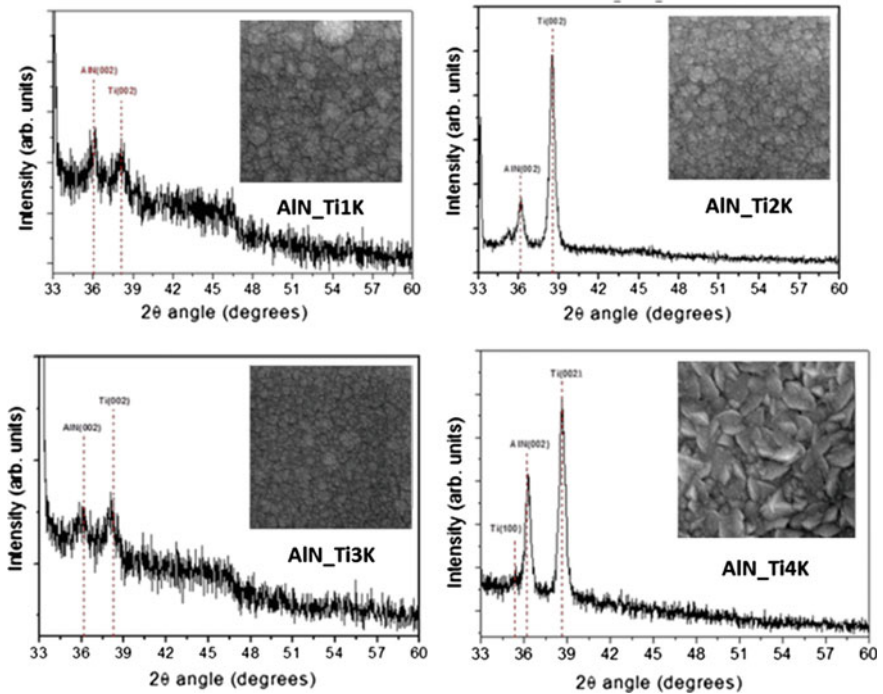
Fig. 2 XRD spectra and respective SEM surface images of AlN thin films deposited on different Ti bottom electrodes grown on kapton substrate

preferentially along c-axis on all Ti bottom electrodes deposited on kapton substrate but with a very different quality, as can be observed in Fig. 2, where the XRD spectrum and the AlN surface morphology are reported.

The best structural quality can be observed for AlN on Ti2 K and on Ti4 K. Except for the cases where the AlN films are affected by the presence of (100)-oriented grains in the Ti underlayer, the films morphology consists of fine and rounded grains which generally agglomerate in coarser structures, separated by voids. When Ti(100) peak is detected together with the (002) one (Ti4 K), the formation of a leaves-like morphology is promoted.

The AlN_Ti4 K sample, showing the best (002) orientation, was selected for a deeper structural and morphological investigation by transmission electron microscopy.

Figure 3a, b report the bright field (BF) and dark field (DF) TEM images of the AlN_Ti4 K film, showing the sequence of the layers from the kapton/Ti interface to the AlN surface. The Ti and AlN films are polycrystalline, have a quite uniform thickness and form slightly corrugated interfaces, as a result of the deposition on a rough substrate.

The relevant diffraction pattern is shown in Fig. 3c, evidencing the diffraction maxima (labelled with a circle) used for obtaining the DF image.

Fig. 3 HAADF images of the of the layers from the substrate/Ti interface to the AlN surface, (**a**) in bright field (BF) and (**b**) scanning transmission electron microscope (STEM); (**c**) TEM BF and (**d**) TEM DF images obtained from the diffraction maxima circled in the diffraction pattern (**e**)
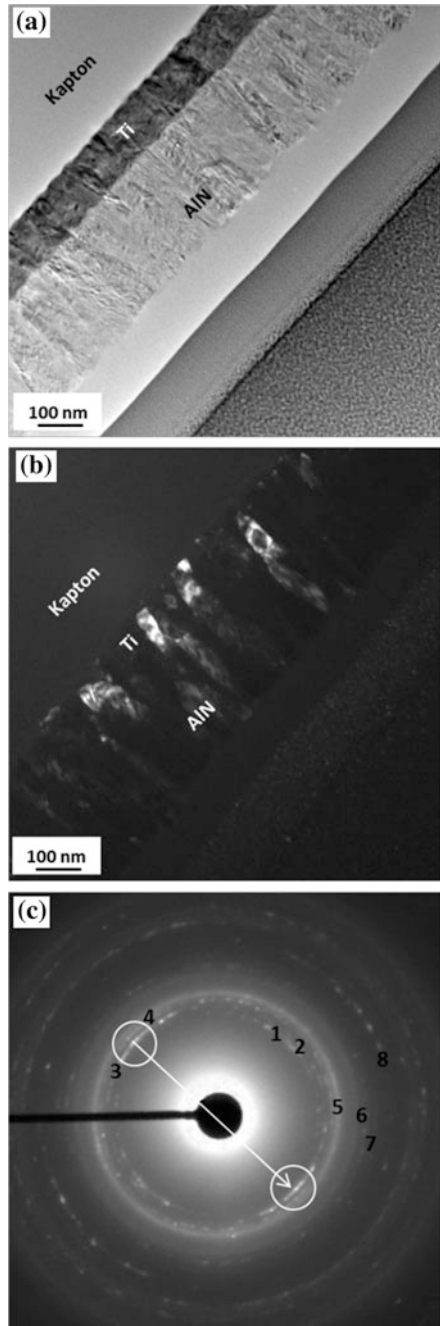
Table 2 reports the lattice distances inferred from the analysis of the DP. Both Ti and AlN exhibit a wide set of lattice reflections, due to the policrystallinity of the films. The peculiar intensity distribution of the (002) ring coming from AlN (n = 3), where an enhancement of the diffracted intensity is observable in correspondence of two small arcs, perpendicular to the interfaces (see the arrow), demonstrates the (002) preferential orientation of the AlN film. The columnar organization of the film is evident, particularly in the dark field image, where the bright columns represent the (002)-oriented columns of the Ti and AlN film; it is worth noting that highly 002-oriented AlN columns start from highly 002-oriented Ti columns.

Figure 4 shows a set of images describing the Ti/AlN interface at different positions. The interface is generally irregular and defected. The high resolution images (a) and (b) show, at two different magnifications, a region of the interface, where AlN follows the orientation of the Ti layer underneath; well oriented AlN columns are visible in figure (a) whereas figure (b) illustrates the (002) lattice fringes arrangement and correlation in the Ti and AlN layers. A highly disordered interface is evidenced in figures (c) and (d), where defected and differently oriented AlN grains propagate from a randomly oriented Ti layer. The FFT (Fast Fourier Transform) pattern, obtained from figure (d) and reported as inset, evidence two intense maxima corresponding to g = 002 and g = 100 spatial frequencies. The fainter extra spots, around the main spots coming from the matrix, indicate the presence of twinning.

Table 2 lattice distances inferred from the analysis of the DP

Experimental lattice distance (n) d(Å)	Theoretical Ti lattice distance d(Å) (hkl)	Theoretical AlN lattice distance d(Å) (hkl)
(1) 2.68		2.69 (100)
(2) 2.53	2.55 (100)	
(3) 2.49		2.49 (002)
(4) 2.34	2.35 (002)	2.37 (101)
(5) 2.23	2.24 (101)	
(6) 1.82		1.83 (012)
(7) 1.73		1.73 (012)
(8) 1.57	1.56 (003)	1.55 (110)
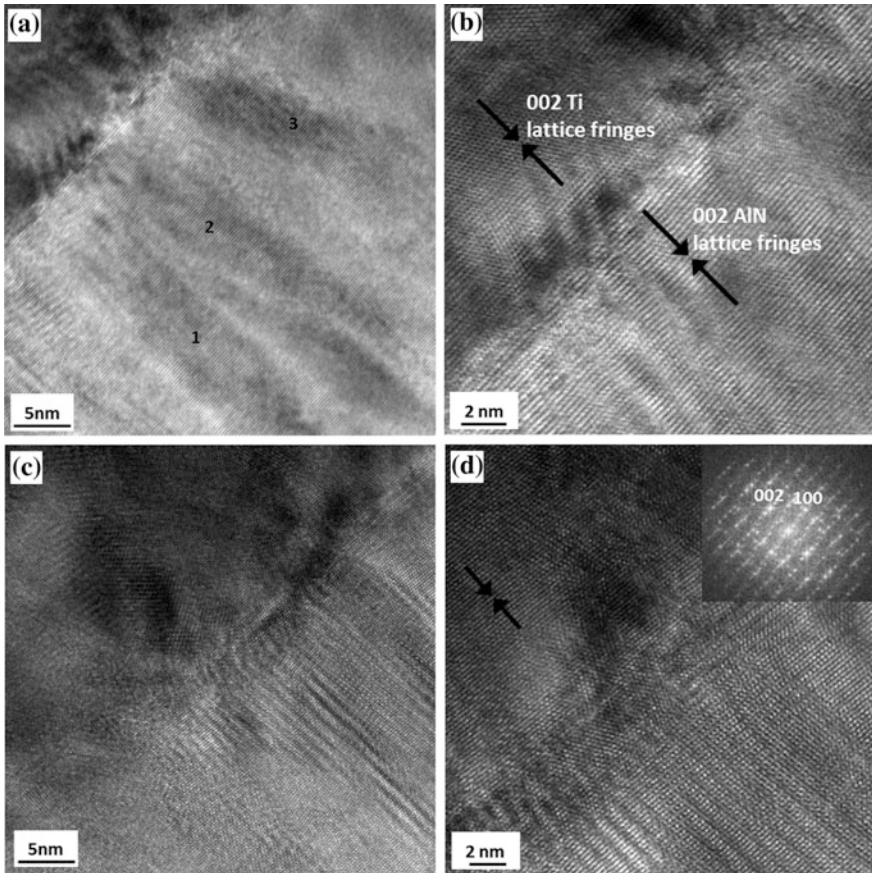
Fig. 4 HR TEM images of AlN_Ti4 K sample

4 Conclusions

AlN thin films have been successfully grown with intense (002) orientation on Ti bottom electrodes deposited on kapton substrate at different sputtering pressure and RF power applied to Ti target. A detailed XRD, SEM and TEM analyses was carried out in order to study the structure and the morphology of both Ti and AlN films, and correlate them to the process parameters. The Ti underlayer has a strong influence on the crystallographic orientation of the overgrown AlN film, promoting a very good quality of the nitride structure along c-axis at optimal deposition conditions. The successful deposition of AlN (002)-textured on kapton substrate opens new interesting perspectives for the integration of this material in flexible piezoelectric electronics.

References

1. Hwang, G.T., Byun, M., Jeong, C.K., Lee, K.J.: Adv. Healthc. Mater. **4**, 646 (2015)
2. Zalazar, M., Gurman, P., Park, J., Kim, D., Hong, S., Stan, L., Divan, R., Czaplewski, D., Auciello, O.: Appl. Phys. Letters **102**, 104101 (2013)
3. Hasan, D., Pitchappa, P., Wang, J., Wang, T., Yang, B., Ho, C.P., Lee, C.: ACS Photonics **4**, 302 (2017)
4. Jin, H., Zhou, J., Dong, S.R., Feng, B., Luo, J.K., Wang, D.M., Milne, W.I., Yang, C.Y.: Thin Solid Films **520**, 4863–4870 (2012)
5. Akiyama, M., Morofuji, Y., Kamohara, T., Nishikubo, K., Ooishi, Y., Tsubai, M., Fukuda, O., Ueno, N.: Adv. Funct. Mater. **17**, 458–462 (2007)
6. Petroni, S., Maruccio, G., Guido, F., Amato, M., Campa, A., Passaseo, A., Todaro, M.T., De Vittorio, M.: Microelectron. Eng. **98**, 603–606 (2012)
7. Pandey, A., Dutta, S., Prakash, R., Dalal, S., Raman, R., Kapoor, A.K., Kaur, D.: Mater. Sci. Semicond. Process. **52**, 16 (2016)
8. Mayrhofer, P.M., Ried, H., Euchner, H., Pollach, M.S., Mayrhofer, P.H., Bittner, A., Schmid, U.: Acta Mater. **100**, 81 (2015)
9. Signore, M.A., Taurino, A., Catalano, M., Kim, M., Che, Z., Quaranta, F., Siciliano, P.: Mater. Design **119**, 151–158 (2017)

Part II
Chemical Sensors

Detection of Tumor Markers and Cell Metabolites in Cell Cultures, Using Nanostructured Chemoresistive Sensors

N. Landini, B. Fabbri, A. Gaiardo, S. Gherardi, V. Guidi, G. Rispoli, M. Valt, G. Zonta and C. Malagù

Abstract Nowadays, tumor markers detection is one of the most dynamic field of research for medical technologies, as it seems a reliable source of screening technologies able to both detect neoplasms before their degeneration into malignant forms, and monitor possible relapses after the main cancer removal. On the other hand, studying neoplastic cell cultures behaviour, and their vitality in real time, places problems given to the high proliferation rate of the tumor cells. In this work, nanostructured chemoresistive sensors, sensing unit able to detect volatile chemicals in concentrations up to part per billions, have been used to detect neoplastic markers, with the idea to develop a technology able to follow in real time cell cultures and neoplasms growth, for both research and application in the medical field.

Keywords Sensors · Nanotechnology · Immortalized cells · Cells
Biomarkers · Metabolites · Cell cultures

N. Landini (✉) · B. Fabbri · A. Gaiardo · V. Guidi · M. Valt · G. Zonta · C. Malagù
Department of Physics and Earth Sciences, University of Ferrara, Via G. Saragat 1/C, 44122
Ferrara, Italy
e-mail: lndncl@unife.it

B. Fabbri
e-mail: fbbbbr@unife.it

A. Gaiardo
e-mail: grdndr@unife.it

V. Guidi
e-mail: gduvcn@unife.it

M. Valt
e-mail: vltmtt1@unife.it

G. Zonta
e-mail: zntgli@unife.it

1 Introduction

The identification of new tumor markers remains today a hot topic in medical research. In particular, taking advantage of those chemicals in order to obtain successful early-screening protocols, with the aim of detecting and thus removing neoplasms before their degeneration into malignant forms, is confirmed as one of the most pressing themes of research in the last decade. One of the main sources of those markers is cellular respiration, due to the exhalation of metabolites of various nature. Nonetheless, cell metabolites vary in chemical typology depending both on cell type and their degeneration into neoplastic forms [1–7]. Moreover, the metabolite volume expelled in a lapse of time changes depending on the proliferation of cells themselves. In this work, a brand new approach to cell metabolism study has been introduced, where volatile chemical metabolites have been analysed by using nanostructured chemoresistive sensors, that already proved to be able to detect colorectal tumor markers in previous works [8–11].

2 Methods

Chemoresistive sensors preparation is widely described in previous works [12–21] from the Laboratory of Sensors and Semiconductors of the University of Ferrara. The semiconductor films are synthesized with different chemical compositions, and fired following the preparation protocol at high temperatures. In this particular work, the sensors here described have been used:

- ST20 650; sensor based on tin oxides and titanium (20%), firing temperature = 650 °C

C. Malagù
e-mail: mlgcsr@unife.it

B. Fabbri · A. Gaiardo · V. Guidi · G. Zonta · C. Malagù
CNR-INO—Istituto Nazionale di Ottica, Largo Enrico Fermi 6, 50124 Florence, Italy

A. Gaiardo
Bruno Kessler Foundation, Via Sommarive 18, 38123 Trento, Italy

N. Landini · S. Gherardi
SCENT S.r.l, Via Quadrifoglio 11, 44124 Ferrara, Italy
e-mail: gherardi@fe.infn.it

G. Rispoli
Department of Life Science and Biotechnology, University of Ferrara, Via Luigi Borsari 46, 44121 Ferrara, Italy
e-mail: rsg@unife.it

- ST25 650 + Au; sensor based on tin oxides and titanium (25%) and gold (1%), firing temperature = 650 °C
- ZnO 850; sensor based on zinc oxide, firing temperature = 850 °C
- SnO2; sensor based on pure tin oxide, firing temperature = 650 °C
- SnS2; sensor based on tin sulfide, firing temperature = 300 °C
- W11; sensor based on tungsten oxide, firing temperature = 650 °C
- WS30 650; sensor based on tungsten oxide and tin (30%), firing temperature = 650 °C

All these sensors require thermo-activation in order to sense the changes in the chemical environment surrounding them, and for this reason their sensitive layers are heated by platinum heaters enveloped in the sensor substrates, at different working temperatures (WT).

Sensors responses are always compared to the environmental or synthetic air in the background of the analytes. This is necessary, because chemoresistive sensors require a steady air stream flowing to the sensitive chamber to function properly, and for this reason laboratory setup or sensing devices require flow circuits and mass flow controllers to keep the flux stable for these kind of experiments (Fig. 1).

To normalize the responses, normally given as a voltage output from the single sensors, the following formula is applied:

$$R = \frac{R_{an}}{R_0} \tag{1}$$

With R normalized, adimensional response of the sensor, R_{an} response in Volts of the sensor to the injection of the analyte in the sensitive chamber, and R_0 response in Volts of the sensor to the background air contribution. The application of this method on different analytes can be appreciated in literature [12–21].
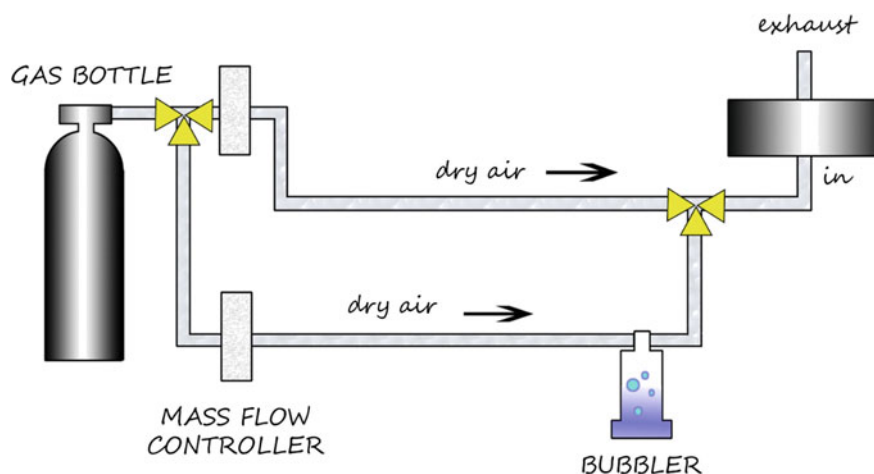
Fig. 1 Schematization of a Sensors Laboratory Setup. The Sensing Chamber is located before the "exhaust" output

In this experiment, two different arrays have been used to identify tumor markers:

Array 1

- SnS2, WT = 300 °C
- ST20 650, WT = 450 °C
- SnO2, WT = 450 °C
- ZnO 850, WT = 450 °C
- ST25 650 + Au, WT = 450 °C

Array 2

- ZnO 950, WT = 450 °C
- W11, WT = 350 °C
- WS30 650, WT = 350 °C
- ZnO 850, WT = 450 °C
- ST25 650 + Au, WT = 450 °C

The reason behind the choice of using multiple combinations of sensors lays in the different sensitive properties of these units, depending on the composition of the semiconductor with which the sensitive layer is prepared, and their WT. The different behaviours given from these properties can be observed in the Results section.

Cell cultures used in this work are from primary (fibroblasts—healthy, cultured directly from a subject which donated them) and immortalized (HEK-293, CHO) cell cultures. Immortalized cells are halfway between normal cells and tumor cells, having no biological memory of their previous functions and reproducing without control, due to the action of an adenovirus. All cells have been kept into breeding grounds composed of DMEM (Dulbecco's Modified Eagle's Medium), FBS (Fetal Bovine Serum), Streptomycin and Glutamine, hosted in common Petri-Dishes, and kept in dedicated incubators, in order to keep them vital and allow them to reproduce without interferences from the external environment.

Three different cell lines have been studied:

- Fibroblasts, from a primary culture of human origin: cells of the connective tissue, they produce extracellular matrix
- HEK-293 (Human Embryonic Kidney), from an immortalized cellular line, originally recovered from the kidney of an aborted human foetus
- CHO (Chinese Hamster Ovary), from an immortalized cellular line, originally from the ovary of a hamster.

3   Results and Discussion

Thanks to the different behaviour in the responses of single sensors, it has been possible to identify the discriminant properties of the sensors from their behaviour to the exhalation from different cell types, or of the same type of cells with different plating time, and thus different rate of proliferation.

Sensors proved to be capable of discriminating the kind of cell cultures undergoing the test, having them being put at the same time (for 48 h) in the incubation chamber (Fig. 2); also, all responses proved to be repeatable.

Sensors also showed their capability of following cellular proliferation, having their responses raising while cells where reproducing in the Petri Dish (Fig. 3).

ST25 650 + Au proved to be the best choice between all the sensors to detect differences between the exhalation of the different cultures and their breeding ground alone, giving the best discrimination between the different specimens (Fig. 4).

Single responses of immortalized cells from Fig. 4 (and obtained from Formula 1), compared to the healthy cell culture and the control sample, are summarized in Table 1.

Fig. 2 Tests on breeding grounds (DMEM 1, 2, 3), fibroblasts (1, 2) and HEK-293 cell cultures (48 h)
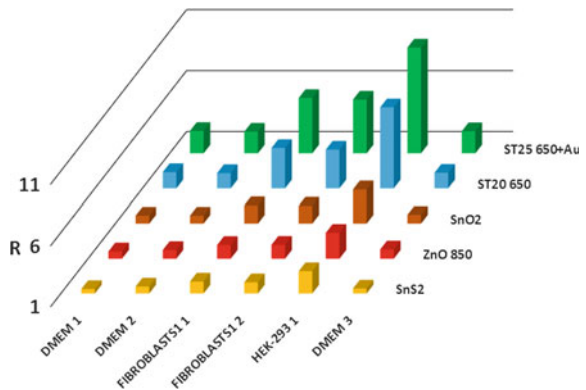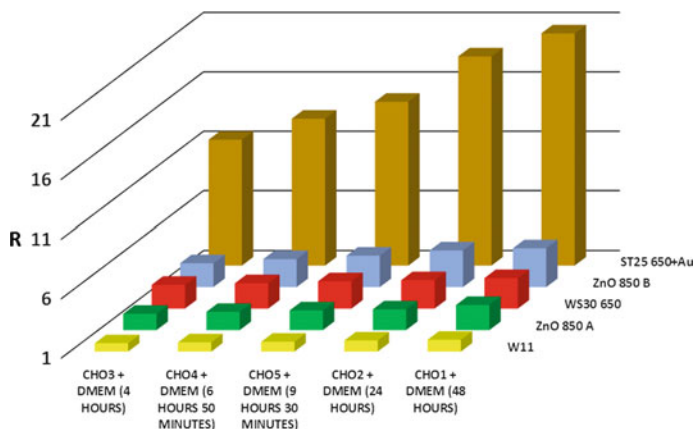
Fig. 3 Progressive increase of responses due proliferation with the passing of time for CHO cell cultures
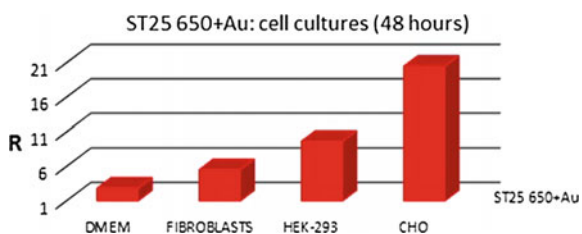
Fig. 4 Responses of ST25 650 + Au sensor to DMEM breeding ground and fibroblasts, HEK-293 and CHO cell cultures measured after 48 h from the plating protocol

Table 1 Responses from ST25 650 + Au sensor to volatile chemicals (DMEM) and metabolites (Fibroblasts, HEK-293, CHO cell cultures)

	DMEM	Fibroblasts	HEK-293	CHO
ST25 650 + Au	2.3	4.3	7.6	20.5

4   Conclusion

Given these results, the experiment has proved that chemoresistive sensors can:

- distinguish immortalized from primary (healthy) cell cultures
- distinguish different kind of immortalized cell cultures
- follow the progressive proliferation of cell cultures with the passing of time

In particular, ST25 650 + Au sensor showed the best discriminant capacity between the specimen, and thus new tin sensors, doped with titanium oxide and noble metals, will be prepared in order to study their behaviour to these biological markers. New studies are already ongoing, on both human cell cultures (A549, HCT 116, etc.) and biopsies, using a device hosting sensors, developed with the same technology [22].

References

1. Peng, G., Hakim, M., Broza, Y.Y., Billan, S., Abdah-Bortnyak, R., Kuten, A., Tish, U., Haick, H.: Detection of lung, breast, colorectal, and prostate cancers from exhaled breath using a single array of nanosensors. Brit. J. Cancer **103**, 542–551 (2010)
2. Altomare, D.F., Di Lena, M., Porcelli, F., Trizio, L., Travaglio, E., Tutino, M., Dragonieri, S., Memeo, V., de Gennaro, G.: Exhaled volatile organic compounds identify patients with colorectal cancer. Brit. J. Surg. **100**, 144–150 (2013)
3. Cairns, R.A., Harris, I.S., Mak, T.W.: Regulation of cancer cell metabolism. Nat. Rev. Cancer **11**, 85–95 (2011)
4. Qiu, Y., Cai, G., Su, M., Chen, T., Zheng, X., Xu, Y., et al.: Serum metabolite profiling of human colorectal cancer using GC—TOFMS and UPLC—QTOFMS. J. Proteome Res. **8**(10), 4844–4850 (2009)
5. Chan, E.C.Y., Koh, P.K., Mal, M., Cheah, P.Y., Eu, K.W., Backshall, A., et al.: Metabolic profiling of human colorectal cancer using high-resolution magic angle spinning nuclear magnetic resonance (HR-MAS NMR) spectroscopy and gas chromatography mass spectrometry (GC/MS). J. Proteome Res. **8**(1), 352–361 (2009)
6. Phillips, M., Gleeson, K., Hughes, J.M.B., Greenberg, J., Cataneo, R.N., Baker, L., et al.: Volatile organic compounds in breath as markers of lung cancer: a cross-sectional study. Lancet **353**(9168), 1930–1933 (1999)
7. Probert, C.S.J., Ahmed, I., Khalid, T., Johnson, E., Smith, S., Ratcliffe, N.: Volatile organic compounds as diagnostic biomarkers in gastrointestinal and liver diseases. J. Gastrointestin. Liver Dis. **8**(3), 337–343 (2009)
8. Zonta, G., Anania, G., Fabbri, B., Gaiardo, A., Gherardi, S., Giberti, A., Guidi, V., Landini, N., Malagù, C.: Detection of colorectal cancer biomarkers in the presence of interfering gases. Sens. Actuators B Chem. **218**, 289–295 (2015)
9. Malagù, C., Fabbri, B., Gherardi, S., Giberti, A., Guidi, V., Landini, N., Zonta, G.: Chemoresistive Gas Sensors for the Detection of Colorectal Cancer Biomarkers. Sensors **14**(10), 18982–18992 (2014)
10. Landini, N., Zonta, G., Malagù, C.: Detection of tumor markers on feces with nanostructured sensors. Scholar's Press (2015)
11. Zonta, G., Anania, G., Fabbri, B., Gaiardo, A., Gherardi, S., Giberti, A., Landini, N., Malagù, C., Scagliarini, L., Guidi, V.: Preventive screening of colorectal cancer with a device based on chemoresistive sensors. Sens. Actuators B Chem. **238**, 1098–1101 (2017)
12. Carotta, M.C., Martinelli, G., Sadaoka, Y., Nunziante, P., Traversa, E.: Gas-sensitive electrical properties of perovskite-type SmFeO3 thick films. Sens. Actuators B Chem. **48**(1–3), 270–276 (1998)

13. Carotta, M.C., Ferroni, M., Gnani, D., Guidi, V., Merli, M., Martinelli, G., et al.: Nanostructured pure and Nb-doped TiO2as thick film gas sensors for environmental monitoring. Sens. Actuators B Chem. **58**(1–3), 310–317 (1999)
14. Carotta, M.C., Benetti, M., Guidi, V., Gherardi, S., Malagù, C., Vendemiati, B., et al.: Nanostructured (Sn, Ti, Nb)O$_2$ solid solutions for hydrogen sensing. Proc. Mater. Res. Societ. **915**, 68210 (2000)
15. Carotta, M.C., Gherardi, S., Guidi, V., Malagù, C., Martinelli, G., Vendemiati, B., et al.: (Ti, Sn)O2 binary solid solutions for gas sensing: Spectroscopic, optical and transport properties. Sens. Actuators B Chem. **130**(1), 38–45 (2008)
16. Carotta, M.C., Cervi, A., Giberti, A., Guidi, V., Malagù, C., Martinelli, G., et al.: Metal–oxide solid solutions for light alkane sensing. Sens. Actuators B Chem. **133**(2), 516–520 (2008)
17. Carotta, M.C., Cervi, A., di Natale, V., Gherardi, S., Giberti, A., Guidi, V., et al.: ZnO gas sensors: a comparison between nanoparticles and nanotetrapods-based thick films. Sens. Actuators B Chem. **137**(1), 164–169 (2009)
18. Carotta, M.C., Guidi, V., Malagù, C., Vendemiati, B., Zanni, A., Martinelli, G., et al.: Vanadium and tantalum-doped titanium oxide (TiTaV): a novel material for gas sensing. Sens. Actuators B Chem. **108**(1–2), 89–96 (2005)
19. Guidi, V., Malagù, C., Carotta, M.C., Vendemiati, B.: Printed films: Materials science and applications in sensors, electronics and photonics. Woodhead Publ. Ser. Electron. Opt. Mater. 278–334 (2012)
20. Gaiardo, A., Fabbri, B., Guidi, V., Bellutti, P., Giberti, A., Gherardi, S., et al.: Metal sulfides as sensing materials for chemoresistive gas sensors. Sensors **16**(3), 296 (2016)
21. Landini, N., Zonta, G., Malagù, C.: Detection of tumor markers on feces with nanostructured sensors. Scholar's Press (2015)
22. SCENT B1, patent number: 102015000057717, property of SCENT S.r.l

Fish Robot Based on Chemical Sensors for Water Monitoring

Giovanna Marrazza, Andrea Ravalli and Claudio Rossi

Abstract In this work, we present a bio-inspired fish robot capable of swimming according to the directives sent in form of chemical messengers. An electrochemical platform measured the hydrogen concentration in the water. The acquired signal was then transformed into electronic signal to be used in robot control electronics. The fish robot's tail movement was thus controlled from pH electrochemical sensors.

Keywords Sensor · Polyaniline · Robot · Electrochemical · Aquaculture

1 Introduction

More than 50% of all the fish consumed each year are now raised on fish farms. The United Nations' Food and Agriculture Organization (FAO) reports that the aquaculture industry is growing three times faster than land-based animal agriculture and that fish farms will become even more prevalent as our natural fisheries become exhausted. In order to keep the health of any aquaculture system at an optimal level and to avoid physiological stress and disease of fish certain water quality and adequate nutrition must be monitored and controlled [1–3].

While land-based autonomous robots have already made a significant breakthrough in markets related service robotics, including the agro-alimentary sector, automation, robotics and advanced information technology tools are still underdeveloped in the fishery sector.

G. Marrazza (✉) · A. Ravalli
Department of Chemistry "Ugo Schiff", University of Florence, Via della Lastruccia 3, 50019 Sesto Fiorentino (Fi), Italy
e-mail: giovanna.marrazza@unifi.it

C. Rossi
Centre for Automation and Robotics, UPM-CICS, University of Madrid, Jose Gutiérrez Abascal 2, 28006 Madrid, Spain

To address this problem, in this work, we investigated the modelling, design and fabrication of a fish robot capable of swimming according to the directives sent in form of chemical messengers. Electrochemical sensors were used in order to detect the presence of the chemical messengers and transform them into electronic signals to be used in conventional control electronics.

Because pH directly affects other water quality variables and thus fish health, we investigated the application of a robot mimicking a swimming fish in order to minimize fish disturbance and stress integrated with a multi-sensors platform sensible to hydrogen ions in the environment. We realized polyaniline-modified sensors that are considered to be useful candidate as electrochemical sensing.

PANI film layer was electrochemically deposited on the graphite electrode surface by cyclic voltammetry technique. Experiments on modified sensors in order to obtain the better sensitivity as chemical sensing were carried out. After the sensors array optimization, a bio-inspired artificial fish unit capable of changing its swimming patterns according to the directives sent in form of chemical messengers from PANI-modified sensors was realized. Open-circuit potential (OCP) measurements were performed by an electrochemical transducer to detect various hydrogen ions concentrations. The acquired signals were then transformed into electronic signal to be used in control of proportional movement of the fish robot's tail. The objective of this work study is to concept-prove the feasibility of using electrochemical processes in order to activate electrically responsive bio-inspired soft actuators based on electroactive polymers functional materials.

In this work, a proof-of-concept for the development of multi-sensors fish robot as future core technology in aquaculture farm management was also introduced.

2 Experimental

2.1 Chemicals

Aniline, perchloric acid, acetic acid, sodium acetate, sodium hydroxide, disodium hydrogen phosphate, sodium dihydrogen phosphate dihydrate, sodium citrate, citric acid, diethanolamine, potassium ferrocyanide, potassium ferricyanide, potassium chloride, were purchased from Sigma Aldrich (Milan, Italy). Sodium chloride, sodium acetate trihydrate and hydrochloric acid were purchased from Merck (Milan, Italy). All chemicals were of analytical reagent grade and were used as received without any further purification. All solutions were prepared using MilliQ (obtained from Milli-Q Water Purification System, Millipore, UK) and HPLC grade water (Merck. Milan, Italy) added with 0.1 M KCl.

2.2 Instrumentation

Electrochemical measurements were carried out in a digital potentiostat/galvanostat AUTOLAB PGSTAT 30(2)/FRA2 controlled with the General Purpose Electrochemical System (GPES) and Frequency Response Analyzer (FRA2) 4.9 software (Eco Chemie, Utrecht, The Netherlands).

The pH sensor was assembled using the screen-printed cells, comprising the graphite-working electrode (2.5 mm in diameter), the counter graphite electrode and the silver/silver chloride (Ag/AgCl) pseudo-reference electrode. Screen-printed cells were produced in house on a DEK 248 screen-printing machine (DEK, Weymouth, UK). Peristaltic pump was purchased from Gilson Inc., USA. Wall-jet electrochemical micro-flow cell polyacrylate was homemade. It is composed by methacrylate with dimensions of $30 \times 10 \times 20$ mm (width $\times$ depth $\times$ height). Low lead internal volume is lower than 500 μL.

2.3 Preparation of PANI Thin-film

The modification of graphite screen-printed electrodes (GPSEs) with polyaniline (PANI) has been performed using the protocol described below, adapted from a previous work of the authors [4, 5].

Firstly, electro-polymerization of polyaniline layer on the GPSEs has been obtained performing 10 cyclic voltammetry scans in the range from −0.4 to +0.8 V at 0.05 Vs^{-1} scan rate using a solution of aniline 2.5 mM in $HClO_4$ 50 mM in the 50 μL drop cell.

2.4 Electrochemical Measurements

The electrochemical screen-printed cell was inserted into homemade flow-cell. The response of the polyaniline (PANI)-modified sensors at various hydrogen ions concentrations has been evaluated by means Open Circuit Potential (OCP) measurements. A linear increase of OCP has been observed in relation of increase of hydrogen ions concentration.

2.5 Fish Robot Control

The fish robot was developed as reported in literature [6, 7]. The robot was controlled by and Arduino Nano[(tm)] microcontroller and six antagonistic actuators

based on the shape memory alloys (SMAs) actuators are powered by in-house developed pulse width modulation-to-direct current (PWM-to-DC) power circuitry.

3 Results and Discussion

Graphite screen-printed electrodes (GSPEs) were modified by electro-polymerization of aniline using cyclic voltammetry. The response of the PANI-modified GPSEs in the presence of various hydrogen ions solutions was investigated by open circuit potential (OCP) measurements.

PANI-modified sensor was inserted into an home-made flow cell connected to the instrument for open-circuit potential (OCP) measurements. Various pH solutions (form acid to basic and vice versa) were flowed into the fluidic system until the coverage of the sensor surface. The Fig. 1 shows the OCP signals obtained by flow cell. 0.1 M NaOH solution (pH 13) was flowed into the cell and the OCP value was taken until a stable signal was obtained. After the flowing of a 0.1 M HCl solution, an increase of OCP value (OCP = 0.3 V) was acquired. Subsequently, NaOH and HCl solutions were alternatively flowed into the flow cell: as can be observed a coherent and reproducible OCP variation was obtained confirming the possibility to detect the H^+ as chemical messengers in the environment. A linear decrease of OCP was observed in relation of increase of pH with a slope of 45 mV (data not shown). The reproducibility of the measurements by three different measurement using three different PANI-modified electrodes was around 15%.

Then, the experiments aimed at testing the experimental setup, composed of two pumps (one for pumping KCl 0.1 M used as carrier solution, one for the sample at different pH), the signal acquisition system and the control system were carried out. The scheme is shown in Fig. 2. The aim is to be capable of transmitting chemical

Fig. 1 The response of the PANI-modified GPSEs with two hydrogen ions concentrations
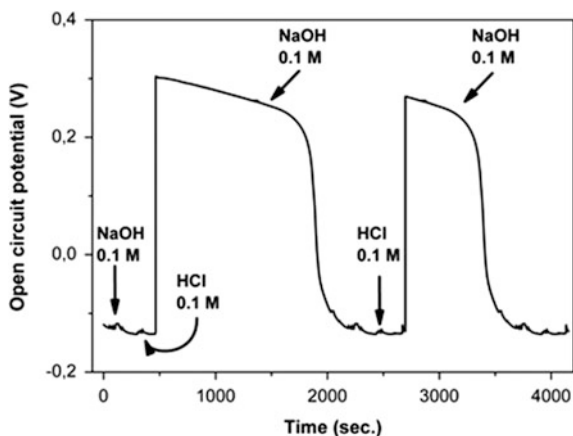
Fig. 2 Scheme of the experimental set-up
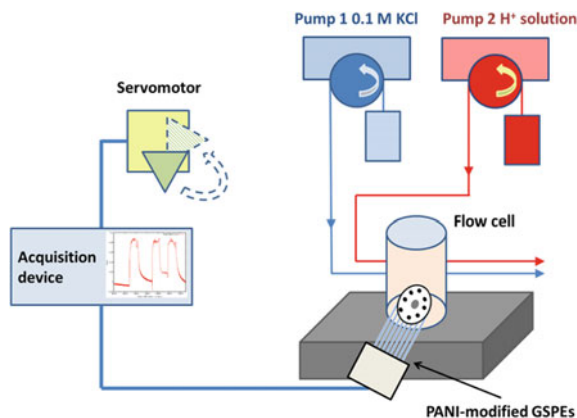
bits through the environment that can be used to activate an actuating element (in this case, a servo-motor).

An activation command is triggered by an operator. This activates the pump 2 for Δt_s time, injecting a certain (to be quantified) quantity of sample into the cell. This is detected by the sensor and converted into a digital signal. If the signal exceeds a threshold of 50% of the maximum amplitude, it is interpreted as a C-bit, and the servo-motor is activated (form 0° to 90°) until the signal falls below the threshold again. Such system was used to assess the sensitivity and reaction time of the sensor in order to determine optimal firing frequencies and quantities of sample for transmitting activation information.

The signals were the sent to the robot's controller via the Arduino. The activation persisted until the signal falls below the threshold again. The system was capable of detecting the concentration of hydrogen ions changes in the environment, and to use such information to bias the activations signal of the robot's actuator. The acquired signals were used in control of proportional movement of the fish robot's tail according to the directives sent in form of chemical messengers.

4 Conclusions

In this work, preliminary studies on electro-chemical sensors platform was performed in order to detect the presence of the hydrogen ions as chemical messengers and transform them into electronic signals to be used in fish robot's tail control.

References

1. Tacon, A.G.J., Metian, M.: Fish matters: importance of aquatic foods in human nutrition and global food supply. Rev. Fish. Sci. **21**, 22–38 (2013)
2. Lafferty, K.D., Harvell, C.D., Conrad, J.M., Friedman, C.S., Kent, M.L., Kuris, A.M., Powell, E.N., Rondeau, D., Saksida, S.M.: Infectious diseases affect marine fisheries and aquaculture economics. Ann. Rev. Mar. Sci. **7**, 471–496 (2015)
3. Justino, C.I.L., Duarte, K.R., Freitas, A.C., Panteleitchouk, T.S.L., Duarte, A.C., Rocha-Santos, T.A.P.: Contaminants in aquaculture: overview of analytical techniques for their determination. TrAC-Trend. Anal. Chem. **80**, 293–310 (2016)
4. Rapini, R., Cincinelli, A., Marrazza, G.: Acetamiprid multidetection by disposable electro-chemical DNA aptasensor. Talanta **161**, 15–21 (2016)
5. Ravalli, A., Lozzi, L., Marrazza, G.: Micro-flow immunosensor based on thin-film interdigitated gold array microelectrodes for cancer biomarker detection. Curr. Drug Deliv. **13**(3), 400–408 (2016)
6. Ravalli, A., Rossi, C., Marrazza, G.: Bio-inspired fish robot based on chemical sensors. Sens. Actuators B: Chem. **239**, 325–329 (2017)
7. Coral, W., Rossi, C., Colorado, J., Lemus, D., Barrientos, A.: SMA-based muscle-like actuation in biologically inspired robots: a state of the art review. In: Berselli, G., Vertechy, R., Vassura, G. (eds.) Smart actuation and sensing systems/Recent advances and future challenges, InTech Open, 53–82 (2012)

QCM Sensors Based on In$_2$O$_3$ Nano-films Obtained by a Pulsed Plasma Deposition Technique

Tommaso Addabbo, Andrea Baldi, Mara Bruzzi, Ada Fort, Marco Mugnaini and Valerio Vignoli

Abstract In this paper Quartz Crystal Microbalance (QCM) gas sensors obtained depositing nano-films of In$_2$O$_3$ over AT-cut 10 MHz resonators are presented. Films are grown by a Low-Temperature Pulsed Electron Deposition (LTPED), a single-stage growth technology by which films can be deposited on a variety of different substrates Rampino et al. (Appl Phys Lett 101(13):132107, 2012 [1]) down to a few nms thickness, allowing for maintaining large quality factors of the quartzes and for realizing very stable oscillators. The gas sensing performance of these devices are studied by means of experiments with a toxic gas, NO$_2$, water vapor and ethanol. The effect of UV irradiation on the sensor response is also studied. The sensors provide stable and repeatable measurements, a large response to water vapor, and respond reversibly to NO$_2$.

Keywords Quartz crystal microbalance · Gas sensors · Nano-film · In$_2$O$_3$

1 Introduction

In the last years the research has shown that In$_2$O$_3$ is a promising material for gas-sensor applications. In particular gas sensors based on In$_2$O$_3$ are suitable for the detection of low concentrations of oxidizing gases like O$_3$, NO$_x$ and Cl$_2$ [2]. On the other hand, it was shown that in some cases In$_2$O$_3$-based gas sensors may have sufficient sensitivity and good selectivity also toward some reducing gases (such as CO in the presence of H$_2$) depending on the preparation route and on the surface stoichiometry. It must be underlined that in general for metal oxide gas sensors the

T. Addabbo · A. Fort (✉) · M. Mugnaini · V. Vignoli
Department of Information Engineering and Mathematics, University of Siena, Siena, Italy
e-mail: ada.fort@unisi.it

A. Baldi
Department of Industrial Engineering, University of Florence, Florence, Italy

M. Bruzzi
Department of Physics and Astronomy, University of Florence, Florence, Italy

preparation route and/or the deposition method are largely influent on the sensor performance, because sensing is strongly dependent on both defect chemistry and micro/nanostructure.

For the deposition of In_2O_3 nano-structured films many different techniques have been proposed such as: chemical vapor deposition; thermal oxidation of In films; spray pyrolysis; sol–gel; atomic layer deposition; pulsed laser ablation; DC and RF-sputtering. These techniques generally require a complex processing for precursors to be formed in the environment of the deposition chamber. In this work we used a novel deposition method, the Low Temperature Pulsed Electron Deposition (LTPED) technique. A pulsed high density electron beam (500 MW/cm^2), interacting with the target, causes material ablation independently of the energy gap (i.e. the optical absorption) of the target itself. The chemical composition of the target is then transferred by a supersonic highly energetic plasma giving rise to thin films directly on the substrate while keeping a low substrate temperature. This technique [1] can grow films both on metal and dielectric substrates, down to a controlled few-nms thickness, with a low-cost process and essentially no need for post-deposition treatments, like high-temperature annealing of the substrate [1].

In this work we describe, characterize and study nano-layers of In_2O_3, used as sensitive layers in a quartz crystal microbalance (QCM). QCMs (unless adopting special piezoelectric resonators) operate at room temperature. For this reason, since usually In_2O_3 is used in resistive chemical sensors, that operate at high temperatures and base their operations on chemisorption, the feasibility of a In_2O_3 QCM gas sensor has to be investigated. Note that even if at RT chemisorption on metal oxides is very limited, physisorption is favored, therefore an adsorption on the sensitive film is possible.

As far as the sensitivity is concerned it must be noted that, in case of adsorption of a gas monolayer, a rough approximation of the maximum adsorbed mass, obtained considering the adsorption on a plane surface and a full coverage of the surface, is of some ng for light molecules. Therefore, the maximum expected frequency shift due to gas adsorption is in the order of some Hertzs. This seems to set a limit to the use of this device for gas sensing applications, but by depositing a very thin sensitive layer by means of LTPED, we can maintain a very large value of the Q of the quartz, which allows to reach very high frequency resolutions. In fact, frequency stability and noise of a quartz oscillator are related to the Q-factor: the larger is the Q factor the more immune to parasitic effects is the oscillator and the smaller is the resultant frequency noise.

2   Measurement System Description

A thin layer of In_2O_3 with a thickness of about 40 nm has been deposited on an AT-cut 10 MHz quartz disk with a diameter of 6 mm and two Au electrodes.

The response of the gas sensor is due to the adsorption of gas on the In$_2$O$_3$ layer increasing the mass of the electromechanical resonator. Sauerbrey equation relates the resonance frequency shift Δf to the mass adsorbed Δm as follows [3, 4]:

$$\Delta f = \frac{-2f_0^2}{A\sqrt{\mu_q \rho_q}} \Delta m \Rightarrow |\Delta f|[\text{Hz}] = 800\, \Delta m[\mu\text{g}] \tag{1}$$

which can be also written as:

$$\Delta m[\text{ng}] = 1.25 |\Delta f|[\text{Hz}] \tag{2}$$

where f_0 is the quartz resonance frequency in Hz (10 MHz), A is the effective area of the electrodes (28×10^{-6} m^2), ρ_q is the quartz density (2.648 g cm^{-3}), μ_q is the shear module for AT-cut quartzes (2.947×10^{11} g cm^{-1} s^{-2}).

As far as the sensitivity is concerned it must be noted that, in case of adsorption of a gas monolayer, a rough approximation of the maximum adsorbed mass, obtained considering the adsorption on a plane surface with the area of the electrode and a full coverage of the surface (adsorbed molecules density in the order of magnitude of 10^{14} cm^{-2}) is about 7 ng for H$_2$O, 19 ng for CO and 11 ng for NO$_2$. Therefore the maximum expected frequency shift is in the order of some Hertzs. The characterization system shown in Fig. 1 [5] was used to test the developed sensor. It consists of an accurate frequency meter and a gas delivering system. The quartz oscillator is inserted in a high resolution measurement system of the frequency shift, which grants a resolution lower than 0.1 Hz.

The gas system used to test the sensor is able to deliver a gas mixture with an accurately controlled composition in a Teflon measurement chamber. Three PC-controlled flow-meters establish the flow from certified gas cylinders containing the components of the gas mixture. The total flow during a measurement is constant
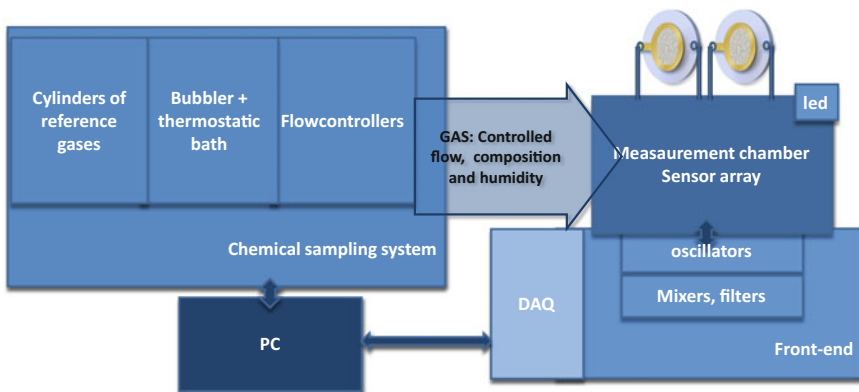
Fig. 1 Measurement system

(100 mL/min in this work) whereas its composition can dynamically change during a measurement.

Either humidity or ethanol partial pressure are set by means of a bubbler containing ultrapure water (ethanol), kept at a known temperature, in which a dry carrier gas is saturated; the desired partial pressure of water (ethanol) is obtained by mixing the flow from the bubbler with the dry carrier gas flow.

The measurement system allows for testing the sensor under UV radiation, for this purpose a led with a peak wavelength of 275 nm was placed in the measurement chamber.

3 Experimental Results and Discussion

Some experimental results are reported in Fig. 2. In the top plot the response of the sensor defined as the frequency shift reached at the end of a fixed time (8 min) of exposure to the target gas is shown. Responses to different test gases are plotted as a function of time in the bottom plot. These latter are obtained by changing the concentration of a test gas in a carrier gas (N_2) according to the protocol described in the figure caption. The response to water vapor is obtained with four pulses of humid N_2 with the following values of relative humidity: 100, 50, 30%. Sensors response to water vapor can be explained by multi-layer adsorption, whereas NO_2 response can be explained by a single layer reversible adsorption. Note that NO_2 adsorption is highly influenced by the presence of humidity, which enhances the sensitivity toward the target gas. As can be seen in Fig. 2, in presence of water the response to NO_2 assumes a complex shape indicating an interaction between the
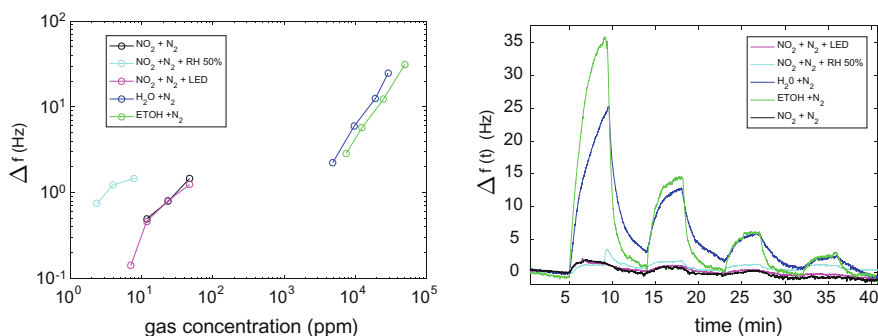
Fig. 2 QCM responses to different test gases. *Left* responses as a function of target gas concentration. *Right* transient responses to different target gas pulses (4 min carrier gas, 8 min target gas + carrier gas concentration #1, 4 min carrier gas, 8 min target gas + carrier gas concentration #2, 4 min carrier gas, 8 min target gas + carrier gas concentration #3, 4 min carrier gas, 8 min target gas + carrier gas concentration #4, 4 min carrier gas, total flow 100 mL/min. The concentration delivered to the test chamber for the different gases are those shown in the leftmost plots

two species and the sensor behavior can no more be explained by simple adsorption-desorption reactions. On the other hand, UV radiation with this power and wavelength doesn't affect the response to NO$_2$. The sensor was tested also with CO, giving an almost negligible frequency shifts.

4   Conclusions

In this work we present first studies on gas sensing properties of In$_2$O$_3$ nano-layers on quartz crystal microbalances (QCMs). A 40 nm-film deposited by LTPED on QCM was tested at room temperature under controlled flows of different gas kinds and concentrations. Experimental results showed that the devices are sensitive to NO$_2$ and water vapour, while negligible effects are observed in presence of CO. The response to NO$_2$ is highly dependent on the relative humidity. Moreover, the experimental results show that the response can't in general be explained by simple adsorption-desorption reactions. The developed device can be used as humidity sensor, whereas the application to NO$_2$ detection needs a controlled humidity environment.

References

1. Rampino, S., et al.: 15% efficient Cu (In, Ga) Se$_2$ solar cells obtained by low-temperature pulsed electron deposition. Appl. Phys. Lett. **101**(13), 132107 (2012)
2. Korotcenkov, G., Brinzari, V., Stetter, J.R., Blinov, I., Blaja, V.: The nature of processes controlling the kinetics of indium oxide-based thin film gas sensor response. Sens. Actuators B: Chem. **128**(1), 51–63 (2007)
3. Addabbo, T., Bertocci, F., Fort, A., Mugnaini, M., Shahin, L., Vignoli, V., Rocchi, S.: A DDS-based multi-harmonic frequency meter for QCM sensor applications. Procedia. Eng. **87**, 288–291 (2014)
4. Fort, A., Rocchi, S., Serrano-Santos, M.B., Ulivieri, N., Vignoli, V., Pioggia, G., Di Francesco, F.: A high-performance measurement system for simultaneous mass and resistance variation measurements on gas sensing polymer films. Sens Actuators B: Chem **111**, 193–199 (2005)
5. Addabbo, T., Bruzzi, M., Fort, A., Mugnaini, M., Tani, M., Vignoli, V.: Quartz crystal microbalance sensors based on TiO$_2$ nanoparticles for gas sensing. In: Proc. of IEEE I2MTC, pp. 1–6 (2017)

Electrocatalytic Activity of α-MoO₃ Plates Synthesized Through Resistive Heating Route

Emanuela Filippo, Daniela Chirizzi, Francesca Baldassarre, Marco Tepore, Maria Rachele Guascito and Antonio Tepore

Abstract Characterization and electrochemical application of α-MoO₃ hierarchical plates achieved through direct resistive heating of molybdenum foils, at ambient pressure and in absence of templates or catalysts, has been reported. The plates with an orthorhombic single-crystalline structure, as observed by SEM, TEM, SAD and Raman-scattering techniques. They are about 100–200 nm in thickness and a few tens micrometers in length. Electrochemical characterization of α-MoO₃ plates casted on Pt electrodes was performed by Cyclic Voltammetry in phosphate buffer to investigate the properties of this material against methanol oxidation. Reported results indicate that α-MoO₃/Pt devices were suitable to promote the electroxidation of methanol in sensing and/or fuel cell anodes development applications.

Keywords Crystal growth · Electron microscopy · Methanol

E. Filippo · M. Tepore
Dipartimento di Matematica e Fisica, Università del Salento, Via per Monteroni, 73100 Lecce, Italy

D. Chirizzi (✉)
Istituto Zooprofilattico Sperimentale di Puglia e Basilicata, Via Manfredonia 20, 71121 Foggia, Italy
e-mail: daniela.chirizzi@unisalento.it

F. Baldassarre · M.R. Guascito
Dipartimento di Scienze e Tecnologie Biologiche e Ambientali, Università del Salento, Via per Monteroni, 73100 Lecce, Italy

A. Tepore
Dipartimento di Beni Culturali, Università del Salento, Lecce 73100, Italy

D. Chirizzi
Dipartimento di Scienze Biologiche Tecnologie ed Ambiental, Università del Salento, Via per Monteroni, 73100 Lecce, Italy

71

1   Introduction

Layered materials, such as graphene, transition-metal dichalcogenides (TMDs) and transition-metal oxides (TMOs) have been widely explored owing to their fascinating physical properties and high specific surface areas [1]. Orthorhombic molybdenum trioxide (α-MoO_3) is a type of layered TMO comprising dual layers of planar crystals of distorted MoO_6 octahedra, held together in the vertical [010] direction by weak van der Waals forces. In recent years MoO_3 nanostructures have attracted much interest for many technological and industrial applications [2, 3] and different methods of synthesis have been proposed, including pulsed laser deposition, thermal evaporation, RF magnetron sputtering sol–gel, hydrothermal, spray pyrolysis, chemical vapour deposition, mechanical exfoliation, molecular beam epitaxy and electrodeposition. In general, to the best of our knowledge most of literature works reported the growth of MoO_3 nanostructures through expensive apparatus.

It is well known that the synthesis of α-MoO_3 by thermal oxidation of metallic molybdenum requires relatively simple and not expensive apparatus and is suitable for high yield preparation of highly crystalline and stratified structures. Recent works have established that in particular experimental conditions, thermal oxidation of bulk metal foils/wire can cause the growth of the metal oxide nanostructures (rods, wires, plates, ...) directly on the surface of bulk [4]. The key factors which govern the growth processes and the structures of the nanostructures are the temperature heating (which can be provided by hot plate, oven or other alternative heating systems such as resistive heating) and the oxidation time (which can be varied from a few seconds to several hours). For this reason we have proposed a thermal resistive oxidation as a simple, no toxic and economic route for preparing MoO_3 nanostructures, ideally free of contaminants (i.e. intercalated chemicals, dispersing agents and surfactants) that could compromise its electrochemical performance owing to the possible blockage of active sites and the added weight/volume of electrochemically inactive contaminants [5]. Monitoring alcohol concentration in a solution with a high sensitivity is important in many industries. Electrochemical alcohol sensing is one of the most promising methods due to its simplicity and accuracy [6]. In addition methanol offers several advantages over hydrogen as a fuel including the ease of transportation and storage, and high theoretical energy density. In Direct Methanol Fuel Cells (DMFCs), the methanol electro-oxidation reaction occurs at the anode [6]. The choice of the anode materials is influenced greatly by their actual surface chemical and physical properties. Because the electro-oxidation rate strictly depends from these parameters new innovative anisotropic metallic materials micro/nano-structured were proposed [7].

In this paper, the electrocatalytic activity of the α-MoO_3 microplate structures to methanol oxidation has been evaluated by cyclic voltammetric experiments in phosphate buffer at neutral pH after deposition on platinum surface by a simple casting method. The morphological and structural characterization of the as synthesized MoO_3 plates synthesized by resistive heating for 80 min has been performed by scanning electron microscopy (SEM), high resolution transmission electron microscopy (HRTEM) coupled with selected area diffraction pattern (SAD), X-ray powder diffraction (XRD) and micro-Raman spectroscopy.

2 Materials and Methods

2.1 Instrumentation

Scanning electron microscopy was performed by using a SEM (Tescan SEM), operating at 20 kV. TEM images and selected area diffraction pattern (SAD) were acquired using a Jeol transmission electron microscope at 200 kV. Specimens for TEM observations were obtained by sonicating the white layers sample of a-MoO₃ in an ultrasonic bath for about 20 min in ethanol. A drop of the obtained dispersion was then placed onto carbon-supported copper grids and let to dry naturally in air. The crystal structure was identified by X-ray diffraction (XRD) Rigaku Minifex diffractometer, Cu Kα irradiation. Information on vibrational modes in α-MoO₃ nanostructures was obtained from Raman backscattering experiments using a Renishaw InVia Raman spectrometer coupled to a Leica metallographic micoscope.

2.2 *α-MoO₃ Plates Synthesis*

For the synthesis of α-MoO₃ plates hierarchical structures a method reported from authors has been employed [8]. Foils of Mo-metal, which was used as source and as substrate, were first washed by dilute hydrochloric acid to remove the native oxide layer and adsorbed impurities, followed by cleaning with acetone, methanol and deionized water under an ultrasonic bath and finally dried by N₂ flow. A cleaned foil was then placed in an open chamber with two Cu electrodes connected to an external alternating current power supply and resistively heated in air while an ammeter was used to measure the electric current. The synthesis temperature was monitored by a thermocouple sensor. The applied voltage was kept constant at 3.0 V for 80 min. The temperature was kept constant at about 800 °C by adjusting the current through the Mo foils by means of a PID controller.

2.3 *Electrochemical Experiments*

All electrochemical experiments were carried out by using a µStat400 DropSens electrochemical workstation controlled by computer. A conventional three-electrode cell was employed by using as working electrode a Pt disk ($A = 0.0314$ cm^2), as counter electrode a Pt wire and as reference an Ag/AgCl electrode. All cyclic voltammetric experiments (CVs) were carried out in phosphate buffer at pH = 7.0 and I = 0.2.

2.4 α-MoO₃/Pt Modified Electrode Preparation

The surface of Pt electrode, initially polished with alumina, was washed and electrochemically pre-treated by CV between −0.2 V and +1.2 V in 0.5 M H_2SO_4. Successively the Pt electrode, washed with deionised water and dried with N_2 flow, was modified by casting 10 μL of α-MoO₃/ethanol suspension directly onto Pt electrode surface. Then, the suspension was lets to evaporate at room temperature. After than α-MoO₃/Pt modified electrode was cycled between −0.6 V and +0.8 V at 0.02 Vs^{-1} until a steady-state current was obtained.

3 Results and Discussion

The formation process of α-MoO₃ hierarchical plates structure through resistive heating of 80 min was investigated through morphological analysis by SEM. The analysis allows to observe surface features of the material that is characterized by an high density of hierarchical branched α-MoO₃ microstructures, where many flakes grew on the substrate with secondary flakes 10–20 μm length, and 0.1–400 μm width (Fig. 1). The synthesized plates appeared clean and flat.

The chemical composition of α-MoO₃ plates was obtained by energy dispersive X-ray (EDX) spectra. The EDX spectra revealed that they contain only molybdenum and oxygen elements. The XRD pattern confirmed the presence of orthorhombic structured α-MoO₃ [JCPDS 05-0508]. The well marked (0 1 0) peaks in XRD pattern reveal that the α-MoO₃ plates have some planes grown along (0 1 0) i.e., "b"-axis, which means the stacking of layers one over the other. However no characteristic peaks of other molybdenum oxides or impurities were detected. This data is important as it indicates the purity of the prepared sample. The chemical characterization was completed by Raman spectroscopy that confirmed the orthorhombic phase of synthesized α-MoO₃ structures according to literature [9, 10]. In particular the peaks recorded at 666, 819 and 994 cm^{-1} are considered the
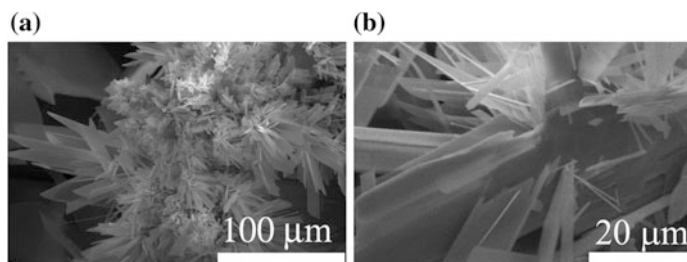
Fig. 1 Typical SEM images of the Mo plate resistively heated for 80 min

fingerprints of the α-MoO₃ phase. In order to study the detailed structure of synthesized α-MoO₃, transmission electron microscopy (TEM) and high resolution transmission electron microscopy (HRTEM) were applied. The low-magnification TEM image (Fig. 2) of α-MoO₃ plate confirms that it is transparent, clean and flat. The highly crystalline nature of the sample is verified by high resolution (HRTEM) imaging from the rectangle-closed area of TEM image. This result is in agreement with many literature reports regarding the growth behavior of α-MoO₃ crystals [11–13].

Electrocatalytic performances of the as-synthesized α-MoO₃ plates deposited onto Pt electrode (α-MoO₃/Pt) for methanol oxidation were evaluated in phosphate buffer at pH = 7 and scan rate v = 50 mVs⁻¹, before and after methanol additions. Results were compared with ones obtained on bare Pt in the same experimental conditions as control. Representative cyclic voltammogram, recorded in alcohol absence, at α-MoO₃/Pt modified electrodes is shown in Fig. 3 (baseline curve). In these experimental conditions a characteristic peak pair, attributed to Mo(V)/Mo (IV) surface red-ox process, respectively in oxidation at $Ep_a(I) = +210$ mV and in reduction at $Ep_c(II) = +100$ mV, is evident on the α-MoO₃/Pt modified electrodes. This characteristic pair of peaks related to molybdenum species adsorbed on to Pt electrode surface is over-imposed to the typical electroactivity of platinum [9]. Electrocatalytic experiments carried out after methanol addition show representative CVs where a significant current rise is observed with methanol increment at 0.1, 0.5 and 1.0 M (Fig. 3). Two well developed oxidation peaks appear in direct scan, coupled with other two oxidation peaks in reverse scan, particularly enhanced at high methanol concentration. This overall current increment suggests a synergic interaction between α-MoO₃ and Pt surface with a co-catalytic effect versus methanol as also reported for a similar system (i.e. Pt-Mox) in acidic conditions [14].

Fig. 2 Typical TEM image of a α-MoO₃ plate. Insert HRTEM image of the rectangle-closed area
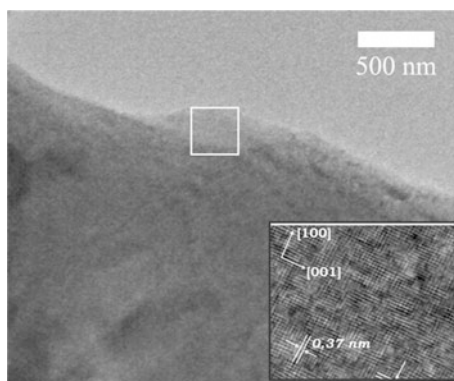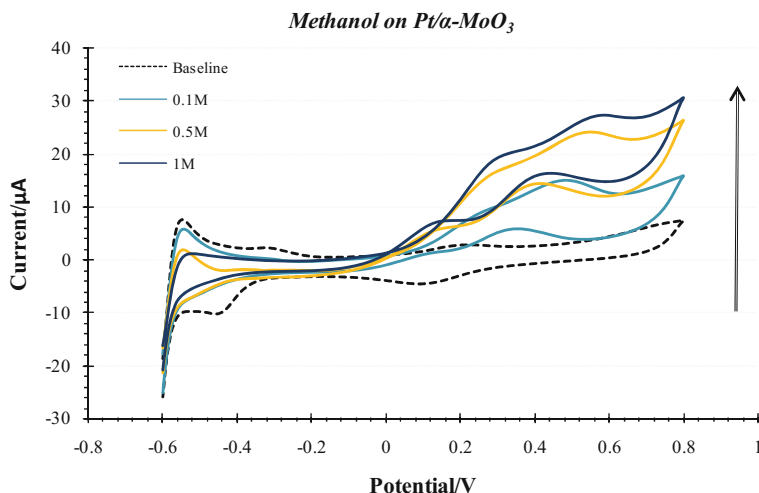
Fig. 3 Cyclic voltammograms recorded in PBS N_2 satured on Pt/α-MoO$_3$ electrode to consecutive additions of methanol. Scan rate 50 mVs^{-1}

4   Conclusions

α-MoO$_3$ belts, plates and flower-like hierarchical structures were obtained by direct oxidation in air of molybdenum metal foil through resistive heating method. SEM, XRD, HRTEM, SAD and Raman, measurements confirmed that the final structure is crystallized orthorhombic α-MoO$_3$. Original results obtained by using α-MoO$_3$ structures platinum modified electrodes as anode in electrochemical oxidation of methanol shows the enhanced catalytic properties of platinum in synergy with α-MoO$_3$ structures.

References

1. Lu, X., Wang, R., Yang, F., Jiao, W., Liu, W., Hao, L., He, X.: J. Mater. Chem. C **4**, 6720–6726 (2016)
2. Zhang, H., Gao, L., Gong, Y.: Electrochem. Commun. **52**, 67–70 (2015)
3. Dighore, N.R., Anandgaonker, P.L., Gaikwad, S.T., Rajbhoj, A.S.: Mater. Sci.-Pol. **33**, 163–168 (2015)
4. Liu, Z., Zhong, M., Tang, C.: Large-scale oxide nanostructures grown by thermal oxidation. In: IOP Conference Series: Materials Science and Engineering, IOP Publishing, pp. 012022 (2014)
5. Martínez, H., Torres, J., Rodríguez-García, M., Carreño, L.L.: Gas sensing properties of nanostructured MoO3 thin films prepared by spray pyrolysis. Physica B **407**, 3199–3202 (2012)

6. Zhao, L., Thomas, J.P., Heinig, N.F., Abd-Ellah, M., Wang, X., Leung, K.: Enhanced catalytic activity of palladium nanoparticles confined inside porous carbon in methanol electro-oxidation. Mater. Chem. **100**(C2), 2707–2714 (2014)

7. Chirizzi, D., Guascito, M.R., Filippo, E., Malitesta, C., Tepore, A.: A novel nonenzymatic amperometric hydrogen peroxide sensor based on CuO@Cu₂O nanowires embedded into poly(vinyl alcohol). Talanta **147**, 124–131 (2016)

8. Filippo, E., Baldassarre, F., Tepore, M., Guascito, M.R., Chirizzi, D., Tepore, A.: Characterization of hierarchical α-MoO₃ plates toward resistive heating synthesis: electro-chemical activity of α-MoO3/Pt modified electrode toward methanol oxidation at neutral pH. Nanotechnology 28:215601 (12 pp) (2017)

9. Py, M., Maschke, K.: Intra-and interlayer contributions to the lattice vibrations in MoO₃. Physica B+C **105**, 370–374 (1981)

10. Seguin, L., Figlarz, M., Cavagnat, R., Lassègues, J.-C.: Infrared and Raman spectra of MoO₃ molybdenum trioxides and MoO₃·xH₂O molybdenum trioxide hydrates. Spectrochim. Acta Part A Mol. Biomol. Spectrosc. **51**, 1323–1344 (1995)

11. Choopun, S., Wongrat, E., Hongsith, N.: INTECH Open Access Publisher (2010)

12. Chernova, N.A., Roppolo, M., Dillon, A.C., Whittingham, M.S.: Layered vanadium and molybdenum oxides: batteries and electrochromics. J. Mater. Chem. **19**, 2526–2552 (2009)

13. Ding, Q., Huang, H., Duan, J., Gong, J., Yang, S., Zhao, X., Du, Y.: Molybdenum trioxide nanostructures prepared by thermal oxidization of molybdenum. J. Cryst. Growth **294**, 304–308 (2006)

14. Kulesza, P.J., Pieta, I.S., Rutkowska, I.A., Wadas, A., Marks, D., Klak, K., Stobinski, L., Cox, J.: A. Electrocatalytic oxidation of small organic molecules in acid medium: enhancement of activity of noble metal nanoparticles and their alloys by supporting or modifying them with metal oxides Electrochim. Acta **110,** 474–483 (2013)

A New Resonant Air Humidity Sensor: First Experimental Results

Nicola A. Lamberti, Monica La Mura, Pasquale D'Uva, Nicola Greco
and Valerio Apuzzo

Abstract In this paper, first experimental results obtained on a new resonant humidity sensor are presented. The resonant sensor is made of a piezoelectric material coated with a hygroscopic material, therefore able to adsorb the water molecules contained in the surrounding air. The adsorbed water increases the sensitive layer mass, thus varying the sensor resonance frequency. The sensor is included in an electronic oscillator that tunes its oscillating frequency with the sensor resonance frequency. The output voltage signal is sampled and processed by a microcontroller in order to measure the resonance frequency. By relating the device resonance frequency to the amount of water adsorbed by the polymeric layer, an accurate air humidity measurement can be obtained.

Keywords Humidity sensor · Resonant sensor · Oscillating circuit
Resonance frequency measurement · Humidity measurement system

1 Introduction

Humidity sensors have been extensively investigated in the past [1, 2], but have been recently subject to renewed attention, mainly due to the widespread diffusion of embedded measurement system [3–5]. During the last years, in fact, an increasing demand for humidity measurement and control systems has grown, together with the diffusion of microcontrollers in many everyday applications. These systems are commonly used where there is a need to create a controlled environment, e.g. for the storage of food and wine, for the containment of moisture sensitive equipment, for the control of industrial processes. However, humidity sensing was recently also requested for the improvement of the yield of agricultural production [6], of in-room thermal comfort [7], for the preservation of artworks and

N.A. Lamberti (✉) · M. La Mura · P. D'Uva · N. Greco · V. Apuzzo
Department of Industrial Engineering, University of Salerno, Fisciano, SA, Italy
e-mail: nlamberti@unisa.it

79

artifacts in museums and archives [8, 9] and many other applications. Therefore, the increasing demand drives the search for new smaller and cheaper sensors.

Humidity can be measured in terms of Relative Humidity (RH), which is defined as the partial pressure of water vapor present in a gas to the saturation vapor pressure of water at a given temperature. For this reason, it depends on the temperature and pressure of the environment. It is a real number between 0 and 1, and is commonly expressed in percentage points.

Commercially available RH sensors are usually resistive or capacitive sensors, which relate the RH variation to the variation of resistance or capacitance of a ceramic or polymeric material. Acoustic sensors rely on the variation of mechanical properties of a material in response to the RH variation; common acoustic methods of humidity measurements are based on surface acoustic waves (SAW) [10, 11], bulk acoustic waves (BAW) [12], quartz crystal microbalances (QCM) [13–17] and quartz tuning forks (QTF) [18].

In this paper, a resonant air relative humidity sensor fabricated by coating both surfaces of a quartz crystal with a hygroscopic polymer is described. The device resonance frequency, acquired by means of a microcontroller, is observed and related to the surrounding air relative humidity. Experimental results obtained by the system prototype, compared to the results obtained by a commercial reference sensor, are presented.

2   The Measurement System

The proposed system is composed of a sensing element, an electronic circuit and a microcontroller. The sensing element is a quartz crystal, whose electrodes are covered by a moisture sensitive polymer. The electronic circuit is an oscillating circuit, whose frequency is tuned with the sensor resonant frequency. The output signal is given to the microcontroller, which samples the voltage waveform and counts the signal periods within a fixed time interval, in order to compute the oscillation frequency. The postprocessing of the acquired frequency data allows the computation of the RH measured during the observation time.

2.1   The Sensor

The fabricated sensor is based on an AT-cut 4 MHz quartz crystal. The quartz has a diameter $d_q = 8$ mm and a thickness $t_q = 0.25$ mm; the electrodes have a diameter $d_e = 6$ mm and the total thickness is $t_t = 0.4$ mm. Both surfaces of the quartz crystal were coated with a humidity sensitive polymer, polyvinyl acetate (PVA). The polymer was diluted in water, cast on the surfaces of the quartz electrodes in multiple layers and left to cure at ambient temperature. Figure 1 shows the quartz before and after the deposition of the water absorbing material.
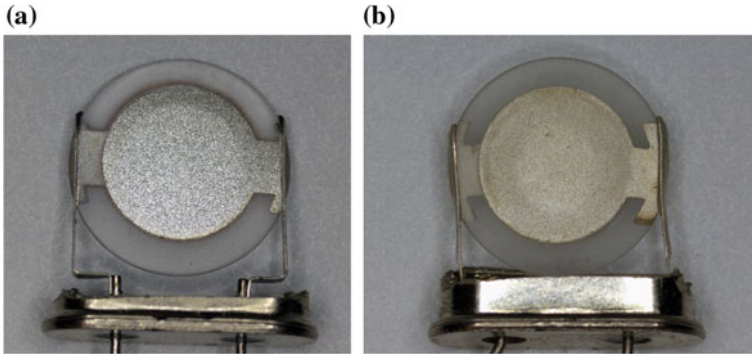
Fig. 1 The quartz used as active element of the humidity sensor, (**a**) without and (**b**) with the polymeric material coating

Fig. 2 The amplitude of the measured electrical input impedance of the quartz, before and after the addition of the polymeric layer
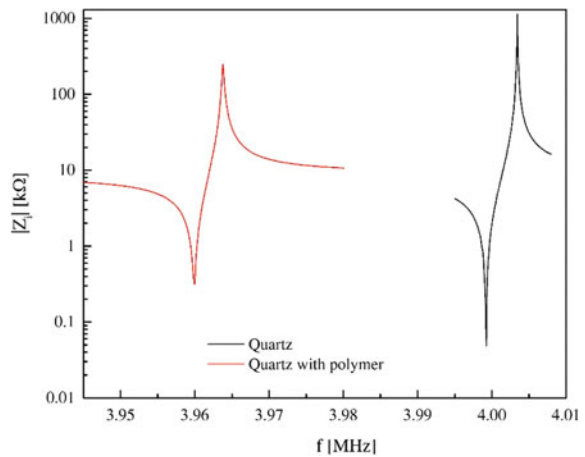
The addition of the mass of the polymeric film causes a decrease of the piezoelectric element thickness-shear fundamental resonance frequency. As can be seen in Fig. 2, the resonance frequency is reduced of about 40 kHz after the polymer deposition, shifting from $f_0 = 4$ MHz to $f_p = 3.96$ MHz.

The sensor works as a quartz crystal microbalance. When exposed to air, the hygroscopic polymer layer adsorbs the water molecules dispersed in the surrounding atmosphere. Therefore, the additional mass on the quartz surfaces increases accordingly with the amount of aqueous vapor present in air. The mass variation causes a shift of the sensor thickness-shear resonance frequency, which can therefore be related to the air RH value.

Under small-load approximation, i.e. by assuming that the variation of the polymer mass is small compared to the quartz mass, the resonance frequency

variation Δf due to the change of mass Δm is given by the well-known Sauerbrey equation [19]:

$$\Delta f = -\frac{2f_0^2}{A\sqrt{\mu\rho}}\Delta m \tag{1}$$

where Δf is the frequency variation, f_0 is the quartz resonance frequency, Δm is the mass variation, A is the quartz surface, μ and ρ are the shear modulus and the mass density of the quartz crystal, respectively.

The frequency variation Δf is defined as

$$\Delta f = f_p - f_0 \tag{2}$$

where f_p is the resonance frequency that depends on the amount of water adsorbed by the polymer.

By assuming that Δm linearly increases with the RH, according to the relation

$$\Delta m = k\,RH, \tag{3}$$

the sensor resonance frequency f_r can be related to the RH by using (1) and (2):

$$f_p = f_0\left(1 - \frac{2f_0}{A\sqrt{\mu\rho}}kRH\right) \tag{4}$$

By using (4) the RH value can be obtained from the sensor resonance frequency measurement.

As it is well known, the sensitivity S can be defined, for the proposed sensor, as

$$S = \frac{df_p}{dRH} = -\frac{2f_0^2}{A\sqrt{\mu\rho}}k \tag{5}$$

The S parameter depends on the polymer adsorption capabilities by the k coefficient, and can be computed by using a reference sensor.

2.2 The Oscillating Circuit

In order to measure the resonance frequency of the device, the sensor was included into a Pierce oscillator. The circuit tunes its oscillation frequency with the sensor resonance frequency. Figure 3 shows the schematic of the electronic circuit implemented in the proposed portable measurement system.

Fig. 3 The humidity resonant sensor (XTAL) used as a resonator in a Pierce circuit
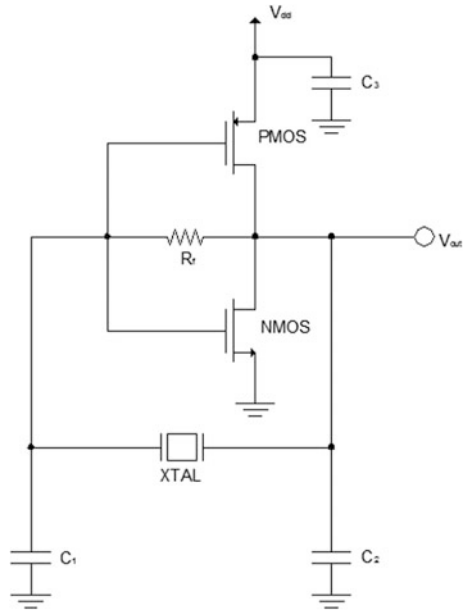
Table 1 Parameters of the Pierce circuit

Parameter	Value
nMOS & pMOS	NOT gate CD4007CN
V_{DD}	5 V
R_f	10 MΩ
C_1	47 pF
C_2	47 pF
C_3	220 nF

The oscillating circuit is based on a CMOS NOT logic port, connected to a feedback network made of the sensor and two equal capacitors. Table 1 lists the circuit components.

In order to compute the sensor resonance frequency, the circuit output is connected to a microcontroller that samples the voltage signal and counts the number of positive slope switching within a given time interval.

The microcontroller also acquires a RH measurement performed by a commercial sensor (DHT-22), used as a reference to calibrate the fabricated device.

A data logger stores the reference RH value, the sensor resonance frequency and the date and time of the measurements in a text file.

The portable relative humidity measurement system is shown in Fig. 4.
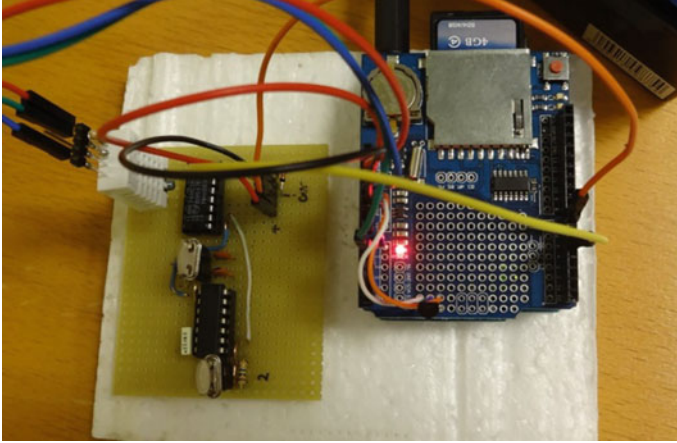
Fig. 4 The portable RH measurement system, made of the fabricated sensor, the Pierce oscillator, a microcontroller and a reference sensor

Fig. 5 The resonance frequency values (*blue dots*), measured by the proposed system, as a function of ambient relative humidity. The *red line* represents the average frequency value computed for each RH value (Color figure online)
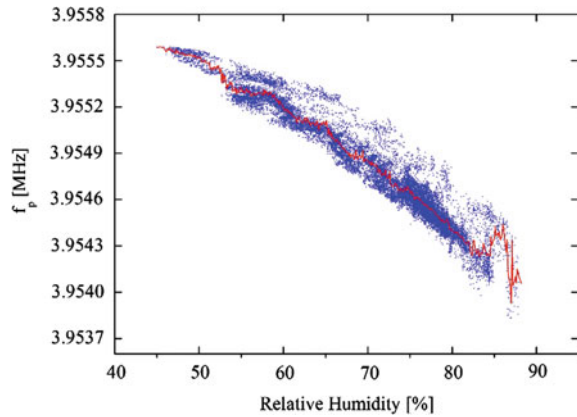
3 Experimental Results

The RH portable measurement system was used to perform outdoor measurements during 4 days. Figure 5 shows the resonance frequency values acquired as a function of the air relative humidity value, measured by the commercial sensor. The red line represents the average frequency value f_m^a corresponding to each RH measured value.

As can be seen in Fig. 5, the resonance frequency exhibits a variability around its average value. This is probably due to a hysteretic behavior of the polymer: the clusters of water molecules inside the polymer structure require different time intervals for growing and for drying. For this reason, the frequency value

corresponding to a given RH value depends on whether the humidity is increasing or decreasing. Hysteresis is one of the main problems of humidity sensors based on polymers, and can only be reduced by changing the polymer structure.

Figure 5 also shows that the average value of the measured resonance frequency varies almost linearly with the RH until the value RH = 85%. Above RH = 85%, the relation between the mass increase and the RH is nonlinear, so also the resonance frequency variation is not linear anymore.

The resonance frequency values measured by the sensor were used to obtain the RH value by means of (4). The sensitivity S in (5) was computed by adjusting the k coefficient, computed as the coefficient that minimizes the error on the RH measurement with respect to the results of the reference sensor. The resulting sensitivity is $S = 35.38$ Hz/RH%.

Figure 6 shows the RH measurements obtained by the commercial sensor used as reference (in black) and by the proposed sensor (in red). The results are in very good agreement, and confirm the capabilities of the proposed device. However, the RH computed by using the frequency measurements results is less accurate when the RH value is very high. As previously observed in Fig. 5, this is due to the nonlinearity of the adsorption phenomenon in PVA for high humidity rates.
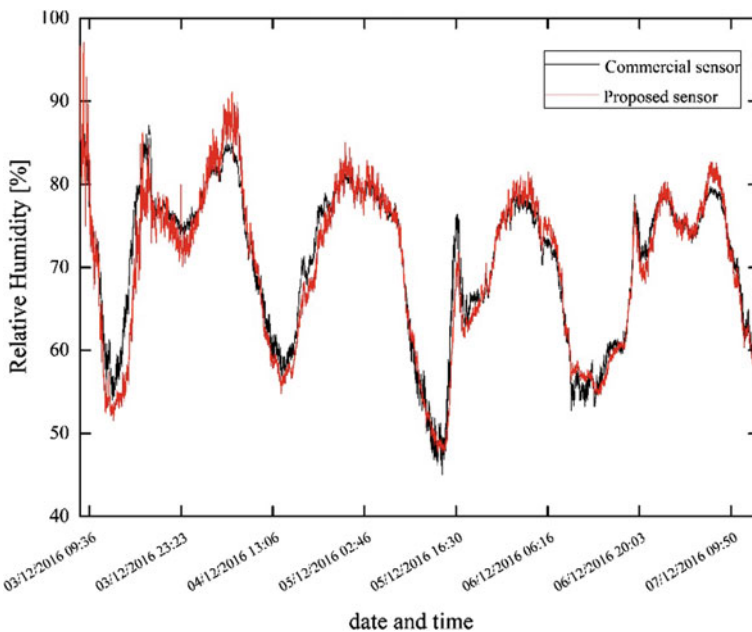
Fig. 6 The RH measurements obtained by the commercial sensor and by using the resonance frequency values measured by the proposed sensor

4   Conclusions

In this paper, a portable system for air humidity measurements was proposed. The system is made of a resonant sensor, an electronic oscillator and a microcontroller. The sensor is fabricated by casting multiple layers of PVA, a hygroscopic polymer, on both surfaces of a quartz crystal. When the humidity increases, the polymer mass increases due to the water adsorption, and therefore the sensor resonance frequency decreases. Vice versa, when the humidity decreases, the polymer dries and reduces its mass, therefore the sensor resonance frequency increases.

The device is included in a Pierce oscillator, in order to obtain a square wave that oscillates at the sensor resonance frequency. The microcontroller samples the output waveform and computes its frequency by counting the periods observed during a fixed time interval. The frequency variation is linear with respect to the RH value measured by a commercial DHT-22 sensor until the humidity value RH = 85%. The coefficient that relates the mass variation to the humidity variation was computed by minimizing the error with respect to the RH measurement obtained by the reference sensor, and was used to compute the sensor sensitivity $S = 35.38$ Hz/RH%.

References

1. Yamazoe, N., Shimizu, Y.: Humidity sensors: principles and applications. Sens. Actuators **10** (3-4), 379–398 (1986)
2. Kulwicki, B.M.: Humidity sensors. J. Am. Ceram. Soc. **74**(4), 697–708 (1991)
3. Fraden, J.: Handbook of Modern Sensors, vol. 3. Springer, New York (2010)
4. Chen, Z., Chi, L.: Humidity sensors: a review of materials and mechanisms. Sens. lett. **3**(4), 274–295 (2005)
5. Farahani, H., Wagiran, R., Hamidon, M.N.: Humidity sensors principle, mechanism, and fabrication technologies: a comprehensive review. Sensors **14**(5), 7881–7939 (2014)
6. Aqeel-ur-Rehman, J., Abbasi, A.Z., Islam, N., Shaikh, Z.A.: A review of wireless sensors and networks' applications in agriculture. Comput. Stan. Interfaces **36**(2), 263–270 (2014)
7. Kang, J.: Integrated comfort sensing system for indoor activity. In: SICE-ICASE International Joint Conference, Busan, pp. 5868–5872 (2006)
8. La Gennusa, M., Rizzo, G., Scaccianoce, G., Nicoletti, F.: Control of indoor environments in heritage buildings: experimental measurements in an old Italian museum and proposal of a methodology. J. Cult. Heritage **6**(2), 147–155 (2005)
9. Staniforth, S., Hayes, B., Bullock, L.: Appropriate technologies for relative humidity control for museum collections housed in historic buildings. Stud. Conserv. **39**(sup2), 123–128 (1994)
10. Nomura, T., et al.: SAW humidity sensor using dielectric hygroscopic polymer film. In: Ultrasonics Symposium, Proceedings, IEEE. Vol. 1. IEEE (1994)
11. Penza, M., Cassano, G.: Relative humidity sensing by PVA-coated dual resonator SAW oscillator. Sens. Actuators B: Chem. **68**(1), 300–306 (2000)
12. Qiu, X., et al.: Experiment and theoretical analysis of relative humidity sensor based on film bulk acoustic-wave resonator. Sens. Actuators B: Chem. **147**(2) 381–384 (2010)
13. Morten, B., De Cicco, G., Prudenziati, M.: A thick-film resonant sensor for humidity measurements. Sens. Actuators A **37**, 337–342 (1993)

14. Schroth, A., Sager, K., Gerlach, G., Häberli, A., Boltshauser, T., Baltes, H.: A resonant poliyimide-based humidity sensor. Sens. Actuators B: Chem. **34**(1), 301–304 (1996)
15. Pascal-Delannoy, F., Sorli, B., Boyer, A.: Quartz crystal microbalance (QCM) used as humidity sensor. Sens. Actuators A **84**(3), 285–291 (2000)
16. Zhang, Y., Ke, Y., Rongli, X., Jiang, D., Luo, L., Zhu, Z.: Quartz crystal microbalance coated with carbon nanotube films used as humidity sensor. Sens. Actuators A **120**(1), 142–146 (2005)
17. Weili, H., Chen, S., Zhou, B., Liu, L., Ding, B., Wang, H.: Highly stable and sensitive humidity sensors based on quartz crystal microbalance coated with bacterial cellulose membrane. Sens. Actuators B: Chem. **159**(1), 301–306 (2011)
18. Zhou, X., et al.: Humidity sensor based on quartz tuning fork coated with sol–gel-derived nanocrystalline zinc oxide thin film. Sens. Actuators B: Chem. **123**(1), 299–305 (2007)
19. Sauerbrey, G.: Verwendung von Schwingquarzen zur Wägung dünner Schichten und zur Mikrowägung. Zeitschrift für Physik A Hadrons and Nuclei **155**(2), 206–222 (1959)

Part III
Biosensors

Food Allergen-IgE Impedance Measurements Evaluation in Allergic Children

**Simona Barni, Tommaso Addabbo, Ada Fort, Matteo Becatti,
Claudia Fiorillo, Marco Mugnaini, Niccolò Taddei, Valerio Vignoli,
Elio Novembre and Francesca Mori**

Abstract We propose a new strategy for the evaluation of the interaction between IgE proteins and allergens in allergic subjects by impedance measurements. Additionally, reactive oxygen species (ROS) production in leukocyte subpopulations from non-allergic and allergic children was evaluated. On the basis of our results, these new approaches show advantages in terms of diagnostic efficacy with respect to traditional UNICAP and prick skin tests, which are commercially available nowadays. Here we describe in detail the instrument for impedance evaluation and the measurement protocols, defining univocally, in this way, the overall measurement technique.

Keywords Impedance measurement · Allergy diagnosis · ROS production

1 Introduction

Food allergy is a disorder secondary to abnormal immunologic response to food antigens. Immunoglobulin E (IgE) mediated reactions are most common and include a variety of symptoms in some cases severe (anaphylactic shock). Allergen-specific immunoglobulin E (IgE) antibodies play a pivotal role in the development of food allergy which is characterized by the release of chemical mediators such as histamine and leukotrienes from activated mast cells and

S. Barni · E. Novembre · F. Mori
Allergy Unit, Department of Pediatric, Anna Meyer Children's
University Hospital, Florence, Italy

T. Addabbo · A. Fort (✉) · M. Mugnaini · V. Vignoli
Department of Information Engineering and Mathematics,
University of Siena, Siena, Italy
e-mail: ada.fort@unisi.it

M. Becatti · C. Fiorillo · N. Taddei
Department of Experimental and Clinical Biomedical Sciences "Mario Serio",
University of Florence, Florence, Italy

basophils. Cross-linking of IgE receptors with an allergen is required for the activation of these cells; therefore, more than two IgE antibodies are required to bind to one allergen molecule. The binding between antigen and the variable domain of the antibody is weak and essentially non-covalent. Electrostatic interactions, hydrogen bonds, van der Waals forces, and hydrophobic interactions are all known to be involved depending on the interaction sites [1, 2]. In every patient the possible prevention of mild or severe allergic reaction should represent the main goal for clinicians however the traditional UNICAP and Skin Prick tests are not useful regarding this aspect.

Hence, it has been recently suggested an alternative method to measure IgE-allergen interaction by means of impedenzimetric measurements [3]. The proposed method is simpler with respect to the traditional UNICAP and skin prick tests and can supply different information not only in terms of mass reaction but also in terms of speed reaction interaction. In this paper the authors, starting from an existing design, try to prove that the system can perform repeated measurement over time with an appreciable repeatability degree once used to asses allergy to casein and parsley. This aspect is crucial to determine whether the system can provide reliable results on not. The impedenzimetric measurements have been performed in parallel with cytofluorimetric analyses (in 20 Non-allergic and 15 Allergic children) which can give additional and complementary information about the allergic reaction.

2 Measurement System Description

The idea at the basis of the proposed measurement technique relies on the fact that the interaction between the IgE and the corresponding allergen takes place through an electrochemical bonding mechanism which changes serum impedance according to the number of IgE which bind to the allergen. Therefore the choice of developing an ad hoc impedance measurement system as the one depicted in Fig. 1, seems reasonable. The instrument comprises an integrated circuit (AD5933), which performs the impedance measurement, a fluid sampling system, which delivers the MUT across the measuring electrodes, and finally a control unit, a touch screen and a memory card and is able to operate in the range 10–100 kHz in AC regime. Preliminary measures have been performed on different allergic and non-allergic subjects using a common (casein) food allergen (Fig. 2). Measurement repeatability and capability to discriminate among positive and control subjects are evident. The first one in particular is very effective among children forcing the subjects to painful, repeated and extensive tests over time for trustable assessment.
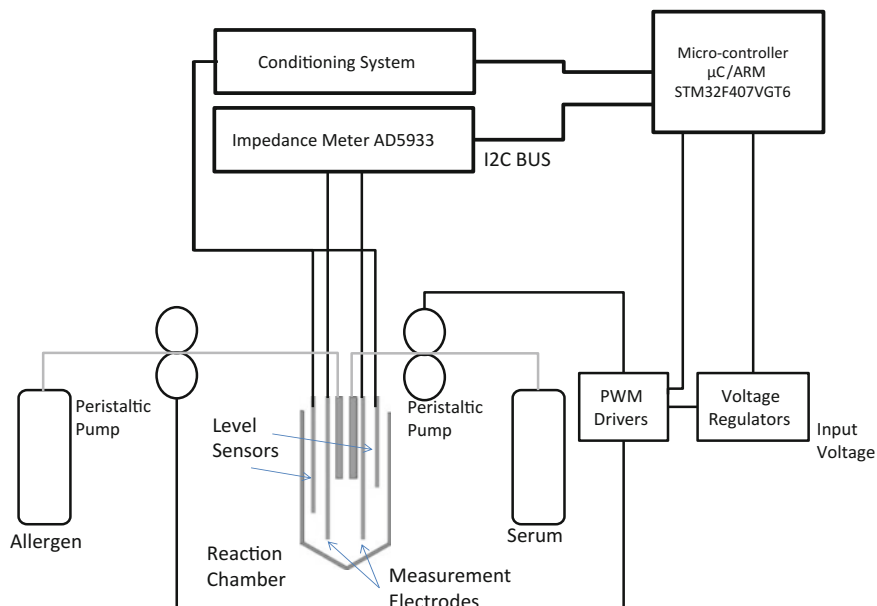
Fig. 1 Schematic of the proposed device. Set up messages are generated from the ARM controller for the Impedance meter (using I2C bus). Measurement results are return by the Impedance meter IC to the ARM processor on the same bus. The arm microcontroller controls also the sampling system containing the MUT

3 ROS Determination by Flow Cytometry Analysis

Citofluorometric analysis of intracellular ROS production in Lymphocytes, Monocytes and Granulocytes from Non-allergic and Allergic children (15 Allergic and 20 Non Allergic children) was performed. Data are reported in Fig. 3.

All blood samples were collected from the antecubital vein in a seated position, using EDTA as anticoagulant, between 9 and 10 AM. The blood samples were transported to the laboratory and analyzed not > 2 h from the time of collection. An aliquot of the whole blood was used for FACS analysis determinations. WBC were separated from the whole blood by BD FACS Lysing Solution (BD Biosciences, Canada), following manufacturer's protocol. Cell viability was assayed by flow cytometry with propidium iodide staining and was found to exceed 95%.

As previously reported [4], after collection, EDTA-anticoagulated blood (100 μl) was resuspended in 2 ml of BD FACS Lysing Solution (Becton Dickinson Biosciences, San Jose, CA, USA), gently mixed, and incubated at RT in the dark for 10 min, following manufacturer's protocol. Next, cells were centrifuged, supernatant discarded and cells washed twice in PBS. To determine the level of
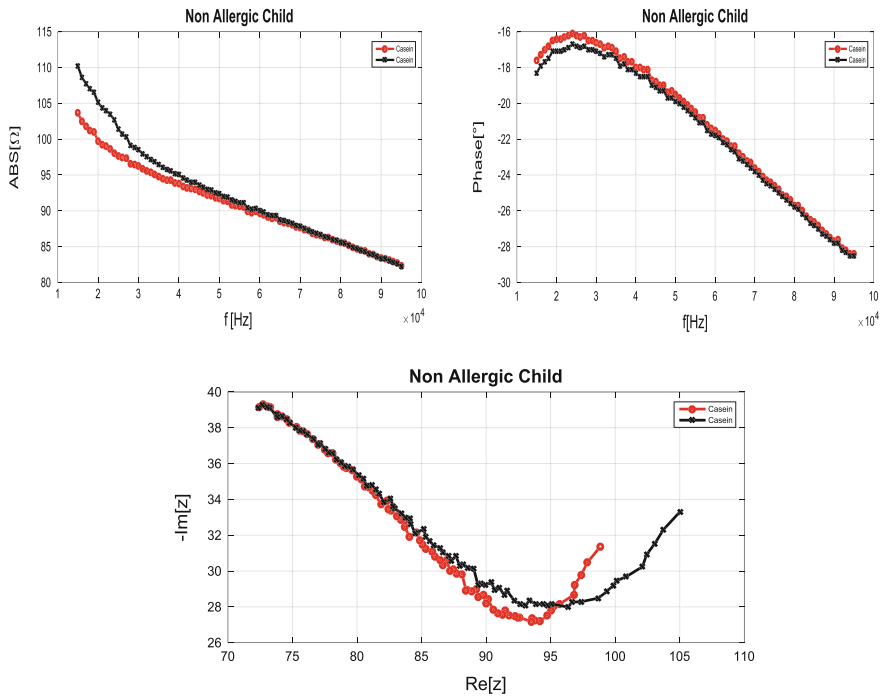
Fig. 2 Phase, Absolute value and Impedance spectrogram of the IgE Allergen interaction in non-allergic (Vernal Keratocongiuntivitis) and casein allergic subjects with UNICAP results greater than 100 kU/L. Figures show high measurements system repeatability

intracellular leukocyte ROS production (lymphocyte, monocyte and granulocyte subpopulations), cells were incubated with H2DCF-DA (2.5 μM) (Invitrogen, CA, USA) in RPMI without serum and phenol red for 15 min at 37 °C. After labelling, cells were washed and resuspended in PBS and analysed immediately using a FACSCanto flow cytometer (Becton-Dickinson, San Jose, CA). The sample flow rate was adjusted to about 1000 cells/s. For a single analysis, the fluorescence properties of 5000 monocytes were collected. The respective gates were defined using the distinctive forward-scatter and side-scatter properties of the individual cell populations. Moreover, cell viability was controlled by flow cytometry with propidium iodide staining and was found to exceed 95%. Data was analysed using BD *FACSDiva software* (Becton-Dickinson, San Jose, CA, USA).
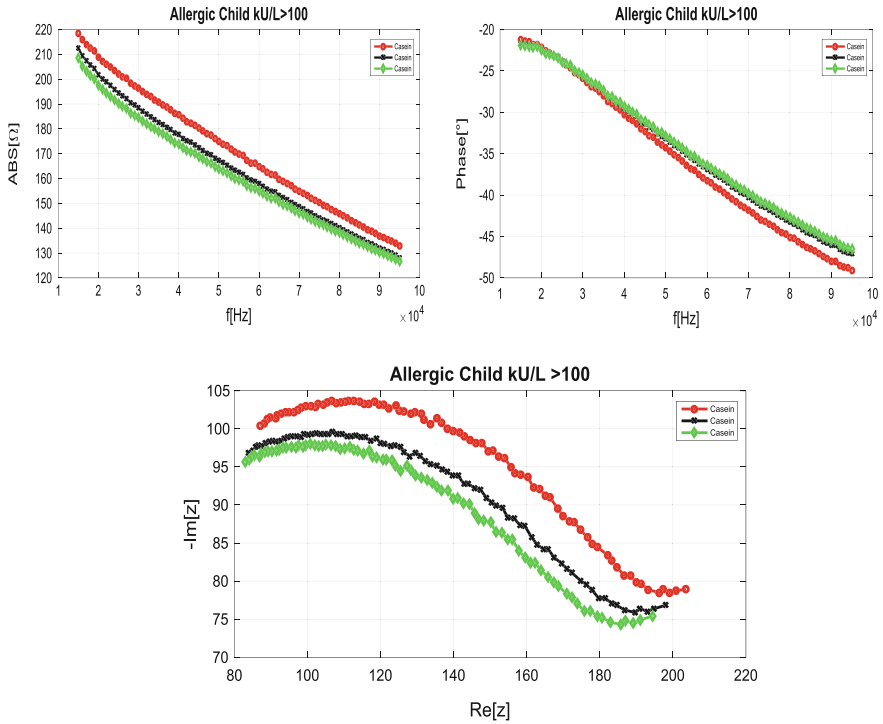
Fig. 2 (continued)

Fig. 3 Citofluorometric analysis of intracellular ROS production in Lymphocytes, Monocytes and Granulocytes from Non-allergic ($n = 20$) and Allergic children ($n = 15$). Group mean $\pm$ SD, calculated by considering the overall mean of different experiments/replicates as single value for each subject, are reported
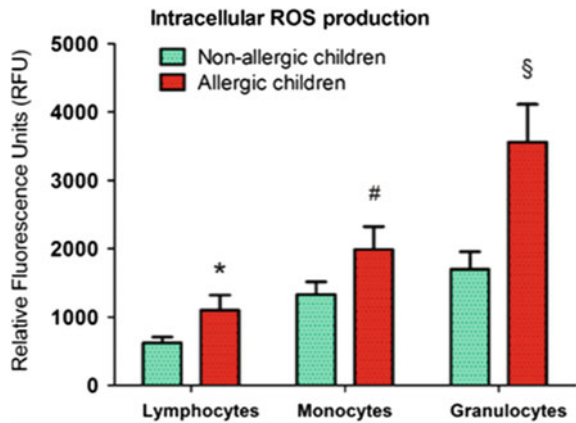
4   Discussion

Free radicals, atoms or molecules with one or more unpaired electrons, derive from oxygen, nitrogen, or various organic compounds. Oxygen-derived reactive molecules are part of the normal metabolism of living cells. They are very reactive substances which can pair their unpaired electron with an electron taken from other compounds, causing their oxidation, and they become reduced. In the biological and medical fields, they play a role mainly in the processes of aging, cancerogenesis, cardiovascular, various metabolic, neurodegenerative and endocrine diseases, in addition to their roles in several immune and autoimmune mechanisms. In fact, the association between chronic inflammation and oxidative stress is well documented. In particular, increased ROS levels may induce a variety of pathological changes that are highly relevant in nasal and airway mucosas (increased nasal mucosal sensitivity and secretions, production of chemoattractant molecules, and increased vascular permeability).

It has been recently shown that allergic children are exposed to severe oxidative stress, in fact in allergic disease eosinophils, neutrophils, and basophils are involved being eosinophils the most dominant inflammatory cells. Additionally, when activated, eosinophils have an even greater ability of ROS synthesis than neutrophils [5].

In line with this, numerous studies reported that degranulation of mast cells induced by chemical agents or by physiological stimuli is accompanied by ROS generation [6]. Activation of mast cells by phagocytosis-inducing factors can also be accompanied by ROS production. Moreover, bone marrow mononuclear cells (BMMCs) stimulated with silicone dioxide produce inflammatory mediators in a ROS-dependent manner. Thus, it was shown that inhibition of ROS accumulation using a cell-permeable superoxide dismutase (SOD) mimetic, prevents degranulation and secretion of leukotrienes in mouse BMMCs [7]. Interestingly, the use of different antioxidants (SOD-mimetics, resveratrol) in vitro and in vivo has been found to inhibit degranulation of mast cells as well as cytokine production. Endogenic antioxidants such as thioredoxin-1 and heme oxygenase-1 also affect the activation of mast cells [8].

In line with this, previous studies performed on selected group of patients with food allergies confirmed an increased metabolic activity of neutrophils [9]. Similarly, increased ROS production, both by resting and stimulant-induced neutrophils, were observed in studies conducted on a large group of children with well-documented food allergies [10].

Based on these findings, we suggest that leukocyte ROS estimation can represent a useful test for cross validation in allergic children. ROS detection can be specifically and sensitively performed in leukocyte subpopulations (lymphocytes, monocytes and granulocytes) by cytofluorimetric method [4, 11–13]. In the present study, we used peripheral leukocytes as a new model for studying oxidative stress-mediated homeostasis alterations in allergic children. In particular, we propose the assessment of leukocyte redox status as an innovative tool to monitor oxidative stress so minimizing the risk of developing allergy-related adverse events.

The combination of these two valid and cheaper techniques, alternative to traditional UNICAP and prick skin tests, can be proposed as a new laboratory test able to accurately diagnose symptomatic food allergy greatly facilitating clinical practice.

References

1. Absolom, D.R., Van Oss, C.J.: The nature of the antigen-antibody bond and the factors affecting its association and dissociation. CRC Critical Reviews in Immunology **6**(1), 1–46 (1986)
2. Schroeder, H.W., Cavacini, L.: Structure and function of immunoglobulins. The Journal of allergy and clinical immunology **125**(2S2), S41–S52 (2010)
3. Barni, S., Fort, A., Becatti, M., Fiorillo, C., Mugnaini, M., Vignoli, V., Addabbo, T., Pucci, N., Novembre, E.: Detection of allergen-IgE interaction in allergic children through combined impedance and ros measurements. IEEE Trans. Instrum. Meas. **66**(4), 616–623 (2017)
4. Becatti, M., Fiorillo, C., Gori, A.M., Marcucci, R., Paniccia, R., Giusti, B., Violi, F., Pignatelli, P., Gensini, G.F., Abbate, R.: Platelet and leukocyte ROS production and lipoperoxidation are associated with high platelet reactivity in Non-ST elevation myocardial infarction (NSTEMI) patients on dual antiplatelet treatment. Atherosclerosis. **231**(2), 392–400 (2013 Dec)
5. Emin, O., Hasan, A., Aysegul, D., Rusen, D.: Total antioxidant status and oxidative stress and their relationship to total IgE levels and eosinophil counts in children with allergic rhinitis. J Investig Allergol Clin Immunol. **22**(3), 188–192 (2012). PubMed ID: 22697008
6. Suzuki, Y., Yoshimaru, T., Inoue, T., Niide, O., Ra, C.: Role of oxidants in mast cell activation. Chem. Immunol. Allergy **87**, 32–42 (2005)
7. Brown, J.M., Swindle, E.J., KushnirSukhov, N.M., Holian, A., Metcalfe, D.D.: Silicadirected mast cell activation is enhanced by scavenger receptors. Am. J. Respir. Cell Mol. Biol. **36**, 43–52 (2007)
8. Catalli, A., Karpov, V., Pundir, P., Dimitrijevic, A., Kulka, M.: Comparison of the inhibitory effects of resveratrol and tranilast on IgE, 48/80 and substance P-dependent mast cell activation, Allergy Asthma Clin. Immunol. **6**, 1–14 (2010)
9. Żbikowska-Gotz, M., Pałgan, K., Socha, E., et al.: Measurement of effector properties of neutrophilic granulocytes in patients with allergic hypersensitivity to food. Postepy Dermatologii i Alergologii **28**(3), 175–180 (2011)
10. Kamer, A., Zeman, K., Tchórzewski, K.: Chemiluminescencja neutrofilów krwi obwodowej u niemowląt i małych dzieci z alergią pokarmową. Medycyna Wieku Rozwojowego **7**(1), 35–41 (2003)
11. Barygina, V.V., Becatti, M., Soldi, G., Prignano, F., Lotti, T., Nassi, P., Wright, D., Taddei, N., Fiorillo, C.: Altered redox status in the blood of psoriatic patients: Involvement of NADPH oxidase and role of anti-TNF-α therapy. Redox Rep. **18**, 100–106 (2013). doi:10.1179/1351000213Y.0000000045
12. Sofi, F., Whittaker, A., Cesari, F., Gori, A.M., Fiorillo, C., Becatti, M., Marotti, I., Dinelli, G., Casini, A., Abbate, R., Gensini, G.F., Benedettelli, S.: Characterization of Khorasan wheat (Kamut) and impact of a replacement diet on cardiovascular risk factors: cross-over dietary intervention study. Eur. J. Clin. Nutr. **67**(2), 190–195 (2013 Feb)
13. Becatti, M., Emmi, G., Silvestri, E., Bruschi, G., Ciucciarelli, L., Squatrito, D., Vaglio, A., Taddei, N., Abbate, R., Emmi, L., Goldoni, M., Fiorillo, C., Prisco, D.: Neutrophil Activation Promotes Fibrinogen Oxidation and Thrombus Formation in Behçet Disease. Circulation **133**(3), 302–311 (2016 Jan 19)

Enhancement in PDMS-Based Microfluidic Network for On-Chip Thermal Treatment of Biomolecules

G. Petrucci, N. Lovecchio, M. Nardecchia, C. Parrillo, F. Costantini, A. Nascetti, G. de Cesare and D. Caputo

Abstract In this paper, we present an improved microfluidic network based on polydimethylsiloxane (PDMS) and thin film heaters for thermal treatment of biomolecules in lab-on-chip systems. It relies on the series connection of two thermally actuated valves, at both inlet and outlet of the network, in order to reduce leakage of sample when its process temperature approaches 100 °C. The spatial arrangement of valves and microfluidic channels in between has been optimized using COMSOL Multiphysics, through the investigation of the system thermal behavior. Taking into account the simulation results, the geometries of the heaters have been defined following standard microelectronic technologies and the microfluidic network has been fabricated by soft lithography. The experiments demonstrate that with the proposed configuration the liquid evaporation is strongly reduced since more than 80% of the sample is recovered after a practical thermal treatment experiment.

1 Introduction

Lab-on-Chip (LoC) are miniaturized systems performing analytical and bioanalytical analysis in small units [1]. Typical applications require flow control in microfluidic channels through micro pumps and/or micro valves as well as thermal treatments by means of thin film heaters [2, 3]. An important example is the

G. Petrucci (✉) · N. Lovecchio · M. Nardecchia · C. Parrillo · G. de Cesare · D. Caputo
D.I.E.T, Sapienza University of Rome, Via Eudossiana, 18, 00184 Rome, Italy
e-mail: Giulia.Petrucci@uniroma1.it

M. Nardecchia · F. Costantini · A. Nascetti
S.a.E, Sapienza University of Rome, Via Salaria, 851/881, 00138 Rome, Italy

F. Costantini
Department of Chemistry, Sapienza University of Rome, P.le A. Moro, 5, 00185 Rome, Italy

Polymerase Chain Reaction (PCR) technique for DNA amplification [4]. During PCR, samples experiment repeatedly heating and cooling cycles.

PDMS is a common material used in microfluidics due to its low cost and ease of fabrication [5, 6]. However, due to the permeability of PDMS, evaporation of droplets at elevated temperatures occurs. Therefore, most platforms for PCR require off-chip thermal cycling to prevent evaporation [7]. At the same time, however, different on-chip solutions have been proposed to overcome this issue [8, 9].

Furthermore, in order to avoid external components such as tygon tube, compressed air line or magnets, thermal actuated valves driven by thin film heaters can be employed. Also in this case sample evaporation is an important limiting factor when heating of very small volumes is performed. Indeed, it occurs through the thinner valves membrane during the PCR denaturation step when the process-chamber temperature approaches 100 °C. Sample reduction of 100% in less than 4 min at 95 °C was measured [10].

Within this framework, we present an improved microfluidic network based on polydimethylsiloxane (PDMS) and thin film heaters able to strongly reduce the liquid evaporation thanks to the series connection of two thermo-actuated valves at both the inlet and outlet of the microfluidic network.

The paper is organized as follows: section two reports the working operation of the system, section three presents the simulations, section four shows the experimental results and finally section five draws the conclusions.

2   Working Principle of the System

The working principle of the thermally actuated microvalves relies on the deflection of a PDMS membrane to close the channels. A sketch of the system in its basic configuration is reported in Fig. 1.
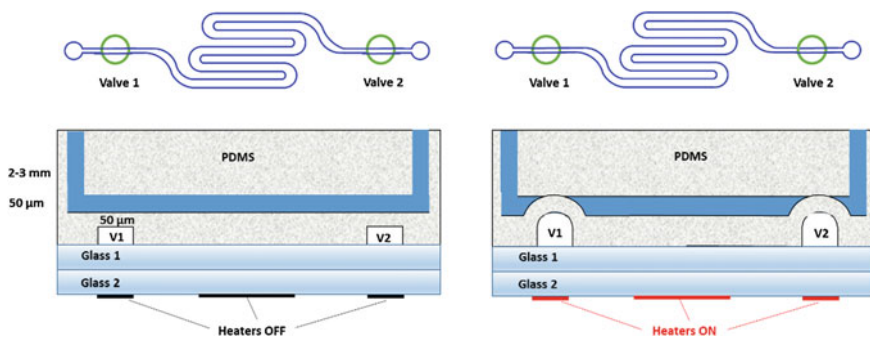
Fig. 1 Top view (*upper part*) and cross section (*bottom part*) of a simple configuration of PDMS valves actuated by thin film heaters
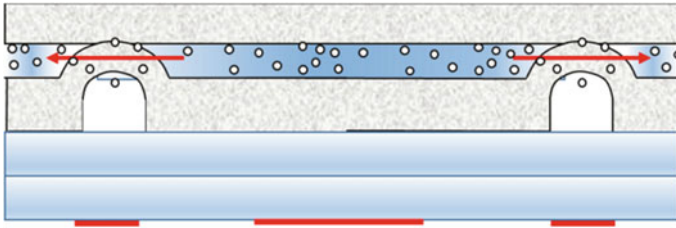
Fig. 2 Schematic illustration of the sample loss through the thin film PDMS membrane

It consists of two coupled glass substrates: a bottom glass which hosts the thin film heaters and a top glass which hosts the microfluidic network. The network includes: an inlet, an outlet, a process chamber where the thermal treatment is performed and two thermo-actuated valves. The valves (V1 and V2 in Fig. 1) are 50 μm-thick PDMS layers which act as deformable membranes. Three heaters are present on the bottom glass: two are aligned with the valves and the third is located in correspondence of the process chamber. After filling the microfluidic channel, the heaters underneath the valves are turned ON (Fig. 1 right). The resulting heat increases the temperature inside the air chamber, pushing up the valves (V1 and V2) and closing the channel. Subsequently, turning ON the heater under the process chamber, the thermal energy for the biomolecular treatment is provided.

As mentioned in the introduction, a limiting issue in the use of this configuration is the leakage that can occur through the thin PDMS membrane when the temperature of the process chamber approaches 100 °C (see Fig. 2). Due to the gas permeability and to the small thickness of the PDMS membrane layer, a decrease of the sample volume is expected.

In order to overcome this issue, we designed and investigated a new microfluidic network (Fig. 3) that includes a second valve close to the inlet, a second valve close to the outlet and a U-shaped microfluidic channel between each couple of valves.

The physical concept underneath this design is that, due to the spatial arrangement of the microfluidic channel connecting the two valves, the filling fluid of this region is kept at a lower temperature reducing evaporation from the process chamber.

3 Thermal Behavior Modeling

The thermal behavior of the system has been studied using COMSOL Multiphysics, a finite element numerical simulator that couples the thermal and electrical problems through the Joule effect when a voltage is applied to the heater.
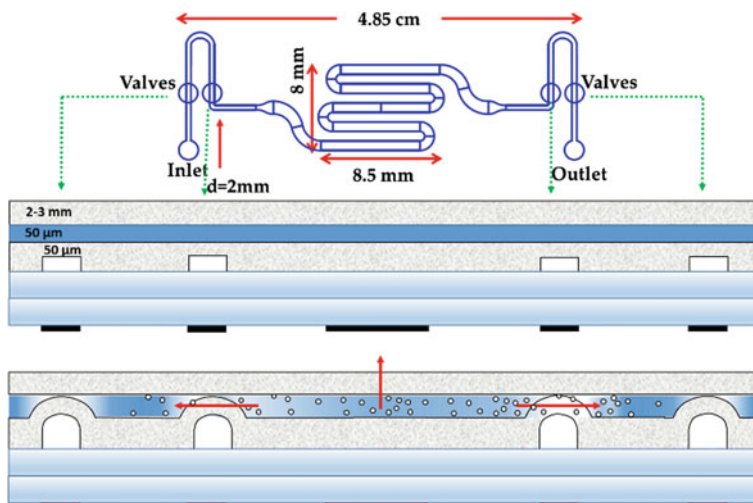
Fig. 3 Top view (*upper part*) and cross section (*bottom part*) of the two-valve system

Fig. 4 Geometries of the thin film heaters utilized in the two-valve system
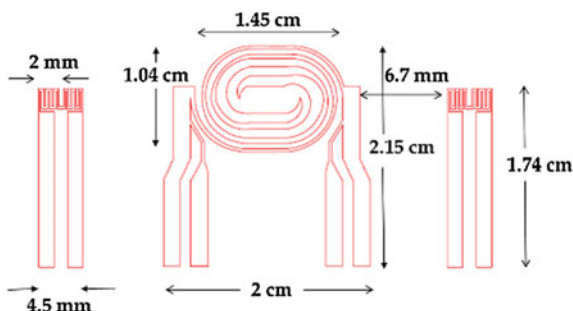
In particular, we focused on the valve heaters influence on the temperature uniformity needed for the PCR implementation and on the temperature of the channel between the two valves.

The simulated structure consists of two superimposed glass substrates with size equal to (50 x 50 x 1.1) mm. The geometries of the thin film heaters placed on the bottom side of the bottom glass are reported in Fig. 4.

The heaters below the valves is the series connection of two meander shaped resistors. Therefore, the corresponding valves are simultaneously actuated. Their geometry is quite simple because the requirements on the uniformity of the temperature distribution are not critical, while as reported in [11] the central heater has a double concentric spiral shape to guarantee a temperature uniformity of ±0.5 °C in the process chamber.

The temperature distribution of the system has been evaluated when the valves are at around 90 °C, which is the temperature able to deflect the PDMS membrane

and close the channel [12]. The distance between the valve and the central heater has been optimized and fixed at 6.7 mm. At this distance, Fig. 5 shows that, activating the valve heaters only, the temperature of the process chamber is around 40 °C. This value is low enough to avoid significant effect on the implemented biological procedure. For example, this temperature is lower than each temperature of the PCR steps (denaturation at 95 °C, annealing at 55 °C, extension at 72 °C).

With this configuration, the temperature of the fluid in the channel between the two valves has been also monitored. Figure 6 reports a zoom of the temperature distribution in correspondence of the two valves at the inlet and in the U-shaped microfluidic channel. We observe a temperature difference of about 40 °C between the two valves and the fluid in the farthest region of the microfluidic channel in between. In particular, the valves are at 102 °C (higher than the simulated 90 °C to ensure the perfect channel closure), while the coldest part of the channel is at 62 °C.

Fig. 5 Temperature distribution due to the activation of the valve heaters along the *dashed green line* of Fig. 4
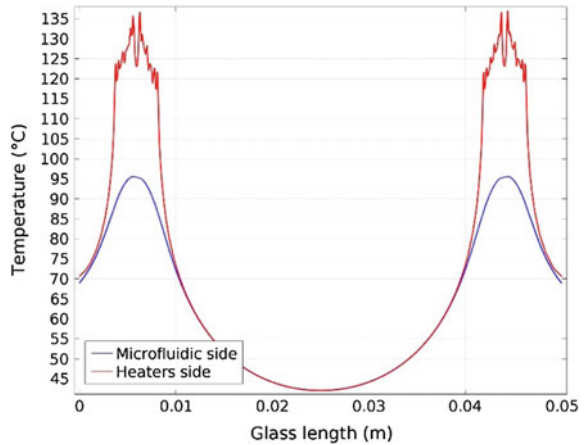
Fig. 6 Detail of the temperature distribution on the microfluidic side in correspondence of valves and of the U-shaped microfluidic channel
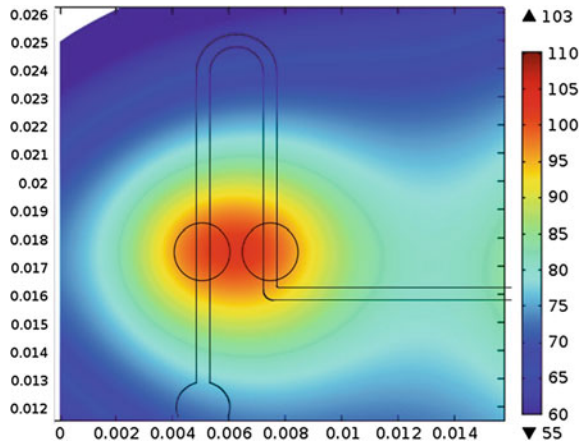
4   Experimental Results

The microfluidic network has been made by soft lithography as described in [12]. The valves have a cylindrical geometry with height and diameter equal to 50 μm and 2 mm, respectively. The height of the microfluidic channel is 50 μm.

The heaters are a stack of Cr/Al/Cr (100 nm/600 nm/100 nm) metal layers deposited by vacuum evaporation and patterned by standard photolithography processes following geometries reported in Fig. 4. Material selection and layer thickness design allow a USB power supply (at maximum 5 V and 500 mA).

The fabrication of the system has been completed placing the glass with the PDMS microfluidic system on the top of the glass hosting the thin film heaters and connecting this last glass to an electronic board to drive the heaters.

In order to show the enhancement in the PCR implementation, we have performed a comparison between the performances of the one-valve system (reported in Fig. 1) and the two-valves system (reported in Fig. 3). For both experiments, the microfluidic network has been first filled with colored water, then the valves have been activated to close the channels and to isolate the process chamber. After 2 min, the central heater has been turned on to reach 95 °C. Pictures in Fig. 7 report the situation 3 min after turning on the heater below the process chamber.
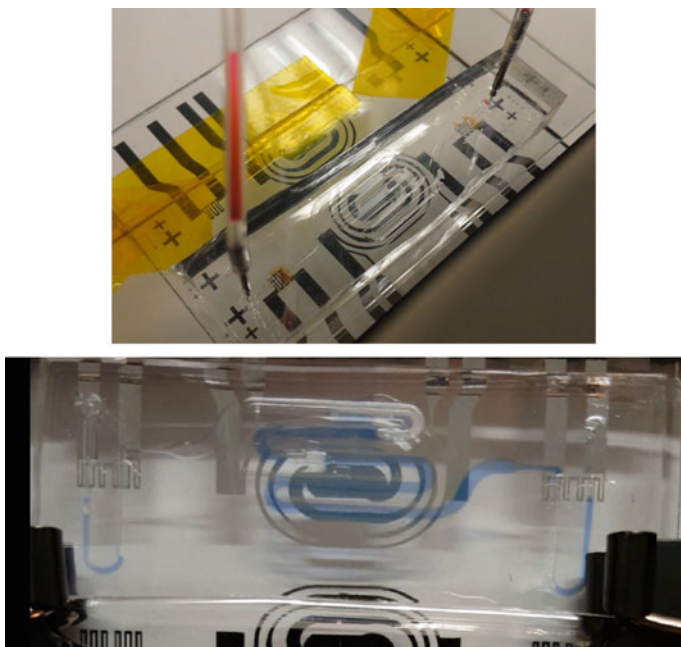
Fig. 7 Time evolution of the fluid inside the process chamber at 95 °C for the one-valve (*left*) and the two-valve (*right*) systems

For the one-valve system, the chamber is completely empty: the red colored water, present in the process chamber at the beginning of the experiment, has migrated to the tygon tubes connected at the inlet and outlet of the channel.

For the two-valves system, instead, the chamber is still almost full. The fluid shows a slight decrease, but the cold liquid in the "U" shaped channel minimizes the liquid loss. Indeed, collecting the sample at the end of the experiment we have found that more than 80% of the sample was recovered.

Therefore, our results demonstrate that with the new configuration the liquid evaporation is strongly reduced. Taking into account that a standard PCR is composed by 30/40 thermal cycles at the three different temperatures (30 s @ 95 °C, 30 s @ 55 °C, 30 s @ 72 °C) we infer that a whole PCR experiment can be reasonably implemented.

5 Conclusions

In this work, we have developed a new microfluidic network based on polydimethylsiloxane (PDMS) and thin film heaters for reducing sample losses during thermal treatment of biomolecules in lab-on-chip systems. For each inlet/outlet, the new network presents two thermo-actuated valves and a U-shaped microfluidic channel between each couple of valves.

Spatial positioning of the valves and of the U-shaped channel with respect to the process chamber, where the treatment of the biomolecules occurs, has been optimized by using the COMSOL Multiphysics.

Experiments performed comparing the standard and the new configuration the demonstrate the ability of the improved microfluidic network in minimizing fluid evaporation from the process chamber and suggest its potential application in practical biological analysis as DNA amplification through the PCR technique.

References

1. Abgrall, P., Gué, A.M.: Lab-on-chip technologies: making a microfluidic network and coupling it into a complete microsystem—a review. J. Micromech. Microeng. **17**, R15–R49 (2007)
2. Lovecchio, N., G. Petrucci, G., Caputo, D., Alameddine, S., Carpentiero, M., Martini, L., Parisi, E., de Cesare, G., Nascetti, A.: Thermal control system based on thin film heaters and amorphous silicon diodes, In Advances in Sensors and Interfaces (IWASI), 6th IEEE International Workshop on, pp. 277–282 (2015)
3. Caputo, D., de Cesare, G., Nardini, M., Nascetti, A., Scipinotti, R.: Monitoring of temperature distribution in a thin film heater by an array of a-Si: H temperature sensors. IEEE Sens. J. **12** (5), 1209–1213 (2012)

4. Parida, M., Sammarangaiah, S., Kumar Dash, P., Rao, P.V.L., Morita, K.: Loop mediated isothermal amplification (LAMP): a new generation of innovative gene amplification technique; perspective in clinical diagnosis of infectious deseases. Rev. Med. Virol. **18**, 407–421 (2008)

5. Wu, J., Cao, W., Wen, W., Chang, D.C., Sheng, P.: Polydimethylsiloxane microfluidic chip with integrated microheater and thermal sensor. Biomicrofluidics **3**(1), 012005 (2009)

6. Caputo, D., Ceccarelli, M., de Cesare, G., Nascetti, A., Scipinotti, R.: Lab-on-glass system for DNA analysis using thin and thick film technologies. Proceedings of Mat. Res. Soc. Symposia **1191**, 53–58 (2009)

7. Tewhey, R., Warner, J.B., Nakano, M.M., et al.: Microdroplet-based PCR enrichment for large-scale targeted sequencing. Nature biotechnology **27**(11), 1025–1031 (2009)

8. Zec, H., O'Keefe, C., Ma, P., Wang, T. H.: Ultra-thin, evaporation-resistant PDMS devices for absolute quantification of DNA using digital PCR, Solid-State Sensors, Actuators and Microsystems (TRANSDUCERS), 18th IEEE International Conference on Transducers, pp. 536–539, (2015)

9. Zec, H., Glover, C. J., Hsieh, W., Liu, L., O'Keefe, C., Wang, T. H.: Method for controlling water evaporation in pdms-based microfluidic devices, 18th International Conference on Miniaturized Systems for Chemistry and Life Sciences, pp. 1743–1745, (2014)

10. Polini, A., Mele, E., Sciancalepore, A.G., Girardo, S., Biasco, A., Camposeo, A., Cingolani, R., Weitz, D.A., Pisignano, D.: Reduction of water evaporation in polymerase chain reaction microfluidic devices based on oscillating-flow. Biomicrofluidics **4**, 036502 (2010)

11. Petrucci, G., Caputo, D., Lovecchio, N., Costantini, F., Legnini, I., Bozzoni, I., Nascetti, A., de Cesare, G.: Multifunctional System-on-Glass for Lab-on-Chip Applications. Biosens. Bioelectron. **93**, 315–321 (2017)

12. Zahra, A., Scipinotti, R., Caputo, D., Nascetti, A., de Cesare, G.: Design and fabrication of microfluidics system integrated with temperature actuated microvalve. Sensors and Actuators A: Physical **236**(1), 206–213 (2015)

A Continuous Flow Microelectrophoretic Module for Protein Separation

A. Capuano, A. Adami, V. Mulloni and L. Lorenzelli

Abstract In this paper, we are presenting the development of a microfluidic electrically driven SPLITT (Split flow thin fractionation) device, which can be used for online protein separation. The microfluidic network is realized by means of a three times laminated structure (thermo-compression lamination) of a thin dry film, Ordyl SY 355, which is patterned through a photolithographic technique. The device has been tested with a Bovine Serum Albumin (BSA) solution, through absorbance measurements with a spectrophotometer, with best achieved separation at the outlet of 40%, measured as relative concentration unbalance at output channels.

Keywords Sample preparation · Protein separation · Microfluidics
Dry film · SPLITT · Electrophoresis

1 Introduction

1.1 Miniaturization and Sample Preparation

Miniaturization of analytical instrumentation has become an important area of research and development over the last two decades. The constant push toward the size reduction of clinical laboratory analyzers in the field that is commonly called lab-on-a-chip (LOC) and in the "point of care" (PPOC) devices has led to a great enhancement of portable equipment and "real-time" and "on-line" applications. Several key benefits are linked to the miniaturization, such as reduced consumption of analytes and reagents, reduced production of waste, improved cost-efficiency and, as mentioned before, thanks to the small size and the portability of the devices, the possibility of "on-field" applications [1].

A. Capuano (✉) · A. Adami · V. Mulloni · L. Lorenzelli
Fondazione Bruno Kessler, Via Sommarive, 18, Trento, Italy
e-mail: capuano@fbk.eu

A. Capuano
University of Trento, Trento, Italy

In the framework of our research work, we are developing a microfluidic system that can be used as a pre-treatment device for the sample preparation in analytical microsystems, for instance coupled to bio-sensors. Sample pre-treatment phase is usually envisaged before chemical and biological analysis. For example, if we want to perform contaminants detection in a complex matrix as milk, we must consider that the sample consists in a solution of butterfat globules and water with dissolved carbohydrates and protein complexes. If we want a bio-sensor to perform a label free detection of some target-contaminants in milk, interferents in the matrix must be removed. Proteins are an important part of these interferents, and their concentration needs to be reduced, in order to avoid fouling and consequently the inhibition of the sensor, or false positive results in the analysis.

1.2 SPLITT System

There are several approaches to the separation of chemical species in a continuous-flow device [2]. Since proteins are charged molecules, electrophoresis is one of the most appropriate techniques for protein separation. We have realized an electrophoretic microchip that performs a differentiated migration of charged chemical species in a microchannel (150 microns depth).

The device that we have developed is based on the SPLITT theory, explained for the first time by J.C. Giddings [3] in 1985 and studied at microscale from early 2000's. According to the SPLITT theory, two different fluids are introduced in the device by means of two inlets: a sample that we want to purify and a carrier solution. Under the action of a driving force, including gravitational, centrifugal, electrical and magnetic forces, the particles that we want to separate from the sample migrate towards the carrier stream and they are flushed out from a dedicated outlet (Fig. 1). In the case of our device, a pulsed vertical electric field is imposed between the two electrodes; proteins are attracted by one of the electrodes and they move from the sample to the carrier stream. Therefore, the carrier solution (enriched in proteins) and the purified sample come out from the separation microchannel through two different outlets. The sample and the carrier simultaneously pass through the microchannel on the top of each other, in laminar-flow conditions. Indeed, there are no turbulences in the microstructure, because of very low flow rate (50 microliters per minute) and, consequently, very low Reynolds number (<10).

Giddings also showed that the laminar flow is maintained by the presence of structures at the ends of the separation microchannel that are called splitters, which precisely separate the streams and prevent mixing (Fig. 1). Thanks to a particular microfabrication technique, which we will show in the next paragraph, we have been able to realize the first dry film-based miniaturized SPLITT system equipped with a real splitting layer and suspended splitters. Narayanan et al. developed a microfabricated electrical SPLITT system, but with an "offset splitter" arrangement, by shifting the upper and the lower parts of the microfluidic microchannel [4]. Moreover, they
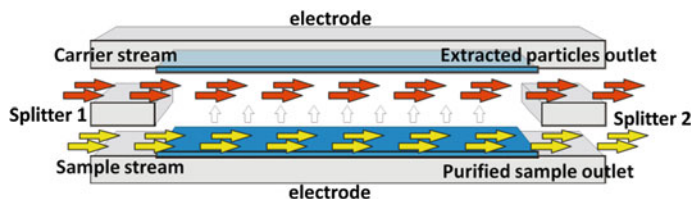
Fig. 1 SPLITT system

tested the device with amino-coated particles ranging from 108 to 220 nm, while we evaluated the separation performance with a protein solution (BSA).

Srinivas Merugu, Sant and Gale developed another interesting SPLITT system, not electrically driven, but based on diffusion [5]. They tested the device with proteins, but the system was not miniaturized at microscale (the thickness of the SPLITT channel was 0.5 mm and the length was 34 cm). On the contrary, our device exploits a very thin separation channel (hundreds of microns), with a length of 5.4 cm, increasing the possibilities to integrate it in micro-TAS systems and biosensing microtechnologies.

2 Fabrication Process

The electrophoretic module was fabricated (Fig. 2) using three different layers of dry film resist (Ordyl 355SY by Elga Europe) subsequently laminated (thermo-compression lamination) on a silicon substrate. Starting from a simple microfabrication process on dry film already proposed in other studies as [6], as we mentioned in the previous paragraph, we have realized a more complex structure providing a middle suspended layer (splitting layer) within the microfluidic network. After several tests we managed to set the best pressure/temperature condition for subsequent laminations and the proper development technique for the dry film after the exposition.

The first layer is laminated on a silicon wafer, then is exposed to UV and, after the development of the dry film, a second and a third layer are laminated on top of it, with a lower pressure and at lower temperature. The three lamination-exposition steps allow us to realize a microfluidic network patterned on the dry film through photolithography, including a splitter layer. The electrophoretic separation chamber is realized through two platinum electrodes that are deposited respectively on the silicon substrate and on a slide of glass that closes and seals the whole structure.

Details about the design of the separation channel and the microfluidic structure, taking into account the theory and the model of the electrically driven SPLITT are shown in a previous work [7] from our group. Once the fabrication process is finished, the silicon wafer is diced into chips of 2.4×5.4 cm^2, which are bonded together with the corresponding glass cover under vacuum using a wafer bonder. Two acrylic blocks are glued to the device inlets and outlets, as shown in Fig. 3.

Fig. 2 Fabrication process

1) Resist patterning and Platinum deposition

2) Lift-off Platinum (electrodes)

3) Lamination of 1st dry film layer

4) Dry film exposure and development

5) Lamination of 2nd dry film layer

6) Dry film exposure and development

7) Lamination of 3rd dry film layer

8) Dry film exposure and development

9) Glass cover bonding

10) Final device
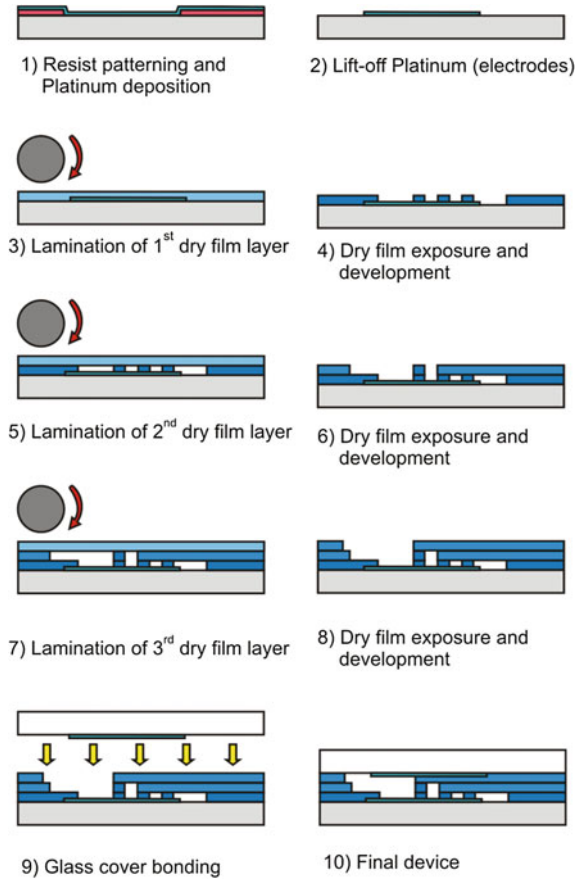
Fig. 3 The device equipped with the two acrylic connectors
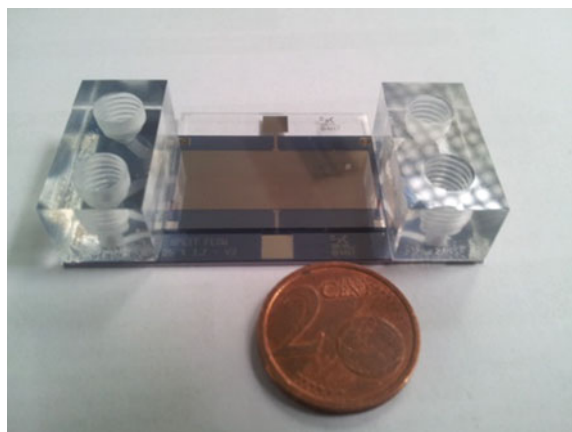
An unexposed film (20 μm thick) of Ordyl 320SY was used as an adhesive layer. The acrylic blocks were positioned by means of a pick and place equipment and then attached to the device by thermo-compressive bonding.

3 Results and Discussion

3.1 Experimental Setup

The electric field used for the electrical SPLITT separation was generated through a DAQ system, controlled with a LabVIEW dedicated software, which allowed the setting of all the parameters (peak to peak potential, offset potential, wave form, frequency and duty cycle for square waves) of the signal. The voltage selected for the measurements was 5 V (peak to peak voltage) and the waveform was a square wave. The device was attached on a PCB board through epoxy resin and the electrodes were connected to the pins of the PCB, by using gold ball-bonding. Two 10 ml syringe pumps, controlled from PC through a COM port, were used to drive the infusion flowrate through specific shell commands in the two inlets of the device. No carrier solution was used for this proof-of-concept test, but the same BSA solution was infused in the two inlets.

3.2 Performance Test

The two outlets were connected to two 2 ml tubes through two Teflon capillaries (1/16″), and the absorbance of the samples was measured at 280 nm with a spectrophotometer, in order to evaluate the concentration of the protein in the two output streams of the device. The results of a separation test are shown in Fig. 4.

Fig. 4 Separation test (Color figure online)
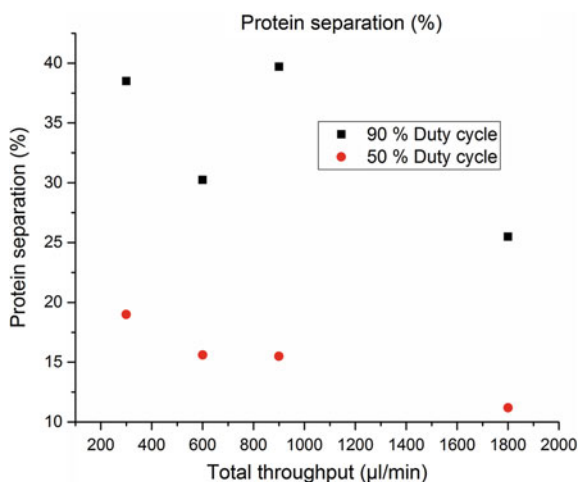
Table 1 Best conditions for the electrically driven SPLITT separation

Flow rate	900 µl/min
Voltage (electrodes)	5 V (peak to peak)
Frequency	10 kHz
Duty cycle	90%

Comparing the two samples, the difference in protein content between the two outlets is up to 40% within the tested conditions (Table 1). The difference of concentration is measured as relative unbalance at the output channels. According to the electrical SPLITT theory, as we can see, the best separation is achieved when the square-wave duty cycle is 90% (black dots), in comparison with the 50% duty cycle (red dots). This is reasonable since, in the first case, the signal is "high" for a longer time. Moreover, we can notice that if the test is performed in the range of 300–900 µl/min, the separation performances are stable, while if we drastically increase the flow rate, a performance reduction is observed, due to a shorter transition time in the separation channel. The phenomenon is particularly evident when the duty cycle is 50%.

4   Conclusion and Future Work

A continuous flow device for protein separation has been developed for this research work. The goal of this project has been the realization of an easy to integrate miniaturized sample preparation device for micro-TAS and biosensing applications. We decided to exploit the SPLITT separation theory, proposed for the first time by Giddings in 1985 and studied at microscale from the early 2000s. We designed and realized an electrically driven SPLITT microdevice, using a laminated thin dry-film (Ordyl SY 355) as structural material for the microfluidic network. We included two patterned platinum electrodes within a very thin separation microchannel (150 microns). The two electrodes have been structured respectively on silicon, used as a substrate for the lamination and on quartz, used to seal the microfluidic network on the top.

The separation performance has been tested through a spectrophotometer, evaluating the difference in protein content (Bovine Serum Albumin; 0,1% weight concentration) of the two different streams coming from the two outlets. Setting the best conditions for the separation (Table 1), it is possible to achieve 40% relative concentration unbalance at the output channels.

Future work will deal with the testing of different designs of the microfluidic network, in order to find the best geometric parameters for the separation channel, the inlets, the outlets and the suspended splitters. After the first offline tests that have proved the effectiveness of the electrical SPLITT separation, we are now going to carry out continuous protein separation measurements, since the technology is focused on continuous flow applications.

References

1. Hardt, S., Schönfeld, F.: Microfluidic Technologies for Miniaturized Analysis Systems, pp. 1–3. Springer
2. Pamme, N.: Continuous flow separations in microfluidic devices. Lab on a Chip **7**(12), 1644–1659 (2007)
3. Giddings, J.C.: Sep. Sci. Technol. **20**, 749 (1985)
4. Narayanan, N., Saldanha, A., Gale, B.K.: A microfabricated electrical SPLITT system. Lab on a Chip **6**(1), 105–114 (2006)
5. Merugu, S., Sant, H.J., Gale, B.K.: Diffusion Split-Flow Thin Cell (SPLITT) system for protein separations. Journal of Cromatography B **902**, 78–83 (2013)
6. Vulto, P., Huesgen, T., Albrecht, B., Urban, G.A.: A full-wafer fabrication process for glass microfluidic chips with integrated electroplated electrodes by direct bonding on dry film resist. J. Micromech. Microeng. **19**, 077001 (2009)
7. Capuano, A., Adami, A., Mulloni, V., Lorenzelli, L.: Design of an electrophoretic module for protein separation, IEEE Ph.D. Research in Microelectronics and Electronics (PRIME), 2016 12th Conference on, doi:10.1109/PRIME.2016.7519511

Thrombin Aptamer-Based Biosensors: A Model of the Electrical Response

Eleonora Alfinito, Lino Reggiani, Rosella Cataldo, Giorgio De Nunzio, Livia Giotta and Maria Rachele Guascito

Abstract Aptamers are target specific single stranded DNA, RNA or peptide sequences having the ability to bind a variety of proteins, molecules and also ions. Aptasensors, sensors based on aptamers, are at the frontier of sensing technology, mainly in diagnosis and therapy. They appear to be competitive with traditional sensors due to the possibility of detecting and measuring very low concentrations of many different ligands, whose detection and quantification are usually complex, expensive and time-consuming. In this paper we report about a thrombin aptasensor, able to resolve concentrations in a range of 6 orders of magnitude, and provide the microscopic interpretation of its electrical response on the basis of a single macromolecule approach. This investigation has been performed in the framework of an emerging branch of electronics devoted to proteins and living matter, also known as proteotronics.

E. Alfinito (✉)
Department of Innovation Engineering, University of Salento,
Via Monteroni, Lecce, Italy
e-mail: eleonora.alfinito@unisalento.it

L. Reggiani · R. Cataldo · G. De Nunzio
Department of Mathematics and Physics, "Ennio de Giorgi",
University of Salento, Via Monteroni, Lecce, Italy
e-mail: lino.reggiani@unisalento.it

R. Cataldo
e-mail: rosella.cataldo@unisalento.it

G. De Nunzio
e-mail: giorgio.denunzio@unisalento.it

L. Giotta · M.R. Guascito
Department of Biological and Environmental Sciences and Technologies,
University of Salento, Via Monteroni, Lecce, Italy
e-mail: livia.giotta@unisalento.it

M.R. Guascito
e-mail: mariarachele.guascito@unisalento.it

1   Introduction

Aptamers are single-stranded DNA, RNA or peptide sequences artificially produced to bind, with high selectivity and specificity, some assigned molecules, ions, proteins [1, 2]. They are generated on demand by an in vitro selection and amplification method called SELEX (Systematic Evolution of Ligands by Exponential Enrichment) [3]. By using this technique, there is the possibility to select aptamers within about 10^{15} templates. This allows one to obtain affinity values higher than those of natural selection [3] and, in general, comparable with those of monoclonal antibodies. This technique is of relevant interest in medicine and drug design, bioassays, food safety and environment monitoring. Aptamers can be used to capture and inhibit specific proteins at the origin of different kinds of cancer [4], so as to pathogens and molecules occurring in several diseases [1]. At present, some of them are under clinical trials and others were patented by pharmaceutical farms.

Concerning their specific mechanism of target binding, few is known, although many studies, performed with several techniques, are currently trying to shed light on the issue. On the experimental side, NMR and X-ray spectroscopy have obtained few but important results concerning their 2D and 3D structures [5, 6]. Furthermore, mainly due to their small size, several computational approaches have been developed to select aptamers with the highest target-binding ability [4]. Finally, and this is the topic of this paper, by using a complex network approach, the topological and electrical features of these macromolecules when used in electronic devices can be properly reproduced so that some predictions can be formulated.

In particular, attention is focused to the DNA aptamer TBA, which binds the exosite II of thrombin. This aptamer is one of the best known, concerning both its structure and its biological activity, since it efficaciously inhibits platelet thrombus formation [7]. As a matter of fact, it passed the first stage of clinical trials for circulatory disease, although it is too small (only 15 nucleobase) to be retained long enough in the body and efficaciously complete its action. Anyway, it has been selected as the active material of a thrombin sensor, with astonishing results. Few years ago, Cai and coworkers [8] proposed a TBA-based label-free sensor, able to detect and quantify thrombin in a wide range of concentration (10^{-12}–10^{-6} M).

By analyzing these data and other finding coming from several different experiments, we have reproduced and interpreted some puzzling results, and conclude that for an in vitro assembly, a resistance measurement can be valued as an affinity indicator.

2   The Experiment

The experiment was performed by using an electrochemical impedance spectroscopy assay. A gold thin film was functionalized with TBA and used as working electrode. The impedance spectra were plotted in the form of Nyquist semi-circular plots, whose diameter represents the electron-transfer resistance, R_e. The working

electrode was incubated with increasing concentrations of thrombin and the value of R_e was correspondingly recorded.

As a result, a monotonic increase of R_e was observed, up to a variation of more than 200% with respect the reference frame (no-thrombin). By using non-specific targets, no significant response was detected [8].

3 The Theoretical Approach

The theoretical approach to set up a microscopic model of the electrical mechanisms underlying the formation of the aptamer–thrombin complex is within the emerging sciene of proteotronics [9]. The main idea is to map the aptamer and the protein in complex networks which reproduce the macromolecules structures and correlate these structures to the electrical responses. This is made by using the available 3D structures of the macromolecules in different states of activations, in particular, before and after the binding. The network is designed by using the following rules: each nucleobase or amino acid is represented by a node, whose position corresponds to that of the C_1 or C_α carbon atom, respectively; two nodes are connected by a link only if they are closer than an assigned cut-off radius, R_C. Too small R_C values produce a disconnected network and too large R_C values produce a regular network. The optimal values are those allowing for a good resolution of the behavior of the macromolecule in different states of activation [9–13].

The next step consists in giving the links the meaning of a physical interaction, that the experiment is able to detect. In the present case, this is of electrical origin, since an impedance is measured. Therefore, each link is equipped with an elementary impedance, Z_{ij}, [9–13] and each node inherits the polarizability and resistivity of the corresponding amino acid/nucleobase. In such a way, each elementary impedance depends on the network structure, specifically on the distance of each couple-ij of nodes and also on the node electrical properties. The first and last node of the network are taken to be connected with ideal electrical terminals. Finally, by using the node Kirchhoff's law with a standard computational procedure [9], it is possible to evaluate the network total impedance, so as many topological features of the biomolecule (TBA alone and complexed with thrombin) in its different activation states. The impedance spectra are plotted as Nyquist plots and the zero frequency impedance (pure resistance) is investigated for different values of R_C.

4 Results

4.1 Materials

To perform our investigation we have used the following 3D structures, taken by the Public Data Bank [14]: 148D that describes TBA in its native form [5], 4DII

that describes the TBA-thrombin complex in the presence of K^+, and 4DIH that describes the TBA-thrombin complex in the presence of Na^+ [6]. We will call *active* the structure the aptamer exhibits when conjugated with thrombin. This is different from the structure of the aptamer in the native state, due to a conformational change.

Crystallographic data suggest a modest difference in structure between complexes formed in the presence of the two cations; anyway, it is well known that potassium increases the TBA affinity to thrombin. Therefore, we have performed our investigation both on the topological and electrical side, in order to be able to appreciate, if any, the differences that our model is able to resolve.

4.2 Topological and Electrical Features

In agreement with [6], the topological analysis, has not identified relevant differences between the structures complexed in the presence of different cations. This is shown in Fig. 1 that reports the degree distribution of the enzyme (thrombin) and of the complex (TBA-thrombin) in the presence of both the ions. The degree distribution represents the number of neighbors of each node vs. the node rank [15]. In this case, calculations refer to $R_C = 13$ Å. By contrast, differences are present between the aptamer in the native state and in the active states (in the presence of K^+ or Na^+). These differences become smaller and smaller when the complete structures (in the presence of K^+ or Na^+) are compared.

Since the structure investigation does not give a clue about the different affinities of the two compounds, we have performed a resistance investigation [13]. As a general result, we have found that the resistance is a probe more sensitive than the structure. Specifically, we have calculated the relative difference in resistance of the native structure with respect the active structures. Ions do not produce differences in this quantity as far as the aptamer alone is considered. On the other hand, when the

Fig. 1 The degree distributions calculated: *a.* in the absence of thrombin (*down curves*) for TBA in its native state (*stars*); TBA in the active state with K^+ (*triangles*); TBA in the active state with Na^+ (*crosses*); *b.* in the presence of thrombin (*top curves*) for the TBA-enzyme complex with K^+ (*circles*); in the presence of thrombin for the TBA-enzyme complex with Na^+ (*squares*)
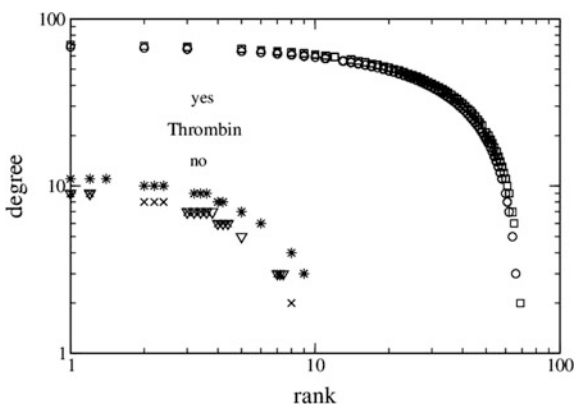
complete structures are compared with the aptamer in the native state, a significant difference in resistance is observed.

We have calculated the electrical resistance of the network describing the native structure of TBA and compared it with those of the networks of the compound in the presence of both K^+ and Na^+. The compound shows an increase of resistance compared with the TBA in the native state. Furthermore, in the presence of K^+ the resistance is significantly larger than those calculated in the presence of Na^+ [13] (see Fig. 2). Finally, the protein *reduces* the resistance of the aptamer in the active state (Fig. 2), because it perfectly completes the (partially disconnected) network corresponding to the TBA alone [13]. This result asserts resistance measurements as a novel test of aptamer-ligand affinity.

The experiment performed by Cai et coworkers [8] can be also described in the perspective of a single macromolecule investigation. In doing so, we should take into account that the real assembly contains a huge number of aptamers and that for increasing thrombin concentrations, more and more of them capture the target. Therefore, in order to calculate the sample resistance variation we have used the following formula [13]:

$$r_{sample} = N \cdot [f \times r_{com} + (1 - f) \times r_{nat}] \tag{1}$$

Where r_{sample} is the resistance of the complete sample, r_{com} the resistance of a single aptamer-thrombin complex and r_{nat} the resistance of the single aptamer in the native state. The sample resistance variation is the ratio between r_{sample}, for a certain value of f, and the resistance of a sample for which $f = 0$.

The capture of thrombin produces a change of the TBA free energy which is described as a change of the interaction radius, R_C, used for building up the network [13]. In particular, we assume that an increasing concentration of thrombin produces a reduction of R_C, i.e. of the link number, in agreement with the Kobilka model [12, 16, 17]. This happens both for the aptamer in the native and active state.

Fig. 2 Relative resistances of the aptamer in: the active state vs. the native state (*dotted line*); the bound state (*continuous line*: in the presence of K^+, *dashed line*: in the presence of Na^+) versus the native state
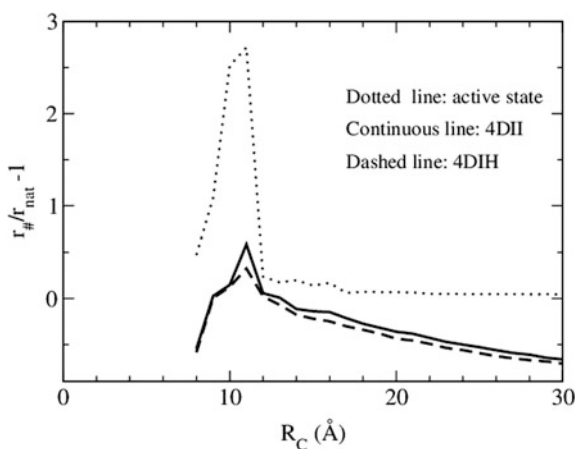
Then, by relating the fraction of aptamers complexed with the protein, f, and R_C a Hill-like relation can be written as [13, 17]:

$$f = \frac{x^a}{b + x^a} \tag{2}$$

where $x = (R_0 - R_C)/R_0$, and R_0 is the value of R_C corresponding to $f = 0$ i.e. a sample consisting only of TBAs in their native state, and a and b are numerical fitting parameters.

By simultaneously using Eqs. (1) and (2) it is possible to reproduce the experimental data within a close agreement (see Fig. 3 and Fig. 4). In the present case, we take $R_0 = 13.3$Å, which is the value corresponding to zero difference between the resistance of the aptamer alone and the complete macromolecule

Fig. 3 Comparison of experimental and theoretical data. The estimated fraction of complexed aptamers for a given concentration of thrombin (*dots*) and the fit performed by using Eq. (2) (see text). In the inset: the sample resistance variation as in experiments (*black*) and the corresponding value (*color*), calculated by using Eq. (1)
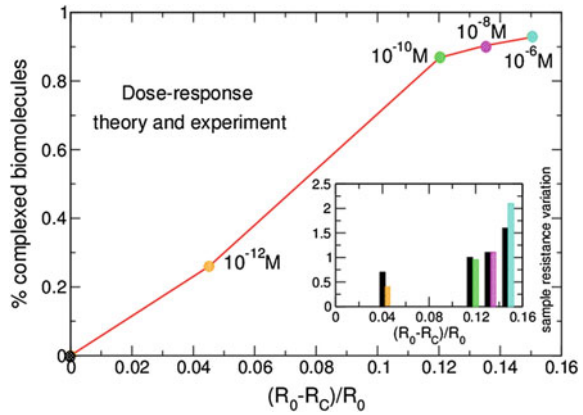
Fig. 4 The Nyquist plots calculated by using Eqs. (1) and (2), for a sample of aptamers in the native state ($R_C = 13.3$ Å), i.e. before that the thrombin is injected and a sample with the 93% of aptamers bound to the thrombin ($R_C = 11.3$ Å), corresponding to a concentration of 1 μM. The *dots* on the *horizontal axis* correspond to the experimental data for different concentrations [8]
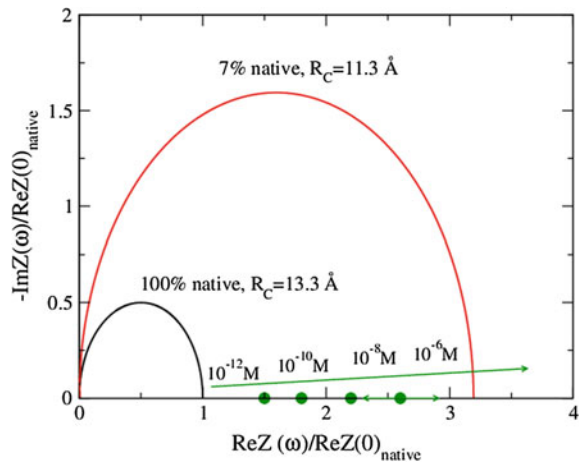
(Fig. 3). A different representation of our results is given in terms of Nyquist plots (Fig. 4). In particular, we report the calculated Nyquist plots for two different samples, one made of aptamers in the native state, the other containing 93% of aptamers bound to thrombin. These samples have been used to describe the experimental condition of: a) total absence of thrombin; b) a thrombin concentration of 10^{-6}M.

5 Conclusions

Within the emerging science of proteotronics we have reported a single-macromolecule theoretical and computational investigation to explore some electrical and topological features of the anti-thrombin aptamer TBA. In particular, we have confirmed that the presence of two different ions, say K^+ and Na^+ does not induce relevant differences between the structures of the TBA-thrombin complex. On the other hand, relevant differences in the resistance response have been detected, which suggest the use of resistance measurements as a complementary tool of affinity investigation. The theoretical modeling has been validated by comparing calculations with the experimental data obtained in the biosensing assembly proposed by Cai et coworkers. Experiments have been well reproduced by using an appropriate rescaling of the single aptamer resistance data.

References

1. O'Sullivan, C.K.: Aptasensors–the future of biosensing? Anal. Bioanal. Chem. **372**, 44–48 (2002)
2. Radi, A.E., Acero Sánchez, J.L., Baldrich, E., O'Sullivan, C.K.: Reusable impedimetric aptasensor. Anal. Chem. **77**, 6320–6323 (2005)
3. Stoltenburg, R., Reinemann, C., Strehlitz, C.: SELEX-a (r)evolutionary method to generate high-affinity nucleic acid ligands. Biomol. Eng. **24**(4), 381–403 (2007)
4. Lee, J.W., Kim, H.J., Heo, K.: Therapeutic aptamers: developmental potential as anticancer drugs. BMB Rep. **48**(4), 234–237 (2015)
5. Schultze, P., Macaya, R.F., Feigon, J.: Three-dimensional solution structure of the thrombin-binding DNA aptamer d (GGTTGGTGTGGTTGG). J. Mol. Biol. **235**(5), 1532–1547 (1994)
6. Russo Krauss, I., Merlino, A., Randazzo, A., Novellino, E., Mazzarella, L., Sica, F.: High-resolution structures of two complexes between thrombin and thrombin-binding aptamer shed light on the role of cations in the aptamer inhibitory activity. Nucleic acids res. gks512, (2012)
7. Li, W.X., Kaplan, A.V., Grant, G.W., Toole, J.J., Leung, L.L.: A novel nucleotide-based thrombin inhibitor inhibits clot-bound thrombin and reduces arterial platelet thrombus formation. Blood **83**, 677–682 (1994)
8. Cai, H., Lee, T.M., Hsing, I.M.: Label-free protein recognition using an aptamer-based impedance measurement assay. Sens. Actuators B **114**, 433–437 (2006)

9. Alfinito, E., Pousset, J., Reggiani, L.: Proteotronics: Development of Protein-Based Electronics, Boca Raton. CRC Press, FL (2015)
10. Alfinito, E., Reggiani, L.: Role of topology in electrical properties of bacterio-rhodopsin and rat olfactory receptor I7. Phys. Rev. E **81**, 032902 (2010)
11. Alfinito, E., Millithaler, J.-F., Pennetta, C., Reggiani, L.: A single protein based nanobiosensor for odorant recognition. Microelectron. J. **41**(11), 718–722 (2010)
12. Alfinito, E., Millithaler, J.F., Reggiani, L., Zine, N., Jaffrezic-Renault, N.: Human olfactory receptor 17-40 as an active part of a nanobiosensor: a microscopic investigation of its electrical properties. Rsc Adv. **1**(1), 123–127 (2011)
13. Alfinito, E., Reggiani, L., Cataldo, R., De Nunzio, G., Giotta, L., Guascito, M.R.: Modeling the microscopic electrical properties of thrombin binding aptamer (TBA) for label-free biosensors. Nanotechnology **28**(6), 065502 (2017)
14. Berman, H.M., Westbrook, J., Feng, Z., Gilliland, G., Bhat, T.N., Weissig, H., Shindyalov, I. N., Bourne, P.E.: The protein data bank. Nucleic Acids Res. **28**(1), 235–242 (2000)
15. Crespo, J., Suire, R., Vicente, J.: Assortativity and Hierarchy in Localized R&D Collaboration Networks. In: The Geography of Networks and R&D Collaborations, pp. 115–128. Springer, Basel (2013)
16. Kobilka, B.K., Deupi, X.: Conformational complexity of G-protein-coupled receptors. Trends Pharmacol. Sci. **28**(8), 397–406 (2007)
17. Alfinito, E., Reggiani, L.: Current-voltage characteristics of seven-helix proteins from a cubic array of amino acids. Phys. Rev. E **93**(6), 062401 (2016)

Chloramphenicol Determination by New Immunosensor Using Two Different Competitive Formats

Elisabetta Martini, Mauro Tomassetti, Riccardo Angeloni, Maria Pia Sammartino and Luigi Campanella

Abstract In the present research has been performed the analysis of Chloramphenicol in bovine milk and rivers water samples, by a new immunosensor using two different competitive formats, one in which the antibody was immobilized on the membrane superimposed to the electrode, the other in which the antigen was immobilized on the membrane. In both cases satisfactory results were obtained, but from an analytical point of view the first format shown better features.

Keywords Chloramphenicol · Analysis · Immunosensor
Two comparative formats

1 Introduction

Chloramphenicol is an antibiotic useful for the treatment of a number of bacterial infections [1–4], including meningitis, plague, cholera, and typhoid fever. Its use is only recommended when safer antibiotics cannot be used. The monitoring both blood levels of the antibiotic and blood cell levels every two days is recommended during treatment [3]. It is available intravenously, by mouth and as an eye ointment. The original indication of Chloramphenicol was in the treatment of typhoid, but the now almost universal presence of multiple drug-resistant Salmonella typhi has meant it is seldom used also for this indication except when the organism is known to be sensitive. Chloramphenicol may be used as a second-line agent in the treatment of tetracycline-resistant cholera. It is an excellent blood-brain barrier penetration (far superior to any of the cephalosporins) and remains the first-choice

E. Martini · M. Tomassetti (✉) · R. Angeloni · M.P. Sammartino · L. Campanella
Department of Chemistry, University of Rome "La Sapienza",
piazzale A. Moro 5, 00185 Rome, Italy
e-mail: mauro.tomassetti@uniroma1.it

treatment for staphylococcal brain abscesses. It is also useful in the treatment of brain abscesses due to mixed organisms or when the responsible organism is not known. In the present research we fabricated a new immunosensor for the analysis of Chloramphenicol, which was used for the analysis in real samples.

2 Method

The immunosensor (see Fig. 1) was competitive and we studied two different measurement formats, one in which the antibody was immobilized on the membrane "Immobilon" superimposed on the electrode, the other in which the antigen was immobilized on the membrane. Two formats were illustrated in detail in previous paper [5].

3 Results and Discussion

Equations of calibration straight lines and the main analytical parameters using two competitive formats are reported and compared in the Table 1.
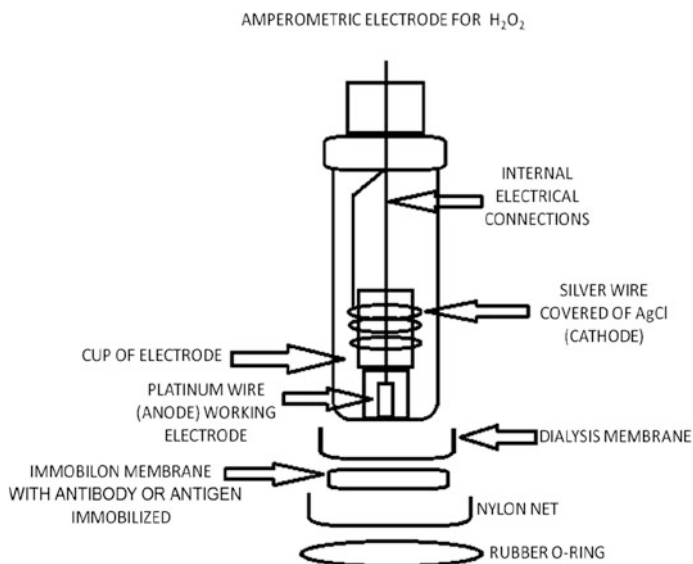
Fig. 1 Immunosensor assembly

Table 1 Main analytical data for the first and second competitive format

Test number	Format 1	Format 2
Transducer	Amperometric electrode for H_2O_2	Amperometric electrode for H_2O_2
Regression equation ($y = \Delta i$, $x = M$)	$y = 29.9\ (\pm 2.3)\ \log x + 232.1\ (\pm 11.6)$	$y = 35.6\ (\pm 1.2)\ \log x + 193.56\ (\pm 8.7)$
Linear range (M)	1.5×10^{-8}–1.2×10^{-3}	4.8×10^{-6}–1.4×10^{-2}
Correlation coefficient	0.9731	0.9867
Repeatability of the measurement (as pooled SD%)	6.5	6.2
Low limit of detection (LOD) (M)	0.9×10^{-8}	2.6×10^{-6}
Instrumental response time (min)	15	15

Table 2 K_{aff} and IC$_{50}$ values obtained using two different formats. (Each values is the mean of three determinations)

	K_{aff} (M^{-1}) RSD% $\leq$ 5.0	IC$_{50}$ (M) RSD% $\leq$ 5.0
Format 1	1.03×10^5	9.70×10^{-6}
Format 2	5.56×10^3	1.80×10^{-3}
Literature data [5]	3.34×10^5	2.99×10^{-6}

The study was also extended to the ability of the marked antibody used and the analyte under test to give the immunocomplex. To this end the K_{aff} values were found to be of the order of 1.03×10^5 M^{-1} in the first competitive format, while of the order of 5.56×10^3 M^{-1} for the second one (see Table 2).

IC$_{50}$ values (obtained by Langmuir curves, in which the "bound fraction" (B/Bo) $\times$ 100 was plotted versus the concentration of Chloramphenicol), were compared with some IC$_{50}$ values reported in the literature by other authors [6] (see Table 2) using other different immunoassay method and were found to be in good agreement with the values obtained by us using the first competitive format. The comparison of the results, obtained by the developed amperometric immunosensor, with two different competitive format, shows that the low detection limit for Chloramphenicol determination are of the order of 0.9×10^{-8} M in the first case, while is of the order of 2.6×10^{-6} M in the second case. The linearity range is of about five decades for the first format method, and about three decades and half for the second format method. Lastly the first competitive format for this classical amperometric method was applied to the determination of Chloramphenicol concentration in bovine milk and Tiber river water, obtaining satisfactory results, see Table 3.

Table 3 Determination of the chloramphenicol values in milks and river water samples. Values expressed both in mg kg^{-1} and M. (Each values is the mean of three determinations)

Samples	Found chloramphenicol (mg kg^{-1}) RSD% $\leq$ 5.0	Reported in the literature chloramphenicol concentration (mg kg^{-1})	Reference
Bovine milk	6.46	0.3 in milk	[7]
Tiber river water sample	11.31	4–28	[8]

4 Conclusions

Found data shown a linear range of about 5 and 3 decades and half, respectively, for the first and second competitive format, while the LOD had an order of magnitude of about 10^{-9} M in the first case and about 10^{-6} M in the second case.

Lastly, the first format was applied to the determination of Chloramphenicol concentration in bovine milk and in the Tiber river water analysis obtaining results acceptably correlated with those one reported in literature.

References

1. Malhadas, C., Malheiro, R., Pereira, J.A., de Pinho, P.G., Baptista, P.: World J. Microbiol. Biotechnol. **33**(3), 46 (2017)
2. Duan, Y., Wang, L., Gao, Z., Wang, H., Zhang, H., Li, H.: Talanta **1**(165), 671–676 (2017)
3. Cagini, C., Dragoni, A., Orsolini, G., Fiore, T., Beccasio, A., Spadea, L., Moretti, A., Mencacci, A.: Curr. Eye Res. **13**, 1–5 (2017)
4. Karaseva, N.A., Ermolaeva, T.N.: Talanta **15**(93), 44–48 (2012)
5. Merola, G., Martini, E., Tomassetti, M., Campanella, L.: Sens. Act. B: Chem. **199**, 301–303 (2014)
6. Fernández, F., Hegnerová, K., Piliarik, M., Sanchez-Baeza, F., Homola, J., Marco, M.P.: Biosens. Bioelectron. **26**(4), 1231–1238 (2010)
7. Commission Regulation (EU) No 37/2010 of 22 December 2009 on pharmacologically active substances and their classification regarding maximum residue limits in foodstuffs of animal origin
8. Choi, K., Kim, Y., Jung, J., Kim, M.H., Kim, C.S., Kim, N.H., Park, J.: Environ. Toxicol. Chem. **27**(3), 711–719 (2008)

Numerical Results on the Exploitation of Gold Nanostructures in Plastic Optical Fibers Based Plasmonic Sensors

N. Cennamo, F. Mattiello, P.A.S. Jorge, R. Sweid, L. De Maria, M. Pesavento and L. Zeni

Abstract The use of Nanostructured SPR sensors on Plastic Optical Fibers opens new challenges, because in an SPR sensor made by a continuous metal layer, the sensor's response is basically related to the metal properties at optical frequencies and to the waveguide characteristics. On the other hand, when a Nanostructured SPR sensor is used, the behavior is also related to the geometric parameters of the Nanostructures. Working on them it is potentially possible to tune the sensor's behavior. In this work the Authors present a numerical investigation in order to evaluate the behavior of two different SPR Nanostructured platforms, made by "long" gold Nanorods, and comparing them to an SPR sensor with a continuous gold layer. The difference between these two Nanostructured platforms is the orientation of the Nanorods, with respect to the light's propagation direction. The numerical results seem to indicate an increase of the sensitivity, when an SPR Sensor with long Nanorods is used, with respect to the sensor made by a continuous gold film, with some benefits.

Keywords Optical sensors · Localized surface plasmon resonance (LSPR) Surface plasmon resonance (SPR) · Nanostructures · Plastic optical fibers

N. Cennamo (✉) · F. Mattiello · R. Sweid · L. Zeni
Department of Industrial and Information Engineering, University of Campania
"Luigi Vanvitelli", Via Roma 29, 81031 Aversa, Italy
e-mail: nunzio.cennamo@unicampania.it

P.A.S. Jorge
Instituto de Engenharia de Sistemas e Computadores, Tecnologia e Ciência (INESC),
4200-465 Porto, Portugal

L. De Maria
Department of Transmission and Distribution Technology, Research
on Energetic System S.p.A, Via Rubattino 54, 20134 Milan, Italy

M. Pesavento
Department of Chemistry, University of Pavia, Via Taramelli 12, 27100 Pavia, Italy

1   Introduction

The study of plasmonic phenomenon is very important, because during the last two decades it has emerged as a suitable and reliable transduction method for label-free bio-molecular interaction based analytical methods [1]. Authors have presented several bio-chemical plasmonic sensors in D-shaped plastic optical fibers [2–5]. It is important to mention here that metals play an important role in plasmonics, besides the dielectric media [6]. In a metal, the optical as well as the electric properties are very different from dielectrics because of the existence of free electrons, that have a fast response to varying fields leading to a peculiar response. In SPR sensor platform, it is possible to modify the metal layer thickness, in order to change the sensor's response to the refractive index changes of the medium in contact with the metal surface [7]. Another approach to increase the performances of the SPR sensors for biochemical applications is to design a special geometry for the SPR platform [8]. An additional photoresist layer placed under the metal layer, in order to increase the performances of the SPR sensor in POF, has been presented [9]. Alternative SPR sensor devices are based on Nano-antenna arrays [10]. In the case of a structure made of holes on a metal screen, the optical transmission properties can be interpreted on the basis of a theory first formulated by Bethe in 1944 [11], for an idealized subwavelength hole, made in a perfectly conducting metal screen, with zero thickness, predicting very weak optical transmission properties. Later, Ebbesen discovered an extraordinary transmission phenomenon through arrays of subwavelength holes made in an opaque metal screen, with orders of magnitude more light than Bethe's prediction [12]. This phenomenon was called Extraordinary Optical Transmission (EOT), and is mainly due to the match between the wavelength of surface plasmon polaritons (SPPs) and the period of the aperture array, resulting in the larger transmittance through the smaller aperture. Another contribution is due to the Localized Surface Plasmon Resonance (LSPR) of the subwavelength hole. The EOT phenomena produced by holes of different shapes into a metal film were studied in [13–16].

In this work we show the numerical results obtained with a plasmonic sensor in a D-shaped POF, obtained by nanostructures into a gold layer. For these simulations we used the Lorentz-Drude model [17] to evaluate the metal dielectric permittivity of the gold, for different wavelengths. The numerical simulations were made for two different models: Classic SPR sensor in D-shaped POF [9] and SPR/LSPR sensor based on gold nanostructures in D-shaped POF. The sensitivity of SPR/LSPR sensor based on nanostructures in D-shaped POF is strongly related to the geometrical parameters of the nanostructures. In particular, changing the period between the structures is possible to obtain SPR, LSPR or both phenomena, as shown for nano-antenna arrays [18]. When a spacing period for which the LSPR phenomenon is produced is used, the polarization of the H-Field and the geometrical parameters of the pattern play a fundamental role. The obtained numerical results seem to indicate the possibility of obtaining an increase in sensitivity, using

an SPR Sensor with gold nanostructures, with respect to the sensor made by a continuous gold layer film.

For an SPR/LSPR sensor the sensitivity is defined as $S = \delta\lambda_{res}/\delta_{ns}$, where λ_{res} is the resonance wavelength and n_s is the refractive index of the sensing layer, placed on the metal layer. The performances of SPR/LSPR sensors based on nanostructures in D-shaped POF are strongly related to the geometrical parameters of the nanostructures, such as their length, width and relative spacing. In particular, by changing the period between the structures it is possible to obtain SPR, LSPR or both phenomena, as shown for nano-antenna arrays [18].

When using a spacing period for which the LSPR phenomenon is produced, the polarization of the incident field and the geometrical parameters of the pattern play a fundamental role.

In this work the authors want to simulate a Nanostructured SPR sensor made by long Nanorods placed on a D-shaped POF. This kind of geometry should be less critical to build, with respect to the subwavelength nano-antenna arrays [18], due to the bigger dimensions of the structures and the spacings between them. The change of the Nanorod's orientation, with respect to the light's propagation direction, can change the sensor's behavior, because different phenomena are involved, SPR, LSPR or both.

2 Sensing Platforms

Figure 1 shows the plasmonic POF sensor platforms considered in this work. In Fig. 1 are present two different SPR Nanostructured platforms, based on "long" Nanorods, with an SPR sensor with a continuous gold layer. The difference between these two Nanostructured platforms is the orientation of the Nanorods, with respect to the light's propagation direction, which is guided by a Plastic Optical Fiber. We have compared the results obtained with the Nanostructured platforms to those obtained with the classic D-shaped POF SPR sensor platform [9], based on the continuous gold film.

The simulations were made for these three platforms (Fig. 1), building a unitary cell model and applying the appropriate boundary conditions. The metal film used in all the three platforms is a thin gold film, with a thickness of 60 nm. For the SPR sensor made by a continuous gold layer, only the TM Mode gives a contribution to the SPR phenomenon. For the Nanostructured SPR sensors, we have used the name "*Pol*1" to indicate that the Nanorods orientation is orthogonal to the light's propagation direction (see Fig. 1c), and "*Pol*2" to indicate that the Nanorods orientation is parallel to the light's propagation direction (see Fig. 1b). For each "*Pol*" configuration we used the Modes TE and TM, calling them respectively "*Mode*1" and "*Mode*2", in order to observe the sensor's behavior for each of these modes. Figure 2 shows the incident field(s) and the geometric parameters used into the models.
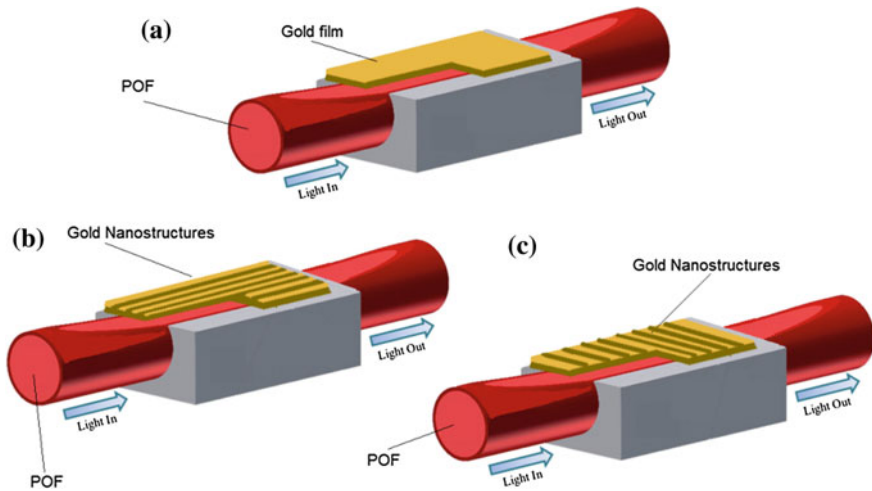
Fig. 1 SPR/LSPR sensors in D-shaped POFs; **a** Sensor with continuous gold layer; **b** Sensor with Gratings parallel to the light propagation direction; **c** Sensor with Gratings orthogonal to the light propagation direction
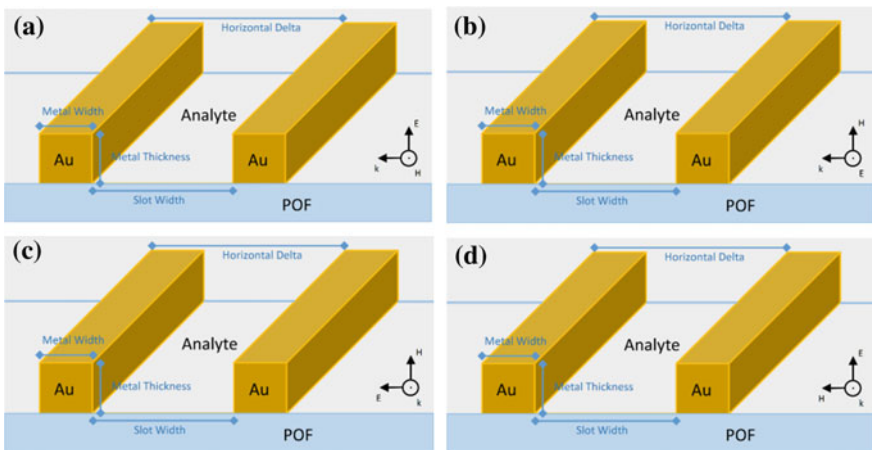
Fig. 2 View of the Nanostructured geometries, including the various polarizations: **a** Pol1 Mode1; **b** Pol1 Mode2; **c** Pol2 Mode1; **d** Pol2 Mode2

For each geometry the simulations are made in order to evaluate the Reflectance parameter, using the following refractive index of the sensing layer: 1.000 (air); 1.332 (water); 1.342 and 1.352 (aqueous medium).

3   Numerical Results

In this section we present the results obtained with a numerical solver used to evaluate the Reflectance parameter of the sensor platforms (shown in Fig. 1), in order to choose the best one in terms of sensitivity, respect to the changes of the analyte's refractive index.

In Fig. 3 is shown the Reflectance of the platform made with the continuous gold film, used as reference, in order to evaluate the sensor's performances. These results are similar to the results obtained experimentally [9].

In the Fig. 3 is possible to see as the resonant dips shift when the refractive index of the medium in contact to gold changes. In this case, the sensitivity (the variation of the dip related to the unit change in refractive index) is about 1350 [nm/RIU].

Figure 4 shows the reflectance values, obtained when the gratings are orthogonal respect to the light's propagation direction ("*Pol*1"), whereas Fig. 5 shows the results when the gratings are parallel to the light's propagation direction ("*Pol*2"). For these two configurations we have used different values of the "*Metal Width*" and "*Slot Width*" parameters (see Fig. 2). In fact, in Figs. 4 and 5 are reported the simulations that gave us the best results, in terms of sensitivity. In particular, the parameters of models with the best sensitivities, used in Figs. 4 and 5, are:

- Gratings orthogonal respect to the light's propagation direction (Pol1)

    - Metal Width = 100 nm; Slot Width = 100 nm;

- Gratings parallel respect to the light's propagation direction (Pol2)

    - Metal Width = 100 nm; Slot Width = 200 nm;

From these results (see Fig. 4) it is possible to see that with "*Pol*1" configuration, only the "*Mode*2" gives an appreciable contribution, with a sensitivity of about 3000 [nm/RIU], related to the LSPR phenomenon.

Using "*Pol*2" configuration, we can see in Fig. 5 a contribution with "*Mode*1", with a sensitivity of about 3400 [nm/RIU], related to the LSPR phenomenon, and
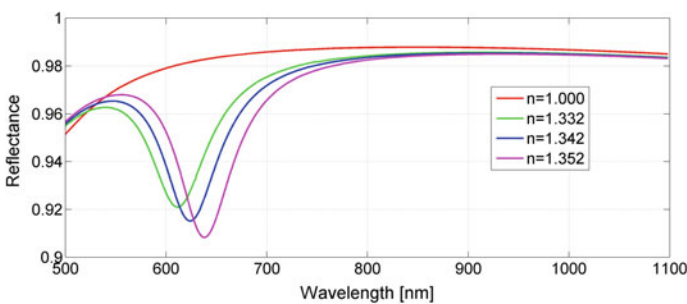
Fig. 3 Reflectance for the platform made with continuous gold layer
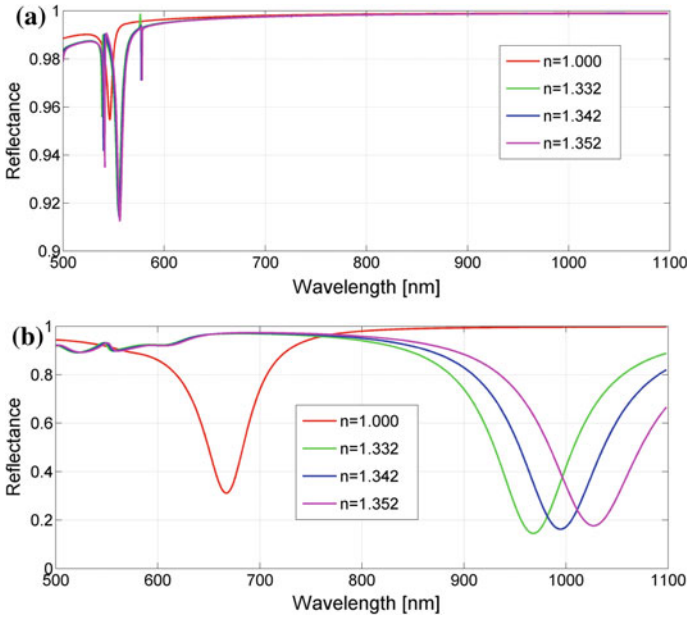
Fig. 4 Reflectance values for: **a** Pol1 Mode1; **b** Pol1 Mode2
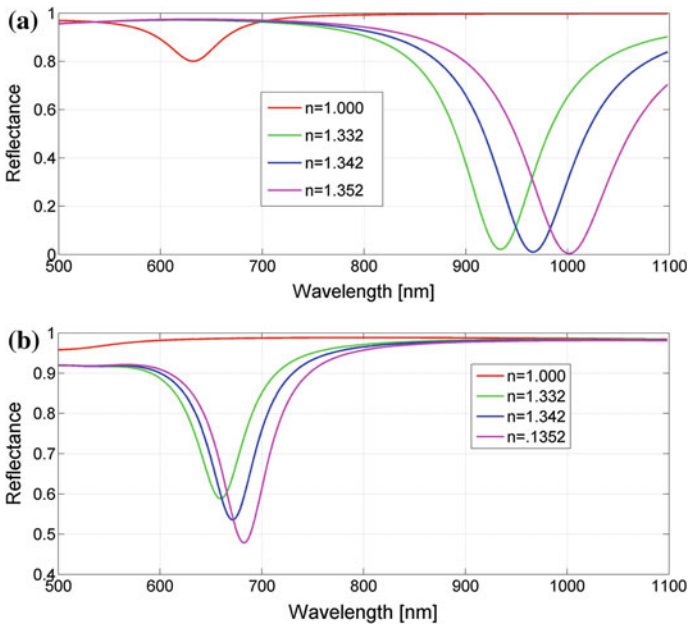
Fig. 5 Reflectance values for: **a** Pol2 Mode1; **b** Pol2 Mode2

another one with "*Mode*2", related to the SPR phenomena, with a sensitivity of about 1200 [nm/RIU].

In particular, the dips shown in Figs. 4b and 5a, relative to the LSPR phenomenon, are very sensitive to the Nanorod's geometrical parameters ("Metal Width" and "Slot Width"). On the other hand, the results shown in Fig. 5b, relative to the SPR phenomenon, don't significantly change when the geometrical parameters change. Finally, we want to observate that the resonance wavelength range changes when LSPR/SPR phenomenon changes.

4   Conclusions

The numerical results obtained show that the sensitivities relative to the Nanostructured configurations are greater than the configuration with a continuous gold film. Moreover, the sensor "*Pol*2" configuration presents, in two different wavelengths ranges, both LSPR and SPR phenomena on the same sensing platform. Hence, this sensing platform is a good candidate to the next step, direct at the realization of Nanostructured SPR/LSPR sensor platform for biosensing applications.

References

1. Nguyen, H.H., Park, J., Kang, S., Kim, M.: Surface plasmon resonance: A versatile technique for biosensor applications. Sensors **2015**(15), 10481–10510 (2015)
2. Cennamo, N., Donà, A., Pallavicini, P., D'Agostino, G., Dacarro, G., Zeni, L., Pesavento, M.: Sensitive detection of 2,4,6-trinitrotoluene by tridimensional monitoring of molecularly imprinted polymer with optical fiber and five-branched gold nanostars. Sensors Actuators, B Chem. **208**, 291–298 (2015)
3. Cennamo, N., De Maria, L., D'Agostino, G., Zeni, L., Pesavento, M.: Monitoring of low levels of furfural in power transformer oil with a sensor system based on a POF-MIP platform. Sensors **2015**(15), 8499–8511 (2015)
4. Cennamo, N., D'Agostino, G., Pesavento, M., Zeni, L.: High selectivity and sensitivity sensor based on MIP and SPR in tapered plastic optical fibers for the detection of L-nicotine. Sens. Actuators B Chem. **191**, 529–536 (2014)
5. Cennamo, N., Pesavento, M., Lunelli, L., Vanzetti, L., Pederzolli, C., Zeni, L., Pasquardini, L.: An easy way to realize SPR aptasensor: A multimode plastic optical fiber platform for cancer biomarkers detection. Talanta **140**, 88–95 (2015)
6. Huang, C.P., Zhu, Y.Y.: Plasmonics: Manipulating light at the subwavelength scale. Act. Passive Electron. Compon. **2007**(30946), 1–13 (2007)

7. Iga, M., Seki, A., Watanabe, K.: Gold thickness dependence of SPR-based hetero-core structured optical fiber sensor. Sens. Actuat. B Chem. **106**, 363–368 (2005)
8. Homola, J., Yee, S.S., Gauglitz, G.: Surface plasmon resonance sensors: review. Sens. Actuat. B Chem. **54**, 3–15 (1999)
9. Cennamo, N., Massarotti, D., Conte, L., Zeni, L.: Low cost sensors based on SPR in a plastic optical fiber for biosensor implementation. Sensors (Basel) **11**, 752–11760 (2011)
10. Eitan, M., Yifat, Y., Iluz, Z., Boag, A., Hanein, Y., Scheuer, J.: Nano slot-antenna array refractive index sensors: Approaching the conventional theoretical limit of the figure of merit, optical sensors 2015 (2015) Proc. of SPIE 9506
11. Bethe, H.A.: Theory of diffraction by small holes. Phys. Rev. **66**, 163–182 (1944)
12. Ebbesen, T.W., Lezec, H.J., Ghaemi, H.F., Thio, T., Wolff, P.A.: Extraordinary optical transmission through sub-wavelength hole arrays. Nature **391**, 667–669 (1998)
13. Wang, Y., Qin, Y., Zhang, Z.: Extraordinary optical transmission property of X-shaped plasmonic nanohole arrays. Plasmonics **9**, 203–207 (2014)
14. Shen, Y., Liu, M., Li, J., Chen, X., Xu, H.X., Zhu, Q., Wang, X., Jin, C.: Extraordinary transmission of three-dimensional crescent-like holes arrays. Plasmonics **7**, 221–227 (2012)
15. Yuan, L., Chen, F.: Characteristics of surface plasmon resonances in thick metal film perforated with nanohole arrays. Optik Inter. Jour. Light Elect. Opt. **127**, 3504–3508 (2016)
16. Hu, Y., Liu, G., Liu, Z., et al.: Extraordinary optical transmission in metallic nanostructures with a plasmonic nanohole array of two connected slot antennas. Plasmonics **10**, 483–488 (2015)
17. Rakić, A.D., Djurišić, A.B., Elazar, J.M., Majewski, M.L.: Optical properties of metallic films for vertical-cavity optoelectronic devices. Appl. Opt. **37**, 5271–5283 (1998)
18. Cennamo, N., Galatus, R., Mattiello, F., Sweid, R., Zeni, L.: Design of surface plasmon resonance sensor in plastic optical fibers based on nano-antenna arrays, 30th Eurosensors Conference, EUROSENSORS 2016, Budapest, 4–7 September 2016

Part IV
Optical Sensors

Design of an Evanescent Waveguide Sensor Based on a-Si:H Photodiodes for Lab-on-Chip Applications

Alessio Buzzin, Rita Asquini, Domenico Caputo and Giampiero de Cesare

Abstract Here we present the design of an amorphous silicon photodetector integrated with an ion-exchanged waveguide on the same glass substrate in order to obtain an evanescent waveguide sensor for on-chip biomolecular recognition in Lab-on-Chip applications. We studied the behaviour of a monochromatic light in a channel waveguide and its coupling into the thin-film sensor, using COMSOL Multiphysics. Simulations show that the presence of the photodiode's insulation layer and transparent electrode strongly affects the coupling efficiency between the waveguide and the sensor.

1 Introduction

A Lab-on-Chip (LoC) is a miniaturized system designed to integrate each step of biological and chemical analysis (injection, reaction, separation and detection) in a single chip [1, 2], offering quick response time, low reagents' consumption, on-field use and high stability [3, 4].

The most used techniques in terms of biological detection usually rely on photosensors, which monitor the optical properties of the analyzed substance, in

A. Buzzin · R. Asquini (✉) · D. Caputo · G. de Cesare
Department of Information Engineering, Electronics and Telecommunications,
University of Rome "La Sapienza", Via Eudossiana 18, 00184 Rome, Italy
e-mail: rita.asquini@uniroma1.it

A. Buzzin
e-mail: alessio.buzzin@uniroma1.it

D. Caputo
e-mail: domenico.caputo@uniroma1.it

G. de Cesare
e-mail: giampiero.decesare@uniroma1.it

terms of absorption, fluorescence or bio-chemiluminescence characteristics through its photo-emitted current, providing high sensitivity and reliability [5, 6].

Usually the photodetection is performed off-chip, measuring the effect of the analyte on the light's propagation in a waveguiding structure, with the help of Bragg gratings, prisms and optical fibers to bring the optical information out of the device [7, 8].

This work presents an integrated optoelectronic device based on an evanescent glass-diffused waveguide, optically coupled with a hydrogenated amorphous silicon (a-Si:H) photosensor, which allows on-chip biomolecular detection in a compact system, providing reduced optical loss.

2   System Design

A qualitative sketch of the system is shown in Fig. 1. The structure includes, on the same glass substrate, two main parts: an optical waveguide and a thin film photodiode.

Optical waveguiding structures can be obtained using different processes and materials. A simple and low cost ion-exchanged glass waveguide technology can be fruitfully used to obtain different optoelectronic devices [9–11].

The optical waveguide is a double ion-exchanged (K^+/Ag^+ and K^+/Na^+) and thermal annealed channel waveguide diffused in a borosilicate BK7 glass substrate [12, 13]: it offers low propagation loss in a large wavelength spectrum (from visible to infrared) [14].

For the photosensor's structure we selected a thin-film hydrogenated amorphous silicon (a-Si:H) p-doped/intrinsic/n-doped stacked junction, since its low-temperature deposition process (below 250 °C), its high efficiency in the visible light spectrum, and its low dark current, together with the opportunity to use glass and polymers as substrates, makes it a great candidate for biomolecular recognition applications [15].

As bottom electric contact for the P-I-N junction we decided for indium tin oxide (ITO), which allows the p-doped side of the junction to be electrically connected to the electronic circuit and, at the same time, permits the transit of light from the waveguide to the sensor [16]. The top metal is a 50 nm-thick chromium layer, which acts both as electrode and as reflector.

3   Simulation Results

The main objective of this work is the study and optimization of the coupling efficiency between the optical waveguide and the amorphous silicon photodetector.

To analyze the system's behavior, we evaluated its coupling efficiency as a ratio between the optical power flux through the waveguide after and before the
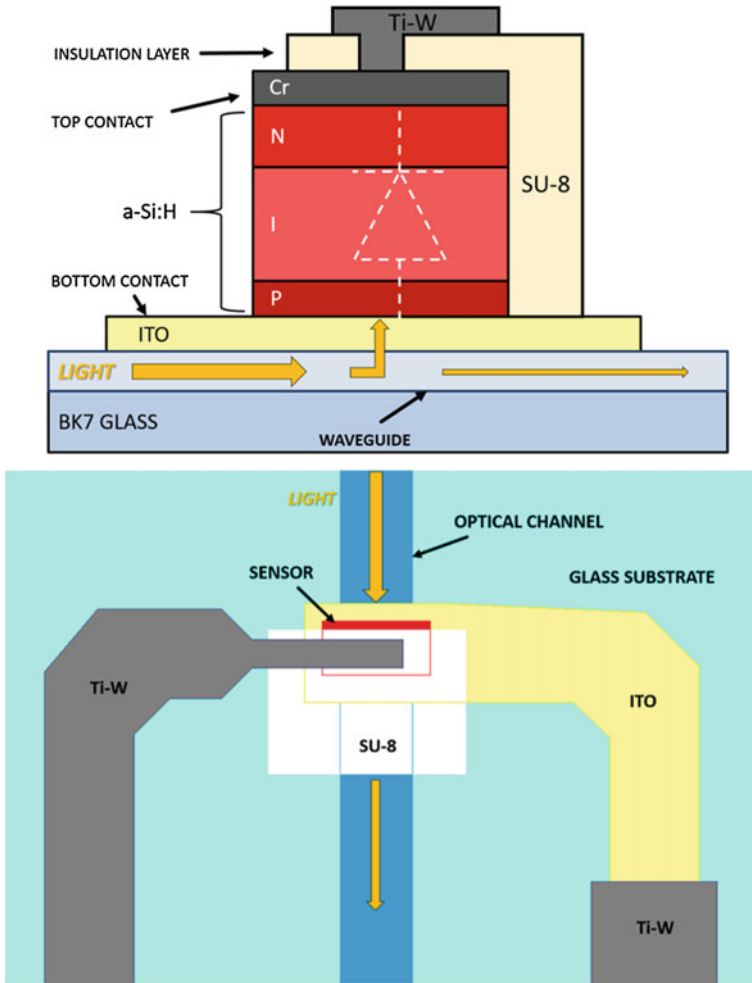
Fig. 1 Cross section (*top*) and top view (*bottom*) of the proposed device

Table 1 Material refractive indices and thicknesses

Material	BK7 glass	Waveguide core	ITO	a-Si	Cr	SU-8
Refractive index	1.52	1.56	1.88	4.45	2.66	1.585
Thickness	1.1 mm	1.5 μm	25 ÷ 700 nm	P: 30 nm I: 500 nm N:100 nm	50 nm	5 μm

ITO/P-I-N stacked structure. The analysis was carried out using the module "electro-magnetic waves: frequency domain" of COMSOL Multiphysics. Table 1 reports the design parameters in terms of materials, thicknesses and refractive

indices of every structure layer. The whole numerical analysis was performed at 532 nm, which is a typical biomolecular emission wavelength [17].

As a result, we observed that when ITO thickness is set at 250 nm, part of the light propagating in the waveguide is absorbed by the P-I-N junction, as Fig. 2 reports. However, this was obtained without taking into consideration the presence of the SU-8 insulation layer.

In particular, we found that the SU-8 layer absorbs most of the optical power routed into the waveguide before it's coupled into the photodetector (see Fig. 2). For this reason, we studied a P-I-N junction which is electrically insulated on three sides and it is designed to receive light from its non-insulated side (see Fig. 1).
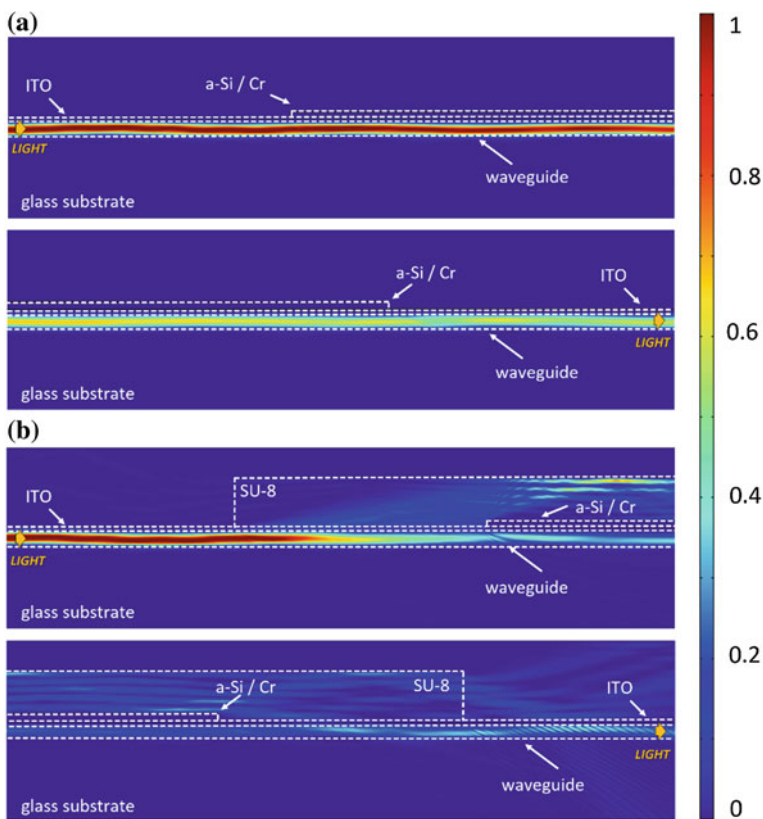
Fig. 2 Distribution of the optical power along the propagation direction (from *left* to *right*) at the beginning (*top*) and at the end (*bottom*) of the a-Si:H sensor, without (*a*) and with (*b*) the SU8 passivation layer. The P-I-N junction is 630 nm-thick, while its length on the waveguide is 150 μm. The ITO layer is 250 nm thick

Fig. 3 Coupling efficiency
versus ITO thickness
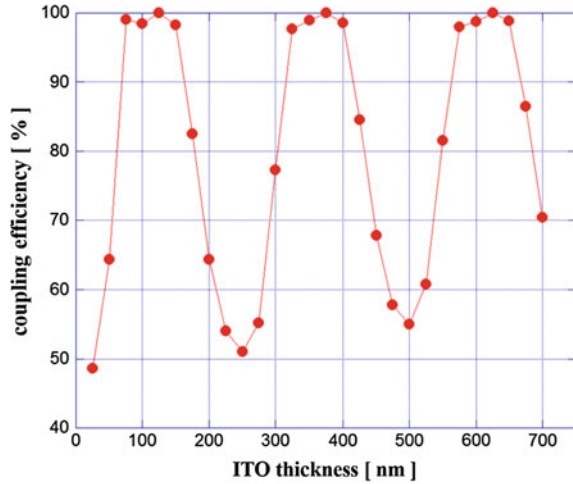
Moreover, ITO film thickness resulted to be a crucial design parameter for the optimization of coupling efficiencies, as reported in Fig. 3. Indeed, variations of the ITO thickness from 25 to 700 nm lead to a cyclic behaviour, with optical coupling peaks over 99% at approximately 120, 375 and 625 nm. The lowest coupling efficiencies occur at ITO thicknesses of around 23, 250 and 500 nm. By increasing the ITO film thickness, its optical absorption becomes more significant, while a thinner ITO film increases the series resistor of the electrical connection between sensor and electronic circuit. However, the device is designed to operate with very low current values and the increase of the resistance does not affect significantly the photosensor's performances [18]. We chose a thickness of 120 nm as the best scenario in terms of optical coupling and electrical conductivity in order to optimize the limit of detection.

4 Conclusions

We reported a novel structure of an evanescent waveguide sensor based on amorphous silicon P-I-N stacked photodetectors and double ion-exchanged glass waveguides. We designed the device and simulated its behavior by means of COMSOL Multiphysics, finding out that the thickness of the ITO buffer layer between the waveguide and the P-I-N junction is a critical parameter in order to optimize the optical coupling. Indeed, the SU-8 electrical insulation layer has an interfering effect on the photodetection, and forced to remove it on the side where the light is received by the sensor. As the results confirm, the structure is a promising candidate in compact and high-sensitive systems for biomolecular recognition applications.

References

1. Caputo, D., Ceccarelli, M., de Cesare, G., Nascetti, A., Scipinotti, R.: Lab-on-glass system for DNA analysis using thin and thick film technologies. Mater. Res. Soc. Symp. Proc. **1191**, 53–58 (2009)

2. De Venuto, D., Vincentelli, A.S.: Dr. Frankenstein's dream made possible: implanted electronic devices. Proc. of Design, Automation and Test in Europe DATE2013, art. no. 6513757, pp. 1531–1536 (2013)

3. Jung, W.E., Han, J., Choi, J.-W., Ahn, C.H.: Point-of-care testing (POCT) diagnostic systems using microfluidic lab-on-a-chip technologies. Microelectron. Eng. **132**, 46–57 (2015)

4. De Venuto, D., Carrara, S., Riccò, B.: Design of an integrated low-noise read-out system for DNA capacitive sensors. Microelectron. J. **40**(9), 1358–1365 (2009)

5. Costantini, F., Nascetti, A., Scipinotti, R., Domenici, F., Sennato, S., Gazza, L., Bordi, F., Pogna, N., Manetti, C., Caputo, D., de Cesare, G.: On-chip detection of multiple serum antibodies against epitopes of celiac disease by an array of amorphous silicon sensors. RSC Advances **4**, 2073–2080 (2014)

6. Fixe, F., Chu, V., Prazeres, D.M.F., Conde, J.P.: An on-chip thin film photodetector for the quantification of DNA probes and targets in microarrays. Nucleic Acids Res. **32**, e70–e75 (2004)

7. Estevez, M.C., Alvarez, M., Lechuga, L.M.: Integrated optical devices for lab-on-a-chip bio-sensing applications. Laser Photonics **6**, 463–487 (2012)

8. Schmitta, K., Schirmera, B., Hoffmanna, C., Brandenburga, A., Meyrueisb, P.: Interferometric biosensor based on planar optical waveguide sensor chips for label-free detection of surface bound bioreactions. Biosens. Bioelectron. **22**, 2591–2597 (2007)

9. Asquini, R., d'Alessandro, A.: Tunable photonic devices based on liquid crystals and composites. In: Liquid Crystals XVII, Proc. of SPIE, SPIE Optics + Photonics, Organic Photonics and Electronics, 25–29 August 2013, San Diego, California, vol. 8828, pp. 88280T (1–14) (2013)

10. Gizzi, C., Asquini, R., d'Alessandro, A.: A polarization independent liquid crystal assisted vertical coupler switch. Mol. Cryst. Liq. Cryst. **421**, 95–105 (2004)

11. Gilardi, G., Asquini, R., d'Alessandro, A., Beccherelli, R., De Sio, L., Umeton, C.: All-optical and thermal tuning of a Bragg grating based on photosensitive composite structures containing liquid crystals. Mol. Cryst. Liq. Cryst. **558**(1), 64–71 (2012)

12. Zou, J., Zhao, F., Chen, R.T.: Two-step K^+–Na^+ and Ag^+–Na^+ ion-exchanged glass waveguides for C-band applications. Appl. Opt. **41**, 7620–7626 (2002)

13. Gizzi, C., Asquini, R., d'Alessandro, A.: An integrated 2×2 SSFLC optical switch with channel ion-exchanged glass waveguides. Ferroelectrics **312**, 31–37 (2004)

14. Asquini, R., d'Alessandro, A.: Bistable optical waveguided switch using a ferroelectric liquid crystal layer. In: Proc. IEEE LEOS 2000 13th Annual Meeting, 13–16 November 2000, vol. 1, pp. 119–120 (2000)

15. Zangheri, M., Di Nardo, F., Mirasoli, M., Anfossi, L., Nascetti, A., Caputo, D., de Cesare, G., Guardigli, M., Roda, A.: Chemiluminescence lateral flow immunoassay cartridge with integrated amorphous silicon photosensors array for human serum albumin detection in urine samples. Anal. Bioanal. Chem. **408**(30), 8869–8879 (2016)

16. de Cesare, G., Caputo, D., Tucci, M.: Electrical properties of ITO/crystalline silicon contact at different deposition temperatures. IEEE Electron Devices Letters **33**(3), 327–329 (2012)

17. Caputo, D., de Cesare, G., Scipinotti, R., Stasio, N., Costantini, F., Manetti, C., Nascetti, A.: On-chip diagnosis of celiac disease by an amorphous silicon chemiluminescence detector. Lect. Notes Electr. Eng. **268**, 183–187 (2014)

18. Caputo, D., de Cesare, G., Nascetti, A., Tucci, M.: Improving the stability of amorphous silicon ultraviolet sensor. Thin Solid Films **515**, 7517–7521 (2007)

Optoelectronic System-on-Glass
for On-Chip Detection of Fluorescence

**N. Lovecchio, F. Costantini, M. Nardecchia, G. Petrucci, M. Tucci,
P. Mangiapane, A. Nascetti, G. de Cesare and D. Caputo**

Abstract In this paper, we present an optoelectronic system-on-glass (SoG), suitable for detection of fluorescent molecule. It integrates, on the same glass substrate, an array of amorphous silicon (a-Si:H) photosensors and a thin film interferential filter. The system can be directly coupled with another glass substrate hosting a polydimethylsiloxane based microfluidic network where the fluorescent phenomena occur. The compatibility of the different technological steps to attain on the same glass substrate the photosensors and the filter determined the sequence, the selection of materials and the deposition parameters of the whole process. The electro-optical characterization of the photodiode, performed after the filter deposition, demonstrated the efficacy of the filter in reducing the excitation light. The system has been successfully tested using the ruthenium complex $[Ru(phen)_2(dppz)]^{2+}$, a fluorescent dye which works as DNA intercalating molecule.

Keywords Optoelectronic system-on-glass · Lab-on-chip
Amorphous silicon photosensors · Interferential filter · Ruthenium complex

N. Lovecchio (✉) · M. Nardecchia · G. Petrucci · G. de Cesare · D. Caputo
D.I.E.T, Sapienza University of Rome, Via Eudossiana, 18, 00184 Rome, Italy
e-mail: Nicola.Lovecchio@uniroma1.it

F. Costantini · M. Nardecchia · A. Nascetti
S.A.E, Sapienza University of Rome, Via Salaria, 851/881, 00138 Rome, Italy

F. Costantini
Department of Chemistry, Sapienza University of Rome,
P.le A. Moro 5, 00185 Rome, Italy

M. Tucci · P. Mangiapane
ENEA Research Center Casaccia, Via Anguillarese 301, 00123 Rome, Italy

1   Introduction

Fluorescent molecules are widespread tools for detection and quantification of biomolecules, genotyping and gene expression profiling [1, 2]. They are a golden standard in the clinical and diagnostic fields thanks to their high sensitivity and specificity [3, 4]. These two features make their use very attractive also in lab-on-chip systems, which carry out laboratory analysis in small-scale device [5–7]. However, a system for detection of fluorescence includes a radiation source, a band pass filter for the selection of the excitation wavelength, a long pass filter for the transmission of the fluorescence and simultaneous rejection of the excitation radiations, focusing optics and, finally, a photosensor for the fluorescence quantification. Of course, the presence of all these components reduces the compactness of the system and its effective miniaturization [8].

In this work, we present the development of a lab-on-chip system for detection of DNA [9–11] through the $[Ru(phen)_2(dppz)]^{2+}$ fluorescent intercalating dye [12]. The system is composed by two optically coupled glass substrates: the first hosts the microfluidic network, the second combines amorphous silicon (a-Si:H) photosensors and a thin film interferential filter for the selective detection of fluorescence [13]. The proposed system-on-glass (SoG), therefore, features a high miniaturization degree thanks to the on-chip detection performed by the a-Si:H photosensors [14–19] and to the reduced distance between the fluorescent and the detection sites [5], which avoids the use of focusing optics.

The paper is organized as follows: section two reports the design and development of the system, section three presents the results and discussions, and finally section four draws the conclusions.

2   System Design and Fabrication

A sketch of the system cross section is reported in Fig. 1.

The system is composed by two optically coupled glass substrates.

The top glass hosts the microfluidic network in which flows the solution containing the fluorescent molecule. It is made by polydimethylsiloxane (PDMS), which is a silicon-based organic polymer featuring optical transparence to visible light, biocompatibility and ease of fabrication. The choice of this material avoids, therefore, the alteration or the contamination of the sample solution.

The bottom substrate, instead, hosts, on the bottom layer, an array of a-Si:H photosensors, and on the top other side the interferential filter.

The fabrication steps of the photodiodes are the following:

1. deposition by magnetron sputtering of a 100 nm-thick Indium Tin Oxide (ITO) layer, which acts as transparent bottom contact of the diodes;
2. patterning of the metal layer by conventional photolithography and wet etching process;

Fig. 1 Cross section of the proposed system
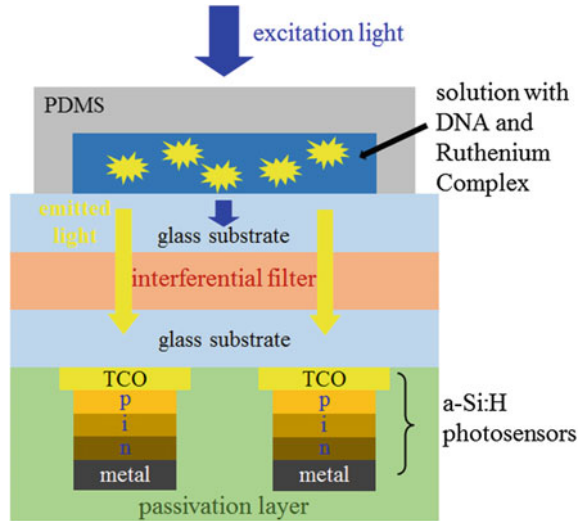
3. deposition by Plasma Enhanced Chemical Vapor Deposition (PECVD) of the a-Si:H p-type/intrinsic/n-type stacked structure;
4. deposition by vacuum evaporation of a 50 nm-thick chromium layer, which acts as top contact of the sensors;
5. wet etching of the chromium and dry etching of the a-Si:H layers for the mesa patterning of the diodes, which dimensions are 1.2×1.2 mm^2;
6. deposition by spin coating of a 5 μm-thick SU-8 3005 (from MicroChem, MA, USA) passivation layer and its pattering for opening via holes over the diodes;
7. deposition by magnetron sputtering of a 150 nm-thick titanium/tungsten alloy layer and its patterning for the definition of the top contacts and of the connection to the pad contacts;
8. deposition by spin coating of a 5 μm-thick SU-8 3005 passivation layer.

The interferential filter is a long-pass filter constituted by alternating layers of Zinc Sulfur and Magnesium Fluoride. It has been designed with a freeware software (XOP with the IMD extension), and deposited by using the electron beam physical vapor deposition technique without any patterning process.

Taking into account the technological steps for the a-Si:H photodiode fabrication and the chemical nature of the interferential filter, we fabricated the photodiodes first and the filter at the end. The filter deposition was performed at room temperature, in order to preserve the functionality of the photosensors previously fabricated on the same substrate.

The proposed system-on-glass (SoG), therefore, features a high miniaturization degree thanks to the on-chip detection performed by the a-Si:H photosensors and to the reduced distance between the fluorescent and the detection sites, which avoids the use of focusing optics.

3 Results and Discussions

The system has been designed and tested for detecting the natural fluorescence of ruthenium complex $[Ru(phen)_2(dppz)]^{2+}$, a DNA intercalating dye. Its luminescence is poor in aqueous solutions but has a sharp increase when the molecule is intercalated into the dsDNA. The absorption peak of the $[Ru(phen)_2(dppz)]^{2+}$ is around 450 nm, while his emission spectrum is centered at 610 nm. In order to excite the ruthenium complex, the radiation is provided by a blue light emitting diode (LED) (Roithner Lasertechnich APG2C1-450). This light has been filtered with a band pass filter in order to shrink the excitation spectrum.

The thin film interferential filter has to transmits only the emission spectrum of the ruthenium complex rejecting at the same time the excitation wavelengths. This reduces the photosensor background signal and avoids the saturation of the read-out electronics. From simulation results, we have found that a stacked structure of 11 layers of Zinc Sulfur (ZnS, 65 nm-thick) alternating with 11 layer of Magnesium Fluoride (MgF_2, 55 nm-thick) satisfies the design requirements.

Measurement performed with a spectrophotometer in order to characterize the fabricated filter response showed excellent agreement with the modeled data: cut-off wavelength of 550 nm, transmittance higher than 80% for wavelength greater than 550 nm and lower than 0.02% for wavelength smaller than 490 nm (Fig. 2). In particular, the ratio between the transmittance at 610 and 450 nm is about 10^5.

To demonstrate the efficacy of the filter in reducing the excitation light the electro-optical characterization of the photodiodes was performed after the filter deposition. The results show an excellent performance of the system that presents a very little attenuation of the ruthenium complex fluorescence (Fig. 3).
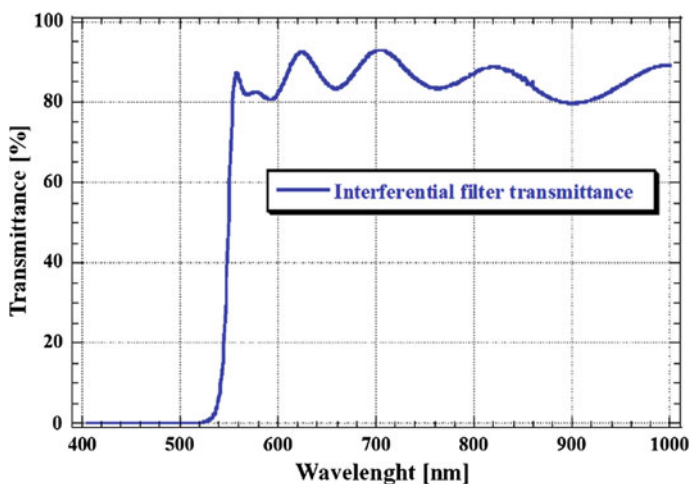
Fig. 2 Measured transmittance of the filter

Fig. 3 Quantum efficiency response of a-Si:H photodiode before (*red curve*) and after (*blue curve*) the filter deposition (Color figure online)
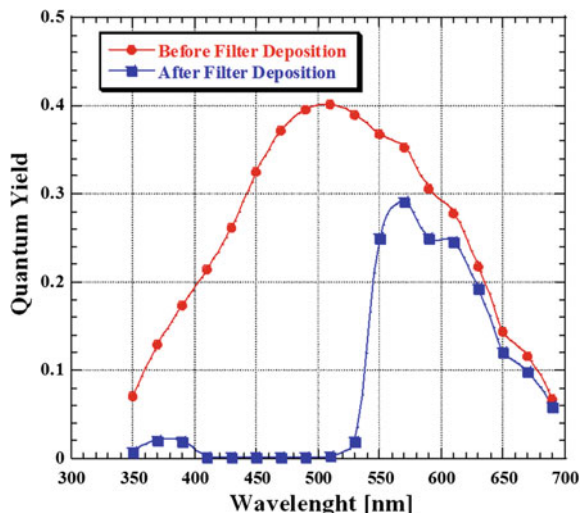
Fig. 4 Photocurrent sensor at different solution conditions (Color figure online)
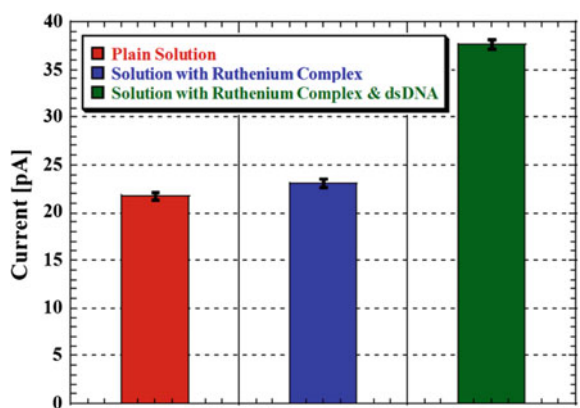
The whole system has been tested using a solution without DNA and a solution containing $[Ru(phen)_2(dppz)]^{2+}$ with dsDNA, commercially available. Results (Fig. 4) show the increase of sensor photocurrent when DNA is present in the solution, demonstrating that the reported system is suitable for detecting the variation of ruthenium fluorescence as DNA intercalating molecule.

4 Conclusions

In this work, we have presented a compact system for the on-chip detection of DNA in presence of fluorescent molecules of ruthenium complex. It integrates on the same glass substrate a-Si:H photosensors and a thin film interferential long pass

filter. The filter transmits the fluorescent radiation and rejects the excitation light in order to reduce the background photosensor current and the related current noise. Experimental data show the success of the developed system in detecting the increase of the fluorescence intensity when the ruthenium complex is intercalated with the dsDNA and suggest its potential application in real biological analysis.

References

1. Parks, J.W., Olson, M.A., Kim, J., Ozcelik, D., Cai, H., Carrion Jr., R., Patterson, J.L., Mathies, R.A., Hawkins, A.R., Schmidt, H.: Integration of programmable microfluidics and on-chip fluorescence detection for biosensing applications. Biomicrofluidics **8**(5), 054111 (2014)
2. Lim, J., Gruner, P., Konrad, M., Baret, J.C.: Micro-optical lens array for fluorescence detection in droplet-based microfluidics. Lab Chip **13**(8), 1472–1475 (2013)
3. Ryu, G., Huang, J., Hofmann, O., Walshe, C.A., Sze, J.Y., McClean, G.D., Mosley, A., Rattle, S.J., deMello, J.C., deMello, A.J., Bradley, D.D.: Highly sensitive fluorescence detection system for microfluidic lab-on-a-chip. Lab Chip **11**(9), 1664–1670 (2011)
4. Xi, Q., Zhou, D.M., Kan, Y.Y., Ge, J., Wu, Z.K., Yu, R.Q., Jiang, J.H.: Highly sensitive and selective strategy for microRNA detection based on WS_2 nanosheet mediated fluorescence quenching and duplex-specific nuclease signal amplification. Anal. Chem. **86**(3), 1361–1365 (2014)
5. Caputo, D., de Angelis, A., Lovecchio, N., Nascetti, A., Scipinotti, R., de Cesare, G.: Amorphous silicon photosensors integrated in microfluidic structures as a technological demonstrator of a "true" Lab-on-Chip system. Sens. Bio-Sens. Res. **3**, 98–104 (2015)
6. Abgrall, P., Gue, A.M.: Lab-on-chip technologies: making a microfluidic network and coupling it into a complete microsystem—a review. J. Micromech. Microeng. **17**(5), R15 (2007)
7. Petrucci, G., Caputo, D., Lovecchio, N., Costantini, F., Legnini, I., Bozzoni, I., Nascetti, A., de Cesare, G.: Multifunctional system-on-glass for Lab-on-chip applications. Biosens. Bioelectron. **93**, 315–321 (2016)
8. Zhu, H., Isikman, S.O., Mudanyali, O., Greenbaum, A., Ozcan, A.: Optical imaging techniques for point-of-care diagnostics. Lab Chip **13**(1), 51–67 (2013)
9. Caputo, D., Ceccarelli, M., de Cesare, G., Nascetti, A., Scipinotti, R.: Lab-on-glass system for DNA analysis using thin and thick film technologies. In MRS Proceedings, vol. 1191, pp. 1191-OO06. Cambridge University Press (2009)
10. Song, Y., Gyarmati, P., Araújo, A.C., Lundeberg, J., Brumer III, H., Ståhl, P.L.: Visual detection of DNA on paper chips. Anal. Chem. **86**(3), 1575–1582 (2014)
11. Ahrberg, C.D., Ilic, B.R., Manz, A., Neužil, P.: Handheld real-time PCR device. Lab Chip **16**(3), 586–592 (2016)
12. McKinley, A.W., Lincoln, P., Tuite, E.M.: Sensitivity of [Ru (phen) 2 dppz] 2+light switch emission to ionic strength, temperature, and DNA sequence and conformation. Dalton Trans. **42**(11), 4081–4090 (2013)
13. Caputo, D., Costantini, F., Lovecchio, N., Viri, V., Tucci, M., Mangiapane, P., Ruggi, A., Petrucci, G., Nascetti, A., de Cesare, G.: Highly miniaturized system for on-chip detection of DNA. In 20th International Conference on Miniaturized Systems for Chemistry and Life Sciences, MicroTAS 2016. Chemical and Biological Microsystems Society (2016)

14. Martins, S.A.M., Moulas, G., Trabuco, J.R.C., Monteiro, G.A., Chu, V., Conde, J.P., Prazeres, D.M.F.: Monitoring intracellular calcium in response to GPCR activation using thin-film silicon photodiodes with integrated fluorescence filters. Biosens. Bioelectron. **52**, 232–238 (2014)
15. Mirasoli, M., Nascetti, A., Caputo, D., Zangheri, M., Scipinotti, R., Cevenini, L., de Cesare, G., Roda, A.: Multiwell cartridge with integrated array of amorphous silicon photosensors for chemiluminescence detection: development, characterization and comparison with cooled-CCD luminograph. Anal. Bioanal. Chem. **406**(23), 5645–5656 (2014)
16. Costantini, F., Sberna, C., Petrucci, G., Reverberi, M., Domenici, F., Fanelli, C., Manetti, C., de Cesare, G., Derosa, M., Nascetti, A., Caputo, D.: Aptamer-based sandwich assay for on chip detection of Ochratoxin A by an array of amorphous silicon photosensors. Sens. Actuators B: Chem. **230**, 31–39 (2016)
17. Costantini, F., Nascetti, A., Scipinotti, R., Domenici, F., Sennato, S., Gazza, L., Bordi, F., Pogna, N., Manetti, C., Caputo, D., de Cesare, G.: On-chip detection of multiple serum antibodies against epitopes of celiac disease by an array of amorphous silicon sensors. RSC Adv. **4**(4), 2073–2080 (2014)
18. Costantini, F., Sberna, C., Petrucci, G., Manetti, C., de Cesare, G., Nascetti, A., Caputo, D.: Lab-on-chip system combining a microfluidic-ELISA with an array of amorphous silicon photosensors for the detection of celiac disease epitopes. Sens. Bio-Sens. Res. **6**, 51–58 (2015)
19. Caputo, D., de Cesare, G., Scipinotti, R., Stasio, N., Costantini, F., Manetti, C., Nascetti, A.: On-chip diagnosis of celiac disease by an amorphous silicon chemiluminescence detector. In Sensors and Microsystems, pp. 183–187. Springer International Publishing, Berlin (2014)

Optical Detection of Antioxidant Capacity in Food Using Metal Nanoparticles Formation. Study on Saffron Constituents

Flavio Della Pelle, Annalisa Scroccarello, Aida Santone and Dario Compagnone

Abstract A simple metal nanoparticles (MNPs) based colorimetric assay for the antioxidant capacity of Saffron polyphenolics is proposed. The proposed method has been compared with the commonly used classical assays (FC and ABTS); a significant similar response trend was found with the ABTS. Additionally, it was also found that the proposed approach was polyphenols selective *versus* other endogenous antioxidants as safranal and crocin.

Keywords Metal nanoparticles · Antioxidants · Polyphenols · Saffron AuNPs · AgNPs

1 Introduction

Food quality control is essential for the consumer protection, satisfaction and also for the food industry. Accessibility rapid and low cost analytical methods is highly required to detect key parameters for evaluation in the field of food safety, quality, traceability and for quality assurance and process control. Foods with bioactive components in the last years have been received increasing attention and have been the subject of several studies. Among these bioactive molecules, polyphenols are a class of chemical compounds of considerable interest for their nutritional, anti-microbial and sensory proprieties [1, 2], beyond the above reported 'food markers' properties. Recent studies have shown that, this heterogeneous class of substances possess a protective effect on human health when consumed in significant levels because of their antioxidant properties [3, 4]. The activity of antioxidants in foods and biological systems depends on a multitude of factors, including the colloidal properties of the substrates, the conditions and the level of oxidation and the localization of antioxidants in the different phases. For these reasons each

F. Della Pelle (✉) · A. Scroccarello · A. Santone · D. Compagnone
Faculty of Bioscience and Technology for Food, Agriculture and Environment,
University of Teramo, 64023 Teramo, Italy
e-mail: fdellapelle@unite.it

in vitro activity evaluation should be carried out using different methods. The most commonly used assays are based on spectrophotometric methods, such as the determination of total phenolic content with the Folin Ciocalteu (FC) assay, the trolox equivalent antioxidant capacity (TEAC), scavenging activity toward stable free radicals (DPPH• and ABTS•), reduction of metal ions (FRAP and CUPRAC assays) and competitive methods (ORAC and TRAP) [5, 6].

In recent years advances in nanotechnology had a decisive impact on the performance of the new generation of sensors and optical sensors. Nanomaterials-based sensors and assays are well established and they have been demonstrated to reach the desired sensitivity and selectivity. In particular, metal nanoparticles (MNPs) employed as novel tools for reliable assessment of food property [7, 8], emerge as novel, simple and inexpensive 'devices' in the field, becoming not only a valuable alternative to classical approaches but also a complementary one [9].

In this work we report a study to develop new MNPs based strategy for detection of different antioxidant of saffron, well known spice with demonstrated healthy effects. The MNPs formation is mediated by saffron endogenous polyphenols. A simple gold and silver nanoparticles (AuNPs and AgNPs) based colorimetric assay for the antioxidant activity determination has been developed, the absorbance is easily followed by the absorption band of localized surface plasmon resonance (LSPR) at 540 and 400 nm for the AuNPs and AgNPs, respectively. The proposed methods has been compared with the commonly used classical assays (FC and ABTS), a significant similar response trend was found with the ABTS. Additionally, it was also found that the proposed approach was polyphenols selective *versus* other endogenous antioxidant in the sample giving as the flavour compound safranal and the pigments crocin. This work represents improves the sustainability of the analysis by the reduction of costs and times, amount of sample, reagents required and waste produced, taking advantage of the MNPs unique properties.

2 Materials and Methods

2.1 Reagents, Stock Solution, and Reference Compounds

Polyphenols Standards (gallic acid, kaempferol, rutin, quercetin), safranal, crocin, cetyltrimethylammonium chloride (CTAC; 25% in water), hydrogen tetrachloroaurate ($HAuCl_4 \cdot 3H_2O$ 99.9%), Folin–Ciocalteau reagent, sodium carbonate, 2,2 o-azino-bis(3-ethylbenzothiazoline-6-sulphonic acid) (ABTS), 6-hydroxy-2,5,7,8-tetramethylchroman-2-carboxylic acid (Trolox), sodium peroxo-hexaodisulfate, disodium hydrogen phosphate anhydrous, sodium dihydrogen phosphate hydrate and methanol were purchased from Sigma Chemicals Co. (St. Louis, MO). Stock solutions of polyphenols, crocin and safranal standard were prepared at a concentration of 1.0×10^{-2} mol L^{-1}, and stored at $-20\ ^\circ C$ in dark.

2.2 Formation of Metal Nanoparticles Mediated by Saffron Polyphenols

AuNPs were formed following the protocol described by Della Pelle et al. [7] based on a controlled reduction of $HAuCl_4$. CTAC (8.0×10^{-1} mol L^{-1}), $HAuCl_4$ solution (2.0×10^{-2} mol L^{-1}), and, eventually, different volumes of the polyphenolic standard compounds were added in the reported order in phosphate buffer solution (pH 8.0; 1.0×10^{-2} mol L^{-1}) up to final volume of 500 μL. The solution was then stirred for 2 min and heated for 10 min at 45 °C in a water bath. The reaction was then blocked in ice for 25 min. Absorbance spectra in the 400 and 800 nm range were then recorded.

AgNPs were formed by taking a specific volume of phosphate buffer solution (pH 8.4; 1.0×10^{-2} mol L^{-1}) to which, first CTAC (8.0×10^{-4} mol L^{-1}), then a specific volume of $AgNO_3$ solution (2.0×10^{-2} mol L^{-1}), the reducing agent (polyphenolic standard compounds) was then added, to reach a final volume was 500 μL. The solution obtained was stirred for 1 min, then heated at 45 °C for 10 min in a water bath, the solution was then frozen abruptly for 10 min to stop the reaction. Both the MNPs calibration curves and sigmoidal curves [7] (only for AuNPs) were realized using the MNPs LSPR peak of absorbance (A_{max}) as a function of the standard polyphenol concentration. The best parameters obtained related to the antioxidant capacity are K_{AuNPs}/X_c^{50} and slope for the sigmoidal curve and for the linear curve, respectively.

2.3 Total Polyphenols Determination

The total polyphenol content (TP) of the polyphenolic standard compounds were evaluated colorimetrically using the Folin–Ciocalteu reagent Phenolic standards were mixed with 0.5 mL of Folin–Ciocalteu reagent and 4 mL of deionized water, and the solution was allowed to react for 3 min. 1.5 mL of a 20% solution of Na_2CO_3 was then added; the volume was finally brought to 10 mL with deionized water. Solutions were stirred at room temperature for 60 min, and the total polyphenols were determined colorimetrically at 760 nm. Calibration curves were realized using the polyphenols standard solutions.

2.4 Radical Scavenging Activity

The ABTS radical scavenging activity of the polyphenolic standard compounds were evaluated following this protocol: ABTS was dissolved in deionized water to 7 mM concentration and $ABTS^{•+}$ was produced by reacting ABTS stock solution with 2.45 mM potassium persulfate (final concentration), allowing the mixture to

stand in the dark at room temperature for 12–16 h before use. The solution was diluted with methanol until the absorbance at 734 nm reached the value of 0.70 (± 0.02). After radical formation, ABTS•+ were mixed with appropriate amount of standard diluted extract, reaching a final volume of 2 mL. After 5 min in the dark at 30 °C, the absorbance at 734 nm was taken. Absorbance of a blank solution (no phenols) was subtracted. Calibration curves were realized using the polyphenols standard solutions.

3 Result and Discussion

The MNPs synthesis was carefully optimized. The ratio of reagents/solvents, reaction times and temperatures (in both progress and stopping reaction) were optimized. Synthesis times longer than 10 min lead to MNPs aggregation (AuNPs)/collapse(AgNPs) and/or grow in size shifting or decreasing the LSPR maximum. Remarkably, it has been observed that MNPs are not formed in the experimental conditions used, in the absence of the capping agent (cetyltrimethy-lammonium chloride). In order to standardize the MNPs based method for the antioxidant capacity assessment in saffron it was necessary to demonstrate that the polyphenols in saffron could drive MNPs formation, and that the reducing power of these polyphenolic compounds is related to their concentration and chemical nature of the molecule. To this aim, following the analytical protocols reported in Sect. 2.2, a microtitration was performed for both MNPs. The ability of gallic acid (classical standard used for the total polyphenols quantification) as well as the ability of endogenous polyphenols most commonly found in saffron (kaempferol, rutin and quercetin) to drive formation of MNPs has been demonstrated. In agreement with Della Pelle et al. [7] for AuNPs sigmoidal curves reporting the absorbance at 540 nm as function of the polyphenolic concentration of each standard were obtained (Fig. 1a). The AuNPs formation curve give information about the polyphenol concentration at which the LSPR absorption reached its half-value, X_c^{50}, and about AuNPs production per polyphenol concentration unit, K_{AuNPs}. Even in this case the ratio K_{AuNAs}/X_c^{50} has been the optimal parameter to report the antioxidant capacity. The data confirmed that the compounds with ortho-diphenols functionality are the most active in reducing gold (III) to gold (0), while kaempferol (mono-phenol) had lower activity than the others antioxidant compounds assayed. However, the flavonoid structure allows a good stabilization of the formed AuNPs. All the curves reported were sigmoidal ($R^2 \geq 0.990$) and had good reproducibility for all the key parameters. In fact RSDs values for K_{AuNPs} was $\leq 12\%$, for X_c^{50} was $\leq 10\%$ and for the ratio K_{AuNPs}/X_c^{50} was $\leq 15\%$.

The three major polyphenols of saffron (kaempferol, rutin and quercetin) and gallic acid were also tested for the formation of the AgNPs. Figure 1b reports AgNPs picture and spectra obtained with increasing Kaempferol concentration. The plot of absorbance obtained from localized surface plasmon resonance (LSPR) at 420 nm as a function of the concentration of the polyphenol used was a straight
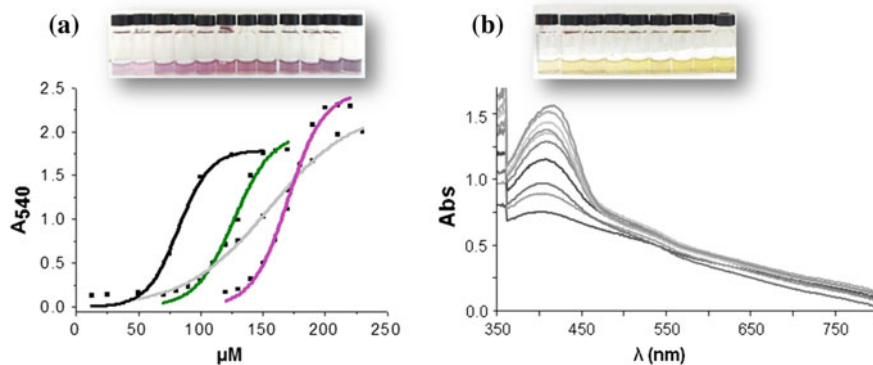
Fig. 1 a Sigmoidal curves obtained increasing the concentration of the polyphenols standards reading absorbance at 540 nm: gallic acid (*black*), quercetin (*violet*), Rutin (*green*), kaempferol (*grey*). *Inset* colloidal gold solutions formed by increasing the concentration of kaempferol. **b** AgNPs spectra obtained with increasing the concentration of kaempferol (from 5 to 90 μM). The *inset photograph* shows the AgNPs formed increasing the concentration of kaempferol (color figure online)

line. The curve slope was employed to evaluate the reactivity of the different polyphenols studied. AgNPs formation allowed to obtain increased sensitivity compared with the AuNPs. Moreover; reactivity is linked to the polyphenols structure. Indeed, in these preliminary studies, higher reactivity has been observed for flavonols structures (Fig. 2.). No MNPs formation was observed in the absence of polyphenols for both the NPs.

Selectivity of the MNPs was also tested, other potential antioxidants as crocins and safranal that are usually found in saffron were studied. Addition of different amounts (50–1000 μM) of these compounds did not produce measurable MNPs in the assay, indicating no chemical interference. Instead, both crocins and safranal are reactive with the ABTS and FC method. Another important control was also carried
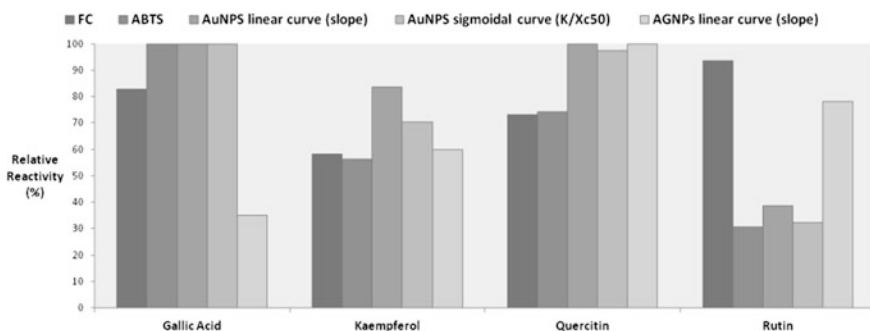
Fig. 2 Method reactivity between the proposed method (AuNPs and AgNPs based) and the reference colorimetric method of Folin-Ciocalteu (FC), for polyphenols determination, and ABTS for antioxidant capacity evaluation

out. The spectra of the saffron at the working dilution factor was also recorded (data not shown) no spectral interference were noticed

In order to compare the proposed method and the ABTS and Folin–Ciocalteu methods, saffron polyphenols standard reactivity were studied using two classical spectrophotometric methods for the evaluation of the antioxidant capacity (Fig. 2). The ABTS methods is related to the radical scavenging activity and is typically used for the antioxidant capacity quantification. Folin–Ciocalteu is a classical method for the polyphenols quantification, being this method based on the reducing ability of polyphenols and therefore is also considered an antioxidant capacity assay. In order to compare the methods the relative reactivity was studied (Fig. 2). All the analytical methods used for the comparison of the antioxidant capacity exhibited an appreciable repeatability that was the following: ABTS $\leq$ 14%, Folin–Ciocalteu $\leq$ 12%. All the calibration curves showed a good linearity and excellent coefficients of determination $R^2 \geq 0.992$. However, both FC and ABTS methods have been reactive towards crocin and safranal. A significant similar reactivity among ABTS and the parameters used in the AuNPs method was found as reported in Fig. 2. This demonstrate, even in this case, the suitability of the proposed method for the antioxidant capacity measurement of the polyphenolic fraction of saffron. For the AgNPs assay an important component of reactivity is due to the molecular structure.

4 Conclusions

A simple double indexes metal nanoparticles (AuNPs and AgNPs) based colorimetric assay for the saffron selective polyphenols antioxidant capacity determination has been proposed, the MNPs formation is easily followed by the absorption band of localized surface plasmon resonance (LSPR) at 540 nm and 420 nm for the AuNPs and AgNPs, respectively. The proposed method exploit the selective formation of AuNPs and AgNPs mediated by polyphenols. The reactivity of phenols together with the ability to form/stabilize the NPs of different metals, makes the assay proportional to the antioxidant capacity and able to discriminate the chemical structure/class. Moreover, this approaches have exhibited excellent analytical performance with good sensitivity and repeatability. The proposed methods has been compared with the commonly used classical assays (FC and ABTS), a significant similar response trend was found with the ABTS. Additionally, it was also found that the proposed approach was polyphenols selective *versus* other endogenous sample flavour (safranal) and pigments (crocin). This multi-metal approach open new gates towards a multi nanoparticles based fingerprinting strategy of polyphenols in food commodities.

References

1. Bendini, A., Cerretani, L., Carrasco-Pancorbo, A., Gómez-Caravaca, A.M., Segura-Carretero, A., Fernández-Gutiérrez, A., Lercker, G.: Phenolic molecules in virgin olive oils: a survey of their sensory properties, health effects, antioxidant activity and analytical methods. An overview of the last decade. Molecules **12**, 1679–1719 (2007)
2. Medina, E., de Castro, A., Romero, C., Brenes, M.: Comparison of the concentrations of phenolic compounds in olive oils and other plant oils: correlation with antimicrobial activity. J. Agric. Food Chem. **54**, 4954–4961 (2006)
3. Carrasco-Pancorbo, A., Cerretani, L., Bendini, A., Segura-Carretero, A., Del Carlo, M., Gallina-Toschi, T., Fernandez-Gutierrez, A.: Evaluation of the antioxidant capacity of individual phenolic compounds in virgin olive oil. J. Agric. Food Chem. **53**, 8918–8925 (2005)
4. Williamson, G., Manach, C.: Bioavailability and bioefficacy of polyphenols in humans. II. Review of 93 intervention studies. Am. J. Clin. Nutr. **81**, 243S–255S (2005)
5. Magalhães, L.M., Segundo, M.A., Reis, S., Lima, J.L.: Methodological aspects about in vitro evaluation of antioxidant properties. Anal. Chim. Acta **613**, 1–19 (2008)
6. Prior, R.L., Wu, X., Schaich, K.: Standardized methods for the determination of antioxidant capacity and phenolics in foods and dietary supplements. J. Agric. Food Chem. **53**, 4290–4302 (2005)
7. Della, Pelle F., Vilela, D., González, M.C., Lo, Sterzo C., Compagnone, D., Del, Carlo M., Escarpa, A.: Antioxidant capacity index based on gold nanoparticles formation. Application to extra virgin olive oil samples. Food Chem. **178**, 70–75 (2015)
8. Della, Pelle F., González, M.C., Sergi, M., Del Carlo, M., Compagnone, D., Escarpa, A.: Gold nanoparticles-based extraction-free colorimetric assay in organic media: an optical index for determination of total polyphenols in fat-rich samples. Anal. Chem. **87**, 6905–6911 (2015)
9. Vilela, D., González, M.C., Escarpa, A.: Nanoparticles as analytical tools for in-vitro antioxidant-capacity assessment and beyond. TrAC Trend. Anal. Chem. **64**, 1–16 (2015)

Part V
Applications

A Multicenter Survey About Companion Robot Acceptability in Caregivers of Patients with Dementia

Grazia D'Onofrio, Daniele Sancarlo, James Oscar, Francesco Ricciardi, Dympna Casey, Keith Murphy, Francesco Giuliani and Antonio Greco

Abstract In the frame of the European Community funded MARIO, caregivers of 139 dementia patients were recruited in National University of Ireland (NUIG), in Geriatrics Unit of IRCCS "Casa Sollievo della Sofferenza"-Italy (IRCCS) and in Alzheimer Association Bari-Italy (AAB) for a multicenter survey on to determine the needs and preferences of caregivers for improving the assistance of dementia patients, and guiding technological development of MARIO. A six minute video on technological devices and functions of MARIO was showed, and all caregivers fulfilled a 43-item questionnaire that explored four areas: (A) Acceptability, (B) Functionality, (C) Support devices, and (D) Impact. Caregivers declared that to facilitate acceptance (over 17.5%) and to improve functionality of MARIO (over 29%) should be important/likely/useful. Over 20.3% of caregivers reported that following support devices in MARIO could be useful for their patients: (1) for monitoring bed-rest and movements, (2) for monitoring the medication use, (3) for monitoring the ambient environmental conditions, (4) for regulating heating, humidity, lighting and TV channel, (5) for undertaking comprehensive geriatric assessment, (6) for link to care planning, (7) for monitoring physiological deterioration, and (8) for monitoring cognitive deterioration. Over 21.8% of caregivers declared that MARIO should be useful to improve quality of life, quality of care, safety, emergency communications, home-based physical and/or cognitive rehabilitation programs, and to detect isolation and health status changes of their patients. MARIO is a novel approach employing robot companions, and its effect

G. D'Onofrio (✉) · D. Sancarlo · A. Greco
Geriatrics Unit & Laboratory of Gerontology and Geriatrics, Department of Medical
Sciences, IRCCS "Casa Sollievo Della Sofferenza", San Giovanni Rotondo,
Foggia, Italy
e-mail: g.donofrio@operapadrepio.it

J. Oscar · D. Casey · K. Murphy
National University of Ireland, Galway, Ireland

F. Ricciardi · F. Giuliani
ICT, Innovation and Research Unit, IRCCS "Casa Sollievo Della Sofferenza",
San Giovanni Rotondo, Foggia, Italy

161

will be: (1) to facilitate and support persons with dementia and their caregivers, and (2) reduce social exclusion and isolation.

1 Introduction

Europe has the highest prevalence of dementia in the world; seven million people are currently affected and this is projected to increase to 13.4 million by 2050 [1]. Across EU countries, participation of people with dementia in family and civic life is diminished by cultures of exclusion and stigmatisation [2]. Less severe and even more widespread, loneliness, isolation and depression are becoming increasingly important within Social Care. The increased mortality risk associated with the effects of these conditions is 200% greater than that of clinical obesity and comparable to the effects of smoking 15 cigarettes a day [3]. These effects include impaired immune functions, increased blood pressure, inflammation, anxiety, increased risk for heart disease, stroke and others [4]. Dementia is characterised by impaired mental functioning, language and thinking [5]. These impairments are often accompanied by personality, functional and behavioural changes.

To fight loneliness and the effects suffered by person with dementia, effective techniques include those that target change of a person's perception of loneliness and those that increase a person's resilience. Resilience is an adaptive capacity that refers to one's ability to 'bounce back' and cope in the face of adversity.

ICT solutions can be used to increase psychological skills like resilience [6], and to manage active and healthy aging with the use of caring service robots as will be explored with the EU funded MARIO project [7].

In this project specific technological tools are adopted that try to create real feelings and affections making it easier for the patient to accept assistance from a robot when—in certain situations—in return the human can also support the machine.

The approach targeted in MARIO is the Comprehensive Geriatric Assessment (CGA) on which the Multidimensional Prognosis Index (MPI) [8] is based. Used effectively, the MPI can improve dramatically diagnostic accuracy, optimize medical treatment and health outcomes, improve function and quality of life, reduce use of unnecessary formal services, and institute or improve long-term care management.

In MARIO, the service robot will provide information to MPI survey and evaluation process based on its observation of the instrumental activities of daily living and detection of changes regarding them.

The aim and ambition of the project are:

- to address and make progress on the challenging problems of loneliness, isolation and dementia in older persons through multi-faceted interventions delivered by service robots
- to conduct near project length interaction with end users and assisted living environments to enable iterative development and preparation for post project uptake
- to assist caregivers and physicians in the CGA of subjects at risk to loneliness, isolation or dementia through the use of service robots
- the use of near state of the art robotic platforms that are flexible, modular friendly, low cost and close to market ready in order to realize field contributions in the immediate future
- to make Mario capable to support and receive "robot applications" similar to the developer and app community for smartphones. This will empower development and creativity, enable the robot to perform new functionalities over time, and support discovery and improve usefulness for end users while lowering costs
- through novel advances in machine learning techniques and semantic analysis methods to make Mario more personable, useful, and accepted by end users (e.g. gain perception of non-loneliness)

to bring MARIO service robot concepts out of the lab and into industry by addressing licensing aspects via Apache, the integration of telecommunication aspects and application hosting environment.

In the first stage of the project, a series of mini-workshops locally at the pilot sites with partner organizations to introduce MARIO to both end users and stakeholders were done. After an interview about determining the needs and preferences of patients were performed.

The caregivers play a pivotal role in the management of the health and care of dementia patients, but although caregiving may be rewarding, providing care to a family member is stressful [9]. These negative consequences can affect the quality of life of patients and informal caregivers, and finally the quality of care of the patients and increase the likelihood of institutionalization [10].

The informal caregivers of dementia patients are early overwhelmed by care responsibilities and others showing stability or even decreases in the burden over time [11].

It was shown that the amount of time of informal care is the frequent reporting of up to 24 h per day, leading to very high cost estimates that may overlook aspects of joint production (i.e. caregivers performing multiple tasks simultaneously) [12]. Several studies were shown that the caregiver burden leads to higher levels of depression and anxiety [13, 14], use of psychotropic medication more frequently [15], engagement in fewer protective health behaviours, and increased risk of medical illness [16, 17] and mortality [18].

In this perspective, the ICT may provide promising new tools to improve the functional and cognitive assessment of patients with dementia and related disorders [19]. Development and implementation of novel computer-based ICT applications

in the field of cognitive impairment mitigation and rehabilitation [20], emerging ICT applications based on virtual reality environments, including Augmented Reality technology, are become important game changers [19]. The ICT concept and approach can support the range of activities of daily living [21], monitor the circadian rhythm [22] for dementia patients.

The goal of this paper was to determine the needs and preferences of formal and informal caregivers for improving the assistance of dementia patients, and guiding the technological development of the MARIO though a questionnaire.

2   Materials and Methods

This study fulfilled the Declaration of Helsinki, the guidelines for Good Clinical Practice, and the Strengthening the Reporting of Observational Studies in Epidemiology guidelines. The approval of the study for experiments using human subjects was obtained from the local ethics committees on human experimentation. Written informed consent for research was obtained from each patient or from relatives or a legal representative in the case of severe demented patients. Caregivers of dementia patients consecutively recruited from May 2015 to February 2016 in the National University of Ireland (NUIG, Galway, Ireland), in the Geriatrics Unit of the Casa Sollievo della Sofferenza Hospital (IRCCS, San Giovanni Rotondo, Italy), and in the Alzheimer Association Bari (AAB, Bari, Italy) were screened for eligibility.

Inclusion criteria were: (1) caregiver of patients with diagnosis of dementia according to the criteria of the National Institute on Aging-Alzheimer's Association (NIAAA) [23]; and (2) the ability to provide an informed consent or availability of a proxy for informed consent. Exclusion criteria were: caregivers of patients with serious comorbidity, tumors and other diseases that could be causally related to cognitive impairment (ascertained blood infections, vitamin B12 deficiency, anaemia, disorders of the thyroid, kidneys or liver), history of alcohol or drug abuse, head trauma, psychoactive substance use and other causes of memory impairment.

The following parameters were collected by a systematic interview about the caregivers: gender, age, educational level (in years), and caregiving type [Informal caregiver (unpaid), Informal caregiver (paid), Formal caregiver (Geriatrician), Formal caregiver (Psychologist) and Forma caregiver (Nurse)].

To all caregivers were shown a video on the technological devices and the functions that should been implemented in MARIO (video weblink: https://www.youtube.com/watch?v=v1s2Hbad1l0).

Shortly after watching the video, a questionnaire was administered to all caregivers (MARIO Questionnaire) designed to find out their perceptions about robot companions, especially what they would like such a robot to do for them, and how robots could be designed to build their resilience.

The MARIO Questionnaire included 43 items that explored four areas: (A) Acceptability; (B) Functionality; (C) Support devices; and (D) Impact.

It was a quantitative questionnaire based on a Likert scale of "Extremely important/likely/useful" and "YES, very useful" to "Not at all important/likely/useful" and "Not useful at all".

All the analyses were made with the SPSS Version 20 software package (SPSS Inc., Chicago, IL). For dichotomous variables, differences between the groups were tested using the Fisher exact test. This analysis was made using the 2-Way Contingency Table Analysis available at the Interactive Statistical Calculation Pages (http://statpages.org/). For continuous variables, normal distribution was verified by the Shapiro–Wilk normality test and the 1-sample Kolmogorov–Smirnov test. For normally distributed variables, differences among the groups were tested by the Welch 2-sample t test or analysis of variance under general linear model. For non normally distributed variables, differences among the groups were tested by the Wilcoxon rank sum test with continuity correction or the Kruskal–Wallis rank sum test. Test results in which the p value was smaller than the type 1 error rate of 0.05 were declared significant.

3 Results

During the enrolment period, 130 caregivers were recruited: 39 caregivers were from NUIG (M = 4, F = 35), 70 caregivers from IRCCS (M = 28, F = 42), and 21 caregivers from AAB (M = 8, F = 13). Table 1 shows that the demographic and clinical characteristics of the three groups of caregivers according to their residence country. The three groups of caregivers did not differ in following parameters: gender distribution ($p = 0.876$) and mean age ($p = 0.473$). Significant differences were observed in educational level (NUIG = 18.88 vs. IRCCS = 14.90 vs. AAB = 15.61 years, $p = 0.006$). NUIG and IRCCS showed an higher presence of nurses (NUIG = 56.1% and IRCCS = 38.6%), and IRCCS showed an high presence of Informal caregivers unpaid (IRCCS = 72.7%), Informal caregivers paid (IRCCS = 85.7%) and Formal caregivers (Geriatrician) (IRCCS = 94.7%) with a significance of $p < 0.0001$ compared to other caregivers types.

3.1 Acceptability and Functionality of Caring Service Robot

As shown in Table 2a within 60.4% of caregivers of dementia patients declared that the Section A Items should be very important/likely/useful or extremely important/likely/useful to facilitate acceptance of caring service robot.

Within 52.8% of caregivers of dementia patients declared that the Section B Items should be very important/likely/useful or extremely important/likely/useful to improve the functionality of caring service robot.

Table 1 Characteristics of dementia caregivers

	ALL	NUIG	IRCCS	AAB	P value
	N = 130	N = 39	N = 70	N = 21	
Gender (M/F)	36/55	4/35	28/42	8/13	0.004
Age (years)*	48.12 ± 15.81	–	48.74 ± 14.90	45.72 ± 19.25	0.473
range	23–88		23–88	24–82	
Educational level (years)*	16.09 ± 6.00	18.88 ± 1.22	14.90 ± 7.06	15.61 ± 5.30	0.006
range	0–24	18–23	0–23	5–24	
Caregiving types					
Informal caregiver (unpaid) N(%)	33 (25.3)	0 (0)	24 (72.7)	9 (27.3)	<0.0001
Informal caregiver (paid) N(%)	7 (5.4)	0 (0)	6 (85.7)	1 (14.3)	
Formal caregiver (Geriatrician) N(%)	19 (14.6)	0 (0)	18 (94.7)	1 (5.3)	
Formal caregiver (Psychologist) N(%)	7 (5.4)	0 (0)	0 (0)	7 (100.0)	
Formal caregiver (Nurse) N(%)	57 (43.9)	32 (56.1)	22 (38.6)	3 (5.3)	
Not indicated N(%)	7 (5.4)	7 (100.0)	0 (0)	0 (0)	

*Values are presented as mean ± standard deviation

Table 2 **a** Percentage of responses by caregivers of dementia patients to the MARIO Questionnaire (Section A: Acceptability, and Section B: Functionality). **b** Percentage of responses by caregivers of dementia patients to the MARIO Questionnaire (Section C: Support Devices, and Section D: Impact)

(a)

Items	Extremely important/likely/useful N(%)	Very important/likely/useful N(%)	Moderately important/likely/useful N(%)	Slightly important/likely/useful N(%)	Not at all important/likely/useful N(%)
Section A: *Acceptability*					
1	69 (53.5%)	33 (25.6%)	22 (17.1%)	0 (0%)	5 (3.9%)
2	72 (55.8%)	39 (30.2%)	15 (11.6%)	1 (0.8%)	2 (1.6%)
3	72 (56.2%)	30 (23.4%)	17 (13.3%)	4 (3.1%)	5 (3.9%)
4	45 (49.5%)	29 (31.9%)	14 (15.4%)	0 (0%)	3 (3.3%)
5	55 (43.0%)	38 (29.7%)	26 (20.3%)	5 (3.9%)	4 (3.1%)
6	61 (48.0%)	41 (32.3%)	18 (14.2%)	2 (1.6%)	5 (3.9%)
7	61 (47.7%)	40 (31.6%)	22 (17.2%)	0 (0%)	5 (3.9%)
8	50 (40.0%)	31 (24.8%)	25 (20.0%)	14 (11.2%)	5 (4.0%)
9	47 (36.7%)	25 (19.5%)	33 (25.8%)	16 (12.5%)	7 (5.5%)
10	52 (40.9%)	35 (27.6%)	28 (22.0%)	8 (6.3%)	4 (3.1%)
11	48 (37.5%)	38 (29.7%)	23 (18.0%)	14 (10.9%)	5 (3.9%)
12	53 (42.1%)	50 (39.7%)	20 (15.9%)	0 (0%)	3 (2.4%)
13	60 (46.9%)	46 (35.9%)	15 (11.7%)	3 (2.3%)	4 (3.1%)
14	52 (40.6%)	40 (31.2%)	23 (18.0%)	8 (6.2%)	5 (3.9%)
15a*	35 (60.3%)	11 (19.0%)	8 (13.3%)	4 (6.9%)	0 (0%)
15b*	31 (54.4%)	17 (29.8%)	5 (8.8%)	2 (3.5%)	2 (3.5%)
15c*	24 (42.1%)	10 (17.5%)	18 (31.6%)	4 (7.0%)	1 (1.8%)
15d*	27 (46.6%)	13 (22.4%)	4 (6.9%)	7 (12.1%)	7 (12.1%)
15e*	13 (22.4%)	18 (31.0%)	9 (15.5%)	11 (19.0%)	7 (12.1%)

(continued)

Table 2 (continued)

(a)

Items	Extremely important/likely/useful N(%)	Very important/likely/useful N(%)	Moderately important/likely/useful N(%)	Slightly important/likely/useful N(%)	Not at all important/likely/useful N(%)
15f*	16 (27.6%)	16 (27.6%)	10 (17.2%)	10 (17.2%)	6 (10.3%)
15 g*	19 (32.8%)	13 (22.4%)	10 (17.2%)	12 (20.7%)	4 (6.9%)
Section B: Functionality					
1	58 (45.7%)	49 (38.6%)	13 (10.2%)	4 (3.1%)	3 (2.4%)
2	63 (49.6%)	46 (36.2%)	14 (11.0%)	1 (0.8%)	3 (2.4%)
3	59 (46.5%)	43 (33.1%)	22 (17.3%)	1 (0.8%)	3 (2.4%)
4	63 (49.6%)	43 (33.9%)	18 (14.2%)	0 (0%)	3 (2.4%)
5	56 (44.4%)	43 (34.1%)	17 (13.5%)	7 (5.6%)	3 (2.4%)
6	59 (46.8%)	45 (35.7%)	17 (13.5%)	2 (1.6%)	3 (2.4%)
7	59 (46.8%)	45 (35.7%)	19 (15.1%)	0 (0%)	3 (2.4%)
8	57 (45.2%)	46 (36.5%)	20 (15.9%)	0 (0%)	3 (2.4%)
9	62 (48.8%)	45 (35.4%)	17 (13.4%)	0 (0%)	3 (2.4%)
10	60 (48.4%)	45 (36.3%)	15 (12.1%)	1 (0.8%)	3 (2.4%)
11	50 (40.0%)	42 (33.6%)	25 (20.0%)	1 (0.8%)	7 (5.6%)
12	67 (52.8%)	37 (29.1%)	19 (15.0%)	1 (0.8%)	3 (2.4%)
13	45 (48.4%)	32 (34.4%)	12 (12.9%)	1 (1.1%)	3 (3.2%)

(b)

Items	YES, very useful	YES, moderately useful	YES, low level of usefulness	Not useful at all
Section C: Support devices				
1	80 (65.0%)	28 (22.8%)	13 (10.6%)	2 (1.6%)
2	81 (65.9%)	25 (20.3%)	14 (11.4%)	3 (2.4%)
3	80 (65.0%)	29 (23.6%)	12 (9.8%)	2 (1.6%)

(continued)

Table 2 (continued)

(b)

Items	YES, very useful	YES, moderately useful	YES, low level of usefulness	Not useful at all
4	66 (53.7%)	37 (30.1%)	16 (13.0%)	4 (3.3%)
5	60 (48.8%)	37 (30.1%)	20 (16.3%)	6 (4.9%)
6	65 (52.8%)	36 (29.3%)	16 (13.0%)	6 (4.9%)
7	70 (57.4%)	35 (28.7%)	13 (10.7%)	4 (3.3%)
8	70 (56.9%)	35 (28.5%)	15 (12.2%)	3 (2.4%)
Section D: *Impact*				
1	65 (52.4%)	38 (30.6%)	18 (14.5%)	3 (2.4%)
2	65 (52.4%)	40 (32.3%)	16 (12.9%)	3 (2.4%)
3	67 (54.0%)	36 (29.0%)	16 (12.9%)	5 (4.0%)
4	80 (64.5%)	27 (21.8%)	14 (11.3%)	3 (2.4%)
5	71 (57.3%)	36 (29.0%)	13 (10.5%)	4 (3.2%)
6	71 (57.3%)	35 (28.2%)	14 (11.3%)	4 (3.2%)
7	70 (57.4%)	34 (27.9%)	15 (12.3%)	3 (2.5%)

*Extremely important/likely/useful = 6–7 ranks; Very important/likely/useful = 4–5 ranks; Moderately important/likely/useful = 3 rank; Slightly important/likely/useful = 2 rank; Not at all important/likely/useful = 1 rank

3.2 Support Devices and Impact of Caring Service Robot

As shown in Table 2b within 65.9% of caregivers reported that following support devices in MARIO could be very useful or moderately useful for their patients: (1) Devices for monitoring bed-rest and movements, (2) Devices for monitoring the medication use, (3) Devices for monitoring the ambient environmental conditions, (4) Devices for regulating heating, humidity, lighting and TV channel, (5) Devices for undertaking comprehensive geriatric assessment, (6) Devices that link to care planning, (7) Devices for monitoring physiological deterioration, and (8) Devices for monitoring cognitive deterioration.

Within 64.5% of caregivers of dementia patients declared that MARIO should be very useful or moderately useful to improve quality of life, quality of care, safety, emergency communications, home-based physical and/or cognitive rehabilitation programs, and to detect isolation and health status changes of their patients.

3.3 Effects of Sex and Age of the Caregivers

As shown in Table 3 the caring service robot were deemed more useful in supporting the female than male in following items: Section (A) Item 1 ($p = 0.008$), Item 2 ($p < 0.0001$), Item 4 ($p = 0.004$), Item 6 ($p = 0.047$), Item 12 ($p = 0.020$), and Item 13 ($p = 0.010$); Section (B) Item 1 ($p = 0.003$), Item 4 ($p = 0.024$), Item 7 ($p = 0.011$), Item 10 ($p = 0.009$), Item 11 ($p = 0.018$), Item 12 ($p = 0.018$), and Item 13 ($p = 0.001$); Section (C) Item 1 ($p = 0.015$), Item 3 ($p = 0.037$), Item 4 ($p = 0.019$), Item 6 ($p = 0.015$), Item 7 ($p < 0.0001$) and Item 8 ($p = 0.005$); Section (D) Item 1 ($p = 0.007$), Item 2 ($p = 0.039$), Item 4 ($p = 0.012$), and Item 7 ($p = 0.006$).

The caring service robot were deemed more useful in supporting the caregivers who had an age ≥ 35 years than younger in following items: Section (A) Item 9 ($p = 0.016$), Item 10 ($p = 0.036$), Item 11 ($p = 0.018$), and Item 14 ($p = 0.005$); Section (C) Item 6 ($p = 0.020$); Section (D) Item 1 ($p = 0.041$) and Item 3 ($p = 0.012$).

3.4 Effects of Educational Level and Caregiving Types of the Caregivers

As shown in Table 4 the caring service robot were deemed more useful in supporting the caregivers who had a low educational level in following items: Section (A) Item 2 ($p = 0.012$), Item 8 ($p = 0.006$), Item 9 ($p = 0.001$), Item 10 ($p = 0.046$) and Item 12 ($p = 0.007$).

Table 3 Effects of sex and age of the caregivers of dementia patients on the "extremely important/likely/useful" and "very important/likely/useful responses" to the MARIO questionnaire

Items	Sex			Age				
	M	F	P value	20–34 years	35–49 years	≥ 50 years	P value	
Section A: *Acceptability*								
1	26 (65.0%)	76 (85.4%)	0.008	11 (68.8%)	29 (85.3%)	32 (84.2%)	0.323	
2	28 (70.0%)	83 (93.3%)	<0.0001	13 (81.2%)	30 (88.2%)	31 (81.6%)	0.700	
3	32 (82.1%)	70 (78.7%)	0.660	13 (81.2%)	31 (91.2%)	34 (89.5%)	0.574	
4	24 (66.7%)	50 (90.9%)	0.004	11 (68.8%)	30 (88.2%)	32 (84.2%)	0.224	
5	26 (65.0%)	67 (76.1%)	0.190	9 (56.2%)	27 (79.4%)	29 (76.3%)	0.199	
6	28 (70.0%)	74 (85.1%)	0.047	11 (68.8%)	27 (79.4%)	32 (84.2%)	0.437	
7	29 (72.5%)	72 (81.8%)	0.231	12 (75.0%)	28 (82.4%)	32 (84.2%)	0.722	
8	24 (60.0%)	57 (67.1%)	0.441	8 (50.0%)	26 (76.5%)	31 (81.6%)	0.050	
9	24 (60.0%)	48 (54.5%)	0.564	7 (43.8%)	27 (79.4%)	30 (78.9%)	0.016	
10	26 (65.0%)	61 (70.1%)	0.564	8 (50.0%)	28 (82.4%)	30 (78.9%)	0.036	
11	25 (62.5%)	61 (69.3%)	0.446	9 (56.2%)	31 (91.2%)	28 (73.7%)	0.018	
12	28 (70.0%)	75 (87.2%)	0.020	10 (62.5%)	31 (91.2%)	29 (76.3%)	0.052	
13	28 (70.0%)	78 (88.6%)	0.010	11 (68.8%)	31 (91.2%)	30 (78.9%)	0.132	
14	26 (65.0%)	66 (75.0%)	0.243	8 (50.0%)	31 (91.2%)	29 (76.3%)	0.005	
Section B: *Functionality*								
1	28 (70.0%)	79 (90.8%)	0.003	12 (75.0%)	27 (79.4%)	31 (81.6%)	0.861	
2	31 (77.5%)	78 (89.7%)	0.068	13 (81.2%)	28 (82.4%)	32 (84.2%)	0.959	
3	29 (72.5%)	72 (82.8%)	0.183	13 (81.2%)	28 (82.4%)	32 (84.2%)	0.959	
4	29 (72.5%)	77 (88.5%)	0.024	13 (81.2%)	29 (85.3%)	33 (86.8%)	0.869	
5	28 (70.0%)	71 (82.6%)	0.110	12 (75.0%)	27 (79.4%)	33 (86.8%)	0.528	
6	30 (75.0%)	74 (86.0%)	0.128	12 (75.0%)	29 (85.3%)	33 (86.8%)	0.538	
7	28 (70.0%)	76 (88.4%)	0.011	10 (62.5%)	27 (79.4%)	33 (86.8%)	0.129	

(continued)

Table 3 (continued)

Items	Sex			Age			
	M	F	P value	20–34 years	35–49 years	≥ 50 years	P value
8	29 (72.5%)	74 (86.0%)	0.067	11 (68.8%)	28 (82.4%)	33 (86.8%)	0.288
9	30 (75.0%)	77 (88.5%)	0.052	11 (68.8%)	29 (85.3%)	31 (81.6%)	0.378
10	29 (72.5%)	76 (90.5%)	0.009	12 (75.0%)	29 (85.3%)	32 (84.2%)	0.641
11	24 (60.0%)	68 (80.0%)	0.018	12 (75.0%)	28 (82.4%)	30 (78.9%)	0.829
12	28 (70.0%)	76 (87.4%)	0.018	13 (81.2%)	28 (82.4%)	31 (81.6%)	0.994
13	24 (66.7%)	53 (93.0%)	0.001	12 (75.0%)	30 (88.2%)	31 (81.6%)	0.487
Section C: *Support devices*							
1	31 (77.5%)	77 (92.8%)	0.015	13 (81.2%)	32 (94.1%)	32 (84.2%)	0.315
2	33 (82.5%)	73 (88.0%)	0.412	13 (81.2%)	32 (94.1%)	35 (92.1%)	0.317
3	32 (80.0%)	77 (92.8%)	0.037	13 (81.2%)	32 (94.1%)	33 (86.8%)	0.367
4	29 (72.5%)	74 (89.2%)	0.019	12 (75.0%)	32 (94.1%)	32 (84.2%)	0.162
5	28 (70.0%)	69 (83.1%)	0.095	11 (68.8%)	32 (94.1%)	31 (81.6%)	0.062
6	28 (70.0%)	73 (88.0%)	0.015	10 (62.5%)	32 (94.1%)	31 (81.6%)	0.020
7	27 (69.2%)	78 (94.0%)	<0.0001	12 (75.0%)	32 (94.1%)	32 (84.2%)	0.162
8	29 (72.5%)	76 (91.6%)	0.005	13 (81.2%)	32 (94.1%)	32 (84.2%)	0.315
Section D: *Impact*							
1	28 (70.0%)	75 (89.3%)	0.007	10 (62.5%)	31 (91.2%)	32 (84.2%)	0.041
2	30 (75.0%)	75 (89.3%)	0.039	12 (75.0%)	32 (94.1%)	32 (84.2%)	0.162
3	30 (75.0%)	73 (86.9%)	0.098	10 (62.5%)	32 (94.1%)	33 (86.8%)	0.012
4	30 (75.0%)	77 (91.7%)	0.012	13 (81.2%)	32 (94.1%)	33 (86.8%)	0.367
5	31 (77.5%)	76 (90.5%)	0.050	12 (75.0%)	31 (91.2%)	35 (92.1%)	0.163
6	31 (77.5%)	75 (89.3%)	0.082	11 (68.8%)	31 (91.2%)	34 (89.5%)	0.074
7	29 (72.5%)	75 (91.5%)	0.006	11 (68.8%)	31 (91.2%)	33 (86.8%)	0.106

Section A *Acceptability*, and Section B *Functionality*, Section C *Support devices*, and Section D *Impact*

Table 4 Effects of educational level of the caregivers of dementia patients on the "extremely important/likely/useful" and "very important/likely/useful responses" to the MARIO questionnaire

Items	Low education	High school diploma	Degree	P value
Section A: *Acceptability*				
1	23 (88.5%)	5 (55.6%)	66 (77.6%)	0.114
2	22 (84.6%)	5 (55.6%)	77 (90.6%)	0.012
3	24 (92.3%)	7 (77.8%)	65 (77.4%)	0.236
4	22 (84.6%)	6 (66.7%)	45 (84.9%)	0.390
5	23 (88.5%)	5 (55.6%)	59 (69.4%)	0.081
6	23 (88.5%)	7 (77.8%)	64 (76.2%)	0.404
7	24 (92.3%)	6 (66.7%)	64 (75.3%)	0.124
8	24 (92.3%)	6 (66.7%)	48 (58.5%)	0.006
9	23 (88.5%)	5 (55.6%)	40 (47.1%)	0.001
10	23 (88.5%)	7 (77.8%)	54 (63.5%)	0.046
11	22 (84.6%)	4 (44.4%)	57 (67.1%)	0.059
12	23 (88.5%)	4 (44.4%)	71 (84.5%)	0.007
13	22 (84.6%)	6 (66.7%)	72 (84.7%)	0.378
14	22 (84.6%)	5 (55.6%)	61 (71.8%)	0.197
Section B: *Functionality*				
1	23 (88.5%)	6 (66.7%)	71 (83.5%)	0.317
2	24 (92.3%)	6 (66.7%)	72 (84.7%)	0.177
3	23 (88.5%)	8 (88.9%)	66 (77.6%)	0.385
4	24 (92.3%)	8 (88.9%)	68 (80.0%)	0.303
5	24 (92.3%)	8 (88.9%)	62 (73.8%)	0.097
6	24 (92.3%)	8 (88.9%)	67 (79.8%)	0.292
7	24 (92.3%)	8 (88.9%)	66 (78.6%)	0.239
8	24 (92.3%)	8 (88.9%)	65 (74.3%)	0.193
9	23 (88.5%)	7 (77.8%)	71 (83.5%)	0.718
10	23 (88.5%)	8 (88.9%)	67 (81.7%)	0.654
11	22 (84.6%)	6 (66.7%)	59 (71.1%)	0.346
12	23 (88.5%)	7 (77.8%)	70 (82.4%)	0.687
13	22 (84.6%)	6 (66.7%)	47 (85.5%)	0.366
Section C: *Support devices*				
1	24 (92.3%)	7 (77.8%)	76 (89.4%)	0.586
2	23 (88.5%)	9 (100.0%)	71 (83.5%)	0.244
3	23 (88.5%)	8 (88.9%)	76 (89.4%)	0.990
4	23 (88.5%)	7 (77.8%)	72 (84.7%)	0.734
5	23 (88.5%)	7 (77.8%)	66 (77.6%)	0.476
6	23 (88.5%)	7 (77.8%)	70 (82.4%)	0.687
7	23 (88.5%)	7 (77.8%)	73 (86.9%)	0.710
8	23 (88.5%)	7 (77.8%)	73 (85.9%)	0.730

(continued)

Table 4 (continued)

Items	Low education	High school diploma	Degree	P value
Section D: *Impact*				
1	23 (88.5%)	8 (88.9%)	70 (81.4%)	0.628
2	23 (88.5%)	8 (88.9%)	72 (83.7%)	0.793
3	23 (88.5%)	8 (88.9%)	69 (80.2%)	0.547
4	23 (88.5%)	8 (88.9%)	73 (84.9%)	0.869
5	24 (92.3%)	9 (100.0%)	71 (82.6%)	0.206
6	24 (92.3%)	9 (100.0%)	70 (81.4%)	0.167
7	23 (88.5%)	8 (88.9%)	70 (83.3%)	0.768

Section A *Acceptability*, and Section B *Functionality*, Section C *Support devices*, and Section D *Impact*

As shown in Table 5, the caring service robot were deemed more useful in supporting the informal caregivers (unpaid or paid) than formal caregivers in following items: Section (A) Item 5 ($p = 0.048$), Item 8 ($p = 0.013$) and Item 9 ($p = 0.001$); Section (D) Item 1 ($p = 0.002$) and Item 6 ($p = 0.010$).

Table 5 Effects of caregiving types of the caregivers of dementia patients on the "extremely important/likely/useful" and "very important/likely/useful responses" to the MARIO questionnaire

Items	Informal caregiver (unpaid)	Informal caregiver (paid)	Formal caregiver (Geriatr.)	Formal caregiver (Nurse)	Formal caregiver (Psychol.)	P value
Section A: *Acceptability*						
1	25 (75.8%)	7 (100.0%)	16 (84.2%)	41 (73.2%)	6 (85.7%)	0.482
2	24 (72.7%)	7 (100.0%)	16 (84.2%)	51 (91.1%)	7 (100.0%)	0.078
3	29 (87.9%)	7 (100.0%)	16 (84.2%)	40 (72.7%)	7 (100.0%)	0.133
4	24 (72.7%)	7 (100.0%)	16 (84.2%)	21 (84.0%)	6 (85.7%)	0.474
5	25 (75.8%)	7 (100.0%)	14 (73.7%)	40 (71.4%)	2 (28.6%)	0.048
6	28 (84.8%)	7 (100.0%)	14 (73.7%)	42 (76.4%)	5 (71.4%)	0.498
7	27 (81.8%)	7 (100.0%)	14 (73.7%)	40 (71.4%)	7 (100.0%)	0.213
8	26 (78.8%)	6 (85.7%)	13 (68.4%)	32 (60.4%)	1 (14.3%)	0.013
9	25 (75.8%)	6 (85.7%)	14 (73.7%)	22 (39.3%)	2 (28.6%)	0.001
10	27 (81.8%)	6 (85.7%)	13 (68.4%)	37 (66.1%)	2 (28.6%)	0.058
11	23 (69.7%)	6 (85.7%)	16 (84.2%)	36 (64.3%)	3 (42.9%)	0.216
12	24 (72.7%)	6 (85.7%)	16 (84.2%)	46 (83.6%)	6 (85.7%)	0.728
13	25 (75.8%)	6 (85.7%)	16 (84.2%)	48 (85.7%)	5 (71.4%)	0.727
14	24 (72.7%)	6 (85.7%)	16 (84.2%)	38 (67.9%)	4 (57.1%)	0.506
Section B: *Functionality*						
1	27 (81.8%)	7 (100.0%)	14 (73.7%)	48 (85.7%)	6 (85.7%)	0.555
2	28 (84.8%)	7 (100.0%)	14 (73.7%)	48 (85.7%)	7 (100.0%)	0.348
3	28 (84.8%)	7 (100.0%)	14 (73.7%)	44 (78.6%)	6 (85.7%)	0.566
4	29 (87.9%)	7 (100.0%)	14 (73.7%)	44 (78.6%)	7 (100.0%)	0.257

(continued)

Table 5 (continued)

Items	Informal caregiver (unpaid)	Informal caregiver (paid)	Formal caregiver (Geriatr.)	Formal caregiver (Nurse)	Formal caregiver (Psychol.)	*P* value
5	29 (87.9%)	7 (100.0%)	13 (68.4%)	40 (72.7%)	6 (85.7%)	0.193
6	30 (90.9%)	7 (100.0%)	14 (73.7%)	43 (78.2%)	7 (100.0%)	0.163
7	30 (90.9%)	7 (100.0%)	13 (68.4%)	45 (81.8%)	5 (71.4%)	0.174
8	30 (90.9%)	7 (100.0%)	13 (68.4%)	43 (78.2%)	6 (85.7%)	0.182
9	28 (84.8%)	7 (100.0%)	14 (73.7%)	48 (85.7%)	6 (85.7%)	0.551
10	29 (87.9%)	7 (100.0%)	14 (73.7%)	43 (81.1%)	7 (100.0%)	0.301
11	26 (78.8%)	7 (100.0%)	14 (73.7%)	36 (66.7%)	7 (100.0%)	0.139
12	27 (81.8%)	7 (100.0%)	14 (73.7%)	48 (85.7%)	6 (85.7%)	0.555
13	25 (75.8%)	7 (100.0%)	16 (84.2%)	24 (88.9%)	5 (71.4%)	0.410
Section C: *Support devices*						
1	27 (81.8%)	7 (100.0%)	16 (84.2%)	50 (89.3%)	7 (100.0%)	0.498
2	30 (90.9%)	7 (100.0%)	16 (84.2%)	45 (80.4%)	7 (100.0%)	0.344
3	28 (84.8%)	7 (100.0%)	16 (84.2%)	50 (89.3%)	7 (100.0%)	0.621
4	26 (78.8%)	7 (100.0%)	16 (84.2%)	46 (82.1%)	7 (100.0%)	0.494
5	26 (78.8%)	7 (100.0%)	16 (84.2%)	43 (76.8%)	7 (100.0%)	0.367
6	26 (78.8%)	7 (100.0%)	16 (84.2%)	47 (83.9%)	4 (57.1%)	0.298
7	27 (81.8%)	7 (100.0%)	16 (84.2%)	47 (85.5%)	7 (100.0%)	0.589
8	27 (81.8%)	7 (100.0%)	16 (84.2%)	47 (83.9%)	7 (100.0%)	0.588
Section D: *Impact*						
1	28 (84.8%)	7 (100.0%)	16 (84.2%)	49 (86.0%)	2 (28.6%)	0.002
2	28 (84.8%)	7 (100.0%)	16 (84.2%)	48 (84.2%)	5 (71.4%)	0.697
3	29 (87.9%)	7 (100.0%)	16 (84.2%)	46 (80.7%)	4 (57.1%)	0.238
4	29 (87.9%)	7 (100.0%)	16 (84.2%)	47 (82.5%)	7 (100.0%)	0.549
5	31 (93.9%)	7 (100.0%)	16 (84.2%)	47 (82.5%)	5 (71.4%)	0.309
6	31 (93.9%)	7 (100.0%)	16 (84.2%)	48 (84.2%)	3 (42.9%)	0.010
7	29 (87.9%)	7 (100.0%)	16 (84.2%)	47 (85.5%)	4 (57.1%)	0.217

Section A *Acceptability*, and Section B *Functionality*, Section C *Support devices*, and Section D *Impact*

4 Discussion

The MARIO robot were deemed very useful in supporting the informal caregivers (unpaid and paid) who were female and had an age $\geq$ 35 and with low educational level. Indeed, the informal caregivers had more difficulty to manage the dementia patients at home; moreover, who were female, younger and with a lower educational level clearly found even more complexity in management of dementia patients, requiring even more help from the companion robot.

Limitations of the present study should also be considered in interpreting our findings. In particular, the differences in educational levels of the caregivers across

the three sites of the MARIO Project reflected the caregiving type of each sites: NUIG is a nursing home where the nurses are more numerous and present, IRCCS is an hospital where formal and informal caregivers are present almost in equal measure, and AAB is an association where psychologists and informal caregiver are more present.

Questionnaires similar to the that developed for the MARIO Project were the HOPE Questionnaire developed for the HOPE Project [24] and the AL.TR.U.I.S.M. Questionnaire developed for the AL.TR.U.I.S.M. Project [25]. Regarding the HOPE Project, the caregivers considered that the ICT system could be useful to improve the management of patients with Alzheimer's disease (AD), especially if they are aged 75–84 years and with moderate dementia. Older and low educated caregivers had higher expectations on the potential role of ICT systems in improving the management of AD patients. Regarding the AL.TR.U.I.S.M. Project, the caregivers considered that a Virtual Personal Trainer (VPT) can improve the functional, nutritional, cognitive, affective, neuropsychiatric state, and quality of life of the patients with AD. The caregiver of masculine sex had higher expectations on the potential role of a VPT in improving the management of AD patients.

So the HOPE and AL.TR.U.I.S.M. Questionnaire results seem otherwise than those obtained in our study.

A previous report from the Keeping In Touch Everyday (KITE) Project demonstrated how a user-centered design process involving people with dementia and their relatives/caregivers could lead to the development of devices which are more acceptable and relevant to their needs [26]. Other projects [27–29] did not report data of questionnaires used to evaluate the preferences of caregivers and their dementia patients.

Our analysis represented a point of crucial importance not only in developing and improving the system by taking into considerations the end-users' (both patients and caregivers) expectations and needs, but also in leading to the development of a first prototype and to the experimentation stage as well.

5 Conclusion

The testing stages are still ongoing in order to improve the working patterns of the system and to better integrate all of its elements with particular and always renewed regard to the end-users and their needs, limits and requirements.

This first stage of experimentation activity aimed mainly at drawing clear conclusions on the interaction between the user and the MARIO and in general on the acceptability level of this service robot by the patient.

These data, however, are of great importance since they not only give useful indications to assess what has been accomplished up to now, but also they provide important guidelines in order to improve the system while specific clinical experimentation stages are expected to be carried out over the next months.

The work achieved through a fruitful and continuous interaction among the different subjects involved in the process of development of the system and stakeholders enabled the implementation of a platform which can be further and easily integrated and improved.

Finally, the collected and abovementioned data show a satisfactory integration between the patient and the system along with a great level of acceptability of MARIO by the end-user, both the patients themselves and the caregivers or medical providers, those who, day by day, take care and assist their patients.

References

1. Prince, M., Jackson, J.: Advance Access published May 2016. Alzheimer's Disease International. World Alzheimer Report (2009). http://www.alz.co.uk/research/worldreport/
2. Murphy, K., Casey, D.: Advance Access published May 2016 (2015). http://www.alzheimer-europe.org/Conferences/Previous-conferences/2015-Ljubljana/Detailed-programme-abstracts-and-presentations/PO1-Dementia-Friendly-Society
3. Holt-Lunstad, J., Smith, T.B., Layton, J.B.: Social relationships and mortality risk: a meta-analytic review. PLoS Med. **7**(7), e1000316 (2010)
4. Steptoe, A., Shankar, A., Demakakos, P., Wardle, J.: Social isolation, loneliness and all-cause mortality in older men and women. In Proceedings of the National Academy of Sciences of the USA (PNAS), doi:10.1073/pnas.1219686110, 25 Mar 2013
5. O'Shea, E.: Implementing policy for dementia care in Ireland. The time for action is now. In Irish Centre for Social Gerontology, National University of Ireland, Galway (2007)
6. Norris, F.H., Stevens, S.P., Pfefferbaum, B., Wyche, K.F., Pfefferbaum, R.L.: Community resilience as a metaphor, theory, set of capacities, and strategy for disaster readiness. Am. J. Commun. Psychol. **41**, 127–150 (2008)
7. http://www.mario-project.eu/portal/
8. Pilotto, A., Ferrucci, L., Franceschi, M., D'Ambrosio, L.P., Scarcelli, C., Cascavilla, L., Paris, F., Placentino, G., Seripa, D., Dallapiccola, B., Leandro, G.: Development and validation of a multidimensional prognostic index for 1-year mortality from the comprehensive geriatric assessment in hospitalized older patients. Rejuvenation Res. **11**, 151–161 (2008)
9. Schulz, R., Martire, L.: Family caregiving of persons with dementia: prevalence, health effects and support strategies. Am. J. Geriatr. Psychiatry **12**, 240–249 (2004)
10. Gaugler, J.E., Kane, R.A., Langlois, J.: Assessment of family caregivers of older adults. In: Kane, R.L., Kane, R.A. (eds.) Assessing Older Persons: Measures, Meaning and Practical Applications, pp. 320–359. Oxford University Press, New York (2000)
11. Gaugler, J.E., Davey, A., Pearlin, L.I., Zarit, S.H.: Modeling caregiver adaptation over time: the longitudinal impact of behavior problems. Psychol. Aging **15**, 437–450 (2000)
12. Jönsson, L., Wimo, A.: The cost of dementia in Europe: a review of the evidence and methodological considerations. Pharmacoeconomics **27**(5), 391–403 (2009)
13. Schulz, R., O'Brien, A.T., Bookwala, J., Fleissner, K.: Psychiatric and physical morbidity effects of dementia caregiving: prevalence, correlates, and causes. Gerontologist **35**, 771–791 (1995)

14. Mahoney, R., Regan, C., Katona, C., Livingston, G.: Anxiety and depression in family caregivers of people with Alzheimer disease: the LASER-AD study. Am. J. Geriatr. Psychiatry **13**, 795–801 (2005)
15. Clipp, E.C., George, L.K.: Psychotropic drug use among caregivers of patients with dementia. J. Am. Geriatr. Soc. **38**, 227–235 (1990)
16. Vitaliano, P.P., Zhang, J., Scanlan, J.M.: Is caregiving hazardous to one's physical health? A meta-analysis. Psychol. Bull. **129**, 946–972 (2003)
17. Son, J., Erno, A., Shea, D.G., Femia, E.E., Zarit, S.H., Stephens, M.A.: The caregiver stress process and health outcomes. J. Aging Health **19**, 871–887 (2007)
18. Schulz, R., Beach, S.R.: Caregiving as a risk factor for mortality: the Caregiver Health Effects Study. JAMA **282**, 2215–2219 (1999)
19. König, A., Aalten, P., Verhey, F., Bensadoun, G., Petit, P.D., Robert, P., et al.: A review of current information and communication technologies: can they be used to assess apathy? Int. J. Geriatr. Psychiatry **29**, 345–358 (2014)
20. D'Onofrio, G., Sancarlo, D., Ricciardi, F., Ruan, Q., Yu, Z., Giuliani, F., Greco, A.: Cognitive stimulation and Information-Communication Technologies (ICT) in Alzheimer's disease: a systematic review. In: Pamela Garza (ed.), Cognitive Control: Development, Assessment and Performance (2016). https://www.novapublishers.com/catalog/product_info.php?products_id=58756 (Nova Science P)
21. McKenzie, B., Bowen, M.E., Keys, K., Bulat, T.: Safe home program: a suite of technologies to support extended home care of persons with dementia. Am. J. Alzheimers Dis. Other Demen **28**(4), 348–354 (2013)
22. Espie, C.A., Kyle, S.D., Williams, C., Ong, J.C., Douglas, N.J., Hames, P., et al.: A randomized, placebo-controlled trial of online cognitive behavioral therapy for chronic insomnia disorder delivered via an automated media-rich web application. Sleep **35**(6), 769–781 (2012)
23. McKhann, G.M., Knopman, D.S., Chertkow, H., Hyman, B.T., Jack Jr., C.R., Kawas, C.H., et al.: The diagnosis of dementia due to Alzheimer's disease: recommendations from the National Institute on Aging-Alzheimer's Association workgroups on diagnostic guidelines for Alzheimer's disease. Alzheimers Dement. **7**, 263–269 (2011)
24. Pilotto, A., D'Onofrio, G., Benelli, E., Zanesco, A., Cabello, A., Margelí, M.C., Wanche-Politis, S., Seferis, K., Sancarlo, D., Kilias, D.: Information and communication technology systems to improve quality of life and safety of Alzheimer's disease patients: a multicenter international survey. J. Alzheimers Dis. **23**(1), 131–141 (2011)
25. Caroppo, A., Leone, A., Siciliano, P., Sancarlo, D., D'Onofrio, G., Giuliani, F., et al.: Cognitive Home Rehabilitation in Alzheimer's Disease Patients by a Virtual Personal Trainer. Ambient Assisted Living, 147–155 (2014)
26. Robinson, L., Brittain, K., Lindsay, S., Jackson, D., Olivier, P.: Keeping In Touch Everyday (KITE) project: developing assistive technologies with people with dementia and their carers to promote independence. Int. Psychogeriatr. **21**, 494–502 (2009)
27. Duff, P., Dolphin, C.: Cost-benefit analysis of assistive technology to support independence for people with dementia—part 1: development of a methodological approach to the ENABLE cost-benefit analysis. Technol. Disabil. **19**, 73–78 (2007)
28. Duff, P., Dolphin, C.: Cost-benefit analysis of assistive technology to support independence for people with dementia—part 2: results from employing the ENABLE cost-benefit model in practice. Technol. Disabil. **19**, 79–90 (2009)
29. Virone, G., Sixsmith, A.: Monitoring activity patterns and trends of older adults. Conf. Proc. IEEE Eng. Med. Biol. Soc. **2008**, 2071–2074 (2008)

Breath-Printing of Heart Failure in Elderly

A. Zompanti, P. Finamore, C. Pedone, M. Santonico, S. Grasso,
F.R. Parente, G. Ferri, V. Stornelli, D. Lelli, L. Costanzo,
R. Antonelli Incalzi and G. Pennazza

Abstract Comorbidity represents a confounding factor in exhaled breath analysis, in particular with elderly population, which often shows both respiratory and heart diseases. Congestive heart failure (CHF) is the first cause of hospitalization and a primary cause of death and disability in the elderly population. CHF has important metabolic implications, thus exhaled VOCs analysis may support CHF severity assessment and CHF discrimination against controls. VOCs pattern in CHF has not been yet investigated so far, even if an increase in acetone and pentane has been observed. Here, breathprint based CHF diagnosis and severity classification have been studied. Moreover, studying an elderly population, Chronic Obstructive Pulmonary Disease (COPD) patients have been enrolled, being COPD an important comorbidity in aged population.

Keywords Breathprint · Congestive heart failure (CHF) · Elderly
Gas sensor array · Chronic obstructive pulmonary disease (COPD)

A. Zompanti (✉) · M. Santonico · S. Grasso · G. Pennazza
Unit of Electronics for Sensor Systems, Department of Engineering, Campus Bio-Medico
University of Rome, Rome, Italy
e-mail: A.Zompanti@unicampus.it

P. Finamore · C. Pedone · D. Lelli · L. Costanzo · R. Antonelli Incalzi
Chair of Geriatrics, Unit of Respiratory Pathophysiology, Campus Bio-Medico University,
Rome, Italy

M. Santonico
CNR-IDASC, Rome, Italy

F.R. Parente · G. Ferri · V. Stornelli
Department of Industrial and Information Engineering and Economics, University of
L'Aquila, L'Aquila, Italy

1 Introduction

In the elderly population, congestive heart failure (CHF) is the first cause of hospitalization and a primary cause of death and disability [1]. Considering that CHF has important metabolic implications, exhaled VOCs analysis may support CHF severity assessment and CHF discrimination against controls. VOCs pattern in CHF has not been yet investigated so far, even if an increase in acetone and pentane has been observed [2]. Here, breathprint based CHF diagnosis and severity classification have been studied. Applying gas sensor arrays in the discrimination among comorbidities, often present in elderly people, represents an advance on the state of art of breath printing applications: commonly elderly patients are suffering from both Chronic Obstructive Pulmonary Disease (COPD) and CHF [3]. The aim consists of understanding if these two pathologies give different exhaled breath fingerprint, in order to better classify the characteristic volatile response [4, 5]. The application of this classification scheme should support personalized treatment to be monitored at home or in point of care facilities, thanks to the easiness and non invasivity of the sampling procedure.

2 Experimental

2.1 Requirements

Eighty-two subjects have been studied among those admitted with a diagnosis of decompensated CHF to the geriatric acute care ward of the University Hospital "Campus Bio-Medico" in Rome (Italy). CHF severity was assessed by NYHA (New York Heart Association) index. Two control groups have been enrolled to test CHF discrimination: 56 individuals free from chronic cardiac, respiratory, or renal diseases and without active neoplastic disease attending the University Hospital "Campus Bio-Medico" for routine blood tests; 66 patients affected by COPD that were enrolled among people attending the pulmonary medicine outpatient clinic of the University Hospital "Campus Bio-Medico". Exhaled breath has been collected with Pneumopipe® (European patent n. 12425057.2, Rome–Italy) during inpatient visit or the day after admission, in the morning, in subjects with CHF. This device allows non invasive collection of exhaled breath into an adsorbent Tenax GR cartridge (Supelco/Sigma-Aldrich, Bellefonte, PA, USA) by an individual normally breathing into it for 3 min [6]. Cartridge content is then thermally desorbed into BIONOTE's sensor cell, a gas sensor array developed and fabricated by the Lab of Electronics for Sensor Systems at the University Campus Bio-Medico of Rome. The array used for this study is composed of seven quartz microbalance (QMB) sensors covered with anthocyanins extracted from three different plant

tissues (red rose, red cabbage, blue hortensia) and used as chemical interactive materials. The collected VOCs, when desorbed into the sensor cell, interact with the chemicals covering the sensor's surface and they are adsorbed via weak bounding forces. The desorption of the exhaled breath collected into the cartridge is controlled by a temperature program with four temperature stages (50, 100, 150, 200 °C). The achieved twenty-eight responses (seven QMB tested per four different temperatures) form a sort of fingerprint of the exhaled breath, named breathrpint (BP) [3]. The multidimensional data set, composed of all the collected BPs, is the object of the statistical analysis. To evaluate the discriminative capacity (diagnosis and severity of CHF) of VOCs we used Partial Least Square Discriminant Analysis (PLS-DA) on a random subset of patients including 66% of our sample, and we assessed the strength of the predictive relationship in the remaining 33% of the sample (test set). To avoid overfitting we used a "repeated k-fold cross validation" (Fig. 1).

3 Results

Three models have been calculated. The first has the aim of discriminating CHF patients against: the test data set was composed of 46 subjects, 37 of them were correctly discriminated (80% of accuracy), 7 were false/negative (74% of sensitivity) and 2 were false/positive (89% of specificity). A second model was build in order to discriminate CHF versus COPD patients: the test data set was composed of 49 subjects, 38 of them were correctly discriminated (77.6% of accuracy), 2 were
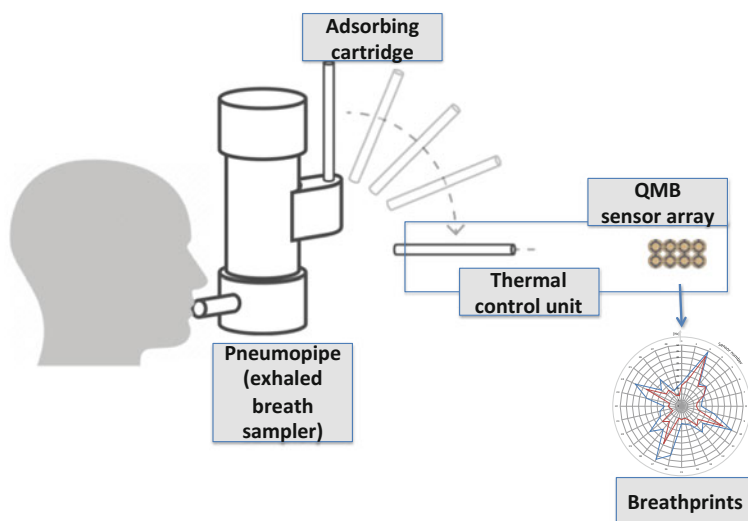
Fig. 1 Block scheme of the exhaled breath measure chain

(a)

Model 1, CHF vs CTRL		Clinical diagnosis	
		CHF	Controls
Breathprint based diagnosis	CHF	20	2
	Controls	7	17

(b)

Model 2, CHF vs COPD		Clinical diagnosis	
		CHF	COPD
Breathprint based diagnosis	CHF	18	2
	COPD	9	20

Fig. 2 Confusion matrices relative to the two PLS models calculated: **a** CHF-Controls discrimination; **b** CHF-COPD classification

false/negative (91% of sensitivity) and 9 were false/positive (66.7% of specificity). A third model was calculated in order to identify CHF severity based on NYHA index; 44 patients shown a change between NYHA determined at the admission and at the discharge. The model has the capability of correctly identifying subjects whose NYHA index significantly changed at the discharge: 40 of them were correctly discriminated (91% of accuracy), 3 were false/positive (81% of sensitivity) and 1 was false/negative (96% of specificity). In this proof-of-concept study we found that VOCs pattern is able to discriminate older CHF patients from both controls with no major chronic diseases and a population with COPD, and to identify CHF severity (Fig. 2).

4   Conclusions

Breathprints based analysis can discriminate between CHF diseased patients and control individuals with a good sensitivity and a satisfactory specificity. Moreover, the breathprints collected for COPD and CHF patients appear to be quite different and able to allow a good percentage of correct discrimination. This suggests that the composition of the exhaled breath in the two pathologies is quite different. Two points deserve deeper investigation: (1) a more deatailed study on VOCs composition in CHF and COPD population, also adding analytical chemistry techniques; (2) enrolling people affected by both COPD and CHF.

References

1. Ziaeian, B., Fonarow, G.C.: Epidemiology and aetiology of heart failure. Nat. Rev. Cardiol. **13** (6), 368–378 (2016)
2. Samara, M.A., Wilson Tang, W.H., Cikach, F., Gul, Z., Tranchito, L., Paschke, K.M., et al.: Single exhaled breath metabolomic analysis identifies unique breathprint in patients with acute decompensated heart failure. J. Am. Coll. Cardiol. **61**(13), 1463 (2013)
3. Incalzi, R.A., Scarlata, S., Pennazza, G., Santonico, M., Pedone, C.: Chronic Obstructive Pulmonary Disease in the elderly. Eur. J. Intern. Med. **25**, 320–328 (2014)
4. Antonelli, Incalzi Raffaele, Pennazza, G., Simone, Scarlata, Marco, Santonico, Massimo, Petriaggi, Domenica, Chiurco, Claudio, Pedone, Arnaldo, D'Amico: Reproducibility and respiratory function correlates of exhaled breath fingerprint in chronic obstructive pulmonary disease. PLoS ONE **7**, e45396 (2012)
5. Samara, M.A., et al.: Single exhaled breath metabolomic analysis identifies unique breathprint in patients with acute decompensated heart failure. J. Am. Coll. Cardiol. **61**(13), 1463 (2013)
6. Pennazza, G., Santonico, M., Incalzi, R.A., Scarlata, S., Chiurco, D., Vernile, C., et al.: Measure chain for exhaled breath collection and analysis: a novel approach suitable for frail respiratory patients. Sens. Actuators B Chem. **1**(204), 578–587 (2014)

Active Sensors/Actuators-Based Flow and Noise Control for Aerospace Applications

Maria Grazia De Giorgi (ORCID)**, Elisa Pescini, Antonio Suma, Maria Assunta Signore, Luca Francioso, Chiara De Pascali and Antonio Ficarella**

Abstract The present work introduces a method for flow and noise control using plasma actuation. The Single Dielectric Barrier Discharge Plasma Actuator (SDBDPA) device is object of study. A discussion of potential applications in flow and noise control in aerospace field is initially done. Then experimental results on separation control applications are presented. The investigated SDBDPA was manufactured by means of photolithographic technique. Particular attention was paid in materials selection because of possible degradation in plasma environment. The device separation control authority was investigated locating it on a curved plate with a shape designed to reproduce the suction surface of a low pressure turbine (LPT) rotor blade. The changes in the device performances with aging were quantified by monitoring in time the actuator power consumption. Scanning electron microscope (SEM) images on the new and used device were also used to complement the investigation.

M.G. De Giorgi (✉) · E. Pescini · A. Suma · A. Ficarella
Department of Engineering for Innovation, University of Salento,
Via Monteroni, Lecce, Italy
e-mail: mariagrazia.degiorgi@unisalento.it

E. Pescini
e-mail: elisa.pescini@unisalento.it

A. Suma
e-mail: antonio.suma@unisalento.it

A. Ficarella
e-mail: antonio.ficarella@unisalento.it

M.A. Signore · L. Francioso · C. De Pascali
Institute for Microelectronics and Microsystems—CNR–IMM,
Via Monteroni, Lecce, Italy
e-mail: signore@le.imm.cnr.it

L. Francioso
e-mail: luca.francioso@le.imm.cnr.it

C. De Pascali
e-mail: depascali@le.imm.cnr.it

185

1 Introduction

The applications of new and innovative aerodynamic flow and noise control technologies are critical to the needs of modern aircrafts, which have stringent goals of emissions and noise levels. In general, flow control methods involve passive and active control devices. Passive control devices (i.e. flow control via geometric modification) do not use external energy or momentum input to control the flow. Even if these techniques are still attractive, active control methods have recently received more attention since they can be operated only when they are effectively requested. Active flow control methods use external mechanical or electrical energy/momentum source and they generally include mass injection, piezoelectric flaps and plasma actuators. Among active flow control devices, plasma actuators are of great interest due to the high dynamic responses given by the absence of moving parts. Furthermore, they present low weight, are easy to build and are backward compatible with existing aerodynamic surfaces. During actuation, they can meaningfully change the status of the boundary layer development on the aerodynamic surfaces. For this reason, they have been widely investigated for flow separation control in aeronautical applications, as for lift enhancement and drag reduction [1]. Plasma actuators have been also applied to control friction drag by delaying transition, and to control global instabilities of the flow [2–4].

In the present work a discussion of potential applications on flow and noise control in aerospace fields is initially presented. Then separation control applications are discussed and complemented by the results of an experimental campaign. A SDBDPA device was designed and a particular attention was paid in the fabrication procedure and materials selection. The device separation control authority on the suction surface of a LPT rotor blade and at a Reynolds number of 2×10^4 was investigated in closed loop wind tunnel. Planar Laser Doppler Velocimetry (LDV) measurements were used. The changes in the performances of the device with aging were quantified by monitoring in time the actuator power consumptions. SEM images on the new and used device were also used to complement the investigation.

2 The DBD Plasma Actuator Devices

2.1 *Basic Principles*

Plasma actuators are simple devices that create a wall bounded jet which permits to control the near flow without moving mechanical parts. In the recent literature

different geometries have been proposed with the aim to improve the performance of these devices in view of their aptitude for boundary layer control applications. In the particular SDBDPA, the Plasma Synthetic Jet Actuator (PSJA) and the Multiple Encapsulated Electrodes Plasma Actuator (MEEPA) have been experimentally and numerically studied [5].

The SDBDPA investigated in the present work is composed of two metallic electrodes separated by a dielectric layer: one electrode is supplied with a high voltage (HV) waveform and exposed to the surrounding flow, the other one is grounded and completely covered by an insulating material. Typical operating mode involves the application of a voltage waveform in the kV and kHz ranges (with or without modulation or pulsing), which causes the air near the plasma actuator to weakly ionize. In these working conditions, heat generation is negligible and a "cold plasma discharge" is thus formed. The electric field interaction with the charged particles results in a net body force that acts on the ambient (neutrally charged) air. If operated in quiescent air, a wall jet is generated [6]. If applied in an existing flow, the body force can be applied to energize the boundary layer and suppress separation [7]. The flow control methods using plasma actuators offer thus also possibilities to control noise (without the need to physically change the shape of the aerodynamic surface), as flow and surface interaction represents one of the dominant sources of aerodynamic noise [8].

2.2 Noise and Flow Control

Flow and noise control technologies can be applied to reach desired performances and noise goals in several applications. These objectives can be realized by the control of the adverse flow characteristics. Some desired characteristics consist in maintaining laminar flow and delaying the onset of laminar-turbulent transition, avoiding boundary layer separation, suppressing the vortex shedding, improving flow uniformity and inducing turbulence for enhanced mixing.

Generally the demand for active acoustic control in aerodynamics has received less attention than the flow control applications, as actuators are predominantly investigated to enhance the aerodynamic performance.

A fundamental linkage exists between noise and flow control technologies. The principle of using plasma actuators in aeroacoustics for noise control is to modify the flow field to disrupt the mechanisms of flow-induced noise.

In previous studies plasma actuators have been applied to the leading edge boundary flow of a cavity [9]. The use of symmetric plasma actuators aligned in the streamwise direction to the oncoming flow to the cavity can, in fact, lead to an attenuation of the dominant cavity tone. The induced flow from the plasma actuators generates spanwise variations in the boundary layer that can alter the development of the shear layer and thus the development of the discrete spanwise vortices that are important to cavity-mode oscillations. Therefore, the plasma actuators should be designed to create disturbances upstream of the cavity, to

impede the development of the discrete vortices shed from the leading-edge corner of the cavity. It was quite clear by the experiments performed by Chan et al. [9] in which flow field and acoustic measurements were made in the cavity with and without plasma actuation. The attenuation of flow-induced tones using plasma actuators was demonstrated. The works showed that the dominant cavity mode and its harmonics were attenuated to broadband level when the plasma actuators were activated. The level of attenuation provided by the plasma actuators for a given flow speed was dependent on their operating voltage. High-frequency tones were produced by the plasma actuators, corresponding to the operating frequency of the applied potential. The amplitude of the high-frequency tones increased with the input power, but the rate of increase reduced with it.

In Huang et al. [10] plasma actuators were used to control flow-induced broadband noise radiated from a bluff body. The model consisted in a cylinder and a component (torque link) that was installed on the lee side of the cylinder. Acoustic measurements using a near-field microphone array and a far-field microphone arc were conducted at 30 m/s. Either the upstream-directed actuation or the downstream-directed actuation was applied on the cylinder surface. Flow measurements using PIV suggested that the cylinder wake could be manipulated with plasma actuation. Acoustic measurements also showed that the strength of the dominant noise source was reduced. It was also found that the noise control effect with the upstream-directed actuation was better than that of the downstream-directed actuation.

3 Experimental Test Case

The SDBDPA object of this study was designed and manufactured by means of photolithographic technique, which ensured a thin metal deposition with high manufacturing reliability control. As the device materials degradation is a significant issue, emphasis was put in selecting materials that could withstand the plasma environment. A Schott alkali-free borosilicate glass substrate (AF-32) was chosen as dielectric and tungsten (W) as electrode material [11]. In order to enhance the device durability and thus prevent electrode degradation by plasma, a PECVD (plasma-enhanced chemical vapor deposition) silicon nitride (Si_xN_y) 2 microns thick layer was deposited on the backside of the device. This last layer was absent in a small area of the electrode to permit its connection to the ground.

A cross-sectional view of the SDBDPA and its geometrical parameters dimensions are reported in Fig. 1. The deposition layers composition and thicknesses are instead in Fig. 2.

After the assessment of the actuator design and fabrication, the paper was focused on the experimental investigation of the potentialities of the fabricated SDBDPA to reattach the separated flow at a low Reynolds number.

The experimental approach comprised the actuator testing over a curved plate with a shape designed to reproduce the suction surface of a LPT rotor blade [12–
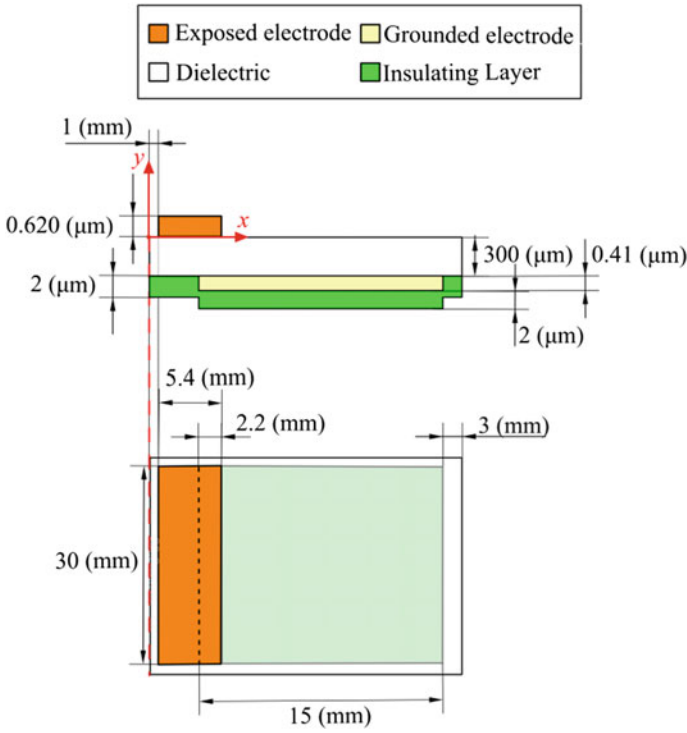
Fig. 1 Actuator geometry and dimensions
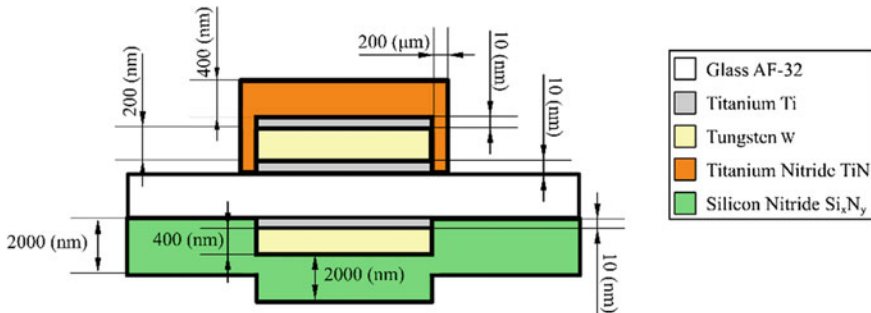
Fig. 2 Actuator deposition layers thicknesses

14]. A closed loop wind tunnel was employed. The curved plate was mounted directly on the bottom wall of the test section. The SDBDPA was placed in a grove made in the middle of the curved plate and located at the front side of the adverse pressure gradient region. In particular, the actuator lower electrode (denoted as "grounded electrode" in Fig. 1), its insulating layer and the AF-32 dielectric layer

were flush mounted at the wall of the profile, whereas the upper electrode (denoted as "exposed electrode" in Fig. 1) emerged from the surface and was exposed to the surrounding air flow. The time averaged free stream velocity at the wind tunnel inlet $v_{\infty,x}^{in}$ was set at 3 m/s. The Reynolds number based on the $v_{\infty,x}^{in}$ value and on the length c (100 mm) of the curved wall was 2×10^4.

Figure 3a shows the curved wall plate with the SDBDPA allocated, along with the adopted x-y Cartesian coordinate system. A magnified view of the SDBDPA geometry is also depicted. It has to be noticed that, for each x-coordinate, the origin of the y positions follows the curved wall plate. Figure 3b shows instead a photograph of the experimental setup and techniques.

The plasma actuators were operated by an alternate current (AC) voltage waveform generated by a function generator (Enertec Schlumberger 4431) and then amplified to HVs with a Trek Model 40/15 amplifier. The actuator exposed electrode was connected to the output of the HV amplifier and powered with sinusoidal
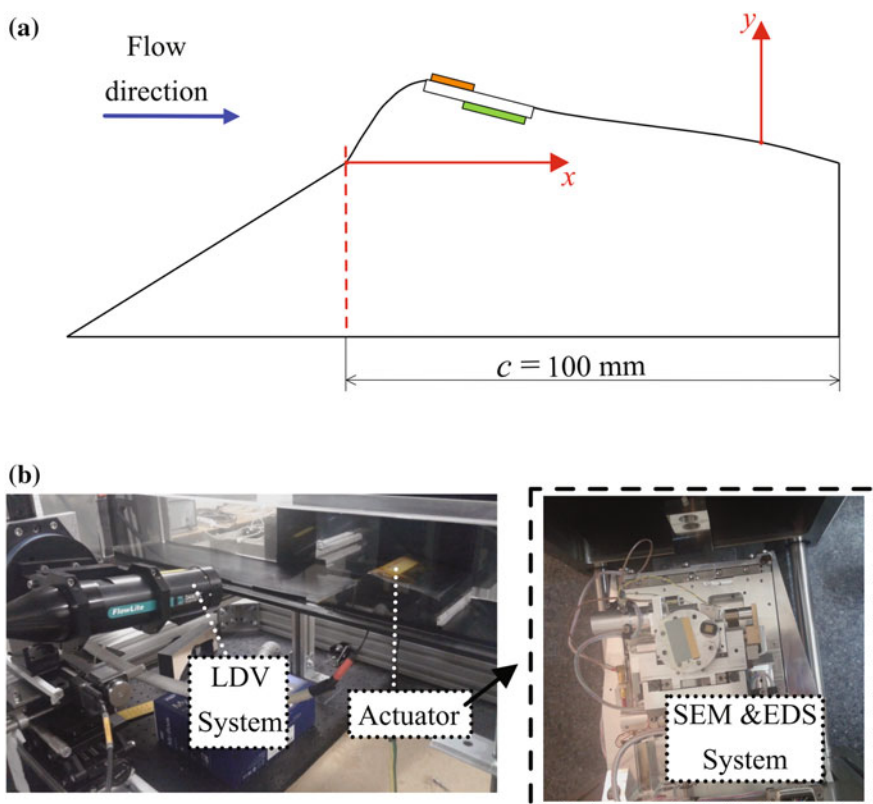
Fig. 3 a Curved wall plate, reference system and actuator details; b Experimental setup and techniques

Table 1 List of the test cases (sinusoidal applied voltage with frequency equal to 2 kHz)

Test case	Applied voltage amplitude (kV)
1	0
2	7.2
3	7.6
4	8.0

voltage at different amplitudes and 2 kHz frequency. The grounded electrode was instead connected to the ground. The different test cases are reported in Table 1.

The applied voltage was measured with the voltage output monitor built into the amplifier (accuracy better than 0.1% of full scale). The current was instead measured by a current transformer (Bergoz Current Transformer CT-B1.0) placed in series between the lower electrode and the ground. Both the amplifier voltage output monitor and the current transformer Bayonet Neill-Concelman (BNC) connector terminals were connected to an oscilloscope (Tektronix TDS2024C) and the respective signals were recorded with an accuracy of ±3%. For each input voltage, 128 single acquisitions were recorded and averaged. This allowed retrieving the voltage-current characteristic curves (as a function of time, t) used for the electrical power dissipation P_c calculation by:

$$P_c = \frac{1}{T} \int_0^T I(t)\, V_a(t)\, dt \tag{1}$$

$V_a(t)$ is the averaged applied voltage, $I(t)$ is the averaged current and T is the waveforms period.

Figure 4 shows an example of the recorded signals of applied voltage and current flowing in the discharge.

Fig. 4 Example of the current–voltage characteristic curves obtained by averaging 128 single acquisitions, for a sinusoidal applied voltage with 8 kV amplitude and 2 kHz frequency
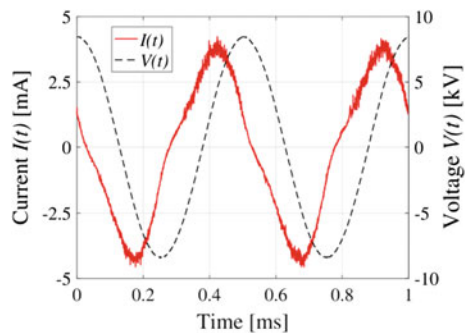
Simultaneously to the power dissipation measurements, flow velocity acquisitions—with and without actuation—were carried out. Planar LDV measurements were performed at the midspan plane of the curved wall plate and the velocity profiles were acquired at different streamwise locations.

Figure 5 shows the streamwise velocity (V_x) and the 2D-turbulence intensity Tu (%) profile acquired at $x = 87$ mm and for the four test cases in Table 1. The Tu (%) values were calculated according to Pescini et al. [12, 13] (normalized by the $v_{\infty,x}^{in}$ velocity). Results show that, among the actuated test cases, the test case 4 leaded to the highest reduction of the negative velocity and the highest Tu (%) values in the boundary layer.

Consequently, measurements in other streamwise x-sections were performed at the same excitation conditions of the test case 4 and results are reported in Fig. 6. Looking at the velocity profiles in Fig. 6a, it is evident that the actuation, together with the reduction of the negative velocity, always brought to a substantial decrease of the boundary layer thickness. Probably a slight higher level of voltage amplitude or frequency and so, of power, could bring to the complete reattachment of the flow.

Figure 6b shows the Tu (%) profiles. It is evident that the actuators act energizing the boundary layer in its proximity. In fact, the high turbulence region moves closer to the curved wall surface [12–14].

The power consumption results for the actuated test cases are reported in Fig. 7. In order to evaluate its stability, the power consumption was measured different times during all the fluid dynamic tests. This ensured that the actuator control authority was not changing during the scanning of each velocity profile or when scanning different profiles at same excitation conditions. Moreover, the actuator degradation is also trackable by measuring the electrical power dissipation in continuous, in fact, as shown in Pescini et al. [15], the power consumption of actuator rises with aging when electrodes degradation occurs.

Figure 7 shows the power dissipation evolution during the velocity profiles acquisitions of each actuated test case. The mean electrical power dissipation $\bar{P}_c$ resulted in about 4.2 ± 0.2 W for test case 2, 5.1 ± 0.3 W for test case 3 and 6.7 ± 0.3 W for test case 4. The standard deviation between the individual
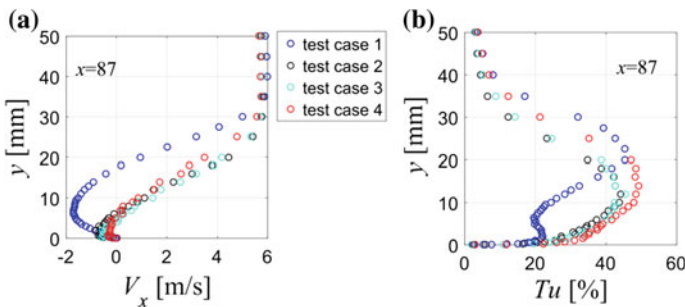
Fig. 5 Streamwise velocity profile (**a**) and Tu profile (**b**) for a vertical section located at $x = 87$ mm. Comparison between the actuator OFF test case (*test case 1*), and the actuated test cases (*test cases 2–4*)
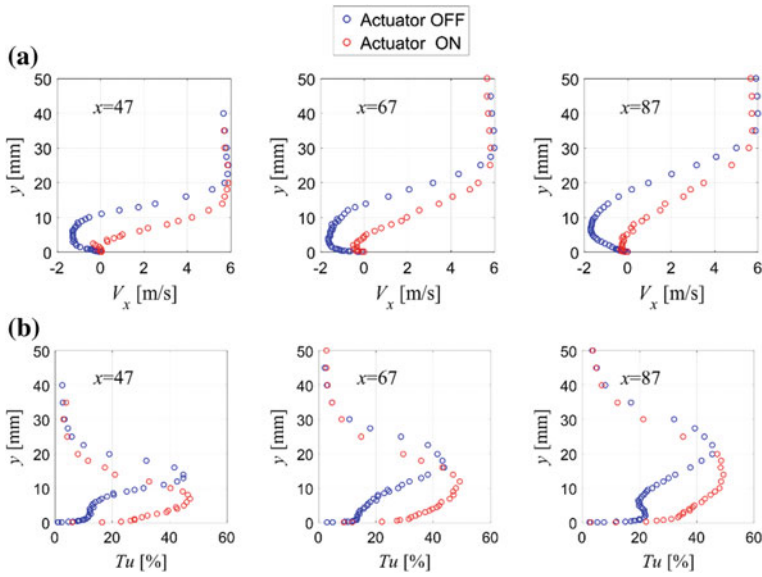
Fig. 6 Velocity (**a**) and turbulence intensity (**b**) profiles taken at different *x*-sections with actuator OFF (*test case 1*) and ON (*test case 4*)

Fig. 7 Actuator power dissipation in time, during the velocity profiles acquisitions for the *test cases 2, 3* and *4*
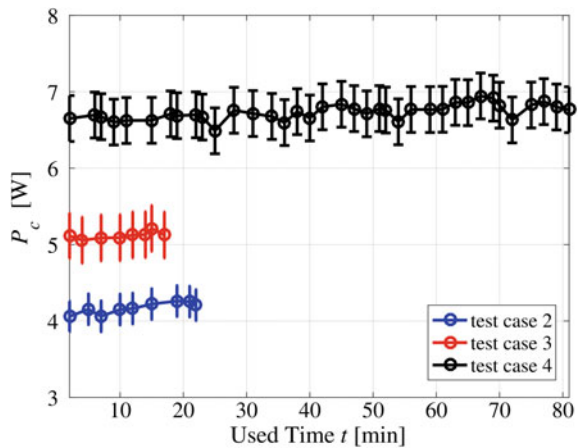
measurements was at worst 0.1 W. In general, it is possible to conclude that the power dissipation was quite stable over time.

It is pertinent to note that after the acquisition of the last profiles reported in Fig. 6, at about 141 min of operating time, the device broke, due to arching between the exposed and grounded electrode. As during each test it was not noticed a clear change in the power dissipations over time, the actuator degradation with
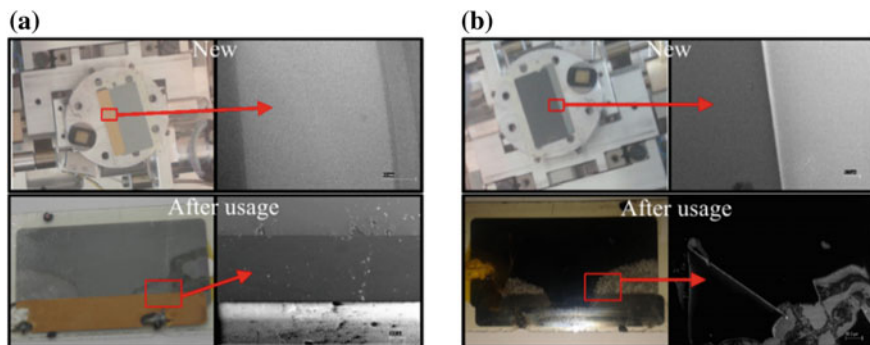
Fig. 8 Picture of the actuator exposed side (*left*), SEM analysis on the region indicated by the *red box* (*right*): **a** exposed electrode side; **b** grounded electrode side (Color figure online)

usage was then evaluated by the SEM images made on the actuator when it was new and after usage (at the end of all the tests).

The acquired images of the exposed electrode side are presented in Fig. 8a, while the grounded side images are shown in Fig. 8b. In particular, the top images show the actuator surface before usage, while the bottom ones the actuator surface after usage (about 140 min of operating time). For the exposed electrode side it is clear that, while in the new actuator the border of the electrode deposition was well defined, after usage a detachment of some parts of the border deposition occurred; moreover surface imperfections started to appear. The presence of surface imperfections becomes more evident by observing the back side of the actuator. As shown in Fig. 8b the grounded electrode exhibited a degradation process more important than the exposed electrode one. In fact, during usage, big areas of electrode deposition also detached.

The SEM analysis underlined the criticality in the SDBDPA material selection, matter that is starting to be investigated in the literature [11, 15]. This dispositive is meant to be used in realistic applications. Its durability has thus to be guaranteed. The authors aim to perform more experiments with new devices, characterized by same actuator geometry but with a thicker TiN coating on the exposed electrode and with a same coating on the grounded one, removing the Si_xN_y coating that resulted not resistant probably because of possible heating effects. Moreover, investigations on the noise reduction phenomena will be performed.

4 Conclusions

The aim of this work is to discuss about potential applications of dielectric barrier discharge plasma actuators for flow and noise control. An experimental investigation has been performed on separation control applications. A SDBDPA was designed and accurately manufactured. Flow measurements through LDV underlined the

device separation control authority. Furthermore, the device degradation with aging was assessed by comparing the SEM images on the new and used SDBDPA. It was found that while in the new actuator the border of the electrode deposition was well defined, after usage a detachment of some parts of the border deposition occurred on the exposed electrode; moreover surface imperfections started to appear. On the grounded electrode side, big areas of electrode deposition detached. Hence, this work underlines that improvements on coatings and actuator materials are required for their real applications on aircraft components.

References

1. Bérnard, N., Jolibois, J., Moreau, E.: Lift and drag performances of an axisymmetric airfoil controlled by plasma actuator. J. Electrostat. **67**(2), 133–139 (2009). doi:10.1016/j.elstat.2009.01.008
2. Duchmann, A., et al.: Dielectric barrier discharge plasma actuators for in-flight transition delay. AIAA J. **52**(2), 358–367 (2014). doi:10.2514/1.J052485
3. Choi, K.-S., Jukes, T., Whalley, R.: Turbulent boundary-layer control with plasma actuators. Philos. Trans. R. Soc. Lond. A: Math. Phys. Eng. Sci. **369**(1940), 1443–1458 (2011). doi:10.1098/rsta.2010.0362
4. Corke, T.C., Enloe, C.L., Wilkinson, S.P.: Dielectric barrier discharge plasma actuators for flow control. Ann. Rev. Fluid Mech. **42**, 505–529 (2010). doi:10.1146/annurev-fluid-121108-145550
5. Rodrigues, F.F., Pascoa, J.C., Trancossi, M.: Analysis of innovative plasma actuators geometries for boundary layer control. In: ASME International Mechanical Engineering Congress and Exposition, vol. 1. Advances in Aerospace Technology: V001T03A007. ASME, Phoenix (2016). doi:10.1115/IMECE2016-66495
6. Pescini, E., Francioso, L., De Giorgi, M., Ficarella, A.: Investigation of a micro dielectric barrier discharge plasma actuator for regional aircraft active flow control. IEEE Trans. Plasma Sci. **43**, 3668–3680 (2015). doi:10.1109/TPS.2015.2461016
7. Huang, J., Corke, T., Thomas, F.: Plasma actuators for separation control of low-pressure turbine blades. AIAA J. **44**, 51–57 (2006). doi:10.2514/1.2903
8. Huang, X., Zhang, X.: Plasma actuators for noise control. Int. J. Aeroacoustics **9**, 679–703 (2010). doi:10.1260/1475-472X.9.4-5.679
9. Chan, S., Zhang, X., Gabriel, S.: Attenuation of low-speed flow-induced cavity tones using plasma actuators. AIAA J. **45**(7), 1525–1538 (2007). doi:10.2514/1.26645
10. Huang, X., Zhang, X., Li, Y.: Broadband flow-induced sound control using plasma actuators. J. Sound Vib. **329**(13), 2477–2489 (2010). doi:10.1016/j.jsv.2010.01.018
11. Houser, N., Gimeno, L., Hanson, R., Goldhawk, T., Simpson, T., Lavoie, P.: Microfabrication of dielectric barrier discharge plasma actuators for flow control. Sens. Actuators A: Physical **201**, 101–104 (2013). doi:10.1016/j.sna.2013.06.005
12. Pescini, E., Marra, F., De Giorgi, M., Francioso, L., Ficarella, A.: Investigations of the actuation effect of a single DBD plasma actuator for flow separation control under simulated low-pressure turbine blade conditions. In: ASME Paper No. GT2016-57432 (2016). doi:10.1115/GT2016-57432
13. Pescini, E., Marra, F., De Giorgi, M., Francioso, L., Ficarella, A.: Investigations of the boundary layer characteristics for assessing the DBD plasma actuator control of the separated flow at low Reynolds numbers. Exp. Therm. Fluid Sci. **81**, 482–498 (2016). doi:10.1016/j.expthermflusci.2016.09.005

14. Matsunuma, T., Segawa, T.: Effect of input voltage on flow separation control for low-pressure turbine at low reynolds number by plasma actuators. Int. J. Rotating Mach. 1–10 (2012). doi:10.1155/2012/902548

15. Pescini, E., De Giorgi, M., Francioso, L., Taurino, A., Martucci, M., Lavoie, P.. Electrode material degradation monitoring for durable dielectric barrier discharge plasma actuators manufacturing. In: AIAA Paper No. 2016-0196 (2016). doi:10.2514/6.2016-0196

Wireless Smart Parking Sensor System for Vehicles Detection

**V. Stornelli, G. Ferri, M. Muttillo, L. Pantoli, A. Leoni, G. Barile,
D. D'Onofrio, F.R. Parente and T. Gabriele**

Abstract The proposed paper shows a novel and feasible solution for the realization of a smart-parking system. The proposed parking sensor circuit represents a robust and low cost solution for the automotive market to perform parking operations faster and simpler. The sensing strategy is based on both the electromagnetic coupling with the car platform and on an innovative dedicated algorithm implemented in a digital sensor interface for data acquisition and manipulation.

Keywords Bluetooth low emission · IoT · Smart parking · Sensor interface

1 Introduction

Statistics reveal that the car number per family will rapidly increase in the next years and in this perspective, the introduction of parking monitoring systems will lead benefits both in terms of time and pollution fight. Nowadays, different approaches and solutions are currently under investigation for the detection and management of parking [1, 2]. Among them, the optical/electromagnetic systems are surely the more explored and both of them show some drawbacks, due, for instance, to high sensitivity to local disturbances. The novel proposed circuit and algorithm here addressed overcome these drawbacks. It is well known, in fact, that a variable current flowing through an inductor generate a magnetic flux proportional to it; moreover, according to Faraday law, any change in this magnetic flux linkage produces a self-induced voltage in each coil and, consequently, a self-inductance

V. Stornelli (✉) · G. Ferri · M. Muttillo · L. Pantoli · A. Leoni · G. Barile
D. D'Onofrio · F.R. Parente
Department of Industrial and Information Engineering and Economics,
University of L'Aquila, L'Aquila, Italy
e-mail: vincenzo.stornelli@univaq.it

T. Gabriele
Research and Development Departmant, Engineering and Economics University,
2bite Srl, L'Aquila, Italy

value. Thanks to both the electromagnetic coupling with the car platform and the use of an innovative dedicated algorithm implemented in a digital sensor interface for data acquisition and manipulation the parking availability is detected and communicated trough a Bluetooth Low Emission (BLE) transmitter to surround connected devices.

2 The Proposed Solution

In the proposed architecture, see Fig. 1 at block level, the RF sensing element is embedded in a modified Colpitts oscillator, with different coils, that senses the presence of the parked car. In other words when a car stops above the sensor, the output frequency changes; these deviations are checked by a digital interface that includes a fast analog-to-digital converter and a microcontroller.

The designed prototype board has been obtained by modifying a commercial *RFduino* board, as shown in Fig. 2. Advanced hardware and software solutions have been adopted also in the design of a power-saving module, suitable to optimize the detection time step and the parking lot occupation check. The circuitry is able to switch on each module only when a dedicated activity is required. A power-saving algorithm (Fig. 3) has been also developed to control the overall functionality, also optimizing, for instance, the monitoring time as a function of the elapsed parking time. Finally, by using the BLE transmitter, the sensor data can be transferred to any BLE device in the surrounding and, so, to a data server. The reduced system dimension allows it to be easily integrated in a standard CMOS technology. The high performances and the need for low capacity battery make our architecture a promising solution for wireless smart parking and in particular for real time car parking sensor systems.

Simulations have shown a detection time of 46 ms and a detection current consumption of 82 mA. Under these conditions, using a battery of 2200 mAh and considering that the algorithm is able to save the 99% of resources for a typical use of the parking slot, the sensor lifetime achieves nearly 2 years. Some results
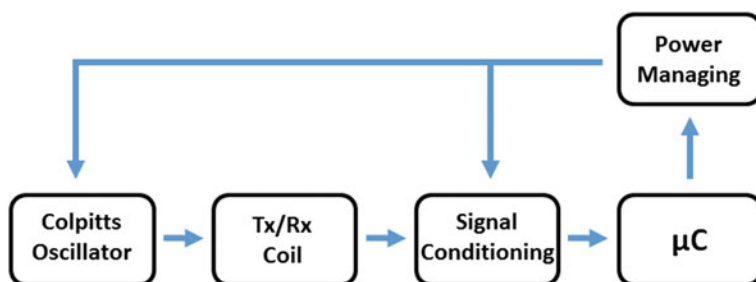
Fig. 1 Simplified block scheme of the designed sensing element
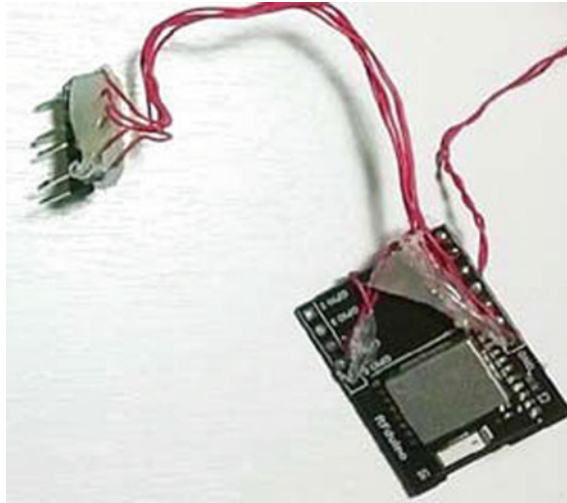
Fig. 2 Prototype board of the designed system

Fig. 3 Simplified diagram of the sampling time algorithm

Table 1 Test results

Electrical parameters	Vehicles	
	AUDI A4	TOYOTA AYGO
DC voltage supply	3.3 V	
Current consumption	81 mA	
Resting voltage amplitude	4.90 Vpp	
Resting signal frequency	74.55 kHz	
Ground to platform distance (cm)	12	17
Parking voltage amplitude (Vpp)	4.13	4.42
Parking signal frequency (kHz)	74.91	74.82

obtained sensing two different car types are shown in Table 1. IC low voltage and low power interface solution redesign both in current and voltage mode approach are currently in progress taking advantages from previous published circuits and architectures [3–6] as well as energy harvesting technologies approach in order to increase the sensor battery lifetime [7].

3 Conclusions

We have here briefly presented a low cost and feasible novel solution for the realization of a smart-parking system using BLE devices. Thanks to a dedicated strategy the battery powered sensor lifetime is as long as two years representing a robust solution for the automotive market to perform parking operations faster and simpler.

References

1. Tahon, M., et al.: Parking sensor network: economic feasibility study of parking sensors in a city environment is well. In: 9th International Conference on Telecommunications Internet and Media Techno Economics, pp 1–8 (2010)
2. Revathi, G., Dhulipala, V.R.S.: Smart parking systems and sensors: a survey. In: International Conference on Computing, Communication and Application, pp 1–5 (2012)
3. Stornelli, V.: Low voltage low power fully differential buffer. J. Circ. Syst. Comput. **18**, 497–502 (2009)
4. Stornelli, V., Pantoli, L., Leuzzi, G.: Active resonator for low-phase-noise tunable oscillators. Microwave Opt. Technol. Lett. **58**, 1032–1035 (2016)
5. Pantoli, L., Stornelli, V., Leuzzi, G.: Class AB tunable active inductor. Electron. Lett. **51**, 65–67 (2015)
6. Stornelli, V., Ferri, G.: A 0.18 μm CMOS DDCCII for portable LV-LP filters. Radioengineering. **2**, 434–439 (2013)
7. Di Marco, P., Stornelli, V., Ferri, G., Pantoli, L., Leoni, A.: Dual band harvester architecture for autonomous remote sensors. Sens. Actuators A **247**, 598–603 (2016)

Heat Sink Free Wearable Thermoelectric System with Low Startup Voltage, High Efficiency DC–DC Converter

L. Francioso, C. De Pascali, C. Veri, M. Pasca, S. D'amico, F. Casino and P. Siciliano

Abstract Thermoelectric energy harvesting represents a promising approach to partially or totally supply ultra-low power wearable devices, by using the human body heat as energy source. Few works were published on wearable and truly ready-to-use TEGs. The work presented in this contribute proposes development and assessment of operational properties of a system composed by a flexible heat sink free thermoelectric generator (TEG) and a DC–DC ASIC converter with 80 mV start-up input voltage. For a first functional investigation, a prototype of 45 thermocouples into a footprint area of about 2.2×10^{-3} m^2 was fabricated and tested to evaluate its thermoelectric performance stand-alone and coupled with the DC–DC converter. A mean Seebeck coefficient of about 60 µV/K for pn couple was calculated from experimental data, and a power of about 27 nW was measured at 10 K on matched load of about 6.8 kΩ. A temperature difference of about 1.8 °C was achieved between the junctions in working conditions next to those typical of human body wearing in indoors.

Keywords Wearable thermoelectric generator · Flexible thermoelectric
Wearable power source · ASIC converter

1 Introduction

In the last years, the growing market demand for wearable electronics devices created new technological challenges for suppliers and manufacturers, which are working to develop new materials and fabrication technologies for integration of ultra-low power consumption sensors, actuators and circuits into smart textiles for

L. Francioso (✉) · C. De Pascali · F. Casino · P. Siciliano
Institute for Microelectronics and Microsystems—CNR–IMM,
via Monteroni, Lecce, Italy
e-mail: Luca.Francioso@le.imm.cnr.it

C. Veri · M. Pasca · S. D'amico
Department of Innovation Engineering, University of Salento, Lecce, Italy

201

functional clothing. Innovative encapsulation solutions are investigated to increase the lifetime of wearable devices, but still much work has to be done to have devices which can be rolled, bent or folded without losing functionality. Energy harvesting technology represents a promising opportunity to achieve a fully exploitation of self-powered wearable devices in practical implementations. The human body heat is a possible energy source, by which ultra-low power wearable devices can be partially or totally supplied. A thermoelectric generator is compact, silent, devoid of moving parts, lightweight and maintenance-free and it finds application in a wide variety of fields, from biomedical to industrial. A flexible planar TEG formed by sputtered thin films as active p- and n-type thermocouples and structured by a wavy-shaped PDMS/Kapton assembled package was designed, fabricated and tested by authors in [1–5]. An open circuit output voltage of about 2 V at temperature difference of 5 K and internal resistance of about 2.3 MΩ was measured for a thermopile of 2778 thermocouples into an area of 25 cm^2. Other interesting examples of planar TEGs were proposed in [6–9]. In this paper, an heat sink free flexible TEG was designed and fabricated by low cost screen printing technology, to be used as power source for ultra-low power consumption wearable devices. Although main critical aspects related to the fabrication process were deal with and solved, practical and technological limitations constrained the TEG design with respect to the optimal dimensioning for maximum harvested power. Screen printable p-Sb_2Te_3 and n-Bi_2Te_3 alloys were prepared and characterized. Morphology, composition and transport properties of cured materials were analyzed and a comparison with silver particles filled alloys was also investigated. The thermopile was obtained by dispensing the thermoelectric materials into a pre-patterned PDMS mold. The realized TEG is flexible, weight-less and heat sink free, three key issues for the its unobtrusive integration in wearable systems. The fabrication process is cost-effective and scalable; the materials printing technique is easy and fast and it allowed to obtain PDMS mold integrated thermoelectric legs about 2 mm tall, by overcoming the technological limit imposed by various MEMS technologies on the maximum film thickness can be deposited, typically ranging from few microns to few hundred of microns.

2   Experimental

Functional tests were performed on the device stand-alone to evaluate its thermo-electric performance, by using a PID controlled thermal bench, in single- and double-plate configuration. A temperature difference on TEG of about 1.8 °C was measured in conditions of static air room temperature convection on TEG cold side and temperature of 34.8° Con TEG hot side. A mean Seebeck coefficient of 60 μV/K for single thermocouple was experimentally calculated; an output power of about 27 nW was measured at 10 K in matched load condition, with Figure of Merit of 2.6 × 10^{-5}. The TEG internal resistance (of about 6.8 kΩ) is higher than expected and it is probably caused by contact resistivity, mechanical fracture of

pillars, and undesired surface oxidation of the semiconductor pillars occurred before silver contact deposition. Then, the TEG was coupled to a custom designed DC–DC ASIC converter to evaluate the operational compatibility of the system: the test shown that the converter starts to work with a threshold input voltage of about 66 mV (lower than that of CMOS design parameters), by feeding an output voltage of about 320 mV. With a thermal gradient of about 2.0 °C, a thermopile of 450 thermocouples electrically in series is able to switch-on the ASIC oscillator for providing a boosted voltage to a connected load (sensor, battery or supercapacitor for power storage). Present work represents a good innovation in terms of devices fabrication and system integration; in fact our work uses flexible screen printed TEG devices instead of commercial ones reported in [10, 11]. FEA simulations were also performed and validated with experimental results and used for an improved version of the realized TEG. Feasibility of the fabrication process and compatibility of the complete system composed by TEG and ASIC chip were successfully assessed. However, further optimization of the thermoelectric materials and metal-semiconductor interfaces are needed for improving the system performance. In this work, printable slurries of p-type Sb_2Te_3 and n-type Bi_2Te_3 were obtained from high purity Bi, Sb and Te powders (100 mesh, from Alfa Aesar), which were ball-milled for 24 h under purified Argon atmosphere and then were incorporated into a solution of water dispersed polystyrene nanoparticles as binder agent (100 nm) and alpha-Terpineol. Stoichiometric pastes were obtained with solid load of 56 and 60% for p- and n-type. 2 vol.% of Ag particles (from Sigma Aldrich) was added to a dedicated pastes batch, in order to evaluate the effect of the metal filling on the thermoelectric properties of materials, in terms of electrical and thermal conductivity modulation. The mean bulk resistivity of the materials was measured by a Jandel RM-3000 four-point probe station at room temperature on different samples of the same alloy and average resistivity results are reported in Table 1

A PDMS through holes mold of total area 98 × 98 mm^2 containing 900 cavities with diameter of 1.5 mm and pitch of 1 mm was realized, according to the minimum feature size obtainable by using the internally available CNC facilities. The prepared thermoelectric pastes of stoichiometric Sb_2Te_3 and Bi_2Te_3 were deposited by blade coating into the cavities of the pre-patterned PDMS through-holes layer, then were hot-pressed and annealed into a conventional tubular oven under nitrogen gas flow at 250 °C for 1 h (heating rate of 5 °C min^{-1}) to compact the materials and to remove the solvent in excess (Fig. 1).

Experimental results of tests performed in dual-side imposed temperature mode are shown in Fig. 2, for increasing thermal gradients applied between hot/cold

	Bulk resistivity (Ωcm)
Sb_2Te_3	13.24 ± 2.27
Bi_2Te_3	15.31 ± 1.16
Ag–Sb_2Te_3	45.99 ± 5.16
Ag–Bi_2Te_3	44.22 ± 1.60

Table 1 Four-point bulk resistivity of Sb_2Te_3, Bi_2Te_3, Ag–Sb_2Te_3 and Ag–Bi_2Te_3 alloys after firing
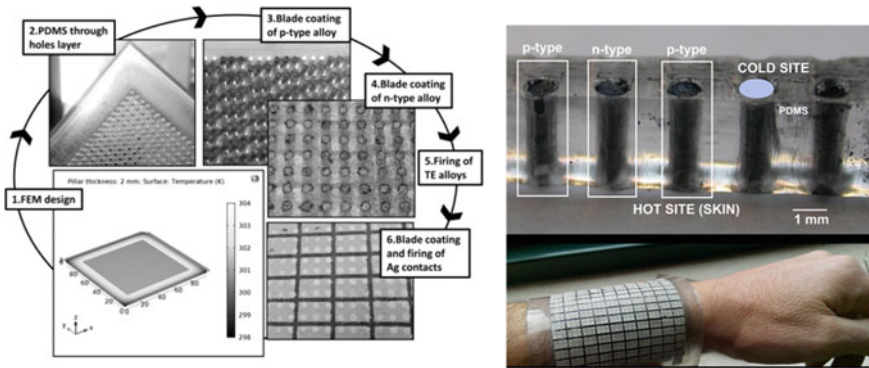
Fig. 1 Different phases of the design and fabrication process of TEG (*left*); Cross section of TEG with vertical pillars filled with p- and n-type alloys before metals deposition and wearable complete fabricated TEG on wrist location (*right*)

thermocouples junctions and as a function of the output load. The mean Seebeck coefficient calculated from experimental data of measured open circuit voltage is about 60 µV/K for the single p-n couple. The maximum power of about 27 nW is measured at 10 K of thermal gradient and for an applied load of about 6.8 kΩ (close to the internal resistance of the generator). The internal resistance is higher than expected and it is also probably caused by a silver-semiconductor contact resistance not yet optimized at this stage. The high electrical resistance generated a low Figure of Merit, while the major potential losses are related to contact resistivity; in fact, the calculated full generator resistance from 4-point probe resistivity measurements in Table 1 is about 4.8 kΩ, so about 2 kΩ might be attributed to contact resistivity, mechanical fracture of pillars, and undesired surface oxidation of the semiconductor pillars occurred before silver contact deposition. The investigation performed by coupling TEG with ASIC shown that the converter starts to work with a threshold input voltage of about 66 mV (lower than that of CMOS design parameters), by feeding an output voltage of about 320 mV (Fig. 2, right, ASIC voltage not reported). The ASIC chip operates stably when the thermal gradient on the TEG sides is higher than 20 °C; in principle, such a limit is reduced to 2.0 °C when a complete generator with 450 thermocouples operates interfaced to the DC–DC converter.

The calculated efficiency and Figure of Merit of the generator for different hot side temperatures are shown in Table 2; the calculated values are lowest respect to those of other published TEGs, but an enhancement could be obtained by optimizing the thermoelectric materials.

Different already optimized active materials could be easily transferred into our PDMS template by blade coating technique, keeping unaltered the fabrication process and contacts layout.
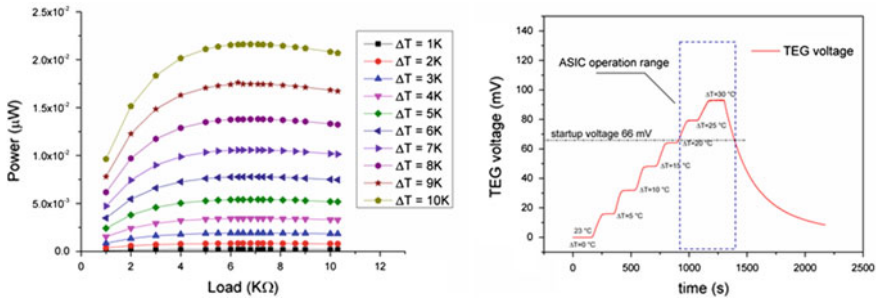
Fig. 2 TEG output power versus load for increasing thermal gradient between hot and cold TEG sides (*left*), TEG output voltage versus ΔT and ASIC coupling operating window (*right*)

Table 2 Efficiency and Figure of Merit calculated at different hot side temperatures

Carnot efficiency T_h = 33 °C T_c = 23 °C	γ factor T_h = 33 °C T_c = 23 °C	Figure of Merit ZT T_h = 33 °C T_c = 23 °C	Figure of Merit ZT T_h = 50 °C T_c = 23 °C	Figure of Merit ZT T_h = 100 °C T_c = 23 °C	Figure of Merit ZT T_h = 200 °C T_c = 23 °C
3.26%	2.14E-8	2.6E-5	2.7E-5	2.9E-5	3.3E-5

References

1. Francioso, L., De Pascali, C., Farella, I., Martucci, C., Cretì, P., Siciliano, P., Perrone, A: Flexible thermoelectric generator for ambient assisted living wearable biometric sensors. J. Power Sources **196**(6), 3239–3243 (2011). doi:10.1016/j.jpowsour.2010.11.081

2. Francioso, L., De Pascali, C., Farella, I., Martucci, C., Cretì, P., Siciliano, P.: Polyimide/PDMS flexible thermoelectric generator for Ambient Assisted Living applications. Proc. SPIE Int. Soc. Opt. Eng. **8066**, 80662H (2011). doi:10.1117/12.887836

3. Francioso, L., De Pascali, C., Bartali, R., Morganti, E., Lorenzelli, L., Siciliano, P., Laidani, N.: PDMS/kapton interface plasma treatment effects on the polymeric package for a wearable thermoelectric generator. ACS App. Mater. Interfaces **5**(14), 6586–6590 (2013). doi:10.1021/am401222p

4. Francioso, L., De Pascali, C., Siciliano, P., De Risi, A., D'Amico, S., Veri, C., Pasca, M: Thin film technology flexible thermoelectric generator and dedicated ASIC for energy harvesting applications. In: Proceedings of the 2013 5th IEEE International Workshop on Advances in Sensors and Interfaces, IWASI 2013, 6576100, pp. 104–107 (2013). doi:10.1109/IWASI.2013.6576100

5. Francioso, L., De Pascali, C., Siciliano P.: Experimental assessment of thermoelectric generator package properties: simulated results validation and real gradient capabilities. Energy. **86**, 300–310 (2015). doi:10.1016/j.energy.2015.04.041

6. Carmo, J.P., Goncalves, L.M., Wolffenbuttel, R.F., Correia, J.H.: A planar thermoelectric power generator for integration in wearable microsystems. Sens. Actuators A **161**(1–2), 199–204 (2010). doi:10.1016/j.sna.2010.05.010

7. Kao, P.H., Shih, P.J., Dai, C.L., Liu, M.C.: Fabrication and characterization of CMOS-MEMS thermoelectric micro generators. Sensors **10**, 1315–1325 (2010). doi:10.3390/s100201315

8. Yuan, Z., Ziouche, K., Bougrioua, Z., Lejeune, P., Lasri, T., Leclercq, D.: A planar micro thermoelectric generator with high thermal resistance. Sens. Actuators A **221**, 67–76 (2015). doi:10.1016/j.sna.2014.10.026

9. Jin Bae, E., Hun Kang, Y., Jang, KS., Yun Cho, S.: Enhancement of thermoelectric properties of PEDOT: PSS and Tellurium-PEDOT: PSS hybrid composites by simple chemical treatment. Scientific Reports 6, Article number: 18805 (2016). doi:10.1038/srep18805

10. Leonov, V., Gyselinckx, B., Van Hoof, C., Torfs, T., Yazicioglu, RF., Vullers, RJM., Fiorini, P., Wearable self-powered wireless devices with thermoelectric energy scavengers. In: Proceedings of Smart Systems Integration, Barcelona, Apr. 9–10, pp. 217–224 (2008). doi:10.1109/BSN.2009.10

11. Leonov, V., Torfs, T., Van Hoof, C., Vullers, R.J.M.: Smart wireless sensors integrated in clothing: an electrocardiography system in a shirt powered using human body heat. Sens. Transducers J. **107**, 165–176 (2009)

An Innovative Electro-Optic Sensor for Point-Like Electric Field Measurements

Application Example: Electric Field Shields Characterization

Umberto Perini, Elena Golinelli, Letizia De Maria and Rudi Bratovich

Abstract The quantitative measurement of the electric field is a demanding task that has to be accomplished without perturbing the spatial distribution of the field itself and by using systems that can be operated safely also when intense electric fields have to be measured. In this paper it is presented an innovative fully dielectric electro-optic sensor suitable for measuring electric field in the range 150 V/m÷1 MV/m. An application example: the electric field shields characterization will be presented as a novel application.

Keywords Electro-optic sensor · Birefringent crystal
Electric field measurements · Shields characterization

1 Introduction

Electro-optic sensors, where only dielectric components are employed, are the most appropriate candidates for Electric Field (E-F) measurements. Until today no commercial electro-optic sensor for such measurements is available. To overcome this problem, RSE optimized and tested a sensor based on a birefringent crystal [1]. This sensor is of quite small dimensions (the sensing element is 10 mm × 10 mm × 20 mm) and is completely dielectric. For these reasons it has a manifold of possible applications, ranging from insulating defects detection to the mapping of electric fields to which human being can be exposed, or for innovative applications, such as the characterization of innovative shielding masks for live line work (LLW), that we

U. Perini (✉) · E. Golinelli · L. De Maria
RSE Spa, via R.Rubattino, 54, 20134 Milan, Italy
e-mail: Umberto.Perini@rse-web.it

R. Bratovich
N.T.W. New Technology Workshop S.r.l, via Sant'Uguzzone n. 5, 20126 Milan, Italy

are presenting here. For High Voltage LLW works, protective conductive clothing needs to be integrated with a proper facial screen which must fulfil the requirements of the International Standard Specification [2] as for the electric-field screening efficiency. Facial screen must guarantee high electric-field screening efficiency (>50 dB) and low sheet resistance (<1 Ω/sq) [2]. In this work the electro-optic sensor is used both to assess the exposure of the LLW [3] operator in the facial region and to compare new facial screen based on transparent conductive multilayer films performances with the metallic grid ones.

2   Principle of Operation

The schematic layout of the sensor is shown in Fig. 1. The sensing element is a Lithium Niobate crystal through which a polarized light beam is fed. The electric field applied to the crystal modifies the polarization state of the travelling optical radiation. Polarization variations are then converted to intensity modulation by a proper choice of polarizing analysers. The intensity variations can be easily detected and related to the applied electric field.
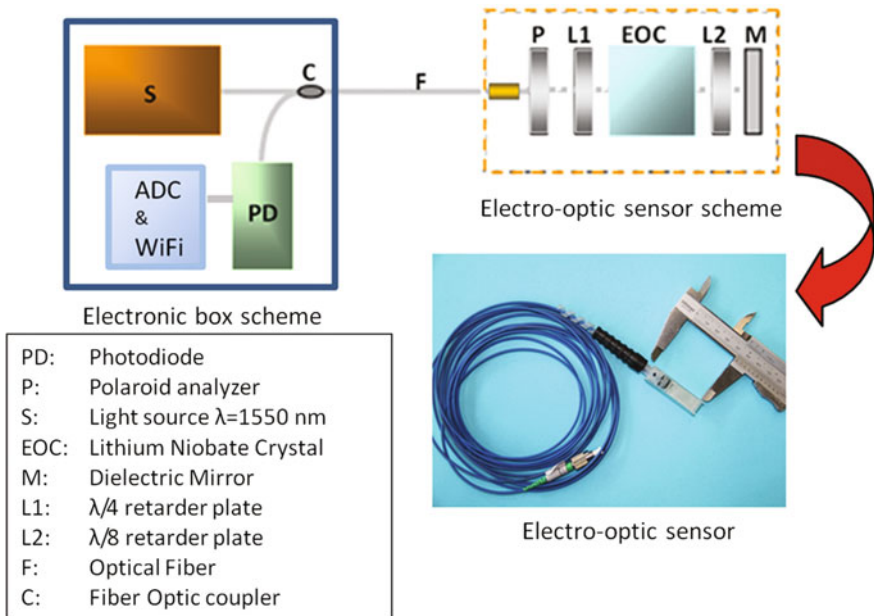
Fig. 1 Schematic layout of the electric field optical sensor and detail of the electro-optic sensor

3   Experimental Apparatus

The electric field optical sensor is composed by two units: the electro-optic sensor and the electronic box. The electro-optic sensor is composed by a collimator, some optical polarizing components, a dielectric mirror and a Lithium Niobate crystal. The electronic box containing the light source, the detection/acquisition unit, the wireless data transmitter is connected with the electro-optic sensor by an optical fibre. The system is battery operated and portable, data from the acquisition/ detection unit are wireless transmitted to a remote computer for data archiving and analysis.

Tests performed by inserting the sensor in known electric fields were made to characterize the sensor itself. In Fig. 2, the graph (a) shows the electric field measurements after calibration and the plot (b) is an example of real time field detection of an AC 50 Hz field by means of two different sensors (the green and the blue curve). As a result the sensor showed a good linearity and repeatability over a quite wide range of applied electric fields (150 V/m÷1 MV/m, 5 Hz÷150 kHz).

4   Sensor Application: Characterization of Facial Masks

The electro optic sensor, thanks to its fully dielectric implementation, small dimensions and its high sensitivity range, has been used for a critical measurement: the detection of the electric field close to the face of live line working operators, where the minimization of field distortions, that could be due to the sensor itself, and a point like detection are features of crucial importance.
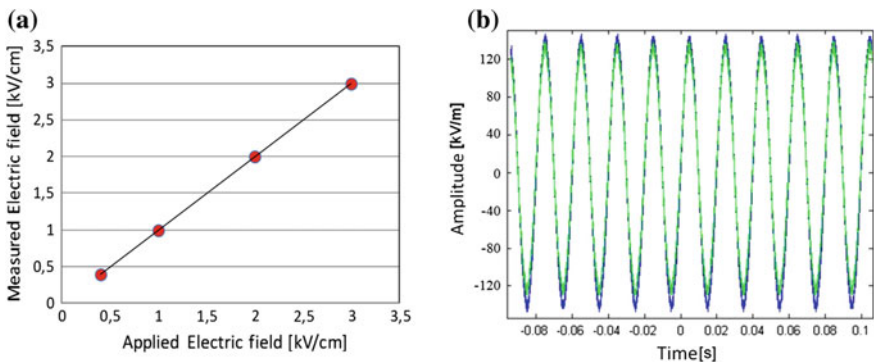
Fig. 2 **a** Measurements after calibration showing good linearity of the sensor, **b** 50 Hz electric field real time measurement for a 100 kV/m eff. field

4.1 Transparent Conductive Multilayers Shields

Transparent conductive multilayer films have been recently proposed by RSE [4] as an alternative solution to the more conventional metallic grid facial masks for LLW (Live Line Working). A multilayer structure consisting of two separate layers of Indium Tin Oxide (ITO) with a gold thin interlayer on a polycarbonate substrate was realized. An electron beam evaporation process with the assistance of an oxygen ion beam impinging on the growing film (Ion Beam Assisted Deposition—IBAD) was exploited to guarantee a highly transparent and conductive film without the need of high temperature deposition [5]. Optical transmission was measured by using a halogen lamp, a spectrometer (mod.HR 4000 Ocean Optics) and an integrating sphere. Sheet resistance was measured with a 4 point probe (van der Pauw method). The electric field shielding efficiency was measured under AC voltage (400 Vrms, 5 kHz frequency) according to the IEC 60895 Standard, by means the electro optic sensor.

4.2 Point Like Electric Field Measurements

The electro optic sensor was employed to compare the innovative multilayer shield and a more conventional fencing face screen [4]. A test set-up has been assembled in a HV laboratory (Fig. 3) where a mannequin with protective suit has been placed close to a high voltage conductor and exposed to an electric field representative of real operating condition. The optical sensor has been placed close to the face of the
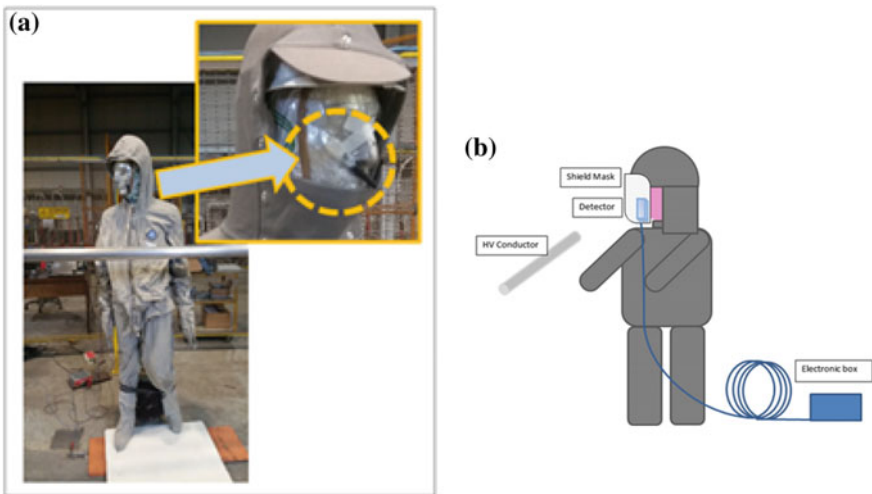
Fig. 3 E-Field shields measurement: **a** laboratory picture, **b** sketch of the setup

Table 1 Comparison of electrical characteristics with and without facial screen

Protective equipment	Electric field rms (kV/m)	Schield.Eff.(dB)
Without face screen	38.4	38
With fencing face screen	0.43	72
With multilayer film face screen	0.50	74

mannequin to detect the electric field under three measurement conditions: mannequin without face screen, with a fencing mask and with the multi-layered face screen.

Experimental data are reported in Table 1 [5]: by comparing the E-F rms measurement without facial screen shield and the two E-F measurements with the facial screens, it clearly appears that both the solutions can greatly reduce the E-F close to the face of the operator.

Experimental data also confirm that the electric screening efficiency of the multilayer film positively fulfil the face screen requirements with the further advantages of a better visual and wearing comfort, thanks to their lighter weight, flexibility and transparency.

5 Conclusions

The innovative electric field optical sensor, thanks to its full dielectric implementation, small dimensions and high sensitivity, allows to perform measurements where it is important to minimize the distortion of the spatial distribution of the E-F caused by the sensor itself. The innovative sensor described here can overcome the limitation of conventional E-F sensors, where metallic parts are necessarily present. The novel application concerning the characterization of innovative facial masks, reported herein, has shown its potential as a future tool for safety clothing testing.

References

1. Pirovano, G., Perini, U., Barberis, F., Bratovich, R., Barberis, A.: An innovative electro-optic sensor for AC and DC electric field detection: experimental results, presented at the ISH. Seoul, Korea (2012)
2. International Electrotechnical Commission IEC 60895 ed.2/CD Live working—conductive clothing (2002)

3. Malgesini, R., Valagussa, C., Villa, A., Carraro, R., De Donà, G., Milanello, C.D., Patrizia, A. A.: Conductive clothing for Live Line Working. In: ICOLIM 2014 11th International on Conference Live Maintenance, Budapest, Hungary (2014)
4. Barbieri, L., De Maria, L., Chemelli, C., Gondola, M., Malgesini, R., Villa, A., De Donà, G.: A comprehensive analysis of facial screens—Sensitivity analysis and construction technologies. In: ICOLIM 2017 12th International Conference on Live Maintenance, Strasbourg, France (2017)
5. Chemelli, C., De Maria, L., Marchionna, S., Pirovano, G.: Optical and electrical properties of transparent conductive ultrathin films for electric grid O&M applications. In: Proceedings of XXX International Conference on Surface Modification Techn (SMT30) (2016)

A Sensor Fusion Method Applied to Networked Rain Gauges for Defining Statistically Based Rainfall Thresholds for Landslide Triggering

Grazia Fattoruso, Annalisa Agresta, Saverio De Vito, Antonio Buonanno, Claudio Marocco, Mario Molinara, Francesco Tortorella and Girolamo Di Francia

Abstract Timely alerts provided to the communities at risk of landslides can prevent casualties and costly damages to people, buildings and infrastructures. The rainfalls are one of the primary triggering causes for landslides so that empirical approaches based on the correlation between landslides occurrence and rainfall characteristics, are considered effective for warning systems. This research work has intended to develop a landslide alerting system by using a Sensor Fusion method based on the SVC (Support Vector Classification) techniques. This method fuses rainfall data gathered in continuous by networked rain gauges and returns confidence degrees associated to the *not occurrence* of the landslide event as well as to the *occurrence* of one. By using a k-fold validation technique, an SVC-model, with AUC (Area Under the Curve) mean of 0,964733 and variance of 0,001243, has been defined. The proposed method has been tested on the regional rain gauges network, deployed in Calabria (Italy).

Keywords Landslides warning system · Networked rainfall gauges
Sensing systems · Sensor fusion methods · Support vector machine

G. Fattoruso · S. De Vito · A. Buonanno · G. Di Francia
UTTP-ENEA RC Portici, P.le E. Fermi, 1, 80055 Portici Naples, Italy

A. Agresta (✉)
Civil, Architectural and Environmental Engineering Department, University of Naples, via Claudio, 21, Naples, Italy
e-mail: annalisa.agresta@unina.it

C. Marocco · M. Molinara · F. Tortorella
Electromagnetism, Information Engineering and Mathematics Department, University of Cassino and Southern Lazio, via G. di Biasio, 43, Cassino, Italy

1   Introduction

Forecasting landslides occurrence and timely alerting the communities at risk can be fundamental for preventing casualties and costly damages to people, buildings and infrastructures.

For facing the landslide emergency, the modern control rooms are armed with comprehensive sets of decision making capabilities based on advanced technologies. In particular, warning and safety management systems are available, based on numerical modeling, computational intelligence algorithms, geomatics techniques as well as networked sensing systems. In situ sensing networks are linked to control centers by telemetry, providing data in continuous which assimilated by forecasting and alerting sub-systems allow the operators of monitoring the situation and giving warnings against indicators or triggers.

Indeed, the rainfalls are one of the primary triggering causes for landslides [1, 2] so that they have often been analysed to define a statistical or empirical correlation between landslides occurrence and rainfall characteristics [3, 4, 5]. On the basis of this correlation, rainfall thresholds triggering landslides have been defined and referred as statistically based ones [6, 7, 8]. Assuming that the correlation observed for the past is valid for the future [9], whenever the threshold is exceeded the occurrence of one or more landslides can be expected.

The empirical approaches are traditionally considered effective [7, 5] for warning systems at various scales, although physically based models are applied more effectively at basin scale [10, 11, 12].

Thus, warning systems which make use of only rainfall data as input parameters can be implemented [7, 13, 14, 15].

This research work has intended to investigate and develop a novel landslide alerting system by using a Sensor Fusion method based on the Support Vector Classification (SVC) techniques. This method empirically captures the correlation between landslides occurrence and rainfall characteristics, the latter derived by multiple networked rain gauges. Then, on the basis of this correlation, for each real rainfall event, it returns confidence degrees associated to the *not occurrence* of the landslide event as well as to the *occurrence* of one. A threshold value within the confidence degree range is defined so that whenever it is exceeded the occurrence of one or more landslides can be expected.

The SVC-method has been tested on rainfall data collected by the regional rain gauges network, deployed in Calabria (South Italy) and managed by the Local Civil Protection Authority and the AVI catalogue [16], including the landslides events occurred in Italy from 1917 to 2000.

2 Methodology

All sensing technologies, currently available, from geotechnical sensors to remote sensing, automated terrestrial surveys, GPS technology, GNSS Ground Portable Permanent Stations, and so on, used by themselves or in combination with each other, have been recognized instrumental to provide effective forecasting and alerting services to communities at risk of landslides.

However, the only rainfall data gathered in continuous by traditional networked rain gauges can generate robust alerts by using statistically-based methodologies, enable to capture the spatio-temporal correlation between landslides occurrence and rainfall characteristics.

In this regards, this research work has intended to investigate a sensor fusion method based on SVC techniques, enable to integrate rainfall data from the networked rain gauges closest to the landslides and to return the confidence degree associated to the occurrence of the landslide events.

In particular, the problem has been formalized as following:

$$y = f(x), \ conf : R^n \rightarrow [0, 1] \tag{1}$$

where f is the SVC-model that returns for each feature vector x, related to the rainfall reading, a real value (i.e. confidence degree) within the interval $[-1, 1]$. A value near to -1 means a less likely landslide event while a value near 1 means a more likely landslide event.

A decision boundary within the confidence degree range has to be defined so that whenever it is exceeded the occurrence of one or more landslides can be expected.

Given a feature vector x to be classified, a label is assigned according to its relationship to the decision boundary, and the corresponding decision function is:

$$f(x) = \sum_{i=1}^{l} \alpha_i k(x, x_i) \tag{2}$$

where $f(x)$ is defined as Support Vector Expansion; $k(x, x_i)$ is the kernel function [17]; α_i are positive real numbers that maximize:

$$C \sum_{i=1}^{n} \alpha_i - 0.5 \sum_{i,j} \alpha_i \alpha_j y_i y_j k(x_i, x_j) \tag{3}$$

subject to

$$0 \leq \alpha_i \leq C \quad and \quad \sum_{i=1}^{n} \alpha_i y_i = 0 \tag{4}$$

For building the SVC-models, the following steps have been performed: (1) clustering of rain gauges and landslides based on *Harversine* geographical distance [18]; (2) extraction of the intensities (I) and durations (D) of the rain storms associated with the initiation of landslides; (3) plotting and analysis of these values on a diagram and (4) extraction of the feature vectors set for the model training and test phases.

Concerning the first step, we have defined the spatial correlation between landslides and rain gauges through the Harversine geographical distance [18]:

$$dxF(x_i, F_j) = \min(d(x_i, f_k)) \quad \forall f_k \in F_j \tag{5}$$

$$dFF(F_i, F_j) = \min(d(f_m, f_n)) \quad \forall (f_m, f_n) \in F_i F_j \tag{6}$$

where $dxF(x_i, F_j)$ is the distance between a point (x_i) (related to a landslide or a rain gauge) and a landslide cluster (F_j) and $dFF(F_i, F_j)$ is the distance between the landslide cluster F_i and the landslide cluster F_j.

Thus, the clusters are built by the following algorithm: (1) for each landslide f_i an cluster F_j is defined; (2) for each f_k, it falls within f_k whereby $dxF(f_{mk}, F_j) < D_f$; (3) the clusters F_i and F_j are merged whereby $dFF(F_i, F_j) < D_f$; (3) for each rain gauges p_i, whereby $p_i < D_{pF}$, p_i, p_i falls within the cluster F_i.

D_f and D_{pF} are threshold distances where D_f is the maximum distance between landslides within the same cluster and D_{pF} is the maximum distance between a rain gauge and a cluster.

As second step, we have defined the temporal correlations in the following way. For each cluster F_j and related landslide f_j, the rainfall intensity-duration (I-D) curve, weighted by coefficients based on the related rain gauge-landslide distance, is associated to the landslide f_j. Then, for each landslide f_j, started at the time $t_{j,0}, [t_{j,0} - M * 24 * 60, t_{j,0}]$ is defined as the time interval of the rainfall sequences as well as the total minutes of M days. So, $Ap_{i,j}(m) = \sum_{k=0}^{N*60} p_i(t_{j,0} - M * 24 * 60 + m * N * 60 + k)$ is defined as cumulated rainfall value at time m related to the landslide f_j occurred at time $t_{j,0}$. Finally, for each cluster F_r and included landslide f_j^r, one or more rainfall sequences $Ap_{i,j}^r(m)$ are associated to the landslide f_j^r, one for each rain gauge that falls within cluster F_r.

By using normalized coefficient $k_{i,j}^r$, we have obtained normalized rainfall intensity $NAp_j^r(m)$, defined as following:

$$NAp_j^r(m) = \sum_{i=1}^{q} k_{i,j}^r * Ap_{i,j}^r(m) \quad m \in \{0, \ldots, \Delta\} \tag{7}$$

where

$$k_{i,j}^r = \frac{\sum_{i=0}^{q} dist_{i,j}^r dist_{i,j}^r}{dist_{i,j}^r}$$

On the basis of normalized rainfall intensity $NAp_j^r(m)$, the feature vector (x) are calculated as:

$$x = \{max, min, med, var, dyMax, dyMin, dyMed, dyVar, month\} \qquad (8)$$

where:

$$max = max_m\left(NHAp_j^r(m)\right) \qquad (9)$$

$$min = min_m\left(NHAp_j^r(m)\right) \qquad (10)$$

$$med = \sum_{m=0}^{\Delta} NHAp_j^r(m)/\Delta \qquad (11)$$

$$var = \sqrt{NHAp_j^r(m) - med^2/\Delta} \qquad (12)$$

$$dyMax = max_m(dy(m)) \qquad (13)$$

$$dy(m) = NHAp_j^r(m) - NHAp_j^r(m-1) \qquad (14)$$

$$dyMin = min_m(dy(m)) \qquad (15)$$

$$dyMed = average_m(dy(m)) \qquad (16)$$

$$dyVar = var_m(dy(m)) \qquad (17)$$

$$month = \left\{ \begin{array}{c} june,\ july,\ august,\ september,\ october, \\ november,\ december,\ january,\ february, march, april, may\} \end{array} \right. \qquad (18)$$

Each calculated feature vector is labelled with a real value within the interval $[-1, +1]$ where a value near to -1 means a less likely landslide event while a value near 1 means a more likely landslide event.

3 The Case Study

The investigated sensor fusion method has been tested on the pilot rain gauges network of the Local Civil Protection Authority, deployed in Calabria (South Italy), aimed at setting a regional alerting system for landslide initiation based on the only rainfall data gathered in continuous by traditional networked rain gauges.

The proposed system intended to provide the pilot operating room of tools more easy to be used, for generating effective landslide alerting services. Indeed, currently, a Regional Alerting System is used for generating several alert states on the

basis of meteorological data gathered in continuous by networked fixed and mobile gauge stations as well as rainfall thresholds derived by physically-based approaches.

The historical landslides events (trigged by rainfall) in Calabria have been extracted by AVI (Damaged Urban Areas–http://avi.gndci.cnr.it/) database landslides. This database was originally designed to respond to a request of the Italian Minister of Civil Protection, and was aimed at helping the regional assessment of landslide and flood risk in Italy [16].

By integrating the two datasets, it has been possible used only 56 rain gauges stations of the pilot network, over the period 1990–1996 with 1-h time step, while the selected landslides dataset counted only 66 landslides, on the same period (Fig. 1).
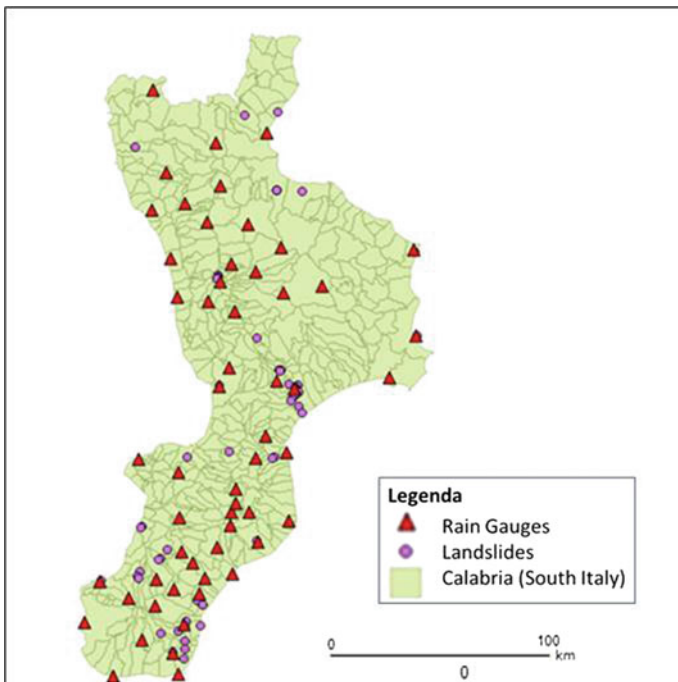
Fig. 1 Map of the networked rain gauges and landslides over the period 1990–1996 located in Calabria (South Italy)

4   Results and Discussion

A SVC model, captures the spatio-temporal correlation between landslides and rainfall events, has been built for the case study by using the selected datasets of the landslides and rain gauges.

In particular, the landslide events occurred over the period 1990–1993 have constituted the training set while those ones occurred over the period 1994–1996 the testing set.

Applying the aforesaid procedure, the feature vectors dataset has been performed for the training/testing sets. The feature vectors related to rainfall records $NHAp_j^r$ correlated to landslide events (rainfall triggering landslide) have been classified as the positive values of the training dataset while the feature vectors related to rainfall records $NHAp_j^r$ do not correlated to landslide events (rainfall not triggering landslide) have been classified as the negative values.

By setting the distances $D_f = 10$ km and $D_{pF} = 10$ km, the rainfall time range $M = 30$ days and the rainfall intensity on 24 h, the proposed procedure has extracted 6 landslide clusters without rain gauges (all rain gauges are distant more than D_{pF}); 12 landslide clusters including rain gauges. Thirty rain gauges don't fall within any defined landslides cluster.

Just as an example, the landslide cluster indexed 8 is shown in the Fig. 2. It included 22 landslides occurred in the past years and only 2 rain gauges. In order to
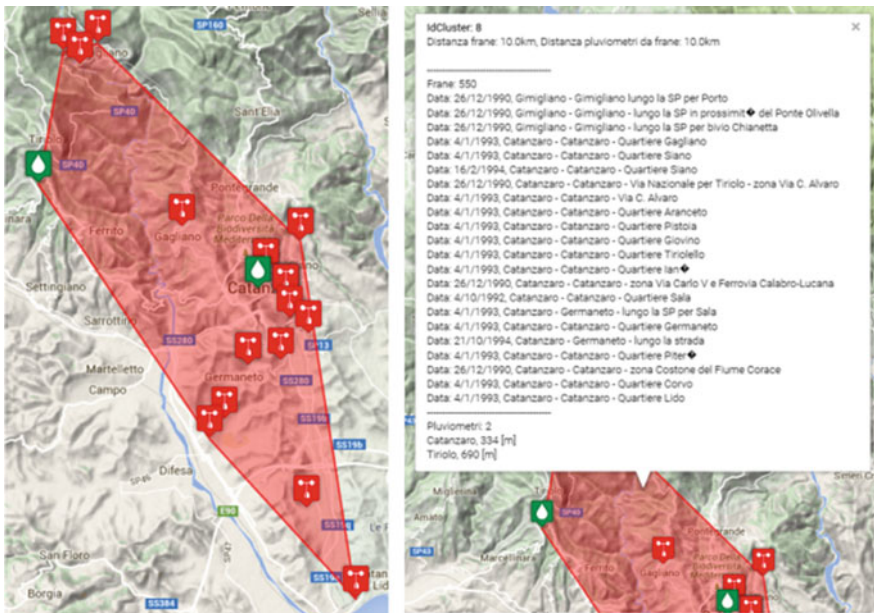
Fig. 2 View of the rain gauges and landslides cluster 8

build robust training/testing sets, 528 not-real landslides have been added as negative value.

Thus, for each performed landslides cluster, the feature vectors have been extracted with $\mu = 0$ and $\sigma = 1$.

By using the Libsvm package [19], for building the SVC model, the RBF (σ, C) linear kernel has been selected after different trials with linear and polynomial kernels. The couple (σ, C) is calculated maximizing the following training performance value:

$$Accuracy(ACC) = \frac{TP + TN}{TP + TN + FP + FN} \tag{19}$$

by the grid search method [20], obtaining an optimal value ACC = 94.2308% for $(\sigma, C) = (0.0078125, 32)$ (Fig. 3).

A k-fold validation technique has been used for the experimental characterization due to the small dataset. In this regards, k = 10 disjoint training/testing sets have been randomly selected evaluating the performance, by using the indices AUC (Area Under the Curve) and accuracy of the ROC (Receiver Operating Caractheristic)-curves (Fig. 4).

By using the ROC curves, AUC values for each *fold* has been evaluated. Thus, the SVC-model, with AUC mean of 0,964733 and AUC variance of 0,001243 has been defined. It can be considered satisfactory though the small number of rainfall data for each landslide event and the small number of landslide events.

Finally, on the basis of the defined SVC-method, a landslides alert system has been developed. More specifically, it returns a value less than or equal to 0 (and more than or equal to −1) if the confidence degree associated to the *not occurrence* of the landslide event is high (i.e. the daily rainfall intensity during the last 30 days cannot certainly trigger a landslide) and a value more than 0 (and less than or equal

Fig. 3 Grid search for C and σ (gamma in Libsvm). The *green* iso-line is related to the optimal ACC value (Color figure online)
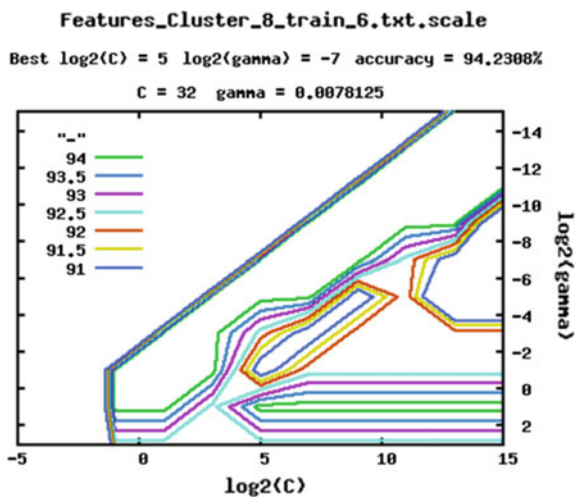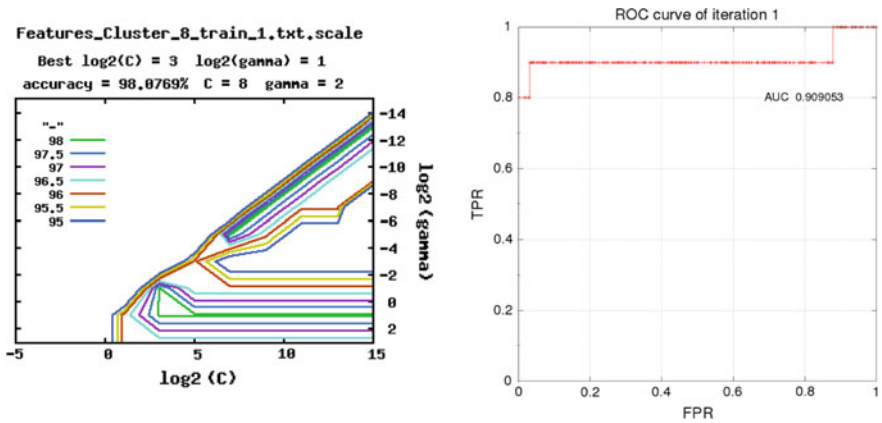
Fig. 4 Applying k (=10)-fold cross validation, for each fold k, training and testing performance indices are given by ACC, ROC curve and AUC. View of grid search and ROC curve for fold 1 (AUC mean: 0.9; AUC variance: 0.0308642)

to 1) if the confidence degree associated to the *occurrence* of the landslide event is high (i.e. the daily rainfall intensity during the last 30 days certainly triggers a landslide).

The proposed method can be standardized and can consistently replicated in early warning systems.

References

1. Wieczorek, G.F.: Landslide triggering mechanisms. Landslides Inv. Mitig. **247**, 76–90 (1996)
2. Farahmand, A., AghaKouchak, A.: A Quasi-global landslide model using remote sensing data. In AGU Fall Meeting Abstracts, vol. 1, p. 07. (2012, December)
3. Montgomery, D.R., Dietrich, W.E.: A physically based model for the topographic control on shallow landsliding. Water Resour. Res. **30**(4), 1153–1171 (1994)
4. Aleotti, P.: A warning system for rainfall-induced shallow failures. Eng. Geol. **73**(3), 247–265 (2004)
5. Tiranti, D., Rabuffetti, D.: Estimation of rainfall thresholds triggering shallow landslides for an operational warning system implementation. Landslides **7**(4), 471–481 (2010)
6. Caine, N.: The rainfall intensity: duration control of shallow landslides and debris flows. Geografiska Annaler. Ser. A. Phys. Geo. 23–27 (1980)
7. Aleotti, P.: A warning system for rainfall-induced shallow failures. Eng. Geol. **73**(3), 247–265 (2004)
8. Guzzetti, F., Peruccacci, S., Rossi, M., Stark, C.P.: Rainfall thresholds for the initiation of landslides in central and southern Europe. Meteorol. Atmos. Phys. **98**(3), 239–267 (2007)

9. Wilson, R.C., Wieczorek, G.F.: Rainfall thresholds for the initiation of debris flows at La Honda. California. Environmental & Engineering Geoscience **1**(1), 11–27 (1995)

10. Guzzetti, F., Carrara, A., Cardinali, M., Reichenbach, P.: Landslide hazard evaluation: a review of current techniques and their application in a multi-scale study. Central Italy Geomorphol. **31**(1), 181–216 (1999)

11. Segoni, S., Leoni, L., Benedetti, A.I., Catani, F., Righini, G., Falorni, G., Rebora, N.: Towards a definition of a real-time forecasting network for rainfall induced shallow landslides. Nat. Hazards and Earth Syst. Sci. **9**(6), 2119 (2009)

12. Mercogliano, P., Segoni, S., Rossi, G., Sikorsky, B., Tofani, V., Schiano, P., Casagli, N.: Brief communication "A prototype forecasting chain for rainfall induced shallow landslides". Nat. Hazards Earth Syst. Sci. **13**(3), 771 (2013)

13. Sirangelo, B., Versace, P.: A real time forecasting model for landslides triggered by rainfall. Meccanica **31**(1), 73–85 (1996)

14. Capparelli, G., Tiranti, D.: Application of the MoniFLaIR early warning system for rainfall-induced landslides in Piedmont region (Italy). Landslides **7**(4), 401–410 (2010)

15. Martelloni, G., Segoni, S., Fanti, R., Catani, F.: Rainfall thresholds for the forecasting of landslide occurrence at regional scale. Landslides **9**(4), 485–495 (2012)

16. Guzzetti, F., Cardinali, M., Reichenbach, P.: The AVI Project: A bibliographical and archive inventory of landslides and floods in Italy. Environ. Manage. **18**(4), 623–633 (1994)

17. Scholkopf, B., Smola, A.J.: Learning with kernels: support vector machines, regularization, optimization, and beyond. MIT press (2001)

18. Hughes, M., Jones, G.J., O'Connor, N.E.: Visual and geographical data fusion to classify landmarks in geo-tagged images (2012)

19. Chang, C.C., Lin, C.J.: LIBSVM: a library for support vector machines. ACM Trans. Int. Syst. Technol. (TIST) **2**(3), 27 (2011)

20. Bao, Y., Liu, Z.: A fast grid search method in support vector regression forecasting time series. In International Conference on Intelligent Data Engineering and Automated Learning, pp. 504–511. Springer, Berlin, Heidelberg (2006, September)

Particle Manipulation by Means of Piezoelectric Actuators for Microfluidic Applications

Marco Demori, Marco Baù, Marco Ferrari and Vittorio Ferrari

Abstract In this paper the possibility to generate acoustic waves such as FPW (Flexural Plate Wave) for fluid and particle manipulation by piezoelectric actuators applied on non-piezoelectric substrates is explored. A test device with two Lead Zirconate Titanate (PZT) actuators deposited on an alumina (Al_2O_3) substrate by screen printing technique is presented. The experimental results show that, by exciting the actuators at their resonance frequencies, FPW modes are generated in the substrate. Circular vortex rotations are obtained in a fluid drop placed on the substrate by exciting a single actuator. In addition, micrometric particles dispersed in the drop allow to demonstrate that particle accumulation along circular lines is obtained by exciting both the actuators. These results suggest the possibility to employ the proposed actuators for fluid mixing and controlled positioning of dispersed particles.

1 Introduction

Controllable and accurate fluid and particle manipulation in microfluidic devices represents a very important tool for many applications in biological, chemical and physical research. The forces generated by the interaction between acoustic waves and fluids can be used to actuate fluid and suspended particles, such as cells, at small scale with micrometric resolution. SAW (Surface Acoustic Wave), BAW (Bulk Acoustic Wave) or FPW (Flexural Plate Wave) [1] acoustic modes can be generated and detected by piezoelectric actuators driven at suitable frequencies to obtain wavelengths in the order of up to 100 μm. SAWs or BAWs can be used for fluid steering and motion of liquid drops or for fluid mixing by generating vortex

M. Demori (✉) · M. Baù · M. Ferrari · V. Ferrari
Department of Information Engineering, University of Brescia, Brescia, Italy
e-mail: marco.demori@unibs.it

rotation in a drop [2]. Controlled positioning of particles can be obtained by generating standing waves by means of pairs of opposite actuators. Particles dispersed in a liquid are attracted in the pressure nodes of the standing waves and their position can be controlled by changing the excitation frequency or the phase difference between the oppositely generated waves [3, 4]. Thus, a controlled positioning or separation of heterogeneous particles [5] can be performed within the acoustic field. An interesting application of this manipulation technique is in the field of tissue engineering where the accurate positioning of cells is necessary for a controlled tissue growing [6].

The typical configuration of the microfluidic devices used for fluid and particle manipulations exploiting SAWs or FPWs requires piezoelectric substrates with InterDigital Transducers (IDTs) to realize the actuators [2–6]. In this paper the possibility to generate acoustic waves by piezoelectric actuators applied on non-piezoelectric substrate is explored. This possibility gives the advantage to obtain fluid and particle manipulation by acoustic waves on generic substrates, including transparent substrates, suitable for the fabrication of microfluidic devices.

2   Test Device Description

A test device with two piezoelectric actuators for the generation of acoustic waves in an alumina (Al_2O_3) substrate is presented. The actuators have been fabricated by the screen-printing technique. Figure 1a, b, and c show a sketch, a cross section, and a picture of the device, respectively.
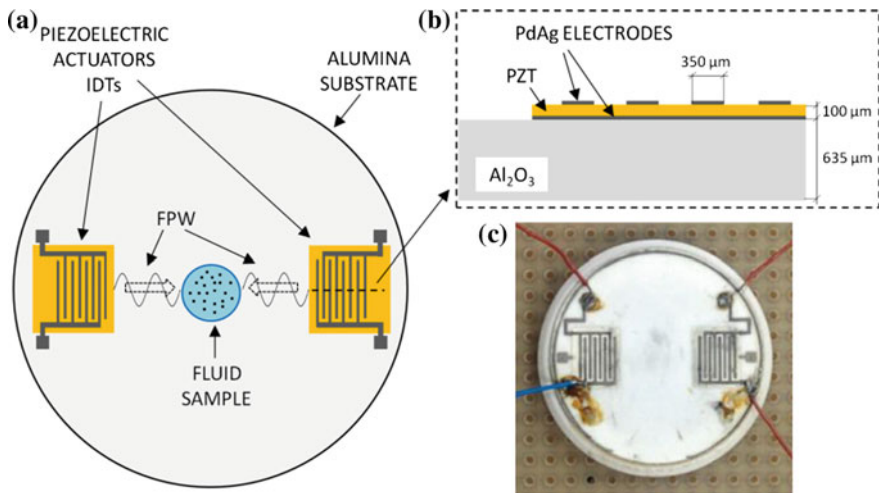
Fig. 1 Sketch of the test device (**a**) with a cross section of the PZT actuator (**b**) and picture of the device (**c**)

The fabrication process of the actuators starts with the alumina substrate where a bottom PdAg electrode, with the area of the actuator, is deposited by screen printing. Then a drying at 150 °C and firing at 850 °C processes are applied to finalize the bottom electrode. A Lead Zirconate Titanate (PZT) layer is realized on top of the bottom electrode with multiple screen printing depositions to obtain the final thickness. Drying at 150 °C and firing at 950 °C peak temperature are carried out to each PZT deposition. Finally, an InterDigital Transducer (IDT) is realized on top of the PZT layer by a new deposition of PdAg electrodes and applying a final drying and firing processes.

The actuators consist thus of IDTs realized on the PZT layer with the bottom electrode. The PZT layer was poled at 4 MV/m along the thickness using the IDT pair and the bottom conductive electrode as the two armatures. Thus, a sinusoidal excitation voltage applied between the two IDT fingers generates sinusoidal deformation of the PZT-layer thickness by exploiting the d_{33} mode, acting as actuator for the generation of the acoustic waves in the substrate.

The IDTs have both finger width and spacing of 350 μm, as shown in Fig. 1b. The PZT layer and the substrate have a thickness of about 100 and 635 μm, respectively. The actuators have been placed diametrically opposed on the alumina substrate which has a circular shape with a 25-mm diameter. With the proposed configuration the acoustic-wave actuation can be tested by placing fluid samples on the substrate between the actuators, where acoustic wave-fronts parallel to the IDT fingers are expected.

3 Experimental Results

The actuators have been experimentally characterized in order to extract the frequencies where the maximum actuation effectiveness is expected. Figure 2 shows the admittance measured from the IDTs, in which resonances around frequencies of about 6.7, 8.2 and 12 MHz have been obtained, that are expected to correspond to the propagation of FPW modes in the substrate.

Figure 3 shows the tailored electronic interface developed to drive the IDTs of the actuators. The excitation signals are generated by a programmable DDS (DirectDigital Synthesizer AD9959) that allows to excite the actuators with two independent channels and with the possibility to set both the common excitation frequency and the phase difference between the channels. The output stage has been realized using dedicated amplifiers (ADA4870) to properly drive the impedance of the actuators. The electronic interface allows to excite the actuators with a signal with amplitude and frequency of up to 20 Vpp and 15 MHz, respectively.

Preliminary tests have been carried out to verify the ability of the generated acoustic waves to manipulate fluid drops and particles. The device has been placed under a microscope and a water drop with dispersed light-reflective microspheres has been placed between the actuators to acquire the generated fluid and particle motion, as shown in Fig. 4a. The comparison between Fig. 4b and Fig. 4c shows
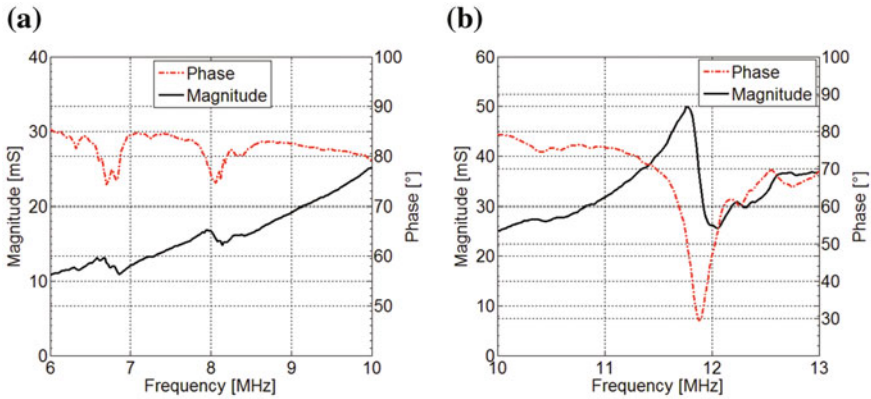
Fig. 2 Measured admittance (magnitude and phase) as a function of frequency. Resonances at 6.7 and 8.2 MHz (**a**); resonance at 12 MHz (**b**)
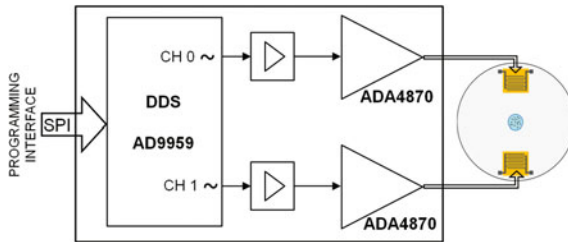
Fig. 3 Block diagram of the tailored electronic interface

that a circular vortex rotation has been obtained in the drop by exciting a single actuator with a sinusoidal signal at a frequency of 12 MHz. By exciting both the actuators at a frequency of 8.2 MHz a particle accumulation along a circular line has been obtained, as shown in Fig. 4d.

4   Conclusions

The use of PZT actuators to generate acoustic waves in non-piezoelectric substrates has been proposed for fluid and particle manipulation in microfluidic devices. A test device with two PZT actuators fabricated by screen printing technique and used to generate acoustic waves on an alumina substrate has been realized. A tailored electronic driving circuit has been developed to generate the excitation signals for
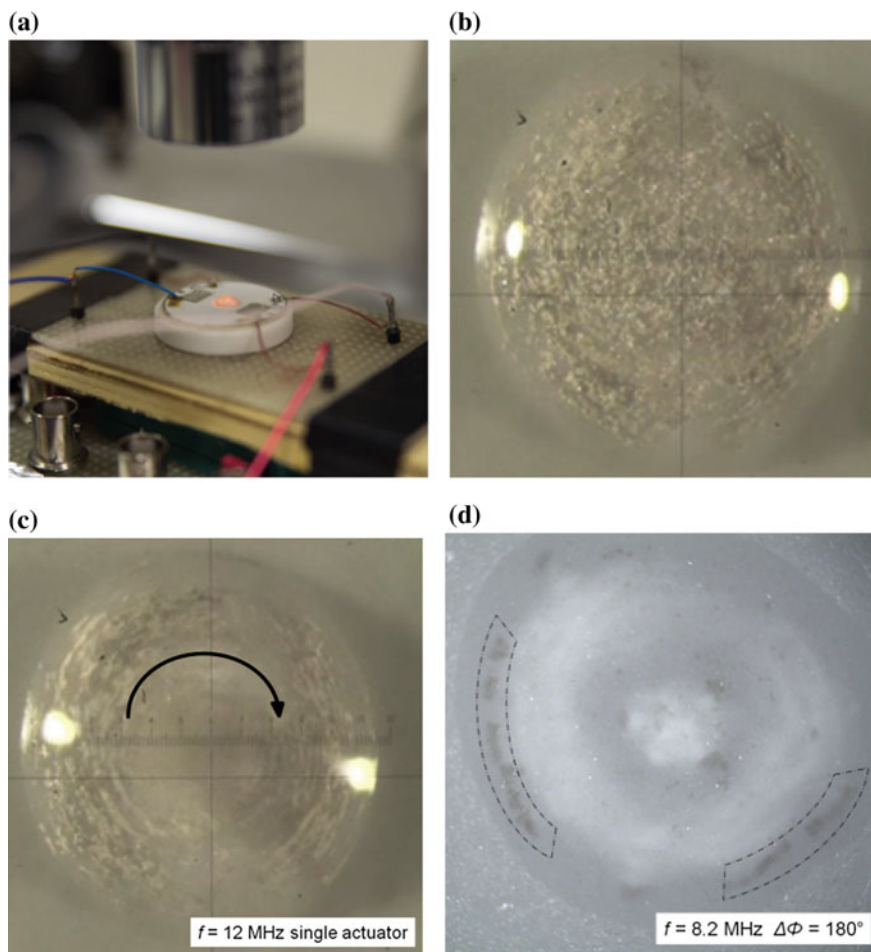
Fig. 4 Experimental setup showing the device placed under the microscope (**a**); Pictures of a water drop with dispersed light-reflective particles with a 25-μm diameter: no actuation (**b**); Vortex rotation caused by the acoustic waves generated by exciting one single IDT at 12 MHz (**c**); Particle accumulation on circular line caused by the acoustic waves generated by exciting both the IDTs at 8.2 MHz with a phase difference of 180° (**d**)

the actuators. Experimental results demonstrate that, by exciting the actuators at their resonance frequencies, FPW modes are generated in the substrate. In fact, either vortex rotation of a water drop and accumulation of micrometric particles dispersed in a drop on circular lines can be obtained by changing the excitation frequency of the IDTs and exciting a single or both the actuators. These results demonstrate the ability of the proposed PZT actuators to generate acoustic waves for applications in microfluidic devices as fluid mixing and controlled positioning of particles dispersed in liquid.

References

1. Ferrari, V., Lucklum, R.: Overview of acoustic-wave microsensors. In: Vives, A.A. (ed.) Piezoelectric Transducers and Applications, 2nd edn., pp. 39–62, Springer, Berlin (2008)
2. Shilton, R., Tan, M.K., Yeo, L.Y., Friend, J.R.: Particle concentration and mixing in microdrops driven by focused surface acoustic waves. J. Appl. Phys. **104,** 014910 (2008)
3. Ding, X., Lin, S.S., Kiraly, B., Yue, H., Li, S., Chiang, I., Shi, J., Benkovic, S.J., Huang, T.J.: On-chip manipulation of single microparticles, cells, and organisms using surface acoustic waves. PNAS **109**, 11105–11109 (2012)
4. Orloff, N.D., Dennis, J.R., Cecchini, M., Schonbrun, E., Rocas, E., Wang, Y., Novotny, D., Simmonds, R.W., Moreland, J., Takeuchi, I., Booth, J.C.: Manipulating particle trajectories with phase-control in surface acoustic wave microfluidics. Biomicrofluidics **5,** 044107 (2011)
5. Ai, Y., Sanders, C.K., Marrone, B.L.: Separation of Escherichia coli bacteria from peripheral blood mononuclear cells using standing surface acoustic waves. Anal. Chem. **85**, 9126–9134 (2013)
6. Guo, F., Mao, Z., Chen, Y., Xie, Z., Lata, J.P., Li, P., Ren, L., Liu, J., Yang, J., Dao, M., Suresh, S., Huang, T.J.: Three-dimensional manipulation of single cells using surface acoustic waves. PNAS **113**, 1522–1527 (2016)

Theoretical and Experimental Analysis of Residual Stress Mitigation in Piezoresistive Silicon Nitride Cantilever

M. Kandpal, A. Adami, F. Giacomozzi, M. Zen, V. Ramgopal Rao and L. Lorenzelli

Abstract In this work, we reports the design and technology optimization with residual stress balancing of piezo resistive silicon nitride micro cantilever stress sensors, which can be used for surface stress measurements in the liquid medium. In this context, the residual stresses of the thin films in a 600 nm thick cantilever stack (Si_3N_4/Poly Si/Si_3N_4/Au) were evaluated by curvature measurement on a test wafer to refine the balancing of the structure. In particular, the thickness of bottom silicon nitride was optimized to 300 nm to achieve the best trade-off between stress compensation and sensitivity. The cantilever bending curvature angle was calculated to be 45° and 19° with and without Au, as a top immobilization layer for the micro cantilever device. Further, finite element analysis results shows that for the low length/width ratio of cantilever, the stress sensitivity was better as compared to high aspect ratio.

Keywords Residual stress · Silicon nitride thin films · Micro cantilever Bio sensors

1 Introduction

Micro cantilever-based sensors [1–3] can be the ideal choice for development of miniaturized bio sensor systems because of their small size, low level of detection, faster analysis and use of small sample quantity. The biggest advantage of micro cantilever based sensors over the traditional biosensors such as surface plasmon resonance and quartz crystal microbalance is their label free detection and high sensitivity with small size [4–6]. The micro cantilevers with piezoresistive readout system, which transduces the mechanical deflection into electrical signal, are quite

M. Kandpal · A. Adami (✉) · F. Giacomozzi · M. Zen · L. Lorenzelli
Centre for Materials and Microsystem, Fondazione Bruno Kessler, 38123 Trento, Italy
e-mail: andadami@fbk.eu

M. Kandpal · V.R. Rao
Department of Electrical Engineering, IIT Bombay, Mumbai 400076, India

attractive due to simple readout and full integration of the device, in particular for bio sensing applications, were the operation in liquid medium, sensitivity and development of low cost materials for realisation of devices are the major challenges. Today, with the well standardised silicon micro fabrication technology, it is possible to realise very low cost micro cantilever devices by using conventional thin film silicon nitride as structural materials [7]. However, the biggest challenges for realization of micro cantilever by using silicon nitride as structural material is the control of inbuilt residual stress in layers, which can wrap the released micro-cantilever structure. In this work we report an approach to mitigate the residual stress with two methodologies: first, we proposed a stress-compensated structure with optimised layers' thickness and secondly we have used a modified low stress silicon nitride films as structural material.

2 Result and Discussion

2.1 Theory and Model of Beam Properties

Figure 1 depicts the proposed configuration of composite multilayer silicon nitride micro cantilever rectangular beam. It consists of four layers: bottom silicon nitride, the piezoresistive p-type poly silicon layer, top silicon nitride passivation layer and the gold as immobilization layer and for wiring.

The micro cantilever curvature in the presence of residual inbuilt stress was calculated using the mathematical description for multilayered laminates in Eqs. (1) and (2). Equation (2) assumes an ideal circular deformed shape, which is representative of bending at beam tip.

$$\chi = \frac{1}{R} = \frac{\sum M}{\sum EI} = \frac{\frac{1}{2}\sum_i \sigma_i\left(h_i^2 - h_{i-1}^2\right)}{\frac{1}{3}\sum_i E_i\left(h_i^3 - h_{i-1}^3\right)} \ (\text{m}^{-1}) \tag{1}$$

$$\alpha = \frac{L}{R} \ (\text{rad}) \tag{2}$$

Fig. 1 Schematic cross section of silicon nitride cantilever
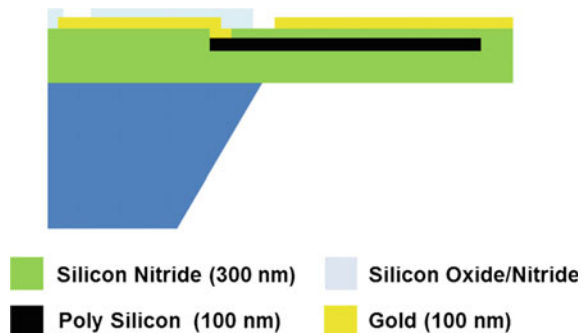
Where the M represents the equivalent bending moment of cantilever beam, E represents the Young's modulus and I is the moment of inertia, h_i the position with respect to center of beam section of i-th interface. As it could be seen from Eqs. (1) and (2), the curvature of multilayer cantilever depends linearly upon the moment and inversely proportional to effective stiffness of micro cantilever beam. Sensitivity, defined as bending versus surface stress of a thin sensitive layer, is inversely proportional to square of thickness and to E as can be inferred from (1). Clearly, the residual bending should be minimized by stress reduction or compensation rather than increased stiffness to avoid loss of sensitivity; nevertheless, a minimum thickness is required to improve robustness to residual unbalance or process spread of residual stresses. Another important point in design is the position of poly silicon piezoresistor in the stack with respect to the neutral axis in order to achieve the maximum bending detection sensitivity of poly silicon piezoresistor. A thicker bottom silicon nitride cantilever can provide the needed beam asymmetry, while top passivation thickness needs to be minimized. Sensitivity can be calculated with Eq. (3), where GF is the gauge factor $\Delta R/R/\Delta\varepsilon$.

$$\frac{\Delta R/R}{\sigma_{sup}} = \frac{\left(h_{sup} - h_{neutr.pl.}\right)\left(\bar{h}_{poly} - h_{neutr.pl.}\right)GF}{\frac{1}{3}\sum_i E_i\left(h_i^3 - h_{i-1}^3\right)} \tag{3}$$

2.2 Thin Film Stress Characterization and Implementation of Model

In order to estimate the residual stress of thin films for realization of silicon nitride cantilever, thin Si_xN_y, Poly-Si, Au films were deposited on 6″ Silicon wafers (Table 1). The test process also included the thermal treatment steps needed, in particular for polysilicon annealing and doping activation. The wafer curvature shift (1/R) was measured after each deposition step by using surface profilometer. The residual stress values of thin films were estimated with the Stoney's equation [8].

Table 1 Specification of thicknesses of cantilever layers and measured stress

S. No	Material	Thickness (nm)	Residual stress (Mpa)	Young's modulus (Gpa)
1	Si_3N_4 (bottom)	300	118	224
2	Poly-Si	100	224	160
3	Si_3N_4 (Top)	100	118	224
4	Au	100	250	79
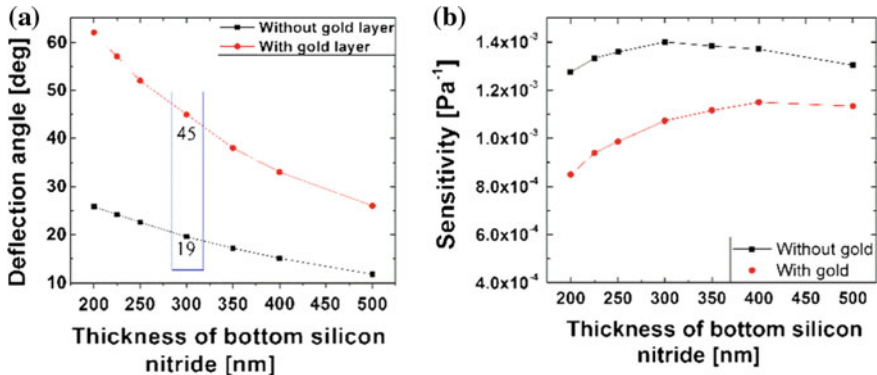
Fig. 2 **a** Cantilever curvature angle versus bottom silicon nitride thickness resulting from residual stress of layers **b** Sensitivity versus bottom silicon nitride thickness

Cantilever bending was estimated by using Eqs. (1)–(2) and Sci. lab code (Scilab Enterprises S.A.S 2015) using the film properties in Table 1. The results of analytical calculation are shown in Fig. 2a, b.

With the increasing thickness of Si_3N_4 the effective stiffness (EI) of micro cantilever increases and curvature decreases. For this reason, the sensitivity decreases at higher nitride thickness. In practical regime of micro fabrication, the optimum tradeoff thickness of bottom Si_3N_4 was evaluated to be 300 nm. A thin Au film of 100 nm, in consideration of its residual stress, increases the beam curvature from 19° to 45°. The analytical evaluation of sensitivity of micro cantilever devices, which primarily depends upon stiffness and the position of piezoresistor location in the stack, is shown in Fig. 2b. Optimum values were obtained at 300 nm thickness of bottom silicon nitride for silicon nitride cantilevers. This model clearly shows that use of modified non-stoichiometric low stress silicon nitride thin film and thicker bottom silicon nitride layer can minimize the cantilever bending by decreasing the moment and increasing the stiffness of micro cantilever beam.

2.3 Optimization of Polysilicon Resistors

To improve the performances, we chose a low temperature poly-Si deposition with p-type doping to improve the performances, based on results in literature [9]. The selected strategy was to use a high doping polysilicon, providing lower sensitivity but better temperature stability [10] and ohmic contact with a single doping step. Given the foreseen resistor geometry discussed in design section, reasonable resistor values and noise level can be better managed with a low resistivity polysilicon. The SIMS doping profile for optimized ion implantation dose is shown in Fig. 3a. The selected doping process parameters for 100 nm polysilicon thin films were: BF_2 implant, dose 3×10^{15} cm^2, implantation energy of 70 keV and
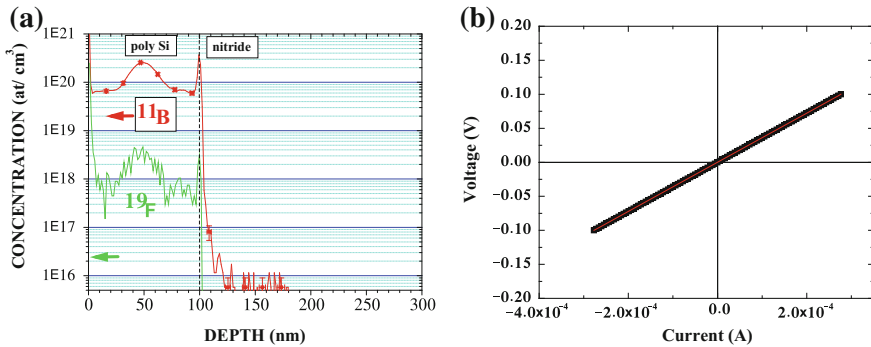
Fig. 3 SIMS profile for ion implanted and annealed poly-Si, 100 nm thick **b** V-I characteristic for fabricated resistor

annealing at 1000 °C for one hour. The peak concentration of doping was observed to be $\sim 10^{20}$ (atom/cm^3). Further, the contact resistance of polysilicon with gold was measured by depositing gold pads on the doped polysilicon. The results of I–V measurements are shown in Fig. 3b.

Figure 3 shows linear relation between the current and voltage in both positive and negative sweep direction of the voltages. It confirms that optimised does is sufficient for achieving the perfect ohmic contact between gold and p- polysilicon.

2.4 FEM Model and Design Optimization

In surface stress biosensing, the interaction with analyte produces a biaxial uniform surface stress on the sensor. Both longitudinal and transverse stress influences piezoresistor readings. In order to understand the role of the effect of geometrical aspect ratio of micro cantilever beam and piezoresistor on sensitivity, we implemented a finite element analysis. For these studies, cantilevers with dimension $250 \times 50 \ \mu m^2$ (Rectangular) and $50 \times 50 \ \mu m^2$ (Square plate) were chosen as test structures for analysis. Surface stress was modeled with a surface stress of 0.05 N/m, which was considered about mid-range of stress for typical surface interaction (e.g. DNA hybridization and self-assembly of alkanethiols on gold). This is equivalent to an applied moment of 0.87–4.3 μN μm depending on beam geometries considered. The obtained strain distribution results of x and y direction stresses for high and low aspect ratio cantilever are shown in Fig. 4.

The stress unbalance was more favorable in the anchor region, and the theoretical response was estimated to be $\Delta R/R \sim 5 \times 10^{-5}$ with cited conditions. The longer design does not have particular advantage in this configuration, since best sensitivity is achieved at anchor and longer beam results in both higher device bending due to internal stress and higher probability of device damage during operation.
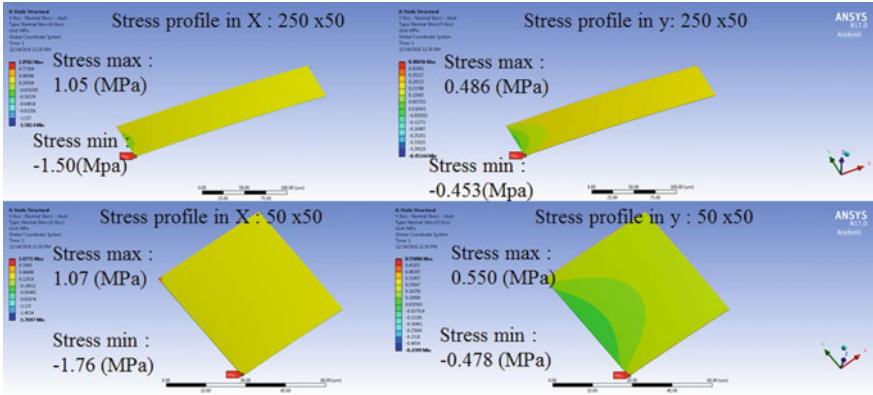
Fig. 4 Stress distribution profile in longitudinal and transverse direction along the length of micro cantilever beam with geometrical aspect ratio L/W = 1:5 & 1:1

3 Conclusions

In this paper, we proposed a silicon nitride based micro cantilever devices with piezo resistive readout system for liquid sensing applications. A numerical model was developed for predicting the cantilever bending due to presence of residual stress and used for the optimization of the cantilever stack. Analytical studies show that, by increasing the thickness of bottom Si_xN_y the residual curvature decreases, while sensitivity is reduced. However, we found there is an optimal bottom silicon nitride thickness of about ~ 300 nm where the efficiency of piezoresistor is maximized by a trade-off of offset of readout with respect to neutral bending plane and beam stiffness. FEM analysis studies shows that low L/W ratio cantilever with meander piezo resistive configuration are the best configuration for surface stress measurement with p-type poly-Si piezoresistors in terms of sensitivity, device yield and robustness to residual stress.

References

1. Boisen, A., et al.: Design & fabrication of cantilever array biosensors. Mater. Today, 32–38 (2009)
2. Datar, R., et al.: Cantilever sensors: nanomechanical tools for diagnostics. MRS bulletin, 449–454 (2009)
3. Etayash, H., et al.: Microfluidic cantilever detects bacteria and measures their susceptibility to antibiotics in small confined volumes. Nat. Commun. 12947 (2016)
4. Fritz, J., et al.: Translating bimolecular recognition into nanomechanics. Science, 316–318 (2000)
5. Arlett, J.L., et al.: Comparative advantages of mechanical biosensors. Nat. Nanotechnol. **6**, 203–215 (2011)
6. Wook, W.K., et al.: Novel electrical detection of label-free disease marker proteins using piezoresistive self-sensing micro-cantilevers. Biosens. Bioelectron. 1932–1938 (2005)
7. Rasmussen, P.A., et al.: Optimized cantilever biosensor with piezoresistive read-out, Ultramicroscopy, 371–376 (2003)
8. Stoney, G.: The Tension of Metallic Films Deposited by Electrolysis. Proc. R. Soc. London Ser. A, **82**,172–175 (1909)
9. French, P.J.: Polysilicon: a versatile material for microsystems. Sens. Actuators A, 3–12 (2002)
10. Kanda, Y.: Piezoresistance effect of silicon. Sens. Actuators A, 83–91 (1991)

Alcohols Traces Checked in River and Rain Water Using a DMFC-Enzymatic Device

Mauro Tomassetti, Riccardo Angeloni, Mauro Castrucci, Giovanni Visco, Maria Pia Sammartino and Luigi Campanella

Abstract Using direct methanol fuel cell (DMFC) with alcohol dehydrogenase enzyme inserted in the anodic site by mean of a small dialysis bag, alcohol (ethanol and methanol) traces have been determined in rain and river natural waters. These two latter different type of natural waters have been also well distinguished using PCA and by performing additional measurements of pH, temperature, and oxygen content.

Keywords Enzymatic DMFC · Alcohol content · Analysis · Rain and river Waters

1 Introduction

The ethanol enrichment of unlead gasoline, but also other fuels as diesel and biodiesel, is a process of considerable interest. In fact, although there are many arguments in favour of fuels ethanol enrichment, such as a purported reduction in air pollutant emissions during engine cars combustion, however one of the aspect of the ethanol enrichment, which is debated, is the potential impact that ethanol-enriched gasoline has on natural waters, (i.e. river-, rain-, ground-water), even for ethanol level of 10% in the gasoline (so called E10). In fact some studies, carried out in contaminated hydrocarbons sites of Brazil, shown that ethanol can enhance the solubilisation of BTX (i.e. Benzene, toluene, xylene hydrocarbons) in natural waters and it might exert diauxic effects, i.e. a preferential substrate utilization from bacterial, during BTX biodegradation [1]. Therefore, since their introduction one or two decades ago, oxygenated components of biofuels such as ethanol, has been mired in controversy.

M. Tomassetti (✉) · R. Angeloni · M. Castrucci · G. Visco · M.P. Sammartino · L. Campanella
Department of Chemistry, University of Rome "La Sapienza",
piazzale A. Moro 5, 00185 Rome, Italy
e-mail: mauro.tomassetti@uniroma1.it

To better clarify the above cited controversial aspects few authors have been conducted a series of experimental studies on the effect that, the presence of ethanol, produces in the natural bioremediation perspective for BTX in natural waters [1]. These studies are mainly of "modellistic type" [2], because in effects little or nothing it is reported in the literature on real ethanol concentrations in natural waters, also owing its rapid and large variability.

2   Results and Discussion

Since recently our research group has experienced the possibility to use, for analytical purposes, a small enzymatic direct catalytic fuel cell (DMFC) for methanol, or ethanol determination [3, 4] (see Fig. 1), obtaining good results, and performing numerous applications operating in real hydro-alcoholic matrices, that were more than satisfactory [4], we considered that maybe interesting to use this simple and inexpensive analytical device, both to determine the ethanol content in different samples of natural waters (in effects what was measured it is the sum of the ethanol and methanol eventually contained) and to verify if the method can be applied throughout the field of concentrations of ethanol content used in the modellistic works cited above [2, 5]. To this end we carried out a number of different ethanol standard additions (in the range used for modellistic researches) to rain and river water samples (that initially were totally devoid of traces of alcohols), by evaluating the values of recoveries obtained, with the standard addition method, using the enzymatic catalytic fuel cell.

In the Table 1 it was reported the results found in several samples of river and rain natural water to which has been applied the standard addition method. Results,

Fig. 1 Picture of the used DMFC enzymatic cell. (*a*) enzymatic bag
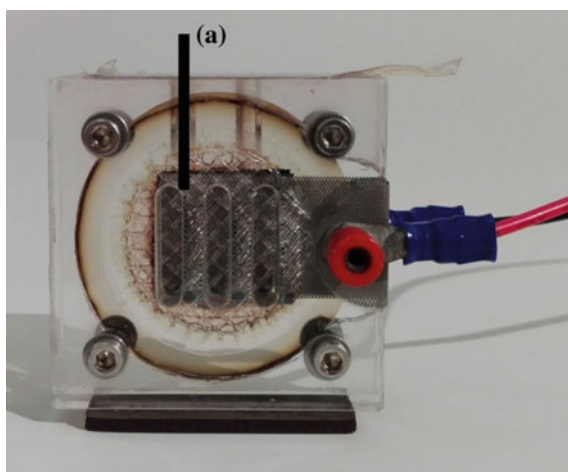
Table 1 Recovery test by standard addition methods applied to rain and river water samples which showed not contained any alcoholic traces, using enzymatic fuel cell

Rain or river water sample number	Total alcohol concentration (mg/L) found in the sample (n = 3) SD% ≤ 2.5	EtOH added value (mg/L)	Found value (mg/L) using fuel cell (n = 3) SD % ≤ 2.9	Recovery %
2 (rain)	0	10.3	11.7	114.4
2 (rain)	0	55.2	55.2	100.0
2 (rain)	0	197.3	168.4	85.4
6 (rain)	0	10.3	11.4	110.7
6 (rain)	0	55.2	47.3	85.7
6 (rain)	0	197.3	176.2	89.3
9 (river)	0	10.3	8.4	82.3
9 (river)	0	55.2	59.8	108.3
9 (river)	0	197.3	168.0	85.1
12 (river)	0	10.3	8.9	86.4
12 (river)	0	55.2	47.4	85.9
12 (river)	0	197.3	169.7	86.1

reported in the same Table 1, show as the method is sufficiently repeatable and in the first instance accurate.

In a second time we measured also other parameters on rain and river water samples (i.e. pH, the dissolved oxygen content and temperature), so that we was able to processing all data for this kind of samples by PCA method.

In the Table 2 values of pH, oxygen, temperature and alcohol content, found in several analyzes rain and river samples, are shown; lastly in Figs. 2 and 3 the scores and loadings representation, obtained by PCA application, have been displayed, obtaining two well distinguished clusters. Probably in one of which two subclusters can be also evidenced.

The application of the "mean eigenvalue criterion" showed that the only first eigenvector practically expressed all the variance (see Fig. 4).

3   Conclusions

An original method, which uses a enzymatic direct catalytic fuel cell for the analytical determination of methanol and ethanol pool in natural waters, i.e. rain and river waters, has been proposed and applied in the present research. Results of standard addition tests confirmed that the method can be applied to check the alcohol content in natural waters (in which the alcohol concentration was of the same order of that one used for modellistic studies reported in the literature) with

Table 2 All experimental values of four measured different parameters in all the analyzed natural water samples. Total alcohol values found using fuel cell

Rain or river water sample number	Total alcohol concentration found (mg/L) (n = 3) SD% $\leq$ 2.8	pH (pH units) (n = 3) SD% $\leq$ 2.3	Dissolved O_2 (p.p.m.) (n = 3) SD% $\leq$ 2.9	T (°C) (n = 3) SD% $\leq$ 1.7
1 (rain)	7.6	5.4	8.89	20.8
2 (rain)	0.0	5.6	8.38	21.3
3 (rain)	9.5	5.7	8.78	21.0
4 (rain)	7.2	5.6	8.65	21.2
5 (rain)	3.9	5.3	8.78	20.7
6 (rain)	0.0	5.4	8.81	20.9
7 (rain)	6.1	5.5	8.45	21.2
8 (rain)	5.3	5.5	8.53	21.1
9 (river)	0.0	7.6	8.5	19.2
10 (river)	3.7	7.5	8.4	19.3
11 (river)	5.2	8.3	8.7	19.3
12 (river)	0.0	7.8	6.5	19.2
13 (river)	3.6	7.7	6.0	19.4
14 (river)	3.0	7.6	7.6	19.5
15 (river)	0.0	7.8	7.9	19.3
16 (river)	0.0	7.9	8.1	19.2

Fig. 2 PCA representation (scores) along components 1 and 2, of rain and river water samples
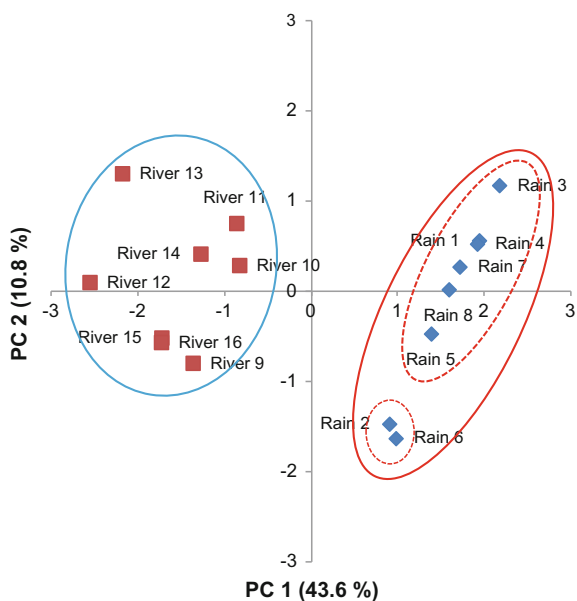
Fig. 3 Respective "loadings" of the PCA representation
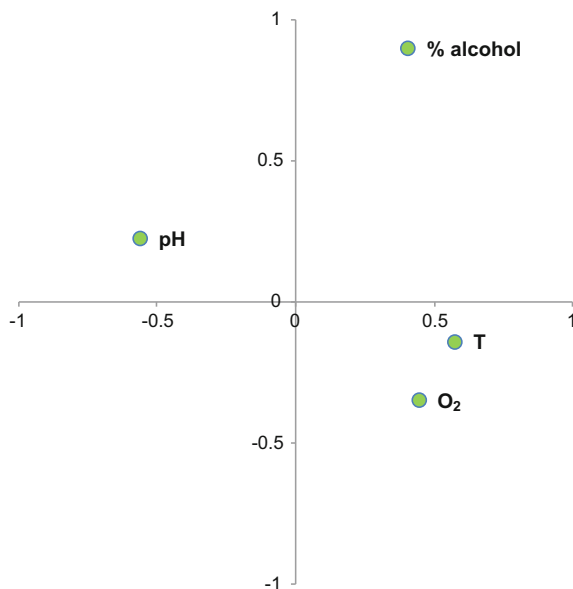
Fig. 4 Principal components versus eigenvalues representation
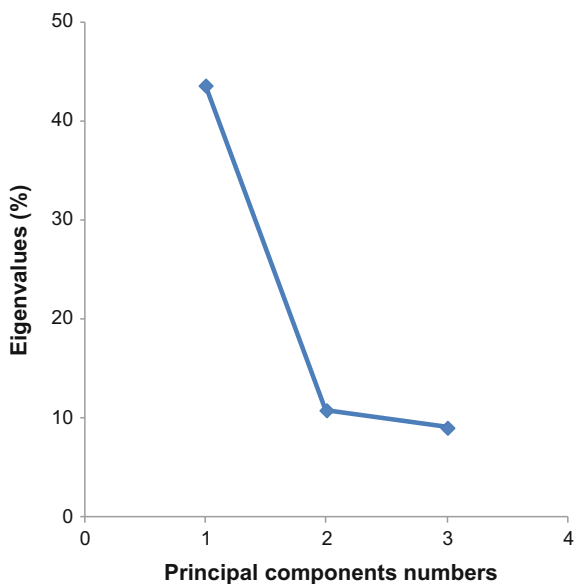
sufficient precision and accuracy. Lastly the application of the PCA to data obtained for alcohol content, pH, oxygen concentration and temperature, it was demonstrated to be able to separate all two types of analyzed natural waters (rain and river), in two well separated clusters, in a simple and suitable manner.

References

1. Niven, R.K.: Ethanol in gasoline: environmental impacts and sustainability review article. Renew. Sustainable Energy Rev. **9**(6), 535–555 (2005)
2. Zhang, Y., Khan, I.A., Chen, X., Spalding, R.F.: Transport and degradation of ethanol in groundwater. J. Contam. Hydrol. **82**(3-4), 183–194 (2006)
3. Tomassetti, M., Angeloni, R., Merola, G., Castrucci, M., Campanella, L.: Catalytic fuel cell used as an analytical tool for methanol and ethanol determination. Application to ethanol determination in alcoholic beverages. Electrochim. Acta **191**, 1001–1009 (2016)
4. Tomassetti, M., Merola, G., Angeloni, R., Marchiandi, S., Campanella, L.: Further development on DMFC device used for analytical purpose: real applications in the pharmaceutical field and possible in biological fluids. Anal. Bioanal. Chem. **408**(26), 7311–7319 (2016)
5. Chen, C.S., Shu, Y.Y., Wu, S.H., Tien, C.J.: Assessing soil and groundwater contamination from biofuel spills. Environ Sci Process Impacts **17**(3), 533–542 (2015)

Electronic Nose Detection of Hydraulic-Oil Fingerprint Contamination in Relevant Aircraft Maintenance Scenarios

M. Salvato, S. De Vito, M. Miglietta, E. Massera, E. Esposito, F. Formisano, G. Di Francia and G. Fattoruso

Abstract Modern aircraft structure, by making use of lightweight composite materials based on carbon fiber reinforced plastics (CFRP), succeeds in reducing CO_2 emissions and transport fuel costs. Nevertheless, its usage cannot leave Non Destructive Tests out to consideration in order to set up a quality assurance procedure of surfaces' contamination status. Here, we show and compare two different e-nose solutions able to detect and quantify hydraulic-oil fingerprint contamination at significantly low contamination levels occurring during aircraft maintenance operations.

Keywords Electronic nose · Aerospace industrial application
Maintenance scenarios · Non destructive test

1 Introduction

In the aerospace industry, the carbon fiber reinforced plastics (CFRP) usage, making weight-light the aircraft primary structures, guarantees a considerable improvement on engine efficiency leading to an important saving in terms of fuel costs (up to 20%), cost efficiency for ground operations (up to 50%) and CO_2 emissions (up to 15% on a per-mile-passenger basis) [1, 2]. Nevertheless, the lack of adequate quality assurance protocol based on Non Destructive Tests (NDT) could be prevent their usage. Indeed, CFRP panels are assembled through adhesive bonding instead of classical riveting. The bond strength is straightly linked with the cleaning state of the composite joints because of its influence on their mechanical properties weakening. Indeed, panel contamination status may produce

M. Salvato (✉) · S. De Vito · M. Miglietta · E. Massera · E. Esposito · F. Formisano ·
G. Di Francia · G. Fattoruso
DTE-FSN-DIN lab, ENEA—Italian National Agency for New Technologies Energy
and Sustainable Economic Development, C.R. Portici, P.Le E. Fermi, 1,
80055 Portici (NA), Italy
e-mail: Maria.Salvato@enea.it

a reduction in mode-I and -II fracture toughness, leading to interlaminar tension (G_{IC}) and sliding shear (G_{IIC}) [3], jeopardizing bonding reliability. So, an efficient NDT procedure has to able to detect and eventually estimate the CFRP panel contamination level occuring during assembly and maintenance operations. In this work, we mainly focus on the contamination affected by Fingerprint/Skydrol, a fire-resistant aviation hydraulic oil using during ordinary operative life operations on the aircraft structures. An efficient NDT assessment protocol e-nose based, enhanced by an ad hoc PARC system architecture, is already carried out during the just ended FP7-ENCOMB project [4, 5]. The ENCOMB experimental setting, characterized by laboratory environment and high panels contamination levels, allowed to put Technology Readiness Level (TRL) of that NDT procedure in the low-end (1–3) of its scale. In order to uplift and extend the TRL of such methodology, in the new European project (H2020-COMBONDT), the application scenarios has been adapted to be more similar to real aircraft maintenance conditions. Substantially, contamination concentration levels has been chosen so that they are significantly lower than previous ENCOMB ones. So, tools and methodologies are conveniently re-adapted at this aim. In this work, we propose two e-nose solutions, one commercial and other one made in ENEA, together with two different sampling methods. Data gathered from each of these different experimental settings are examined by means of principal component analysis allowing to select the setup (e-nose and sampling method) more sensitive to CFRP panel Fingerprint/Skydrol contamination. Analysis performed has shown that the sampling method based on a pre-chemical surface treatment, enhancing e-nose uptake capabilities, helps to mitigate some inherent e-nose limitations in Fingerprint/Skydrol detection. Indeed, both devices, taking advantage from this new sampling method, seems able to improve their hydraulic-oil fingerprint detection capabilities at least at the highest contamination level as well as regression capabilities in the estimation of contamination level. This work is so organized: Section 2 mainly concerns the description of experimental setting (maintenance contamination, e-nose technologies); the problem statement is introduced in the Sect. 3; Sect. 4 is devoted classification and regression results.

2 Experimental Framework

In this section, contamination conditions occurring in aircraft maintenance scenario together with needed tools to detect CFRP panel affected status are described. Generally, the repair operations, to be performed on aircraft structure to ensure airworthyness during the flight, are almost four and vary in scope, duration and frequency [6]. Here, we refer to heavy scheduled maintenance operations during which repairing actions have been carried first, removing outer damaged layers and locally scarfing them, and then substituting them with patches bonded on. In the pre-bond phase, NDT tests are needed to check the cleaning state of the involved surfaces and assuring a reliable and maximum bond strength.

2.1 Maintenance Contamination Setup

During the scheduled aircraft maintenance operations, several types of contaminations could be occurred on the CFRP panel surfaces compromising their cleaning state and so potential bonds' strength. In order to perform our NDT technology, testing samples have to reproduce almost exactly the potential contaminations occurring on the CFRP panels during real maintenance operations. Involved Panels' surface are composed by a Carbon Fiber Reinforced material, i.e. a thermoset matrix with carbon fibres arranged in unidirectional layers (HexPly© M21 matrix from Hexcel and T700 low density carbon fibers). The degradation process is conducted in a such way as to yield different contamination level, each of one causing a loss of bond strength of 30% of the previous one, starting to a no defective panel status (marked with RE). The reference status of a panel has been degraded by means of chemical or physical treatment. In the first case, panel surface has been compromised by a de-icer fluid or an aviation hydraulic-oil. In the latter case, surface damage has been caused by panel exposure to high temperatures so to generate thermal degradation of its structure. In both cases, three different damage levels have been considered by a project partner with specific expertise in this application field. The hydraulic oil contamination is artificially applied to the surfaces using a gloved plastic finger simulator previously dipped in a mixture composed by different concentrations of Skydrol®500-B, an aviation hydraulic fluid, and heptane. The three different contamination levels correspond respectively at 20, 50, 100% (no dilution) of Skydrol in heptane. Potassium formiate based runway de-icer fluid has been characterized by XRF as producing increasing percentage of potassium at surface in the ranges ([6.4 ($\pm$1.8); 10.9 ($\pm$2.3); 12.0 ($\pm$1.4)] at% K). Thermal degradation procedure provides for a heat treatment of panels, at three different temperatures (220 °C; 260 °C; 280 °C), for 2 h. Indeed, starting from 150 °C, as illustrated in Fig. 1, the bond strength decayed significantly.

Fig. 1 After high-temperature exposure, the residual bond strength properties of FRP systems decay significantly starting from 150 °C [7]

2.2 Electronic Noses Technologies

Two differently characterized electronic nose technologies were selected for the sampling campaign: a commercial platform and an ENEA prototype. The first one, Airsense Gas Detection Array (GDA-fr), is an hybrid sensors array featured of 4 metal oxide (MOX), 1 Photo-Ionization Detector (PID) sensor, an integrated Ion Mobility Spectrometer (IMS) sensor and 1 Electrochemical (EC) sensor. Moreover, the sensing platform provides for other 4 virtual instantaneous sensors corresponding to the areas under the curve of the left and right sections (with respect to the water response peak) of the positive and negative IMS spectra.

Several adaptations have been performed to customize the overall system to the specific task. The sampling architecture has been equipped of an Infra-Red (IR) emitter so to slightly increase the temperature of the contaminated CFRP panels. In this way, the volatile desorption is sped up resulting in increased uptake by the e-nose. The measurement methodology has been modified to resemble the sampling procedure of a typical lab based e-nose, characterized by a baseline acquisition phase, a sensor exposure phase (uptake and steady state phase) and a flushing/desorption phase (Fig. 2).

The second platform, named SNIFFI, is a customized ENEA e-nose prototype (Fig. 3). It is a multi-sensor gas analysis system based on a hybrid array of chemiresistors. Designed to work not only in lab controlled environment, SNIFFI returns a graphic visualization of the analyzed sample, starting from a matrix formed by differences among sensors responses. The design allows to analyze air sample either enclosed in a chamber or coming from flat and rigid surfaces. In the last case, an IR emitter can slightly heat the surface to improve the desorption of the Volatile Organic Compounds (VOCs) to be detected. The core of the system is represented by the sensor chamber that is equipped with a mix of commercial

Fig. 2 A typical GDA-2 response to Skydrol®500-B contaminated panel

sensors and unheated chemiresistors based on nanostructured semiconductors. Modularity of its hardware is designed to involve innovative technologies and/or new requirements.

The setting adopted in this context includes 6 metal-oxide (MOX) and 1 photo-ionization detector (PID), temperature and relative humidity sensors. Moreover, multi-sensor array contains also 6 custom conductometric graphene based. The measurement process begins with a baseline phase during which sensors have to stabilize their resistance in a reference environment composed by filtered air. In the following acquisition phase, data are fetched measuring the variation of sensor resistance when SNIFFI is exposed to the volatiles coming off the contaminated panel surface (Fig. 4).

In order to catch dynamic characteristics in the sensor array response, several features, differently typified for each device, are extracted. In Table 1, the description of the 40 features, computed on 8 GDA-2 signal sensors is reported.
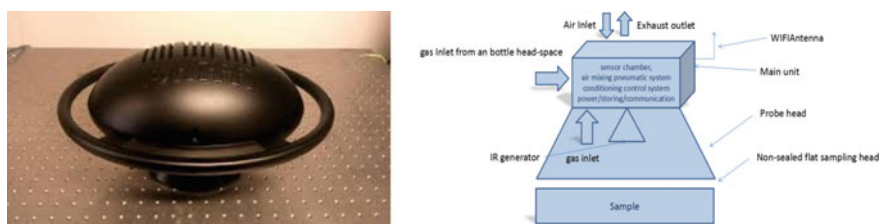
Fig. 3 Sniffi design (on the *left*) and block design of SNIFFI working system (on the *right*)

Fig. 4 MOX sensors response to Fingerprint/Skydrol at the highest available concentration
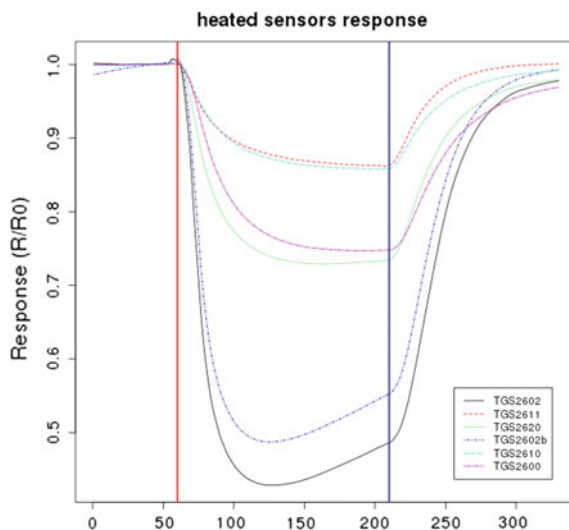
Table 1 Description of the GDA-2 features from 8 sensors

# Feature	Description
Feature 1 (×8)	Uptake phase derivative
Feature 2 (×8)	Steady state response derivative
Feature 3 (×8)	Desorption phase derivative
Feature 4 (×8)	Uptake phase average
Feature 5 (×8)	Steady state response average

Table 2 Description of the SNIFFI features extracted from MOX an PID sensors

# Feature	Description
Feature 1 (×7)	Steady state response (wrt avg baseline)
Feature 2 (×7)	Steady state response—IROff (wrt avg baseline)
Feature 3 (×7)	Desorption status (wrt avg baseline)
Feature 4 (×7)	Uptake derivative
Feature 5 (×7)	Desorption derivative
Feature 6	Temperature
Feature 7	Relative humidity

In Table 2, SNIFFI features, extracted taking in account of 6 MOX, 1 PID and temperature and relativity humidity sensors, are described.

3 Problem Statement

Our main issue concerns the detection on the CFRP panel of Fingerprint/Skydrol contamination and eventually the estimation of its concentration. So, we have in mind to address a 2-class pattern recognition problem into two different stages. Firstly, we aim to distinguish the Fingerprint/Skydrol contaminated class, independently from the concentration level, from the class of interferents. By interferents, we mean all others contaminants, including references samples, differing from Fingerprint/Skydrol contaminated samples. At the second level, we try to estimate the Fingerprint/Skydrol concentration level.

First of all, in this section we deal with the issue concerning the sampling method to be adopted. At this aim, separation capabilities of two different sampling methods are assessed taking advantage of principal component analysis on data fetched from each e-nose.

3.1 Sampling Methods

In the framework of e-nose sampling method, generally the standard "0-method" has been considered. It basically makes use of no additional treatment on the

Table 3 Total amount of data sampled by 0-Method

Data sampled by 0-Method		
	GDA-fr	SNIFFI
FP-1	0	0
FP-2	2	1
FP-3	6	6
ALL	17	18

FP refers to Skydrol contaminated samples at low (*1*), medium (*2*) and high (*3*) concentration level. *ALL* includes not Skydrol contaminated samples: untreated (Reference) plus intereferents (TD, DI) samples

sample. Easily, the CFRP sample is positioned close to the e-nose gas inlet, not more than 4 mm distance, while the extraction of volatiles compounds from the sample surface is aided by switching on the IR emitter. The lighting time is different depending on the employed e-noses. In the Table 3, we report the total amount of measurements sampled by this method. FP tag indicates the Skydrol fingerprint contamination; while -1, -2, -3 are respectively low, medium and high contamination level. Instead, ALL is the mark gathering all other interferents, such as thermal degradation, de-icer fluid contamination and reference samples.

In order to point out the robustness of this sampling method, Principal Component Analysis (PCA) has been performed on the acquired normalized data. This analysis helps in exploring data capabilities to disclose the surface contamination if it occurs. Indeed, according to this technique, multi-dimensional data are projected in a new orthogonal space whose dimensions, linearly correlated with initial ones, are ranked according to the increased amount of data signal variance. Formally, let be data matrix X and its variance-covariance matrix

$$X = \begin{pmatrix} X_1 \\ \vdots \\ X_p \end{pmatrix}, \quad Var(X) = \Sigma = \begin{pmatrix} \sigma_1^2 & \cdots & \sigma_{1p} \\ \vdots & \ddots & \vdots \\ \sigma_{p1} & \cdots & \sigma_p^2 \end{pmatrix}$$

and the following linear combinations:

$$Y_1 = e_{11}X_1 + \ldots + e_{1p}X_p$$
$$\vdots$$
$$Y_p = e_{p1}X_1 + \ldots + e_{pp}X_p$$

where $e_{i1}, \ldots, e_{ip}$ can viewed as regression coefficients. The *first principal component* is the linear combination of X_i-variables that explain maximum variance, specifically we will select $e_{11}, \ldots, e_{1p}$ that maximizes $Var(Y_1)$ subject to the constraint that $\sum_{j=1}^{p} e_{1j}^2 = 1$, required so that a unique solution may be obtained. In general, for i-th principal component, $e_{i1}, \ldots, e_{ip}$ are selected in a way to maximize

$$Var(Y_i) = \sum_{k=1}^{p} \sum_{l=1}^{p} e_{ik} e_{il} \sigma_{kl}$$

with the following constraints:

$$\sum_{j=1}^{p} e_{ij}^2 = 1 \quad \text{and} \quad cov(Y_1, Y_i) = cov(Y_2, Y_i) = \ldots = cov(Y_{i-1}, Y_i) = 0$$

The coordinates of the original data in the new orthogonal space are named "scores". Score plot allows to have easier data visualization than the original dataset. So, in the following figures, each 1-sigma ellipse has been built clustering scores related to each fixed contaminant at a given contamination level. By choosing two, among the first three principal components, the centers are computed as means of scores along these components, while major and minor semi-axes correspond to standard deviations (1-sigma) of these ones. Particularly, the 2-dimensional ellipses have drawn by means of following equations:

$$X = mean(A) + std(A) * \cos \ t$$
$$Y = mean(B) + std(B) * \sin \ t$$

being A and B, respectively, data scores along two of principal components, while "std" is the standard deviation and t is the parameter in $[0, 2\pi]$. Specifically, ALL-ellipse groups scores related to all contaminants i.e. (TD, DI and reference sample) differing from Skydrol/FingerPrint (FP) contaminated samples. So, ALL-ellipse is the cluster of interferents, while FP-ellipses gather the Skydrol/FingerPrint contaminations according to the different contamination level. As regards data sampled by 0-method, Fig. 5 clearly depicts the different e-noses
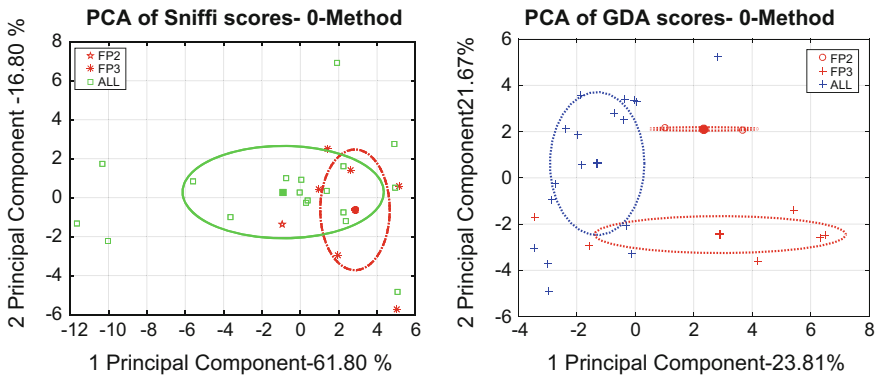

Fig. 5 PCA of scores related to Sniffi and GDA-2 response sampled by 0-method. FP cluster at each contamination levels (2–3) and all other interferents (ALL) cluster are highlighted

response. At the left, we can see as SNIFFI response does not allow for a sufficient 1-sigma level of separation between Skydrol contaminations and interferents cluster. The wide variance oscillation range in the interferent distribution makes it weakly distinguishable from FP distribution. Otherwise, GDA-fr response highlights good capability to discriminate both FP from all other contaminants as well as Skydrol contamination level.

Because of underlined weak SNIFFI capabilities to discriminate FP contamination when it is sampled by means of 0-method, further adaptations in the sampling system has been allowed to emphasize the contamination sensitivity of both devices. The new method foresees the use of a low-boiling solvent over the sample surface allowing to improve the desorption of the volatiles and differentiate the surfaces according to the capacities to retain and desorb the solvent. The wetting process is performed spraying few millilitres of ethanol with an airbrush over the surface of the sample. Because of chemical treatment, this sampling method is indicated as "PC-method" (where PC stands for "Probe Chemical"). The treatment time spanned on each CFRP sample must not last for more than 2 min. Contamination sampling sequence has been randomly executed but at every hour a test performed on a reference sample ensures that boundary conditions (process poisoning and/or environmental setting) are not changed. In the Table 4, the total amount of measurements executed by PC-method.

In Fig. 6, PCA analysis, performed on CFRP panels sampled by PC-method, underlines an overall improvement in the Skydrol/Fingerprint discrimination capability for both devices. In particular, SNIFFI response seems more sensitive at least to the highest concentration level Skydrol/Fingerprint contamination. Indeed, a consistent, more than 1-sigma, separation distance appears between FP-3 and the other contamination levels, like FP-2 and FP-1. These latter samples are however even hardly distinguishable among all others interferents. On the other hand, the already GDA e-nose good enough discrimination capabilities are enhanced by PC-method sampling. Each FP contaminated level is clearly distinguishable from each other by a consistent more 1-sigma level of separability.

So, PC-method shows an overall improvement of both e-nose capabilities to separate the Fingerprint/Skydrol clusters from interferent. Moreover, each Skydrol/Fingerprint concentration level is detected when GDA-fr is employed.

Table 4 Total amount of data sampled by PC-Method

Data sampled by PC-Method		
	GDA-fr	SNIFFI
FP-1	3	3
FP-2	4	3
FP-3	3	7
ALL	28	28

FP refers to Skydrol contaminated samples at low (*1*), medium (*2*) and high (*3*) concentration level. *ALL* includes not Skydrol contaminated samples: untreated (Reference) plus intereferents (TD, DI) samples
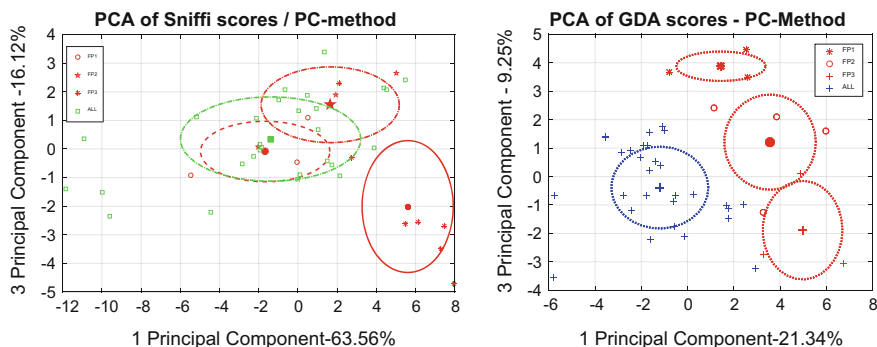
Fig. 6 Cluster of PCA scores related to Sniffi and GDA-2 response sampled by PC-method

Taking advantage of PC-method capabilities to enhance the surface contamination, an classification rate and the concentration level of Fingerprint/Skydrol contamination will be computed starting from data sampled by means of PC-method.

4 Results

This section is devoted to briefly illustrate and compare the first classification and regression results achieved on data sampled by PC-method for both devices. First of all, we explore e-noses capabilities to discriminate Fingerprint/Skydrol (FP) contaminated samples from all other types of contamination. At this aim, reference samples, thermal degraded samples and de-icer contaminated samples are labeled as interferents, constituting a single class named 0-class, while 1-class will contain FP contaminated samples at each contamination level. So, we are dealing with a binary and unbalanced classification problem, because of the highest number of interferent samples respect to FP contaminated ones. The classical machine algorithms provide for both device acceptable correct classification rate. Specifically, Sniffi data measurements are correctly classified, by a linear classifier, as Skydrol contaminated at 73.2% with an false negative rate equals to 31%, as it can be read in the confusion matrix (Fig. 7). The area under the ROC curve (AUC) is set to 0.74 underlying a good tradeoff between TP/FP.

Otherwise, a decision tree classifier provides a correct classification rate for GDA-fr enose equals to 97.4% with a false negative rate set only at 10%, and a AUC near to 1 (Fig. 8).

So, depending on the employed e-nose, different classification results are achieved. Nevertheless, they seem to be perfectly consistent with different separation capabilities highlighted in the previous PCA analysis leading to likewise different estimations in the contamination level. Specifically, regression results are computed taking advantage of a two layers feed forward neural network with ten hidden neurons, trained with Bayesian regularization backpropagation algorithm.
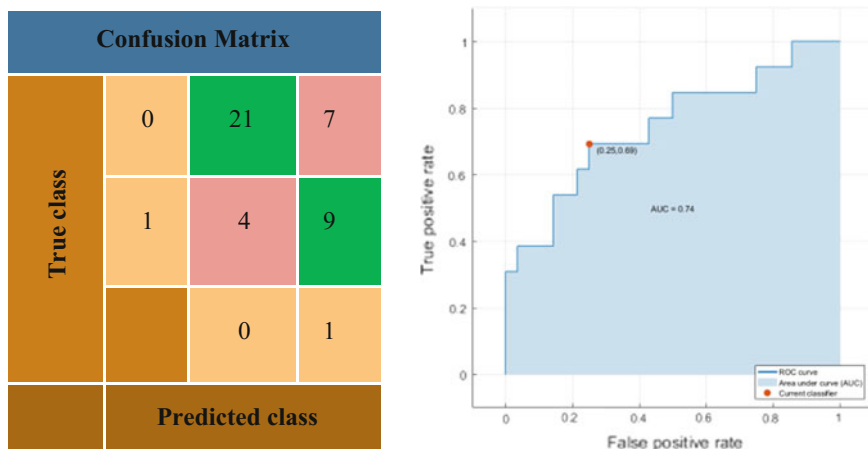
Fig. 7 Confusion matrix and ROC curve for linear discriminant
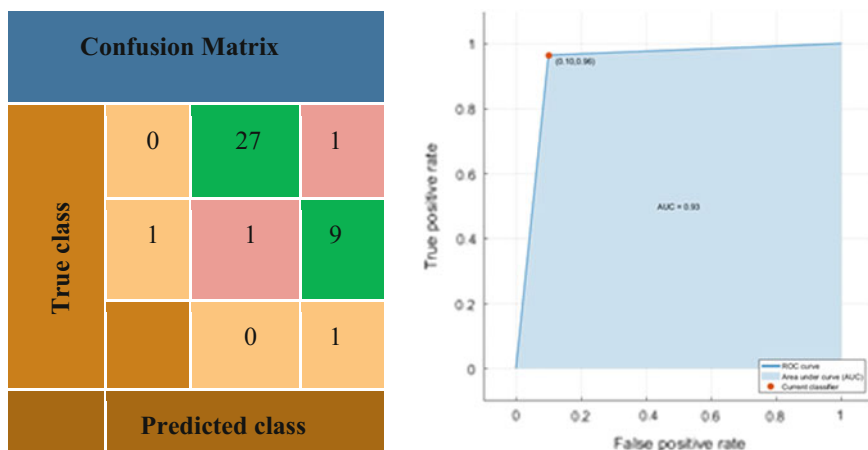
Fig. 8 Confusion matrix and ROC curve related to decision tree classifier

The three different Fingerprint/Skydrol concentration levels are labeled with '1', '2', '3' tag respectively for the low, medium and high contaminated class. Otherwise, label 0 is used to indicate the true concentration level of the interferents class. In Fig. 9 (left), boxplots relating to SNIFFI regression results underline a marked trend to under-estimate all three FP levels when their concentration levels are computed together with 0-level. The mean absolute error is setted to 0.72. Otherwise, regression results, after FP detection contamination, show an improvement on the FP-contamination level estimation mainly into the 2nd and 3rd level (Fig. 9-right).
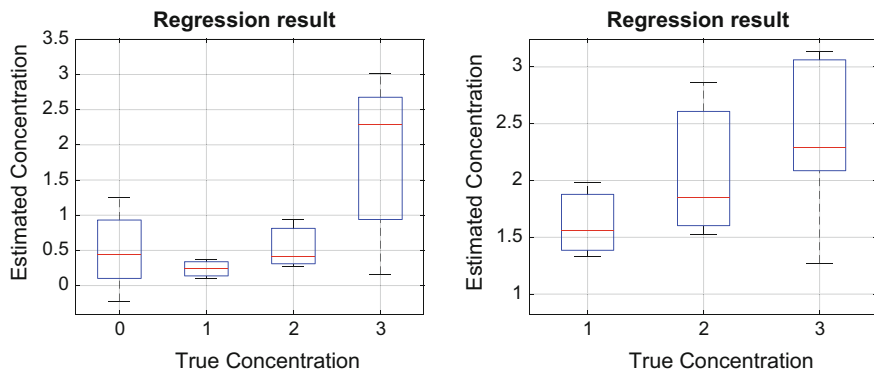
Fig. 9 Sniffi estimation boxplots of concentration level of interferents class (0) and FP classes (1-2-3) (on the *left*); on the right boxplots related to concentration levels of three FP contaminated classes

Fig. 10 GDA-2 estimation boxplots of concentration level of interferents class (0) and the three FP classes (1-2-3)
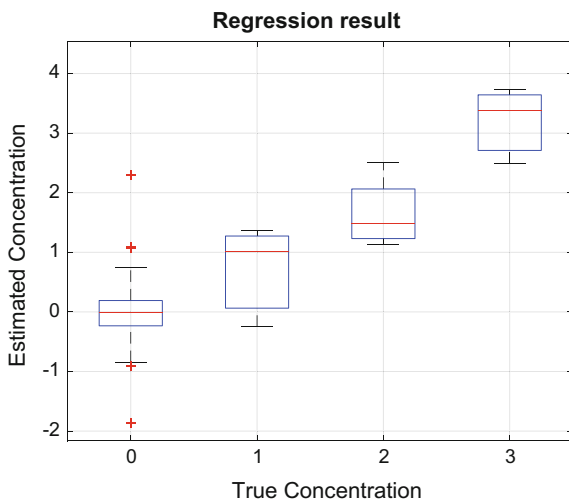
Different considerations can be done about GDA-2 regression results. As it can be seen in Fig. 10, this e-nose provides a good estimation of the interferents and FP-1 contamination level, being the respective medians exactly equals to the correspondent true concentration value.

Other FP concentrations levels (FP-2; FP-3), instead, are slightly under and over estimated respectively. Anyway, their variability range always includes the correspondent true concentration level. So, regression results confirm the PCA findings about GDA-fr sampled data that yet underlined as the FP-1 cluster and interferents cloud are clearly distinguishable from other FP contaminated samples. The others out estimated FP levels can be again explained in PCA terms: their ellipses being tangent (Fig. 6) gives rise to simple misunderstanding. Finally, the Mean Absolute

Error computed on GDA-fr regression results being equals to 0.37 confirms clearly the best performance of this device with respect to SNIFFI e-nose setting.

5   Conclusions

In order to uplift the TRL of NDT technologiesfor detection of Fingerprint/Skydrol oil contamination at low concentration levels, two different e-noses technologies (SNIFFI, ENEA e-nose and GDA-fr commercial solution) and two sampling method (0- and PC-Method) are explored. PC sampling method enhances contaminants cluster separation of both devices mitigating Sniffi limitations and allowing to detect and estimate Fingerprint/Skydrol oil at least at the highest COMBONDT concentration level. With the same methodology, the GDA-2 capabilities extends to the quantification of the level of contamination that is actually present on the samples.

References

1. Timmis, A.J., Hodzic, A., Koh, L., et al.: Environmental impact assessment of aviation emission reduction through the implementation of composite materials. Int. J. Life Cycle Assess. **20**, 233 (2015)
2. COMBONDT Project Website, http://combondt.eu. Accessed 9 May 2017
3. Markatos, et al.: Effects of manufacturing-induced and in-service related bonding quality reduction on mode-I fracture toughness of composite bonded joints for aeronautical use. Composites B, **45**, 556–564 (2013)
4. The ENCOMB Project Final Report Summary—http://cordis.europa.eu/result/rcn/156281_en.html. Accessed 9 May 2017
5. Salvato, M., et al.: An holistic approach to e-nose response patterns analysis—an application to non-destructive tests. IEEE Sens. J. **16**(8), 2617–2626, April 5 (2016). doi:10.1109/JSEN.2015.2513818
6. Van den Bergh, J., et al.: Aircraft maintenance operations: state of the art (2013)
7. Foster, S.K., Bisby, L.A.: Fire survivability of externally bonded FRP strengthening systems. J. Compos. Constr. **12**(5), 553–561 (2008)

Radar-Based Fall Detection Using Deep Machine Learning: System Configuration and Performance

Giovanni Diraco, Alessandro Leone and Pietro Siciliano

Abstract Automatic fall-detection systems, saving time for the arrival of medical assistance, have the potential to reduce the risk of adverse health consequences. Fall-detection technologies are under continuous improvements in terms of both acceptability and performance. Ultra-wideband radar sensing is an interesting technology able to provide rich information in a privacy-preserving way, and thus well acceptable by end-users. In this study, a radar sensor compound of two ultra-wideband monostatic units in two different configurations (i.e., vertical and horizontal baseline) has been investigated in order to provide sensor data from which robust features can be automatically extracted by using deep learning. The achieved results show the potential of the suggested sensor data representation and the superiority of the double-unit vertical-baseline configuration. Indeed, while the horizontal configuration allows to discriminate the body's position around the radar system, the vertical one discriminates the body's height that is more important for fall detection.

Keywords Fall detection · Ultra-wideband radar · Micro-Doppler
Deep learning · GPU computing

1 Introduction

Besides being the fastest growing sector, the population aged 65 and over suffers also the greatest number of falls causing emergency visits for trauma, hospitalizations and injury deaths. These trends contribute to position falls as a major public

G. Diraco (✉) · A. Leone · P. Siciliano
National Research Council of Italy, Institute for Microelectronics
and Microsystems, Lecce, Italy
e-mail: giovanni.diraco@le.imm.cnr.it

A. Leone
e-mail: alessandro.leone@le.imm.cnr.it

P. Siciliano
e-mail: pietro.siciliano@le.imm.cnr.it

257

health problem in developed countries. As some studies pointed out [1], the so called long-lie after a fall (more than one hour) increases risk of both hospitalization and death. Automatic fall-detection systems, saving time for the arrival of medical assistance, have the potential to reduce the risk of these adverse health consequences.

Existing solutions can be roughly categorized on the basis of the positioning modality of sensing elements. Roughly speaking, there are wearable solutions which require the user wears some device, and ambient ones which can be further categorized in contact and contactless. Contact solutions require the installation of sensing elements in proximity of surfaces involved in the fall impact, such as switch, pressure, and vibration sensors. Disappearing in the environment, they are generally well-accepted by users, but their performance depends on the number and careful positioning of sensors, which may require modification or redesign of the home environment. Regarding contactless solutions, they usually adopt sensors able to work remotely, mounted on wall or ceiling of a room. Among them, cameras are the most well-performing and extensively investigated, although they may raise significant privacy concerns. Moreover, hybrid wearable-ambient solutions also exist able to take advantages of each other [2]. Range sensing is a contactless modality based on the remote measurement of distances. Among various range sensors, acceptability and performance are quite good especially in the case of range camera and radar.

So far range camera has been extensively investigated by the authors for various human activity monitoring applications [3–5], whereas now their research is focused on investigating range sensing based on radars. Ultra-Wideband (UWB) radar sensing can exploit either Continuous Wave (CW) or Impulse Radio (IR) architectures, however the second one is particularly interesting since it leads to a single device whose capabilities include [6]: measurement of vital parameters, target detection and localization, through-wall imaging (high penetration power) and secure high-throughput wireless communication. Although poorly investigated for fall detection (UWB-CW Radar is almost universally adopted [7]), the aforesaid capabilities make the UWB-IR radar an interesting multi-purpose technology for unobtrusive in-home monitoring.

2   Materials and Methods

2.1   UWB-IR Radar Sensing

Radar systems can be categorized on the basis of their radio-wave bandwidth into: narrowband (NB) and UWB. The UWB is a radio technology using either pulse (IR) or CW of very short duration, and operating on frequency range wider than 500 MHz or 25% of the centre frequency. More specifically the UWB-IR, operating over a larger bandwidth and wider range of frequencies [6], provides additional features over UWB-CW, particularly useful in AAL (Active and Assisted Living)

contexts. The submillimetre range resolution and high penetration power enable the detection of very small target event through obstacles (e.g., through-wall sensing of vital signs). The shorter pulse duration, lower than the total travel time of the wave even in case of multiple reflections, is helpful to deal with multipath effects particularly insidious in indoor environments. The very low power spectral density prevents interferences with other radio systems operating in the same frequency range, and guarantees a low probability of interception; enabling secure high-data-rate communication in short range (e.g., up to 500 Mbps @ 3 m). The received UWB-IR radar signal can be represented as follows:

$$s(t) = \sum_{i=1}^{N} \alpha_i g(t - \tau_i) + n(t),$$ (1)

where α_i is the amplitude of the pulse reflected from the target (i.e., the human body as well as various structures present in the environment), τ_i is the time delay (or TOA—time of arrival) associated with the distance d_i of the target from the radar equal to $c\tau_i/2$ (with c being the speed of light), $n(t)$ is zero-mean white Gaussian noise, $g(t)$ is the normalised received pulse, and N is the number of pulses in each frame.

In order to remove signal components reflected by static structures (e.g., walls and pieces of furniture) and improve the signal-to-clutter ratio, 16th-order bandpass Butterworth and 4-tap motion filters were preliminary applied. In such a way, TOAs were mostly associated with movements of the monitored person. A radar system consisting of two monostatic radar units was investigated under both horizontally- and vertically-oriented baseline. In a double-unit system, given a generic plane on which the baseline is lying, henceforth named radius-baseline (r, b) plane, the target position can be estimated using bilateration. More specifically, the position of a generic point $C = [C_r, C_b]^T$ belonging to the baseline-radius plane can be estimated by jointly solving the following two equations:

$$d_i = d_i(C_r, C_b) = \sqrt{(C_r - U_{i,r})^2 + (C_b - U_{i,b})^2}, i = 1, 2,$$ (2)

where $U_1 = [U_{1,r} U_{1,b}]^T$ and $U_2 = [U_{2,r} U_{2,b}]^T$ are the positions of the two radar units, and d_1 and d_2 are the distances of C from U_1 and U_2, respectively. The double-unit geometry is illustrated in Fig. 1. The distances d_1 and d_2 can be modelled starting from the noisy measurements δ_1 and δ_2:

$$\delta = \begin{bmatrix} \delta_1 \\ \delta_2 \end{bmatrix} = \begin{bmatrix} d_1(C_r, C_b) \\ d_2(C_r, C_b) \end{bmatrix} + \begin{bmatrix} \eta_1 \\ \eta_2 \end{bmatrix} = D(C_r, C_b) + \eta,$$ (3)

where $\eta = [\eta_1 \eta_2]^T$ is the measurement noise which, under the assumption of TOA-based detection and LOS conditions, can be modelled as a zero mean Gaussian random variable whose probability density function is given as follows:
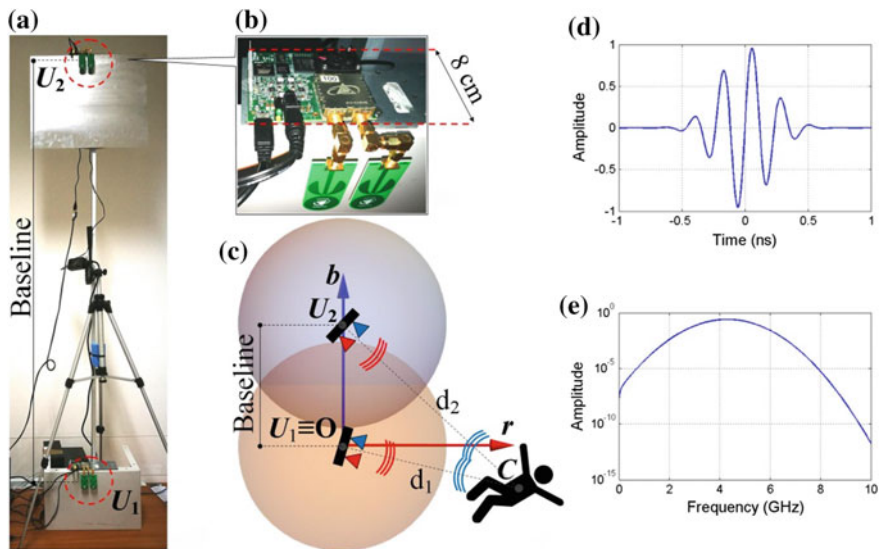
Fig. 1 Radar system setup and related geometry. **a** Two monostatic units, U_1 and U_2, in vertical baseline configuration. **b** Radar sensor unit P410. **c** System geometry with radar units disposed along the baseline b direction and target position C defined as intersection of two circles with radius d_1 and d_2. (**d**, **e**) Pulse waveforms in time and frequency domain

$$p_{\eta_i}(t) = \frac{1}{\sqrt{2\pi}\sigma_i} \exp\left(-\frac{t^2}{2\sigma_i^2}\right), \quad i = 1, 2. \tag{4}$$

Then, the unknown target position $C = [C_r, C_b]^T$ is estimated using the maximum likelihood estimator [8] as follows:

$$\widehat{C} = \arg\max_{C} p(\boldsymbol{\delta}|C) \tag{5}$$

where the conditional probability density function $p(\boldsymbol{\delta}|C)$ represents the likelihood function. Since the function $\boldsymbol{D}(C_r, C_b)$ in (3) is deterministic and the noise $\boldsymbol{\eta}$ is i.i.d., the likelihood function can be written as follows:

$$\begin{aligned}
p(\boldsymbol{\delta}|C) &= p_{\eta_1}(\delta_1 - d_1(C_r, C_b)|C)p_{\eta_2}(\delta_2 - d_2(C_r, C_b)|C) \\
&= \frac{1}{2\pi\sigma_1\sigma_2} \exp\left(-\frac{(\delta_1 - d_1(C_r, C_b))^2}{2\sigma_1^2} \frac{(\delta_2 - d_2(C_r, C_b))^2}{2\sigma_2^2}\right).
\end{aligned} \tag{6}$$

Consequently, thanks to Eq. (6) the target position in (5) can be estimated as follows:

$$\widehat{C} = \arg \min_{[C_r C_b]^T} \left(\frac{(\delta_1 - d_1(C_r, C_b))^2}{\sigma_1^2} + \frac{(\delta_2 - d_2(C_r, C_b))^2}{\sigma_2^2} \right) \qquad (7)$$

and solved by using the gradient descent algorithm [8]. The measurements δ_1 and δ_2 are obtained by matching the squares (energies) of the two radar signals s_1 and s_2, defined in (1), via convolution and cross-correlation operators. More precisely

$$\begin{aligned} \delta_1 &= \frac{c}{4} \left(\arg \max \left(s_1^2 * s_2^2 \right) + \arg \max \left(s_1^2 \star s_2^2 \right) \right), \\ \delta_2 &= \frac{c}{4} \left(\arg \max \left(s_1^2 * s_2^2 \right) - \arg \max \left(s_1^2 \star s_2^2 \right) \right), \end{aligned} \qquad (8)$$

where c is the speed of light, and the symbols $*$ and $\star$ represent the convolution and cross-correlation operators, respectively. For the sake of example, two radar scans are reported in Fig. 2a, b together with the measurements δ_1 and δ_2, and the related convolution and cross-correlation operators (Fig. 2c). The current target position C (estimated from the reported scans) and a set of previous positions are also shown in the same Fig. 2d.

Fig. 2 Estimation of target positions starting from radar scans. a, b Pair of radar scans with distances δ_1 and δ_2 from target to units $U_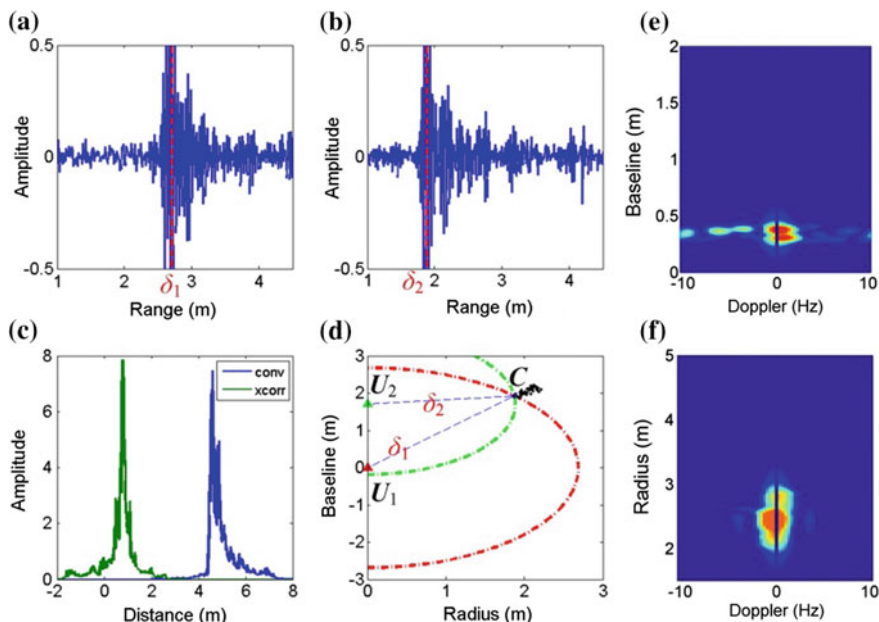1$ and U_2, respectively. c Convolution (conv) and cross-correlation (xcorr) obtained from radar scans. d Set of positions and the current one C estimated from δ_1 and δ_2. e, f micro-Doppler spectrograms along baseline and radius axes

Since the estimated positions are too coarse to be directly used for fall detection, therefore micro-Doppler signature along both radius and baseline directions are considered [9]. As well known, the relative motion between radar and target introduces a Doppler frequency shift which relates directly to the radial velocity: movements towards (or away from) the radar introduce a positive (or negative) frequency shift. Furthermore, a human target consists of different parts (e.g., head, torso, legs, etc.) which move at different velocities during the same action (e.g., walking, sitting, etc.). The multiple Doppler shifts produced by these smaller motions give rise to the micro-Doppler signature. In such a way, the micro-Doppler signature can be used to discriminate between fall and non-fall (i.e., related to various ADLs—Activities of Daily Living) actions. Each micro-Doppler signature is represented by the Doppler spectrogram associated with the last M target positions estimated by using Eq. (7).

Since a sampling rate of 45 Hz was used during experiments, M was taken equal to 18 in order to account for actions lasting about 400 ms, which is compatible with the duration of the critical-phase [10]. Finally, the Doppler spectrograms were computed by applying the short-time Fourier transform of length 64 to the analytic form of both radial and baseline components of (time-varying) target positions. The typical Doppler spectrograms related to a fall actions are illustrated in Fig. 2e, f. As can be seen, the micro-Doppler signature brings together information about both spatial distribution and velocity. More specifically, the radius spectrogram (Fig. 2f) takes into account position and velocity along radius direction of the falling person who was located at about 2.5 m far from the sensors. Instead, the baseline spectrogram (Fig. 2e) is referred to position and velocity along baseline direction. In this case (person who falls down), Doppler frequencies are mostly concentrated at about 0.4 m height from the floor plane and spread over almost all Doppler frequencies, since there are several body's parts moving along the baseline direction. At the end of the processing steps described up to now, the output is a sequence of image (spectrogram) pairs with resolution of 64 × 64 pixels.

2.2 Deep Feature Learning and Action Classification

Given a sequence of spectrogram images, as said in the previous subsection, a certain number of features are normally defined and extracted from each micro-Doppler signature and then applied to a classifier in order to discriminate actions as falls or not [9]. However, the feature definition and extraction is a daunting task requiring development and analysis of complex bio-mechanical models and consequent fine-tuning of several parameters, which nonetheless can show large variances depending on individual characteristics of the subject under monitoring. A viable alternative to such traditional feature design is represented nowadays by deep learning (DL) which straightforwardly leads to automated feature learning.

A deep learning network (DLN) learns features in a hierarchical way: high-level features are derived from low-level ones by using a layer-wise unsupervised pre-training, in such a way that structures of ever higher level are represented in higher layers of the network. After the pre-training phase, a supervised training provides a fine-tuning adjustment of the network via gradient descent optimization. Thanks to that greedy layer-wise unsupervised pre-training followed by supervised fine-tuning [11], features can be automatically extracted (learned) from large sets of unlabelled data and, vice versa, classified on the basis of small labelled datasets.

A general DLN with l layers $L_1, L_2, \ldots, L_l$ is represented in Fig. 3. L_1 and L_l are the input and output layers, and layers from L_2 to L_{l-1} are hidden layers with $n_2, \ldots, n_l$ hidden units, respectively. The network is determined by weights $\boldsymbol{W}^{(i)} \in \mathbb{R}^{n_{i+1},n_i}$, biases $\boldsymbol{b}^{(i)} \in \mathbb{R}^{n_{i+1}}$ and activation state vectors $\boldsymbol{a}^{(i)} \in \mathbb{R}^{n_i}$ for each layer L_i $(i = 1, \ldots, l-1)$, whereas $\boldsymbol{a}^{(1)}$ and $\boldsymbol{a}^{(l)}$ are the input and output vectors, respectively. Thus, given the input vector $\boldsymbol{x} \in \mathbb{R}^N$ the network iteratively computes the forward propagation $h_{\boldsymbol{W},\boldsymbol{b}}(\boldsymbol{x})$ defined as follows:

$$
\begin{aligned}
h_{\boldsymbol{W},\boldsymbol{b}}(\boldsymbol{x}) &= \boldsymbol{a}^{(l)}, \\
\boldsymbol{a}^{(i+1)} &= F\left(\boldsymbol{W}^{(i)}\boldsymbol{a}^{(i)} + \boldsymbol{b}^{(i)}\right) \text{ for } i = 1, \ldots, l-1,
\end{aligned}
\tag{9}
$$

where $F : \mathbb{R}^N \to \mathbb{R}$ is defined as $F(\boldsymbol{z}) = [f(z_1)f(z_2)\ldots f(z_n)]^T$ for $\boldsymbol{z} \in \mathbb{R}^N$, and $f : \mathbb{R} \to \mathbb{R}$ is the activation function, e.g., the sigmoid function or the hyperbolic tangent. More specifically, in this study a stacked auto-encoder (SAE) network was used, which essentially is an unsupervised learning algorithm that sets the outputs to be equal to the inputs. In other words, let $\{\boldsymbol{x}_1, \boldsymbol{x}_2, \ldots, \boldsymbol{x}_m\} \subset \mathbb{R}^N$ be a set of m unlabelled training examples (i.e., spectrogram images), the SAE network tries to learn, using backpropagation, a function $h_{\boldsymbol{W},\boldsymbol{b}}$ such that $h_{\boldsymbol{W},\boldsymbol{b}}(\boldsymbol{x}_i) = \boldsymbol{x}_i$ $(i = 1, \ldots, m)$.

Such task is accomplished by minimizing with respect to $\boldsymbol{W}$ and $\boldsymbol{b}$ the following cost function:

$$
\begin{aligned}
\mathrm{J_{SAN}}(\boldsymbol{W},\boldsymbol{b}) = {} & \frac{1}{2m}\sum_{i=1}^{m}\left\|h_{\boldsymbol{w},\boldsymbol{b}}(\boldsymbol{x}_i) - \boldsymbol{x}_i\right\|^2 + \frac{\lambda}{2}\sum_{k=1}^{l-1}\sum_{i=1}^{n_k}\sum_{j=1}^{n_{k+1}}\left(w_{ji}^{(k)}\right)^2 \\
& + \beta\sum_{k=2}^{l-1}\sum_{j=1}^{n_k}\mathrm{KL}\left(\rho||\hat{\rho}_j^{(k)}\right),
\end{aligned}
\tag{10}
$$

where $\hat{\rho}_j^{(k)} = \frac{1}{m}\sum_{i=1}^{m}a_j^{(k)}(\boldsymbol{x}_i)$ with $a_j^{(k)}(\boldsymbol{x}_i)$ denoting the activation of the corresponding unit (Fig. 3) when the input $\boldsymbol{x}_i$ is given to the network, ρ is a sparsity parameter typically near to zero (e.g., 0.05), and the term $\mathrm{KL}(\rho||\hat{\rho}) = \rho\log\frac{\rho}{\hat{\rho}} + (1-\rho)\log\frac{1-\rho}{1-\hat{\rho}}$ is the Kullback-Leibler (KL) divergence between two Bernoulli distributions with mean ρ and $\hat{\rho}$, respectively.
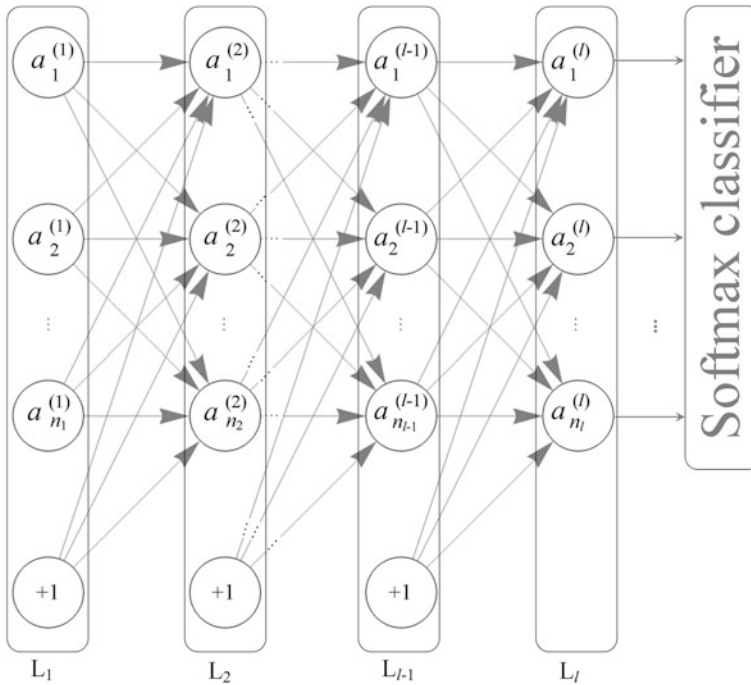
Fig. 3 General architecture of a DLN with l layers. Layers from L_2 to L_{l-1} are hidden, whereas L_1 and L_l are the input and output layers, respectively. A Softmax classifier is located downstream of the DLN

The unsupervised feature learning is followed by a supervised classification layer, namely the M-class softmax classifier defined as follows. Let $T = \{(\boldsymbol{x}_1, y_1), (\boldsymbol{x}_2, y_2), \ldots, (\boldsymbol{x}_n, y_n)\}$ be a training set with $\boldsymbol{x}_1, \boldsymbol{x}_2, \ldots, \boldsymbol{x}_n \in \mathbb{R}^N$ spectrogram images taken as examples and $y_1, y_2, \ldots, y_n \in \{A_1, \ldots, A_M\}$ be the corresponding labels indicating various actions, e.g., $A_1 = $ "*Fall*", $A_2 = $ "*Walking*", etc. The Softmax classification is done by minimizing the following cost function with respect to parameters $\boldsymbol{\theta} = [\boldsymbol{\theta}_1 \boldsymbol{\theta}_2 \ldots \boldsymbol{\theta}_M] \in \mathbb{R}^{N,M}$:

$$\mathrm{J_{SM}}(\boldsymbol{\theta}) = -\sum_{i=1}^{m}\sum_{j=1}^{M} \mathbf{1}\{y_i = A_j\} P\{y_i = A_j | \boldsymbol{x}_i; \boldsymbol{\theta}\} \tag{11}$$

where $\mathbf{1}\{\cdot\}$ is the indicator function ($\mathbf{1}(C) = 1$ if condition C is true, $\mathbf{1}(C) = 0$ otherwise), and the conditional probability $P\{y_i = A_j | \boldsymbol{x}_i; \boldsymbol{\theta}\} = \log\left(e^{\boldsymbol{\theta}_j^T \boldsymbol{x}_i} / \sum_{k=1}^{M} e^{\boldsymbol{\theta}_k^T \boldsymbol{x}_i}\right)$ should be large when $\boldsymbol{x}_i$ belongs to the class A_j and small otherwise.

2.3 Experimental Setup and Data Acquisition

The radar system investigated in this study consists of two PulsON P410 unit manufactured by Time Domain Corporation [12], as shown in Fig. 1a. P410 is a state-of-the-art UWB-IR Radar sensor, working from 3.1 to 5.3 GHz cantered at 4.3 GHz, covering a distance range of about 40 m (with submillimetre accuracy up to 6 m), having good penetration capabilities and compact ($7.6 \times 8.0 \times 1.6$ cm) board dimensions. Furthermore, P410 is an hybrid system that can operate in three modalities: (1) mono-/bi-static radar, (2) range radio, and (3) secure data communication system. Each P410 unit is equipped with an omnidirectional antenna, which in this study has been modified by adding a planar back reflector in order to reduce the azimuth pattern to around $100°$. The pulse generated by each P410 unit is a Gaussian modulated sinusoidal pulse $g(t) = \exp\left(-\frac{t^2}{2\sigma^2}\right)\sin(2\pi f_c t)$, where $f_c = 4.3$ GHz is the centre frequency and σ is about 0.2×10^{-9}. Time and frequency waveforms of the generated pulse are reported in Fig. 1d, e, respectively. The double-unit radar sensor system was experimented under the two different configurations, horizontal and vertical, with baseline length of 1.7 m and centre at 1.8 m above the floor plane.

Regarding the data collection, both fall and non-fall actions were performed in a home-like setting by involving 20 healthy subjects divided into two age groups of avg. 24 and 48 years old, respectively, having different physical characteristics and different ways of performing ADLs and fall actions. For each participant, a total amount of 486 actions were collected, of which 54 were simulated falls and the remaining were "normal" daily actions such as walking, sitting down, standing up, bending, etc. The data collection lasted about one week for each group, during which simulated falls (performed in various directions, such as backward, forward, lateral and vertical slipping, as suggested by Noury et al. [10]) were interspersed with some ADLs (e.g., walking, picking up objects from the floor, eating, watching TV, reading newspaper, resting on the sofa, doing physical activity). All fall events were performed using protective devices (e.g., padded mat and helmets) and after the approval of the local ethics committee. Furthermore, the two groups of participants were separately instructed on how falls should be simulated by a geriatrician and following hints from studies on real-life fall events [13, 14].

The actions performed by the two groups were used for training and testing the system. In order to evaluate the ability of the system to adapt to the user's characteristics, the training phase was specialized for each individual of the older group who acted as end-user (i.e., older adult). A training set was defined for each participant belonging to the older group as follows: $T_i = T_{F,Y} + T_{NF,Y} + T_{NF,O_i}$ ($i = 1, …, 10$), where $T_{F,Y}$ and $T_{NF,Y}$ included, respectively, all falls and non-falls performed by the young group, and T_{NF,O_i} included 70% of non-fall actions performed by the i-th participant belonging to the older group. The testing set included the remaining actions. In such a way, a total amount of $n = 7884$ events (of which 540 falls performed by the young group) were used for training and

1836 events (540 falls performed by the older group) for testing. The softmax classifier was designed to recognize $M = 3$ actions, namely Fall, Walking, Bending. The SAE network was compound of four hidden layers, and the spectrogram image pair (Fig. 2e, f) was the input to the first hidden layer, which was of 8192 units (i.e., two images of 64×64 pixels each). The second hidden layer was of 1024 units, corresponding to a compression factor of 8 times. The following two hidden layers were of 205 and 68 units, respectively, with compression factors of approximately 5 and 3 times. The training phase was performed on Intel i7 3.5 GHz workstation with 16GB DDR3 and equipped with GPU NVidia Titan X using the Theano toolkit [15], lasting about 158 min for each participant belonging to the older group. The testing phase run in real-time on the same computing system (but using CPU only), performing detections at about 30 Hz.

3   Results and Discussion

The detection performance is expressed in terms of sensitivity SN and specificity SP defined as follows:

$$SN = \frac{TP}{TP + FN}, \quad SP = \frac{TN}{TN + FP} \tag{12}$$

where TP is the numbers of True Positive, TN of True Negative, FP of False Positive, and FN of False Negative events. As it is evident from Table 1, in general the double-unit system performed better than the single-unit one, previously developed by the authors [16]. In particular, the best detection performance was achieved with the vertical baseline configuration. This is quite clear, since the body's movements occur mainly in the direction perpendicular to the floor plane during a fall event, and range measurements can be accurately accomplished via bilateration only along the baseline direction in a double-unit radar system.

Regarding the processing aspects, common detection methodologies are generally based on supervised techniques trained and tested with both positive (falls) and negative (non-falls) samples, both simulated by healthy young subjects. Consequently, fall detectors exhibit lower performance when used in real-world conditions, in which monitored subjects are older adults who obviously cannot simulate falls for algorithm training purposes. In this study, the problem of the lack of real-fall data for training has been addressed by suggesting a hybrid supervised-unsupervised methodology. Firstly, by using SAEs the feature space was

Table 1 Detection performance comparison

System configuration	Sensitivity (%)	Specificity (%)
Single-unit [16]	86	75
Double-unit with horizontal baseline	89	82
Double-unit with vertical baseline	97	93

automatically defined, in unsupervised fashion, starting from micro-Doppler sensor data. Secondly, the system was trained for fall detection by using fall and non-fall actions simulated by the young group and non-fall actions observed during ADLs performed by the older group who acted like monitored end-user, i.e., older adults, and so their fall samples were not used for training. In such a way, the suggested methodology allows the customization of the detection system with respect to the specific way the end-user performs non-fall (ADL-related) actions.

To the best of the authors' knowledge, the only study on radar fall detection using deep learning to date is [17], in which one monostatic CW radar for sensing the human motion was used. The best performance reported in [17] was of about 87% success rate (i.e. sensitivity), which is lower than both 89 and 97% sensitivity achieved by using the double-unit system presented here.

4   Conclusion

A novel radar-based fall detection solution has been presented and validated in the present study, by providing a threefold contribution covering sensing, processing and computing aspects. On sensing side, a double-unit UWB radar system able to unobtrusively detect events was suggested. On processing side, micro-Doppler spectrograms were used to obtain motion signatures along baseline and radius directions useful for detection of events in particular falls. On computing side, a deep feature learning approach was suggested, exploiting the potentiality of deep learning and GPU computing and allowing, at the same time, to address the problem of lack of fall real data for training. The overall detection system exhibited very good performance and capability to adapt to specific end-user's characteristics, allowing to suitably address the problem of lack of fall data in real-life contexts.

The ongoing and future work is focused on developing a radar sensor platform for monitoring both human activities and vital signs in assisted living scenarios.

References

1. Bloch, F.: Critical falls: why remaining on the ground after a fall can be dangerous, whatever the fall. J. Am. Geriatr. Soc. **60**, 1375–1376 (2012)
2. Siciliano, P., Leone, A., Diraco, G., Distante, C., Malfatti, M., Gonzo, L., Grassi, M., Lombardi, A., Rescio, G., Malcovati, P.: A networked multisensor system for ambient assisted living application. In: IWASI, IEEE, pp. 139–143 (2009)
3. Diraco, G., Leone, A., Siciliano, P.: In-home hierarchical posture classification with a time-of-flight 3D sensor. Gait & Posture **39**(1), 182–187 (2014)
4. Diraco, G., Leone, A., Siciliano, P.: People occupancy detection and profiling with 3D depth sensors for building energy management. Energy Build. **92**, 246–266 (2015)
5. Diraco, G., Leone, A., Siciliano, P., Grassi, M., Malcovati, P.: A multi-sensor system for fall detection in ambient assisted living contexts. In: SENSORNETS, pp. 213–219 (2012)

6. Nguyen, C., Han, J.: Time-Domain Ultra-Wideband Radar, Sensor and Components: Theory, Analysis and Design. Springer Science & Business Media (2014)
7. Amin, M.G., Zhang, Y.D., Ahmad, F., Ho, K.D.: Radar signal processing for elderly fall detection: the future for in-home monitoring. Sig. Proc. Mag. **33**(2), 71–80 (2016)
8. Sahinoglu, Z., Gezici, S., Guvenc, I.: Ultra-wideband positioning systems: theoretical limits. In: Ranging Algorithms, and Protocols. Cambridge University Press, Cambridge (2008)
9. Wu, Q., Zhang, Y., Tao, W., Amin, M.: Radar-based fall detection based on doppler time frequency signatures for assisted living. IET Radar Sonar Navig. **9**(2), 164–172 (2015)
10. Noury, N., Rumeau, P., Bourke, A., OLaighin, G., Lundy, J.: A proposal for the classification and evaluation of fall detectors. Irbm **29**(6), 340–349 (2008)
11. Erhan, D., Bengio, Y., Courville, A., Manzagol, P.A., Vincent, P., Bengio, S.: Why does unsupervised pre-training help deep learning? J. Mach. Learn. Res., 625–660 (2010)
12. TIME DOMAIN (2017, May 27), PulsON® P410 radar kit, [Online]. Available: http://www.timedomain.com
13. Vlaeyen, E., Deschodt, M., Debard, G., Dejaeger, E., Boonen, S., Goedemé, T., Vanrumste, B., Milisen, K.: Fall incidents unraveled: a series of 26 video-based real-life fall events in three frail older persons. BMC Geriatr. **13**, 103 (2013)
14. Robinovitch, S.N., Feldman, F., Yang, Y., Schonnop, R., Leung, P.M., Sarraf, T., Sims-Gould, J., Loughin, M.: Video capture of the circumstances of falls in elderly people residing in long-term care: an observational study. The Lancet **381**(9860), 47–54 (2013)
15. Bergstra, J., Breuleux, O., Bastien, F., Lamblin, P., Pascanu, R., Desjardins, G., Turian, J., Warde-Farley, D., Bengio, Y.: Theano: a CPU and GPU Math Expression Compiler. In: Proceedings of the Python for Scientific Computing Conference (2010)
16. Diraco, G., Leone, A., Siciliano, P.: Radar sensing technology for fall detection under near real-life conditions. In: Proceedings of TechAAL, London, UK, 5–6 (2016)
17. Jokanovic, B., Amin, M., Ahmad, F.: Radar fall motion detection using deep learning. In: RadarConf, IEEE, 1–6 (2016)

Evaluation of the Volatile Organic Compounds Released from Peripheral Blood Mononuclear Cells and THP1 Cells Under Normal and Proinflammatory Conditions

A. Forleo, S. Capone, V. Longo, F. Casino, A.V. Radogna, P. Siciliano, M. Massaro, E. Scoditti, N. Calabriso and MA. Carluccio

Abstract Leukemia is a group of cancers that usually begin in the bone marrow and result in high numbers of abnormal and dysfunctional white blood cells. Many studies were carried out to investigate metabolism of these cells. Metabolome analysis has been successfully applied to leukemia disease and emerged as a powerful tool for obtaining information about the biological processes that occur in organisms, and as a useful platform for discovering new clinical biomarkers and make diagnosis of disease using different biofluids. Whatever has not been investigated in leukemic cells is volatile metabolic signature that in recent literature is called "volatilome". Volatile organic compounds (VOCs) from the headspace of cultured THP1 cells and normal human peripheral blood mononuclear cells, were collected by headspace solid-phase microextraction (HS-SPME) and analyzed by gas chromatography combined with mass spectrometry (GC–MS), thus defining a volatile metabolomics signature. Styrene, cyclohexanol, cyclohexanone, 1-hexanol-2-ethyl, cyclohexane, 1,1'-(1,2-dimethyl-1,2-ethanediyl)bis-, benzene, 1,3-bis(1,1-dimethylethyl)- were present in higher amount in cultured THP1 cell than in PBMC, while 2-butanone has an opposite trend. Cell stimulation with lipopolysaccharide affected normal cells, but not leukemic cells. The establishment of the volatile fingerprint of THP1 cell lines presents a powerful approach to find endogenous VOCs that could be used to improve the diagnostic tools and explore the associated metabolomic pathways.

Keywords SPME-GC/MS · THP1 Cell lines · VOCs

A. Forleo (✉) · S. Capone · V. Longo · F. Casino · A.V. Radogna · P. Siciliano
Institute for Microelectronics and Microsystems, National Research
Council of Italy, Lecce, Italy
e-mail: Angiola.Forleo@le.imm.cnr.it

M. Massaro · E. Scoditti · N. Calabriso · MA.Carluccio
Institute of Clinical Physiology, National Research Council of Italy, Lecce, Italy

1 Introduction

Over the last few years, breath analysis has attracted a considerable amount of scientific interest as non-invasive technique for early recognition of human diseases by the identification of volatile organic compounds (VOCs) biomarkers in exhaled air [1]. Research in this field seems to give evidence that each pathology has a specific exhaled VOC fingerprint [2]. Leukemia is one of the most devastating cancerous diseases affecting the blood. Although VOC approach has already been applied successfully in the context of some solid cancer (such as for colon and lung cancers), technical difficulties still limit the widespread use of VOC analysis in the clinical setting of blood tumors.Methodological adaptation still needs to be done and breath analysis may benefit from in vitro studies on involved biochemical pathways, in order to correlate the exhaled VOCs with the VOCs released from leukemia cells [3].

The use of cell culture metabolomics enables both the discovery of novel biomarkers of pathological conditions and investigation of the related metabolomic pathways. Many of the metabolic processes in the body, such as lipid peroxidation, energy metabolism through glycolysis and amino acid catabolism are common to all living cells [4]. It is believed that some metabolic pathways might be up- or down-regulated in cancer cells and, therefore, metabolome analysis may reveal differences between biological samples based on metabolic profiles or fingerprints. With regard to normal cells, cancer cells show an altered metabolism that may lead to the production of specific compounds [10]. In the recent years, several studies have addressed the VOC analysis of cancerous cell lines to find potential new cancer biomarkers [5–8].

The aim of this work was to investigate the VOC fingerprint of human leukemia cell lines (THP1) and to evaluate potential VOC biomarkers for non-invasive diagnosis through VOCs analysis in the headspace of THP1 and peripheral blood mononuclear cells (PBMC).

Furthermore, since human monocytes are sensitive to LPS and respond by activating several pro-inflammatory transcriptional factors and expressing the related inflammatory cytokines and chemokines [9], we have also evaluated the LPS-stimulated VOC release in both THP1 cells and PBMC.

2 Materials and Methods

THP-1 cells were obtained from the American Tissue Culture Collection (Rockville, MD, USA) and maintained in RPMI 1640 medium supplemented with 2 mmol/l glutamine, 100 mg/ml streptomycin and 100 IU/ml penicillin, and 10% fetal bovine serum (FBS) in a 5% CO_2 humidified atmosphere at 37 °C.

To isolate human peripheral blood mononuclear cells (PBMC), venous blood obtained from healthy donors was anticoagulated with 0.15% EDTA, and

mononuclear cells were separated by density gradient centrifugation on sterile ready-to-use Ficoll-Paque Plus aqueous media (GE Healthcare, Piscataway, NJ, USA) following manufacturer's instructions.

PBMC and THP-1 were stimulated with 1 µg/mL of lipopolysaccharide (LPS) (Sigma Aldrich, St. Louis, MO, USA).

Cells are incubated for 24 h, and the VOC patterns produced in the cultures headspace were measured and compared with that obtained from other cell type. VOC analysis was performed also for cell-free culture medium.

For the identification of the volatile biomarkers, we applied the gas chromatography mass spectrometry with combination of solid phase micro-extraction (SPME) to the head space (HS) of cells cultures (Fig. 1).

In particular, the VOCs in the HS of the cell cultures and the control blank medium were collected directly from the culture flask using a manual Solid-phase microextraction SPME holder with black coated fiber (Supelco, Bellefonte, USA) after 24 h exposure (as is shown in Fig. 1). After this time the fiber was inserted immediately into Agilent 5973 mass spectrometer (MSD) coupled with 6890 N series gas chromatograph (Agilent Technologies) (Fig. 2) with ZB-624 capillary column with the injector temperature of 250 °C to allow thermally desorption of VOCs. The carrier gas helium flow rate was 1 ml/min. The oven temperature program was as follows: initial 40 °C held for 1 min; then ramped at 10 °C/min to 65 °C, then ramped at 3–120 °C, then ramped at 5–220 °C held for 5 min. The MS analyses were carried out in full-scan mode with a scan range 30–500 amu at 3.2 scans/s. Chromatograms were analyzed by Enhanced Data Analysis software and the identification of the volatile compounds was achieved by comparing mass spectra with those of the data system library (NIST 98, P > 80%). Volatile Organic Compound Cancer DataBase (VOCC; http://smagarwal.in/vocc/search.php) was used to data analysis.

Fig. 1 SPME exposure to headspace of cell culture
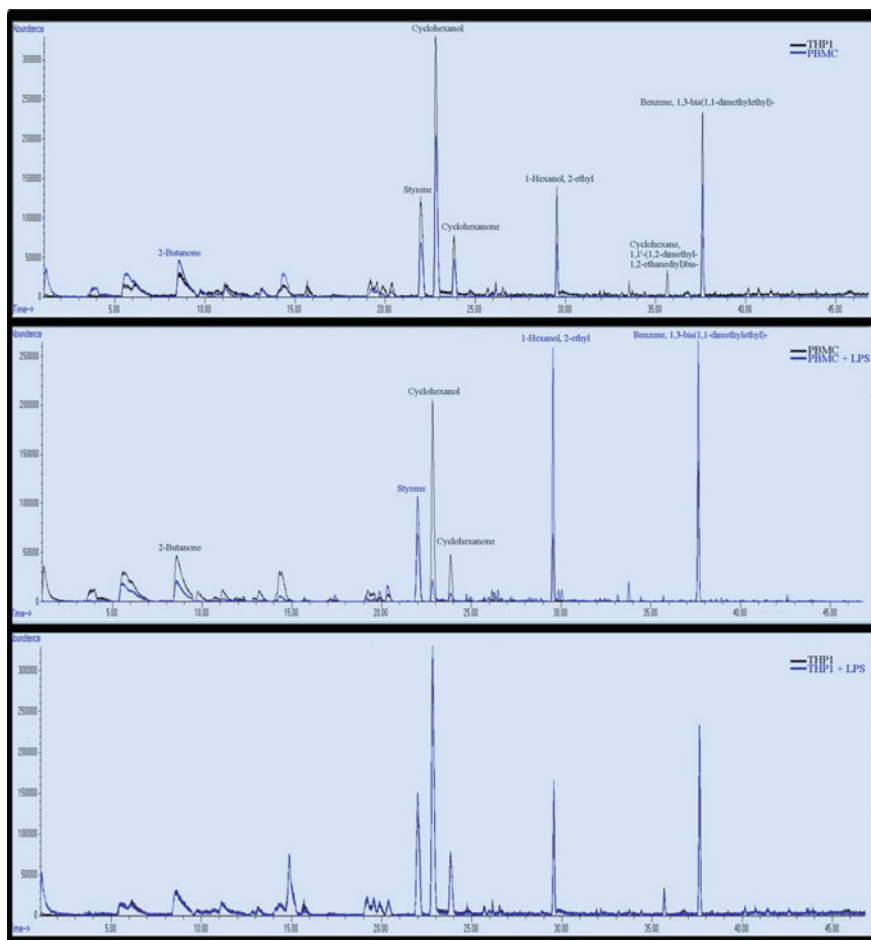
Fig. 2 Overlapping of chromatograms of the three analysis. Panel 1: PBMC versus THP1; panel 2: PBMC versus LPS-stimulated PBMC; panel 3: THP1 versus LPS-stimulated THP1

3 Results and Discussion

Although leukemia is among the cancers with the highest incidence and despite the interest in volatilome analysis has increased enormously in the recent years [10, 11], there are very few studies that analyze VOC pattern in leukemia disease.

Metabolomics applied to cell culture can help to better understand critical pathways of tumorigenesis and the volatinomic fingerprinting is of particular importance in this perspective.

In this paper, we have compared volatile organic compounds present in the headspace of PBMC and THP1 cells and, after that, we have studied changed VOC pattern after LPS-induced inflammation in both cell types.

In Fig. 2, the three chromatogram analysis are shown. The first panel of the figure shows, the VOCs comparative analysis between PBMC and THP1 cells under normal unstimulated conditions. The second one, shows the VOCs comparative analysis of PBMC in the presence or absence of LPS; finally in the last panel, we compared the VOCs production in THP1 cells as obtained in the presence or absence of LPS.

Peek area values are detailed in Table 1 and graphed in Fig. 3.

2-butanone is the only metabolite that are more present in PBMC respect THP1 (Fig. 2, panel 1). This ketone showed a significant decreased also in CALU-1 (Human Lung Cancer Cell Line) cells [12].

Six compounds (styrene, cyclohexanol, cyclohexanone, 1-hexanol-2-ethyl, cyclohexane, 1,1'-(1,2-dimethyl-1,2-ethanediyl)bis- and benzene, 1,3-bis (1,1-dimethylethyl)-) were found to be increased in the headspace of THP1 cells compared with normal mononuclear cells (Fig. 2, panel 1). Some of these VOCs were previously observed in the headspace of cultured cells, tissues and organic fluids.

One of principal chemical group identified was the alcohols, represented mainly by 2-ethyl-1-hexanol and cyclohexanol. These VOCs have already been reported in previous studies using cell lines and in urine from cancer patients [3, 10]. This alcoholic production was higher in THP1 cells than in normal cells and this might be due to the production of lipid peroxidation products as mediated by cytochrome P450 [3, 6]. Anomalous concentrations of 1-hexanol, 2-ethyl have been found in the headspace of lung cancer pleural effusion [13] in lung cancer cell line [14] as well as in breast cancer cell lines [15]. Similar results were also reported upon genetic mutations of lung cancer cells [16] and in lung cancer cells with genetic mutations in TP53 and KRAS [17].

Styrene is a recurrent compound in breath analysis which presence in the breath has been previously associated to lung [18] and ovarian [19] cancer.

Cyclohexanone is already known to be one of three novel diagnostic biomarkers of breast cancer. In particular three potential biomarkers, 2,5,6-trimethyloctane, 1,4-dimethoxy-2,3-butanediol, and cyclohexanone, resulted significantly more concentrated in the exhaled air of breast cancer patients than in the exhaled air from healthy individuals, mammary gland fibroma patients, or patients with cyclomastopathy [20].

Also 1,3-di-tert-butylbenzene has been previously detected in breath samples of breast and lung cancer patients [21–23]. Finally, 1,3-ditert-butylbenzene were relatively higher in JEKO cells (Non-Hodgkin's lymphoma cell line) [24].

Overall these data emphasize the potential role of VOCs as potential biomarkers of solid and liquid cancer and consequentially the importance of "volatilome analysis" as a poltential screening test.

Related to LPS-stimulated inflammation is important to note that, while in PBMC there is a reshaping of VOC pattern with some compounds (2-butanone,

Table 1 List of VOCs with respective peak areas in PBMC, LPS-stimulated PBMC, THP1, LPS-stimulated THP1

Name	CAS number	Entry number	Molecular formula	Molecular weight	Area			
					PBMC	LPS-stimulated PBMC	THP1	LPS-stimulated THP1
2-Butanone	000078-93-3	109956	C4H8O	72.06	14,235,424	5,049,057	9,811,301	10,133,832
Styrene	000100-42-5	118936	C8H8	104.06	7,715,160	12,487,949	14,493,547	17,438,174
Cyclohexanol	000108-93-0	17235	C6H12O	100.09	18,726,645	1,903,820	31,816,571	29,871,427
Cyclohexanone	000108-94-1	111410	C6H10O	98.07	4,438,395	663,576	8,328,858	6,589,300
1-Hexanol, 2-ethyl-	000104-76-7	15889	C8H18O	130.14	3,675,536	251,835	7,864,703	9,217,505
Cyclohexane, 1,1'-(1,2-dimethyl-1,2-ethanediyl)bis-	074663-71-1	22816	C16H30	222.24	0	14,048,133	1,814,812	1,436,425
Benzene, 1,3-bis (1,1-dimethylethyl)-	001014-60-4	125073	C14H22	190.17	7,572,933	5,049,057	12,176,321	12,191,142

Fig. 3 Comparison between peak areas of 7 examined VOCs in 4 cell types
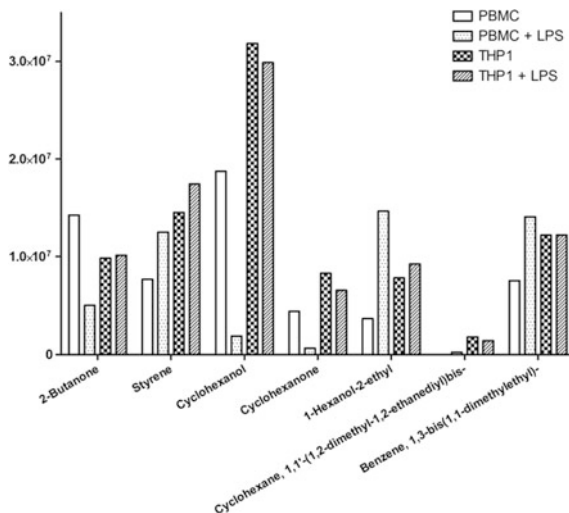
cyclohexanol and cyclohexanone) which were decreased and others metabolites (styrene, 1-hexanol-2-ehtyl, cyclohexane, 1,1'-(1,2-dimethyl-1,2-ethanediyl)bis- and benzene, 1,3-bis(1,1-dimethylethyl)-) which were increased (Fig. 2, panel 2), THP1 volatile metabolome remains unchanged (Fig. 2, panel 3).

This data is in agreement with already known different cytokine expression patterns following LPS-stimulation in PBMC and THP1 cells [25].

4 Conclusion

Although these results need to be integrated with the biochemical cell featuring, the VOCs here identified may represent a potential experimental evidence for the use of VOC markers in the characterization and monitoring of leukemic disease.

This study demonstrated that HS-SPME/GC-MS is a simple, rapid, sensitive and solvent-free method that can be used to establish the volatile metabolomic patterns of normal and leukemic cells.

References

1. Buszewski, B., Kesy, M., Ligor, T., Amann, A.: Human exhaled air analytics: biomarkers of diseases. Biomed Chromatogr. **21**(6), 553–566 (2007 Jun) Review
2. Pereira, J., Porto-Figueira, P., Cavaco, C., Taunk, K., Rapole, S., Dhakne, R., Nagarajaram, H., Câmara, J.S.: Breath analysis as a potential and non-invasive frontier in disease diagnosis: an overview. Metabolites. **5**(1), 3–55 (2015 Jan 9). doi:10.3390/metabo5010003. Review

3. Huang, Y., Li, Y., Luo, Z., Duan, Y.: Investigation of biomarkers for discriminating breast cancer cell lines from normal mammary cell lines based on VOCs analysis and metabolomics. RSC Adv. **6**, 41816–41824 (2016)

4. Suzuki, M., Nishiumi, S., Matsubara, A., Azuma, T., Yoshida, M.: Metabolome analysis for discovering biomarkers of gastroenterological cancer. J Chromatogr B Analyt Technol Biomed Life Sci. **966**, 59–69 (2014 Sep 1). doi:10.1016/j.jchromb.2014.02.042. Epub 2014 Mar 1. Review

5. Amal, H., Ding, L., Liu, B.B., Tisch, U., Xu, Z.Q., Shi, D.Y., Zhao, Y., Chen, J., Sun, R.X., Liu, H., Ye, S.L., Tang, Z.Y., Haick, H.: The scent fingerprint of hepatocarcinoma: in-vitro metastasis prediction with volatile organic compounds (VOCs). Int J Nanomedicine. **7**, 4135–4146 (2012). doi:10.2147/IJN.S32680

6. Hakim, M., Broza, Y.Y., Barash, O., Peled, N., Phillips, M., Amann, A., Haick, H.: Volatile organic compounds of lung cancer and possible biochemical pathways. Chem Rev. **112**(11), 5949–5966 (2012 Nov 14). doi:10.1021/cr300174a

7. Filipiak, W., Sponring, A., Mikoviny, T., Ager, C., Schubert, J., Miekisch, W., Amann, A., Troppmair, J.: Release of volatile organic compounds (VOCs) from the lung cancer cell line CALU-1 in vitro. Cancer Cell Int. **8**, 17 (2008 Nov 24). doi:10.1186/1475-2867-8-17

8. Hanai, Y., Shimono, K., Oka, H., Baba, Y., Yamazaki, K., Beauchamp, GK.: Analysis of volatile organic compounds released from human lung cancer cells and from the urine of tumor-bearing mice. Cancer Cell Int. **12**(1), 7 (2012 Feb 24). doi:10.1186/1475-2867-12-7

9. Guha M, Mackman N. LPS induction of gene expression in human monocytes. Cell Signal. **13**(2), 85–94 (2001 Feb) Review

10. Silva, C.L., Passos, M., Câmara, J.S.: Investigation of urinary volatile organic metabolites as potential cancer biomarkers by solid-phase microextraction in combination with gas chromatography-mass spectrometry. Br J Cancer. **105**(12) 1894–1904 (2011 Dec 6). doi:10.1038/bjc.2011.437

11. Tang, H., Lu, Y., Zhang, L., Wu, Z., Hou, X., Xia, H.: Determination of volatile organic compounds exhaled by cell lines derived from hematological malignancies. Biosci Rep. 2017 May 15. pii: BSR20170106. doi:10.1042/BSR20170106

12. Filipiak, W., Sponring, A., Mikoviny, T., Ager, C., Schubert, J., Miekisch, W., Amann, A., Troppmair, J.: Release of volatile organic compounds (VOCs) from the lung cancer cell line CALU-1 in vitro. Cancer Cell Int. **8**, 17 (2008 Nov 24). doi:10.1186/1475-2867-8-17

13. Liu, H., Li, C., Wang, H., Huang, Z., Zhang, P., Pan, Z., Wang, L.: Characterization of volatile organic metabolites in lung cancer pleural effusions by SPME–GC/MS combined with an untargeted metabolomic method. Chromatographia **77**, 1379 (2014). doi:10.1007/s10337-014-2720-y

14. Sponring, A., Filipiak, W., Mikoviny, T., Ager, C., Schubert, J., Miekisch, W., Amann, A., Troppmair, J.: Release of volatile organic compounds from the lung cancer cell line NCI-H2087 in vitro. Anticancer Res. **29**(1), 419–426 (2009 Jan)

15. Silva, C.L., Perestrelo, R., Silva, P., Tomás, H., Câmara, J.S.: Volatile metabolomics signature of human breast cancer cell lines. Sci Rep. **7**, 43969 (2017 Mar 3). doi:10.1038/srep43969

16. Peled, N., Barash, O., Tisch, U., Ionescu, R., Broza, Y.Y., Ilouze, M., Mattei, J., Bunn, P.A. Jr, Hirsch, F.R., Haick, H.: Volatile fingerprints of cancer specific genetic mutations. Nanomedicine. **9**(6), 758–766 (2013 Aug). doi:10.1016/j.nano.2013.01.008

17. Davies, M.P., Barash, O., Jeries, R., Peled, N., Ilouze, M., Hyde, R., Marcus, M.W., Field, J.K., Haick, H.: Unique volatolomic signatures of TP53 and KRAS in lung cells. Br J Cancer. **111**(6), 1213–1221 (2014 Sep 9). doi:10.1038/bjc.2014.411

18. Amann, A., Corradi, M., Mazzone, P., Mutti, A.: Lung cancer biomarkers in exhaled breath. Expert Rev. Mol. Diagn. 11, 207–217 (2011)

19. Amal, H., Shi, D.Y., Ionescu, R., Zhang, W., Hua, Q.L., Pan, Y.Y., Tao, L., Liu, H., Haick, H.: Assessment of ovarian cancer conditions from exhaled breath. Int J Cancer. **136**(6), E614–E622 (2015 Mar 15). doi:10.1002/ijc.29166

20. Wang, C., Sun, B., Guo, L., Wang, X., Ke, C., Liu, S., Zhao, W., Luo, S., Guo, Z., Zhang, Y., Xu, G., Li, E.: Volatile organic metabolites identify patients with breast cancer, cyclomastopathy, and mammary gland fibroma. Sci Rep. **4,** 5383 (2014 Jun 20). doi:10.1038/srep05383

21. Phillips, M., Cataneo, R.N., Ditkoff, B.A., Fisher, P., Greenberg, J., Gunawardena, R., Kwon, C.S., Rahbari-Oskoui, F., Wong, C.: Volatile markers of breast cancer in the breath. Breast J. **9**(3), 184–191 (2003 May-Jun)

22. Phillips, M., Cataneo, R.N., Ditkoff, B.A., Fisher, P., Greenberg, J., Gunawardena, R., Kwon, C.S., Tietje, O., Wong, C.: Prediction of breast cancer using volatile biomarkers in the breath. Breast Cancer Res Treat. **99**(1), 19–21 (2006 Sep)

23. Ulanowska, A., Kowalkowski, T., Trawińska, E., Buszewski, B.: The application of statistical methods using VOCs to identify patients with lung cancer. J Breath Res. **5**(4), 046008 (2011 Dec). doi:10.1088/1752-7155/5/4/046008

24. Tang, H., Lu, Y., Zhang, L., Wu, Z., Hou, X., Xia, H.: Determination of volatile organic compounds exhaled by cell lines derived from hematological malignancies. Biosci Rep. (2017 May 15). pii: BSR20170106. doi:10.1042/BSR20170106

25. Schildberger, A., Rossmanith, E., Eichhorn, T., Strassl, K., Weber, V.: Monocytes, peripheral blood mononuclear cells, and THP-1 cells exhibit different cytokine expression patterns following stimulation with lipopolysaccharide. Mediators Inflamm. **2013**, 697972 (2013). doi:10.1155/2013/697972

Au-Catalyst Assisted MOVPE Growth of CdTe Nanowires for Photovoltaic Applications

Virginia Di Carlo, Fabio Marzo, Massimo Di Giulio, Paola Prete and Nico Lovergine

Abstract Vertically-aligned CdTe nanowire (NWs) were grown for the first time by metalorganic vapor phase epitaxy, using diisopropyl-telluride and dimethyl-cadmium as precursors, and Au nanoparticles as metal catalysts. The NWs were grown between 485 and 515 °C on (111)B-GaAs substrates, the latter overgrown with a 2-μm thick CdTe epilayer. To favor the Au-catalyst assisted process against planar deposition of CdTe, an alternate precursors flow process was adopted during NW self-assembly. Field emission electron microscopy observations and X-ray energy dispersive analyses of CdTe NWs revealed the presence of Au-rich droplets at their tips, the contact-angle between Au-droplets and NWs being $\sim 130°$. The NW height increases exponentially with the growth temperature, indicating that the Au-catalyzed process is kinetics-limited (activation energy: ~ 57 kcal/mol), but no tapering is observed. Low temperature cathodoluminescence spectra recorded from single NWs evidenced a band-edge emission typical of zincblend CdTe, and a dominant (defects-related) emission band at 1.539 eV.

Keywords CdTe nanowires · Au-catalyzed growth · Metalorganic vapor phase epitaxy · Cathodoluminescence

1 Introduction

Quasi 1-dimensional nanostructures, so-called nanowires (NWs), based on III–V and II–VI compound semiconductors show novel and interesting physical properties, which make them particularly attractive for potential applications as functional

V. Di Carlo · F. Marzo · N. Lovergine (✉)
Dipartimento di Ingegneria dell'Innovazione, Università del Salento, Lecce, Italy
e-mail: nico.lovergine@unisalento.it

M. Di Giulio
Dipartimento di Fisica e Matematica "E. De Giorgi", Università del Salento, Lecce, Italy

P. Prete
Istituto per la Microelettronica e Microsistemi del CNR, Lecce, Italy

building blocks in nanoscale optical and optoelectronic devices [1]. Over the past decade, extensive studies on single semiconductor NWs and NW-based arrays have explored the device potentials of these nanomaterials as platforms for a new generation of high-efficiency and low-cost photovoltaic solar cells [2]. The incorporation of semiconductor NW structures into thin film solar cells offers the potential to overcome losses associated with minority carrier recombination, improve carrier mobility, and reduce optical reflection, allowing for increased photon collection efficiency [3]. Nanowire-based solar cells have developed rapidly, increasing their solar to electric power conversion efficiencies (PCE) from 5 to above 15% in the last 5 years [4]. Researches on next-generation photovoltaics aim to achieve PCE figures greater than 21%, approaching those (28–30%) expected theoretically [5].

CdTe is currently one of the most important semiconductors used for the fabrication of low-cost thin-films photovoltaic solar cells [6]. Indeed, its near-infrared band gap ($E_g \sim 1.5$ eV at 300 K [7]) matches the range of maximum solar irradiance spectrum, and its large bulk absorption coefficient ($>10^4$ cm^{-1} in the red, approaching 10^5 cm^{-1} in the blue [8]) makes it an excellent light harvester for solar energy applications. Compared with its thin film and bulk counterparts CdTe NWs are expected to be promising building blocks in the design of high-efficiency photovoltaic devices. Recent reports on the topic have focused on the fabrication of solar cells based on CdTe core-triple shell NWs, and demonstrated PCE figures $\sim 2.5\%$ [9]. To further improve this value, a main challenge is the development of suitable synthesis techniques enabling the growth of CdTe NWs with high purity, and good crystalline and electronic properties, along with a suitable control of their diameter, height and density.

Currently, NWs of a broad range of semiconductors, such as Si, Ge [10, 11], III–V [12, 13] and II–VI [14, 15] are grown by either chemical vapor deposition (CVD), thermal evaporation, solvothermal synthesis, molecular-beam exitaxy (MBE) or metalorganic vapor phase epitaxy (MOVPE) utilizing the metal-catalyst assisted (so-called vapor-liquid-solid, VLS) mechanism [16, 17]. Through the years VLS growth has emerged as a straightforward technique for growing large quantities of inorganic single crystalline nanowires [18–20]. The technique stems from the ability of a metal (the catalyst) to form a low melting point alloy with one or more metal elements constituting the semiconductor crystal. For temperatures above the eutectic melting point, the catalyst behaves as solvent for the semiconductor metal element (s), the latter supplied from the gas phase (the Vapour), so that the amount of these elements inside the catalyst droplet eventually increases, leading to the formation of a supersaturated liquid droplet (the Liquid) and consequently, to the nucleation and growth of the semiconductor nanowire (the Solid). A most common metal-catalyst used for the VLS growth of semiconductor NWs is Au.

Few reports have been published to date on the VLS synthesis of tellurium-based semiconductor NWs; in particular, only very few have dealt with the Au-catalyzed self-assembly of CdTe NWs [21–23]. None of them has concerned the NW growth by the MOVPE technology.

In this study we describe a new method, i.e. the alternate precursors flow process, especially developed for the Au-catalyzed MOVPE growth of CdTe NWs, and

report in details on the conditions leading to NW self-assembly. After showing that the NWs do grow indeed by the VLS mechanism we report on the kinetics of the VLS process; we also present the morphological and optical properties of as-grown NWs. Finally, the results of low temperature cathodoluminescence (CL) measurements performed on single CdTe nanowires are presented and discussed.

2 MOVPE Growth of CdTe Nanowire by the Separate Precursors Flow Process

CdTe nanowires were grown on (111)B-oriented semi-insulating GaAs substrates using a home-built atmospheric pressure MOVPE reactor. More specifically, GaAs (111)B substrates were first degreased in isopropanol vapors, etched in $4H_2SO_4$: H_2O_2:$2H_2O$ solution to remove native surface oxides, rinsed in deionized water and finally blown-dried under N_2, as described in details in Ref. [17]. As-treated substrates were then annealed at 460 °C for 10 min under pure H_2 in order to remove any residual oxides possibly remained on the GaAs surface. Next, a ~ 2 µm thick (111)-oriented CdTe buffer layer was epitaxially grown at 350 °C for 30 min, under a total H_2 flow of 4.55 slm. Diisopropyl-telluride ($^iPr_2Te$) and dimethylcadmium (Me_2Cd) were used as Cd and Te precursors, each supplied at a flow rate of 55 µmol/min.

As-prepared substrates were then covered with Au NPs, following two different methods: thermal de-wetting of UHV-evaporated Au thin films (thickness between 1 and 2 nm) or direct deposition from a colloidal solution [17]. In both cases, the as-prepared samples were further annealed for 10 min at 445 °C, under H_2 flow, with the aim to (i) allow the Au NPs formation of proper size and density, or (ii) eliminate any possible organic contaminants arising from the colloidal solution.

After raising the sample temperature up to the final growth value, varied between 485 and 515 °C, Te and Cd precursors were provided separately, as shown in Fig. 1. This is a new approach we have developed in order to inhibit the CdTe planar growth, which is otherwise quite efficient at temperatures above the Au-AuTe$_2$ eutectic melting point (~ 7 µm/h at 447 °C), i.e. if both precursors are simultaneously admitted to the reactor chamber. Instead, in the alternate precursor flow process a molar flow rate of 25 µmol/min of $^iPr_2Te$ is first provided for $\Delta t_{Te} = 1$–10 min to the vapor phase, after which 50 µmol/min of Me_2Cd are flowed over the sample for $\Delta t_{Cd} = 10$ min, as illustrated in details in Fig. 1b. While the first Te-flow step ensures the formation of liquid Au–Te alloy droplets onto the surface of the CdTe buffer layer, the subsequent Cd-flow step allows for Cd atoms to enter the liquid Au–Te alloy droplets and, upon reaching supersaturation, finally leads to the growth of CdTe NWs. During the time interval between the Te and Cd flow-steps, pure H_2 is flowed through the reactor chamber to remove unreacted $^iPr_2Te$ molecules from the sample surface and out of the vapor phase. In doing this
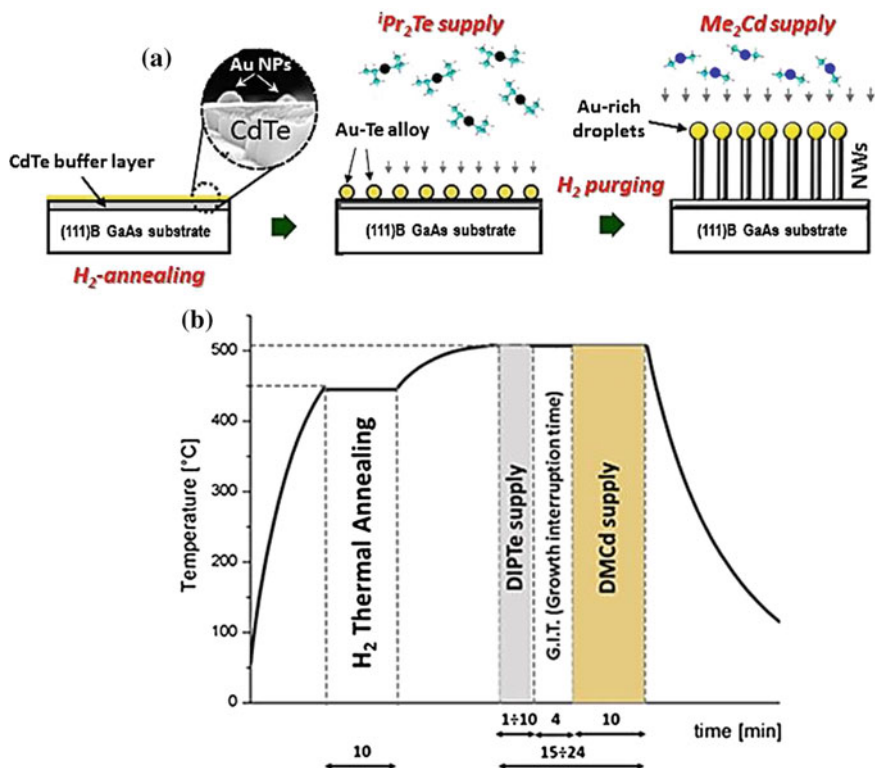
Fig. 1 **a** Schematic of the process steps adopted for the Au-catalyzed MOVPE growth of CdTe nanowires by the separate precursors flow process; **b** Process temperature profile and precursors supply sequence during the growth of CdTe nanowires

we ensure effective suppression of the planar growth rate during the NW self-assembly process. A detailed theoretical analysis of the actual growth mechanisms leading to the VLS growth of present CdTe NWs by the separate precursors flow method has been reported in Ref. [24]. Samples were cooled down to room temperature under pure H_2 flow.

3 Morphological, Structural and Optical Properties of As-Grown CdTe Nanowires

The separate precursors flow process allowed to successfully self-assemble CdTe NWs by MOVPE. Figures 2c shows a FE-SEM micrograph of an as-grown sample, confirming the occurrence of a high yield of straight vertically-standing NW structures, randomly distributed over the surface of the CdTe buffer layer. As the

CdTe epilayer is $\langle 111 \rangle$-oriented onto the GaAs substrate [24], this implies that the nanowire self-assemble homoepitaxially onto the buffer layer, with their major axis along the vertical $\langle 111 \rangle$ crystal direction, as commonly found for most Au-catalyzed III–V and II–VI nanowires [17, 24, 25].

In this work we used NPs obtained either (i) by self-assembling through the de-wetting of a thin evaporated Au film, or (ii) from colloidal solutions (NP average diameters ~ 25 nm). Figure 2a shows the morphology of Au NPs as-obtained from de-wetting of a 1.1 nm thick Au film, upon thermal annealing under pure H_2 at 445 °C for 10 min. The annealing temperature was set below the Au–$AuTe_2$ eutectic melting point (447 °C) with the purpose to limit Au/substrate interactions. In this case, the surface density of Au NPs ranged around 2.4×10^9 cm^{-2}, but decreases to values in the 10^8 cm^{-2} range for samples obtained using the colloidal solution. However, the NW morphology remained independent on the way Au NPs were obtained.

All CdTe NWs grown in our experiments do show a quasi-spherical shaped nano-droplet at their upper tips, with average diameters in the range between 150–230 nm. Chemical information on the nano-droplet composition were obtained by spatially resolved energy dispersive X-ray spectroscopy (EDXS) measurements performed in the FE-SEM microscope. Figure 3 shows the results of EDXS analyses performed on single nano-droplets on top of CdTe nanowires, demonstrating
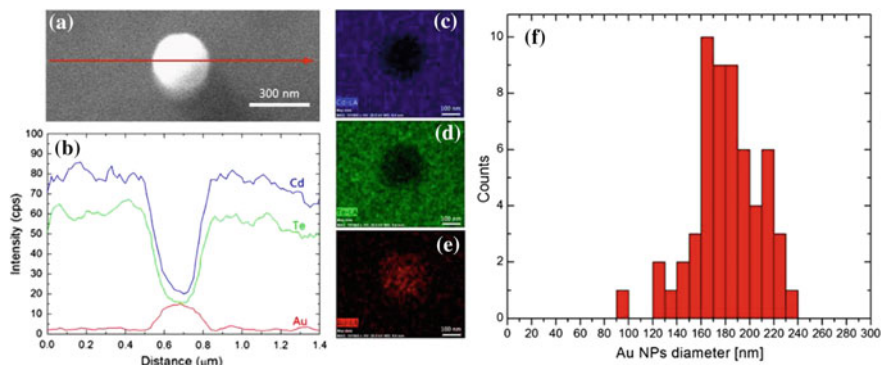
Fig. 3 SEM/EDXS analyses of a ∼200 nm Au-rich NP on top of a [111]-aligned CdTe nanowire grown at 507 °C. **a** SEM micrograph (102,000 × magnification, plan-view) of the NP; **b** EDXS line scans [indicated by the *red arrow* in (**a**)] of Cd Lα (*blue*), Te Lα (*green*) and Au Lα (*red*) EDXS signals; EDXS maps of the same elements (same colors) are shown in (**c**–**e**); **f** Count histogram of the diameters of Au-rich NPs on top of CdTe nanowires grown at 507 °C (Color figure online)

that these droplets are made of an Au-rich alloy. In particular, Fig. 3b shows the Au, Cd, and Te Lα fluorescence signals obtained by scanning a 20 keV primary electron beam along the line drawn in red on the high magnification SEM micrograph of Fig. 3a. The Au EDXS signal intensity increases above the background level at the NP position; EDXS maps of the same elements performed by scanning the electron beam over a small area across the NP further confirmed that Au atoms are indeed concentrated inside the NP (Fig. 3e). This supports our conclusion that present CdTe NWs were grown by the Au-catalyzed (VLS) mechanism.

Figure 3f reports a typical count histogram of the Au-rich NP diameters at the top of CdTe nanowires, as measured from a series of plan-view FE-SEM micrographs.

With regard to the NW heights and diameters, present samples have shown a high degree of uniformity over broad enough surface areas, so that we have been able to investigate their size as function of growth temperature. The NWs showed diameters ranging from 60 to 350 nm and heights between 40 nm and 1.7 μm. Higher growth temperatures promoted their axial (i.e., in the ⟨111⟩-direction) elongation and a better size uniformity. In Fig. 4a the NW average heights are plotted on a semi-logarithmic scale as function of growth temperature (Arrhenius plot); the red curve is the Arrhenius function best-fitting the experimental data, corresponding to a process activation energy E_A = 56.8 kcal/mol. The NW diameter is also constant over their length, showing no indication of the tapering seen in other semiconductor systems [17, 26]. This implies a negligible growth of the material along the NW sidewalls. A count histograms of the NW diameters measured at the NW tip is reported in Fig. 4b. Some CdTe NWs show zigzagged sidewalls as also often observed for III-V NWs [27], which is ascribed to the presence of twin defects along the NW axis. As the energy of stacking fault
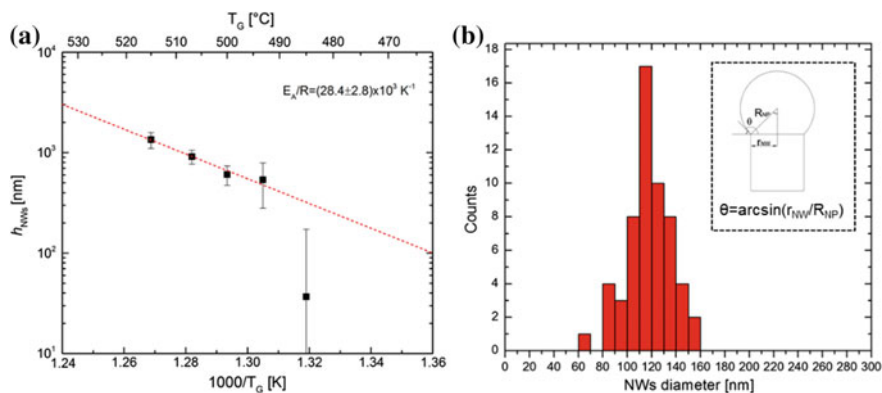
Fig. 4 a Arrhenius plot of the nanowire mean height (symbols) as a function of growth temperature ($\Delta t_{Te} = 1$ min). *Error bars* represent standard deviations. The *dashed (red) line* is the Arrhenius exponential function best-fitting the experimental data above 490 °C, and corresponding to an activation energy $E_A = (56.8 \pm 5.6)$ kcal/mol; **b** Count histogram of the diameters of CdTe nanowires grown at 507 °C; *Inset* in (**b**): geometrical definition of the nanowire radius (r_{NW}), the Au-NP radius (R_{NP}) and the Au-NP/nanowire contact angle (θ) (Color figure online)

(SF) formation in CdTe is fairly low (31–34 erg/cm^2), formation of SFs and twinned-crystal sections is thus expected during the VLS of CdTe NWs. Finally, NW growth below 485 °C resulted in the formation of nearly-hexagonal hillocks onto the CdTe buffer surface with Au-rich NPs still occurring at their tops.

We finally evaluated the average contact angle (θ) between the Au-rich NP and the underlying CdTe nanowire trunk by FE-SEM measurements of the Au NP (R_{NP}) and nanowire (r_{NW}) radius [24]. For all nanowires the estimated value of θ appears quite monodispersed around an average value of 130.5°, and independent on the actual nanowire growth temperatures. Interestingly, this result is in reasonable agreement with values reported in the literature for Au-catalyzed GaAs nanowires [28].

Low temperature CL spectra were recorded from single NWs after removing them from the original growth substrate; to this purpose, the nanowire samples were gently sonicated in isopropanol and the as-obtained solution poured onto Au-evaporated Si substrates. Figure 5a shows the CL spectrum collected at 7 K for one such single CdTe nanowire: the spectrum displays a well resolved band-edge emission at around 1.604 eV, as typical of zincblend CdTe ($E_g = 1.6063$ eV at 4.2 K, Ref. [29]). The NW shows also a broad and dominant band peaked at around 1.539 eV, possibly associated with a transition involving an acceptor level and likely due to Cd vacancies or Te interstitial defects. Interestingly, the CL emission appears uniform along the NW trunk (Fig. 5b). More details and in-depth analyses of the radiative properties of as-grown CdTe NWs are reported in our recent publication [24].
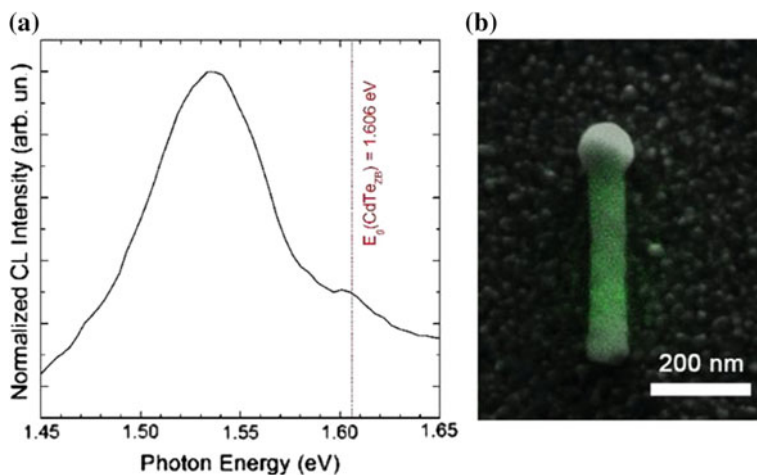
Fig. 5 a CL spectrum collected at 7K from a single CdTe nanowire after sonication and transfer onto an Au/Si substrate; **b** overlapping of a FE-SEM (*grey scale*) and a panchromatic-CL (*green color*) images recorded from the same CdTe nanowire

4 Conclusions

In summary, we demonstrated for the first time the growth of CdTe nanowires by MOVPE through the alternate precursors flow method, a new approach especially devised for the Au-catalyzed growth of CdTe nanowires above 485 °C. The method allows to suppress the conventional planar growth of CdTe in favor of the NW self-assembly by the VLS mechanism. An Au-rich droplet was found at the tip of each NW, confirming that CdTe nanostructures were indeed grown by the VLS process. FE-SEM observations allowed us to analyse the NW morphology and size as function of growth temperature. The NWs appear vertically-aligned along the substrate [111]-direction, the contact angle between the Au-rich NP and the NW being estimated $\sim 130°$. The NW axial growth rate appears kinetically-activated and we estimated a process activation energy ~ 57 kcal/mol. Analyses of the CL emission of single CdTe NWs has shown that as-grown nanostructures display a well resolved band-edge emission typical of zincblend CdTe, and a dominant (defect-related) broad band at around 1.539 eV.

Although additional work appears necessary with the purpose of further improving the growth process and the NW properties, present results open the path towards the manufacturing of high-efficiency CdTe/CdS nanowire-based solar cells by the MOVPE technology.

References

1. LaPierre, R.R., Robson, M., Azizur-Rahman, K.M., Kuyanov, P.: A review of III–V nanowire infrared photodetectors and sensors. J. Phys. D Appl. Phys. **50**, 123001 (2017)
2. Kempa, T.J., Day, R.W., Kim, S., Park, H., Lieber, C.M.: Semiconductor nanowires: a platform for exploring limits and concepts for nano-enabled solar cells. Energy Environ. Sci. **6**, 719–733 (2013)
3. Kapadia, R., Fan, Z., Javey, A.: Design constraints and guidelines for CdS/CdTe nanopillar based photovoltaics. Appl. Phys. Lett. **96**, 103116 (2010)
4. Otnes, G., Borgström, M.T.: Towards high efficiency nanowire solar cells. Nano Today **12**, 31–45 (2017)
5. Schockley, W., Qeisser, H.J.: Detailed balance limit of efficiency of p-n junction solar cells. J. Appl. Phys. **32**, 510–519 (1961)
6. Mathew, X., Thompson, G.W., Singh, V.P., McClure, J.C., Velumani, S., Mathews, N.R., Sebastian, P.J.: Development of CdTe thin films on flexible substrates—a review. Sol. Energy Mater. Sol. Cells **76**, 293–303 (2003)
7. Landolt-Bornstein: Numerical Data and Functional Relationships in Science and Technology, Springer, New York, New Series, Group III, 17a and 22a (1982)
8. Mitchell, K., Fahrenbruch, A.L., Bube, R.H.: Evaluation of the CdS/CdTe heterojunction solar cell. J. Appl. Phys. **48**, 829–830 (1977)
9. Williams, B.L., Taylor, A.A., Mendis, B.G., Phillips, L., Bowen, L., Major, J.D., Durose, K.: Core-shell ITO/ZnO/CdS/CdTe nanowire solar cells. Appl. Phys. Lett. **104**, 053907 (2014)
10. Kodambaka, S., Tersoff, J., Reuter, M.C., Ross, F.M.: Diameter-independent kinetics in the vapor-liquid-solid growth of Si nanowires. Phys. Rev. Lett. **96**, 096105 (2006)
11. Zakharov, N.D., Werner, P., Gerth, G., Schubert, L., Sokolov, L., Gösele, U.: Growth phenomena of Si and Si/Ge nanowires on Si (1 1 1) by molecular beam epitaxy. J. Cryst. Growth **290**, 6–10 (2006)
12. Ohlsson, B.J., Björk, M.T., Magnusson, M.H., Deppert, K., Samuelson, L., Wallenberg, L.R.: Size-, shape-, and position-controlled GaAs nano-whiskers. Appl. Phys. Lett. **79**, 3335–3337 (2001)
13. Duan, X., Huang, Y., Cui, Y., Wang, J., Lieber, C.M.: Indium phosphide nanowires as building blocks for nanoscale electronic and optoelectronic devices. Nature **409**, 66–69 (2001)
14. Huo, H.B., Dai, L., Liu, C., You, L.P., Yang, W.Q., Ma, R.M., Ran, G.Z., Qin, G.G.: Electrical properties of Cu-doped p-ZnTe Nanowires. Nanotechnology **17**, 5912–5915 (2006)
15. Chan, S.K., Cai, Y., Wang, N., Sou, I.K.: Growth temperature dependence of MBE-grown ZnSe Nanowires. J. Cryst. Growth **301–302**, 866–870 (2007)
16. Wagner, R.S., Ellis, W.C.: Vapor-liquid-solid mechanism of single crystal growth. Appl. Phys. Lett. **4**, 89–90 (1964)
17. Paiano, P., Prete, P., Lovergine, N., Mancini, A.M.: Size and shape control of GaAs nanowires grown by metalorganic vapor phase epitaxy using tertiarybutylarsine. J. Appl. Phys. **100**, 094305 (2006)
18. Fan, H.J., Werner, P., Zacharias, M.: Semiconductor nanowires: from self-organization to patterned growth. Small **2**, 700–717 (2006)
19. Dick, K.A.: A review of nanowire growth promoted by alloys and non-alloying elements with emphasis on Au-assisted III–V nanowires. Progr. Cryst. Growth Character. Mater. **54**, 138–173 (2008)
20. Chen, C.C., Yeh, C.C., Chen, C.H., Yu, M.Y., Liu, H.L., Wu, J.J., Chen, K.H., Chen, L.C., Peng, J.Y., Chen, Y.F.: Catalytic growth and characterization of gallium nitride nanowires. J. Am. Chem. Soc. **123**, 2791–2798 (2001)
21. Wojtowicz, T., Janik, E., Zaleszczyk, W., Sadowski, J., Karczewski, G., Dluzewski, P., Kret, S., Szuszkiewicz, W., Dynowska, E., Domagala, J., Aleszkiewicz, M., Baczewski, L.T., Petroutchik, A., Presz, A., Pacuski, W., Golnik, A., Kossacki, P., Morhange, J.F., Kirmse, H.,

Neumann, W., Caliebe, W.: MBE growth and properties of ZnTe- and CdTe-based nanowires. J. Korean Phys. Soc. **53**, 3055–3063 (2008)

22. Ye, Y., Dai, L., Sun, T., You, L.P., Zhu, R., Gao, J.Y., Peng, R.M., Yu, D.P., Qin, G.G.: High-quality CdTe nanowires: synthesis, characterization, and application in photoresponse devices. J. Appl. Phys. **108**, 044301 (2010)

23. Williams, B.L., Halliday, D.P., Mendis, B.G., Durose, K.: Microstructure and point defects in CdTe nanowires for photovoltaic applications. Nanotechnology **24**, 135703 (2013)

24. Di Carlo, V., Prete, P., Dubrovskii, V.G., Berdnikov, Y., Lovergine, N.: CdTe nanowires by Au-catalyzed metalorganic vapor phase epitaxy. Nano Lett. **17**, 4075–4082 (2017)

25. Seifert, W., Borgström, M., Deppert, K., Dick, K.A., Johansson, J., Larsson, M.W., Mårtensson, T., Sköld, N., Svensson, C.P.T., Wacaser, B.A., Wallenber, L.R., Samuelson, L.: Growth of one-dimensional nanostructures in MOVPE. J. Cryst. Growth **272**, 211–220 (2004)

26. Ihn, S.-G., Song, J.-I., Kim, T.-W., Leem, D.-S., Lee, T., Lee, S.-G., Koh, E.K., Song, K.: Morphology- and orientation-controlled gallium arsenide nanowires on silicon substrates. Nano Lett. **7**, 39–44 (2007)

27. Wolf, D., Lichte, H., Pozzi, G., Prete, P., Lovergine, N.: Electron holographic tomography for mapping the three-dimensional distribution of electrostatic potential in III-V semiconductor nanowires. Appl. Phys. Lett. **98**, 264103 (2011)

28. Sakong, S., Du, Y.A., Kratzer, P.: Atomistic modeling of the Au droplet-GaAs interface for size-selective nanowire growth. Phys. Rev. B **88**, 155309 (2013)

29. Landolt-Börnstein. In: Madelung, O., Van der Osten, W., Rössler, U. (eds.) Semiconductors: Intrinsic Properties of Group IV Elements and III–V, II–VI and I–VII Compounds, III-22. Springer, Berlin (1987)

An Electrode Impedance Balanced Interface for Biomedical Application

Francesca Romana Parente, Simone Di Giovanni, Giuseppe Ferri, Vincenzo Stornelli, Giorgio Pennazza and Marco Santonico

Abstract This work reports on the design of an electronic interface performing biomedical signal measurements. The proposed system involves three functional blocks: two leading electrodes, the signal conditioning front-end and a feedback circuitry. In particular, the latter is able to balance the electrodes impedance mismatching so to reduce the noise contribution. In this paper, the design has been tailored for a heart signal recording, however this approach can be easily applied in other types of biopotential measurements requiring a reduced number of electrodes. The reported simulation results show that the proposed system can be a good candidate in some intensive biomedical signal recordings.

Keywords Biomedical electronics · Biosignal recordings

1 Introduction

Low-level signal detection and quantification is an important feature in sensors and their applications, for example in health care where biosignal measurements exploiting interfaces to the skin are still a challenge [1, 2].

The biopotentials represent the physiological activity of the living beings and most of them, as for instance EEG and ECG, range over very low frequencies (<200 Hz) and amplitude levels (at maximum few mV) [3].

These signals have to be sensed and correctly amplified by an interface, formed at least by a suitable electronic system and a multi-electrode sensor [4].

In clinical applications, the coupling between the patient body and the measuring device is usually performed by transducers called electrodes [5, 6]. Unfortunately, in a two-electrode system, some issues such as, for example, a fake contact in the

F.R. Parente (✉) · S. Di Giovanni · G. Ferri · V. Stornelli
University of L'Aquila, L'Aquila, Italy
e-mail: francescaromana.parente@graduate.univaq.it

G. Pennazza · M. Santonico
Campus Bio-Medico University, Rome, Italy

adhesive area may cause electrode-skin impedance mismatching so producing an undesired differential voltage noise that is acquired and amplified by the front-end amplifier block together the useful signal.

For this reasons, impedances matching is an important requirement especially in some applications, e.g. during intraoperative monitoring since the background electrical noise is inherently high while its mismatching may cause a very noisy recording [7].

2 Design Strategies

2.1 Requirements

A biomedical signal reading system must be able to perform a differential acquisition of extremely weak signals between two electrodes, which, concerning the front-end, leads to the use of an Instrumentation Amplifier (*IA*) having a high common-mode rejection ratio (*CMRR*). This parameter is typically improved by means of chopper [8, 9] or bootstrap [10, 11] amplifiers. Moreover, IAs are usually characterized by a high input differential impedance and, on the contrary, by a low input common mode impedance.

As above mentioned, the impedance mismatch in a two-electrode system represents a noise interference source. In last years some balancing techniques have been proposed demonstrating, at simulation level, that the input impedance of an amplifier front-end as a part of Wheatstone bridge branch can be easily driven by a current [12] or a voltage [13].

All these features are met by the here proposed approach, whose block scheme is shown in Fig. 1. The requirements about the input impedance and the common mode rejection are accomplished through an AC coupled bootstrapped instrumentation amplifier as front-end block. Furthermore, the main acquisition circuit also comprises a filters block including an active band-pass filter (that limits the output in a specific frequency range) and a band-stop (notch) filter (that reduces the powerline interference contribution).

In addition, this approach relies on a feedback branch that through a continuous tuning of an impedance included in the input front-end (reported in Fig. 2), allows to reach the bridge equilibrium condition so nulling the common mode interference. The variable impedance is implemented by means of the commercial component AD633 connected in two Zhong configurations [14] so to emulate both the real and the imaginary part of the common mode impedance Z_{cm2} shown in Fig. 2. The same component is used to implement the mixer included in the feedback circuit.
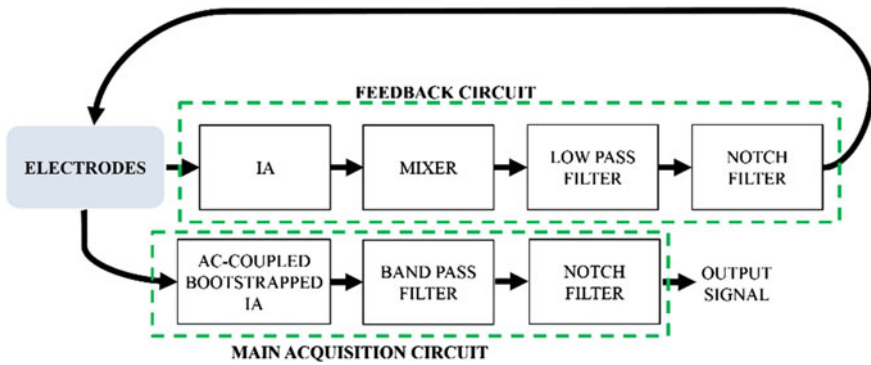
Fig. 1 Block scheme of the proposed front-end

Fig. 2 Equivalent model of the body-amplifier front-end
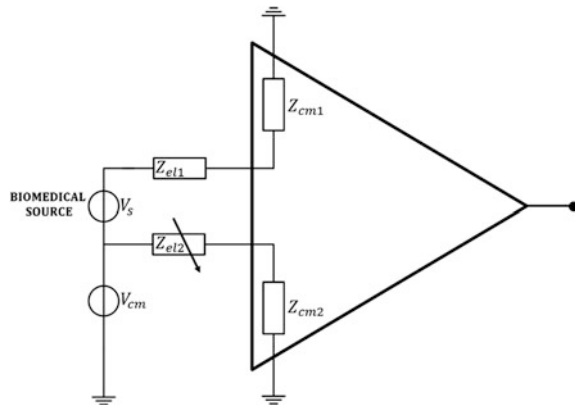
2.2 Heart Signal Recording Application

The proposed approach has been designed for a heart signal recording in order to evaluate its goodness in a specific case-study. Typically, in this kind of application the front-end input signal is characterized by very few mV of AC amplitude (the signal to be acquired), a DC offset (related to the electrode-skin contact) and a common mode noise (in particular, due to the powerline interference) of at least a hundred of mV [6]. Depending on the application, the frequency range of a heart signal goes from 0.05 to 150 Hz, being the most part of the useful signal in the lowest spectral components up to roughly 30 Hz [4]. For this purpose, the selected band pass frequency range is 0.05–30 Hz, whereas the stop-frequency of the filter has been set to 50 Hz.

3   Preliminary Simulation Results

A simulated analysis of the designed interface was performed using the PSpice Suite. In order to emulate an ECG signal as input, a customized ECG waveform based on a piecewise linear function has been implemented. Figure 3a shows the input waveform employed in the simulations represented by an ECG waveform that is completely buried by noise. The corresponding simulated output result is shown in Fig. 3b: it is possible to observe a clear and well-defined ECG-like waveform. ECG purification is achieved by considering the common mode noise as the most significant source of noise: in this sense, the main contribution to this issue is done by the feedback circuit fixing the impedance mismatch.

A frequency domain analysis was performed in order to obtain the transfer function magnitude versus frequency of the signal conditioning front-end (see Fig. 4).

In the reported Bode plot it is possible to observe the influence of both the band-pass and the band-stop filters. In particular, it shows a maximum attenuation of around 40 dB at the powerline frequency (50 Hz) with respect to the main bandwidth of the system.
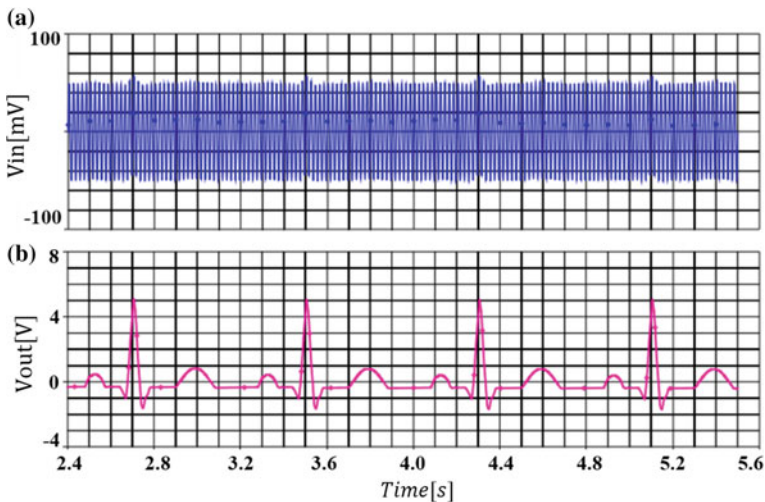
Fig. 3   a Input signal versus time **b** output signal versus time

Fig. 4 Bode plot: transfer function magnitude versus frequency
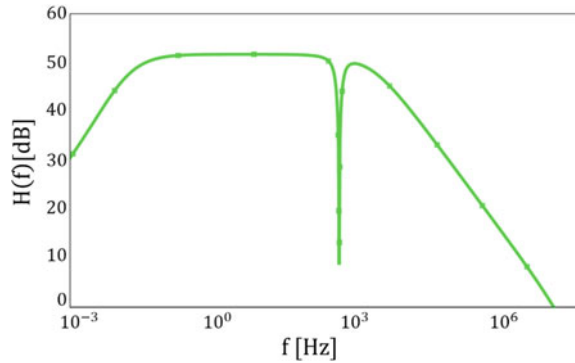
4   Conclusions

An electronic system performing biomedical signal acquisition has been developed and discussed. The here proposed architecture works for very weak signals until a signal-to-noise, thanks to the use of the feedback system and some filtering stages (also for power line frequency—50 Hz—reject).

Preliminary simulation results suggest the feasibility of future improvements and, in order to perform experimental results, work is currently under progress to develop an interface PCB.

References

1. Chu, N.Y.: Surprising Prevalence of Electroencephalogram Brain-Computer Interface to Internet of Things. IEEE Consum. Electron. Mag. **6**, 31–39 (2017)
2. Ha, S., Kim, C., Chi, Y.M., Akinin, A., Maier, C., Ueno, A., Cauwenberghs, G.: Integrated circuits and electrode interfaces for noninvasive physiological monitoring. IEEE Trans. Biomed. Eng. **61**, 1522–1537 (2014)
3. Webster, J. G.: Medical instrumentation application and design. pp. 258–260. Wiley Edition (2009)
4. Prutchi, D., Norris, M.: Design and development of medical electronic instrumentation: practical perspective of the design, construction, and test of medical devices. pp. 2–6. Wiley Edition (2005)
5. Lewis, N.: Bio-electronic interaction: principle and applications. In: 9th IEEE International Conference on Design & Technology of Integrated Systems in Nanoscale Era (2014)
6. Neuman, M.R: Biopotential Electrodes. In: Webster, J.G. (eds.) Medical Instrumentation: Application and Design, 3rd ed, pp. 183–232. Wiley (1997)
7. Legatt, A.D.: Impairment of common mode rejection by mismatched electrode impedances: Quantitative analysis. Am. J. EEG Technol. **35**, 296–302 (1995)
8. Chebli, R., Sawan, M.: Low noise and high CMRR front-end amplifier dedicated to portable EEG acquisition system. In: 35th Annual International Conference of the IEEE Engineering in Medicine and Biology Society (EMBC), pp. 2523–2526 (2013)

9. Yazicioglu, R.F., Merken, P., Puers, R., Van Hoof, C.: A 60 W 60 nV/Hz readout front-end for portable biopotential acquisition systems. IEEE J. Solid-State Cir. **42**, 1100–1110 (2007)
10. Dobrev, D., Neycheva, T.: Bootstrapped instrumentation biosignal amplifier. Ann. J. Electr. **5**, 76–79 (2011)
11. Stornelli, V., Ferri, G.: A single current conveyor-based low voltage low power bootstrap circuit for ElectroCardioGraphy and ElectroEncephaloGraphy acquisition systems. Analog Integr. Cir. Signal Pro. **79**, 171–175 (2014)
12. Dobrev, D., Neycheva, T.: Current driven automatic electrode impedance balance in ground free biosignal aquisition. Ann. J. Elect. pp. 62–65 (2014)
13. Dobrev, D., Neycheva, T.: Analog Approach for Common Mode Impedance Balance in Two-electrode Biosignal Amplifiers. Ann. J Elect. **7**, 68–71 (2013)
14. Datasheet, AD633, http://www.analog.com/media/en/technical-documentation/data-sheets/AD633.pdf (2016, Apr)

Autonomous Microfluidic Capillary Network for on Chip Detection of Chemiluminescence

M. Nardecchia, D. Paglialunga, G. Petrucci, N. Lovecchio, F. Costantini, S. Pirrotta, G. de Cesare, D. Caputo and A. Nascetti

Abstract This work reports on the design, simulation and fabrication of an autonomous microfluidic network. It is a part of a highly integrated, new analytical platform for the multiparametric detection of bio-organic molecules in extra-terrestrial environment. The proposed microfluidic system, made in SU-8 3050, allows to obtain an autonomous microfluidic network able to have simultaneous capillary filling and fresh solution into each site of detection avoiding cross-contamination among different sites. Computational Fluid Dynamics (CFD) simulations have been carried in order to verify the proper operation of the designed microfluidic network and to optimize it. Technological processes have been refined and adapted in order to ensure good adhesion, using low-temperature and low-pressure bonding avoiding the risk of breaking the glass slides. Experiments have been conducted to verify the autonomous capillary filling of the entire network and its rinsing with buffer solution. The experimental results are in good agreement with the simulations.

Keywords Lab-on-chip · SU-8 3050 · Microfluidic · Capillary networks
Bonding

M. Nardecchia (✉) · D. Paglialunga · F. Costantini · A. Nascetti
School of Aerospace Engineering, Sapienza University of Rome, Rome, Italy
e-mail: Marco.Nardecchia@uniroma1.it

M. Nardecchia · G. Petrucci · N. Lovecchio · G. de Cesare · D. Caputo
D.I.E.T, Sapienza University of Rome, Rome, Italy

F. Costantini
Department of Chemistry, Sapienza University of Rome, Rome, Italy

S. Pirrotta
Italian Space Agency, Rome, Italy

1   Introduction

Several studies reported the presence of organic compounds and in particular of amino acids on meteorites. Some of these studies even hypothesized the extraterrestrial origin of prebiotic materials for the beginning of the life on the Earth [1]. One of the main objectives of the research in the field of exobiology is thus the search for organic molecules and compounds in planetary exploration missions and the identification of their origin: biological or non-biological. Current strategies of planetary exploration are oriented toward the development of devices capable of analyzing in situ material samples in search of organic molecules, amino acids, polycyclic aromatic hydrocarbons, nucleic acids, polysaccharides and other molecular systems characteristic of organized biological systems [2].

In the last decades, the increasing development of extremely compact systems relying on microfluidics, commonly known as lab-on-chip devices, has gained much attention thanks to their favorable characteristics in terms of reduced size and weight, very low sample and reagent consumption, reduced analysis time and, often, superior achievable performances in terms of limits-of-detection. Of course, these advantages are extremely attractive for space missions and are indeed under investigation by many research groups [3].

The proposed analytical platform is based on lab-on-chip technology and goes beyond the current approaches that still require bulky external instrumentation for their operation. The PLEIADES project, financed by the Italian Space Agency (ASI), proposes the combination of:

- a microfluidic network based on capillary forces for the handling of samples and reagents;
- a set of functionalized detection sites where antibody or aptamer-based immunoassays relying on chemiluminescent detection will be carried out;
- an array of thin-film hydrogenated amorphous silicon (a-Si:H) photosensors for the detection of the analytical chemiluminescent signal.

A 3D view and a cross-section of the complete system are reported in Fig. 1a, b, respectively.
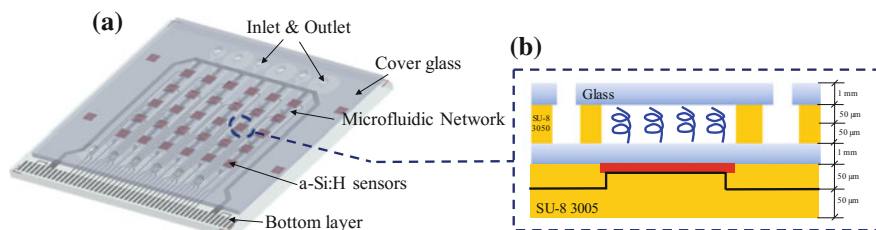

Fig. 1   **a** Three dimensional view of the complete system. **b** Cross section of one detection site

The proposed Lab-On-Chip (Fig. 1a) consists in a bottom glass substrate (light gray glass) hosting on one side the array of amorphous silicon photosensors (physical glass side) and on the other side the microfluidic network with functionalized sites [4] (biochemical glass side). A cross section of one detection site is shown in Fig. 1b. The red rectangle is the a-Si:H photosensors, while the black solid line depicts the sensor top contact. The pig tails on the inner glass surface represent the functionalized site.

In this paper, a technology solution is proposed for the fast and low cost realization, of autonomous capillary systems that can operate with fresh solutions simultaneously in each functionalized site. The structure includes a microfluidic network made in SU-8 and two glasses used as bottom substrate, hosting also the photosensors array, and top channel cover.

The next section reports the design and simulations of a single autonomous microfluidic network, which is aimed to the test of the technology and related processes in order to evaluate their suitability for the proposed task. In section three, details of the proposed technological process are given along with examples of fabricated devices. In section four the experimental results are reported and discussed and finally conclusions are drawn.

2 Design and Simulations

The main requirement for the microfluidic geometry was to get the same flow in each detection site. Fulfilling this requirement allows each detection site to get the same chemiluminescent signal from the same sample in the different sites. Since the chip is required to be autonomous, i.e. to operate without the need of an external syringe- or pressure-pump, the above-mentioned requirement has to be accomplished without using external auxiliary instrumentation for sample handling. This constraint can be satisfied in several ways, e.g. by using electrowetting-on-dielectric (EWOD) techniques [5] or by using capillary forces [6]. Since continuous flow (thus a continuous chemiluminescent signal) instead of a series of droplet is preferred for on chip chemiluminescence detection, sample handling within the microfluidic network has been designed making exclusive use of capillary forces.

The system has been designed taking into account the possibility to have simultaneous capillary filling when fluid is injected through the inlets. This approach has two main features: redundancy and multiparametric detection. Redundancy is guaranteed by injecting the same sample in different microfluidic networks (up to 6 independent circuits within the presented geometry). In this way, in case of sample handling failure of one or more microfluidic circuit for any reason, on chip detection is assured. It is even possible to functionalize each circuit with different reagents: in this way, by injecting the same sample in each microfluidic circuit, it is possible to achieve multiparametric detection on a single chip (up to 6 different kinds of target molecule detection using this geometry). Furthermore, it is possible to trade-off between redundancy and multiparametric

detection, e.g. functionalizing two different circuits with the same reagent, in order to get triple parametric detection and redundancy. In addition, simultaneously injecting sample through the inlets ensures high efficiency, fast response and straightforward analysis. It is important to point out that the filling of detection sites with only fresh sample is necessary to prevent cross-contamination as well as to avoid the imbalance of the analytical signal caused either by sample impoverishment or reagent consumption after its use in a detection site.

The proposed geometry is reported in Fig. 2. This microfluidic network ensures an equal flow rate in all the five detection sites thanks to its symmetry, provided that the fluidic resistance of the load- and drain-channels is low compared with that of the microfluidic circuits passing through each detection site. In particular, 800 μm wide load- and drain-channels and 250 μm wide detection channels were used.

Using the proposed design, once the sample fluid reaches each detection site by the exclusive use of capillary forces, it flows out from the outlet. If necessary, flow can be easily sustained by using a capillary pump (e.g. adsorbent paper) at the outlet connection. This technique can also be used to perform the rinsing of the channel as well as to empty it if necessary. With this procedure, the chip is can reused multiple time, for example, for implementing a sequence of dispensing of sample and reagents with intermediate washing steps with a buffer solution.

Before of manufacturing and testing the autonomous microfluidic capillary network, Computational Fluid Dynamics (CFD) simulations have been conducted in order to verify proper capillary filling throughout the whole circuit. One of the main concern was having the same flow in each detection site. Preliminary analytical calculations have been performed based on the equivalent electrical circuit approach for microfluidic networks [7]. Preliminary analytical results have been verified and refined prior manufacturing by using COMSOL Multiphysics software. A transient simulation with phase initialization approach has been implemented in order to verify proper microfluidic network capillary filling during time. Transient simulations have been performed on a simplified network with only three detection sites after verifying its correct equivalent behavior in steady state conditions. As shown in Fig. 3, detection sites are always filled with fresh solution.

Fig. 2 Designed microfluidic network
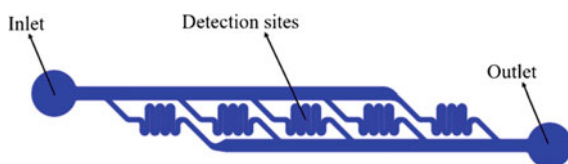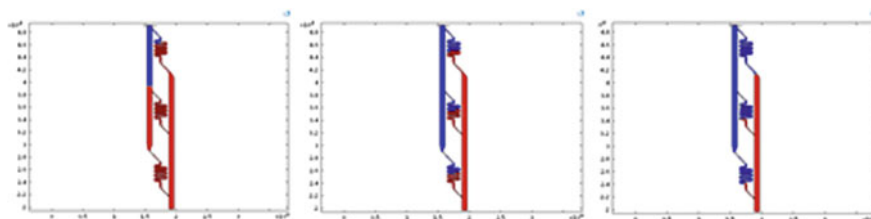
Fig. 3 Capillary filling simulation
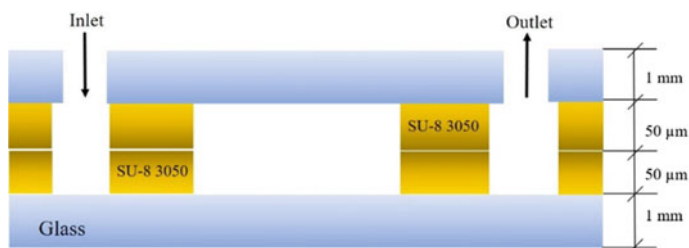
Fig. 4 Cross section of the microfluidic structure

3 Materials and Fabrication

The proposed capillary-driven microfluidic system relies on SU-8 3050-based microchannels that ensure slightly hydrophilic sidewalls, fabricated on a glass coverlid, characterized by highly hydrophilic surfaces. With respect to other solutions, the proposed technology offers fast prototyping and low fabrication cost of microfluidic capillary networks able to autonomously handle saline solutions required in the bioanalytical applications [8].

The channels can be easily defined by conventional lithography and very high aspect ratio can be achieved allowing to define very dense and complex networks. Moreover, the epoxy nature of SU-8 3050 ensures good mechanical properties even in the smallest details and good chemical inertia to reagents used in biological applications. By using different formulations of SU-8 3050 and by changing processing parameters as rotation speed of the spin coater it is possible to obtain the required channel depth. The cover glass features the sealing of the channel and the inlet and outlet access holes. The main technological issue related to the device reported in Fig. 4 is the bonding of the cover glass to the SU-8 channels [9, 10].

Technological step for obtaining the microfluidic structure includes:

- cleaning glass with "piranha process" and plasma oxygen;
- deposition by spin-coating of SU-8 3050 channels on the bottom glass substrate, its soft curing and its patterning by photolithographic steps for the definition of

the microfluidic network but without the final curing step of the SU-8 layer. In this way the SU-8 is still soft and sticky and ready for bonding;

- deposition by spin-coating of SU-8 3050 channels on the cover glass, its soft curing and its patterning by photolithographic steps using a mirrored mask to match the channels on the bottom substrate (without final curing);
- drilling hole on the cover glass on corresponding of the inlets and outlets using high speed (30,000 rpm) drill tips to make hole;
- alignment and coupling of the two glass substrates using vacuum bell to ensure perfect adhesion of the two matched SU-8 layers;
- final curing step for microchannels definition bonding the two SU-8 3050 layers with a handmade press for 60 min @ 185 °C.

A final prototype of the proposed structure is shown in Fig. 5.

A very good and uniform bonding is achieved even in proximity of the fine details of the microfluidic network.

4 Experimental Results

The fabricated device has been tested for capillary flow experiments.

Figure 6 shows the sequence of capillary filling at the same time of a single microfluidic channel and its rinsing. At first the fluid is dispensed at the inlet and collected in the initial reservoir (a) and, after 3 s, it reaches the five functionalized sites (b). When the functionalized sites are completely filled (about 5 s after dispensing) the fluid reaches the outlet through the drain channel (c). All the five channels showed the same behaviour with similar filling time (d).

In order to enable the implementation of an analytical protocol, it has to be possible to rinse and eventually dry the microfluidic network. Both steps can be achieved without the use of mechanical pumps (either syringe or pressure pumps) by using an absorbing paper at the outlet that acts as a capillary pump. Buffer solution is dispensed at the inlet while the channels are filled with the coloured solution and, after five seconds, the buffer flows through the functionalized sites
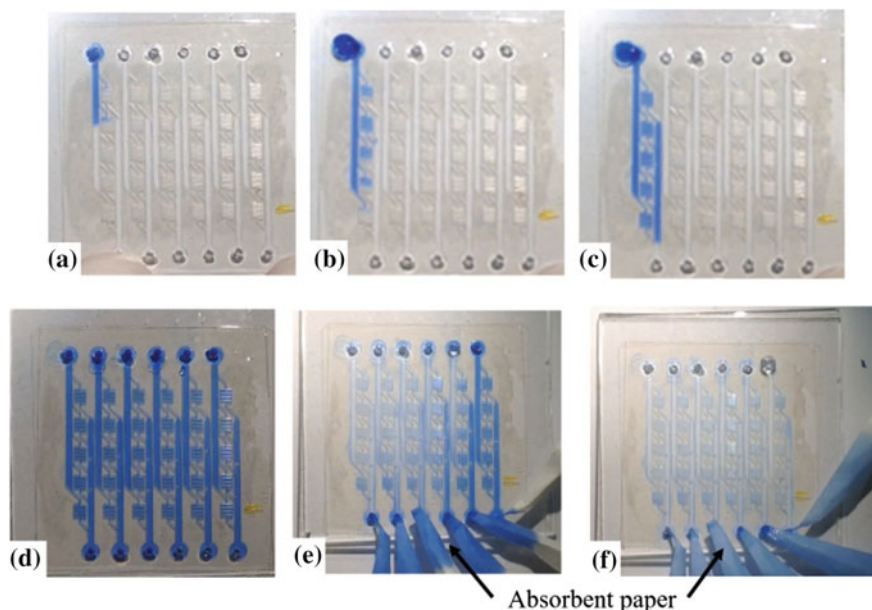
Fig. 6 Sequential filling and rinsing of the capillary-driven microfluidic channels

(e) and rinses the sites from the blue solution (f). After a few minutes, all functionalized sites are completely cleaned. After the experiments, it was possible deplete the microfluidic network and dry it by means of nitrogen flow blown from the chip inlets. A cleaning procedure has been implemented by filling the microchannels with isopropanol and emptying them again by nitrogen blow followed by a drying step on hotplate in vacuum conditions.

After this cleaning procedure, the microfluidic network could be reused and showed unaltered flow characteristics, maintaining a very good capillary action after several wash-and-reuse cycles.

5 Conclusion

A microfluidic network suitable for the execution of multi-parametric analytical reactions for lab-on-chip applications has been presented. The proposed microfluidic circuit has been designed to ensure an even distribution of samples and fresh reagents in the detection sites in autonomous way, driven by capillary forces. The experiment and the simulation results are in good agreement showing a proper behavior of the microfluidic network in all the tested conditions, i.e. filling, continuous flow rinsing and emptying. The microfluidic device also showed a very good mechanical stability: no delamination neither cracks have been observed even when using relatively strong nitrogen pressure to dry the microchannels.

These features, useful for the target space application, can also have a direct impact on the development of lab-on-chip systems suitable for terrestrial purposes.

References

1. Rubenstein, E., Bonner, W.A., Noyes, H.P., Brown, G.S.: Supernovae and life. Nature **306**, 118 (1983). doi:10.1038/306118a0
2. Poinot, P., Geffroy-Rodier, C.: Searching for organic compounds in the Universe. TrAC Trends Anal. Chem. (2014). doi:10.1016/j.trac.2014.09.009
3. Lewotsky, K.: Microfluidics streamlines laboratory operations. SPIE Newsroom (2010). doi:10.1117/2.2201012.01
4. Caputo, D., de Cesare, G., Dolci, L.S., Mirasoli, M., Nascetti, A., Roda, A., Scipinotti, R.: Microfluidic chip with integrated a-Si: H photodiodes for chemiluminescence-based bioassays. IEEE Sens. J. **13**(7), 2595–2602 (2013). doi:10.1109/jsen.2013.2256889
5. Nardecchia, M., Lovecchio, N., Llorca, P.R., Caputo, D., de Cesare, G., Nascetti, A.: 2-D digital microfluidic system for droplet handling using Printed Circuit Board technology. In: AISEM Annual Conference XVIII. IEEE (2015)
6. Safavieh, R., Juncker, D.: Capillarics: pre-programmed, self-powered microfluidic circuits built from capillary elements. Lab Chip **13**(21), 4180 (2013)
7. Chatterjee, A.N., Aluru, N.R.: Combined circuit/device modeling and simulation of integrated microfluidic systems. J. Microelectromech. Syst. **14**(1), 81–95 (2005)
8. Caprini, D., Nascetti, A., Petrucci, G., Caputo, D., de Cesare, G.: Rapid prototyping of glass microfluidic chips based on autonomous capillary networks for physiological solutions. In: AISEM Annual Conference, XVIII, pp. 1–4. IEEE (2015)
9. Nardecchia, M., Bellini, E., Llorca, P.R., Caprini, D., Lovecchio, N., Petrucci, G., Caputo, D., de Cesare, G., Nascetti, A.: Integration of capillary and EWOD technologies for autonomous and low-power consumption micro-analytical systems. In: Procedia Engineering, vol. 168, pp. 1370–1373 (2016)
10. Serra, S.G., Schneider, A., Malecki, K., Huq, S.E., Brenner, W.: A simple bonding process of SU-8 to glass to seal a microfluidic device. In: Proceedings of 3rd International Conference on Multi-Material Micro Manufacture, pp. 3–5. Borovets, Bulgaria (2007)

Assessing the Relocation Robustness of on Field Calibrations for Air Quality Monitoring Devices

E. Esposito, M. Salvato, S. De Vito, G. Fattoruso, N. Castell,
K. Karatzas and G. Di Francia

Abstract The adoption of on field calibration for pervasive air quality monitors, is increasing significantly in the last few years. The sensors data, recorded on the field, together with co-located reference analyzers data, allow to build a knowledge base that is more representative of the real world conditions and thus more effective. However, on field calibration precision may fade in time due to change in operative conditions, due to different drivers. Among these, relocation is deemed among the most relevant. In this work, for the first time, we attempt to assess the robustness of this approach to relocation of the sensor nodes. We try to evaluate the impact on performance of the so called locality issue by measuring the changes in the performance indicators, when a chemical multisensory system operates in a location that differs from the one in which it was on field calibrated. To this purposes, a nonlinear multivariate approach with Neural Networks (NN) and a suitable dataset, provided by NILU (the Norwegian Institute for Air Quality), have been used. The preliminary results show a greater influence of seasonal forcers distribution with respect to the relocation issues.

Keywords Mobile chemical multisensory devices · Machine learning
Distributed air quality monitors · Calibration methods

E. Esposito (✉) · M. Salvato · S.D. Vito · G. Fattoruso · G.D. Francia
Smart Network Division, ENEA, P.le E. Fermi, 1 80055 Portici, Naples, Italy
e-mail: Elena.Esposito@enea.it

N. Castell
NILU—Norwegian Institute for Air Quality, Oslo, Norway

K. Karatzas
Department of Mechanical Engineering, Aristotle University of Thessaloniki,
Thessaloniki, Greece

1 Introduction

The co-location of chemical multisensory devices with conventional analysers, providing ground truth measurements, allows to implement on field calibration strategy. Lately, several results seems to indicate it as the best performing strategy for air quality monitoring devices [1–3].

The use of nonlinear multivariate calibration approaches together with on field recorded data, can strongly reduce the effect of the cross sensitivities. However, costs and the so called locality issue pose a threat to the perceived robustness of the method. Costs depend on the number of days needed to explore the pollutants space so to build a suitable dataset. Conversely, locality issue depends on the difference among the conditions encountered during calibration time and the ones the device will meet during its operative life. Both the issues are well present also in lab based calibration approach though the second may be more easily controlled. Nonetheless, a trade off among costs and robustness apply anyway.

In particular, the term conditions can be better described in terms of the distribution of the forcers (target gases, interferents, environmental conditions) and the sensor model itself.

Relocation may force the calibrated node to operate outside the manifold described by the trajectories of the forcers during calibration hampering the precision of the gas concentrations estimations.

Up to now, no assessment has been conducted on the real influence of the relocation problem on the performances of systems, that have been calibrated in the so called calibration site and are operating in different sites or in mobility conditions.

NILU, The Norwegian Institute for Air Quality research, has recently leaded a recording campaign involving 24 identical AQMesh platforms that have been deployed in Oslo for more than 6 months.

These nodes have been co-located with a conventional analyzer in Kirkeveien (Oslo, Norway) and then distributed among four different locations, where they operated together with the local conventional analyzer.

In next sections we provide an assessment of performance degradation occurring in on field calibrated device when relocated in different sites after calibration. In Sect. 2 the experimental setting is described, in Sect. 3 the results are shown and the performances are analysed; finally, in Sect. 4, conclusions and discussions are reported.

2 Experimental Settings

The recording campaign conducted by NILU, encompasses 24 identical AQMesh platforms, that have been deployed in Oslo for more than 6 months (April to September 2015). The AQMesh platforms may monitor NO, NO_2, O_3, CO, PM10

and PM2.5 plus Temperature and Relative Humidity. PM10 and PM2.5 are estimated by converting the particle counts into PM mass-based fractions assuming a spherical particle shape and standard density. Standard AQMesh nodes provide one-hour averaged data, but can be configured to deliver 15 min averaged data. An integrated GPRS modem allows data transfer to the AQMesh database server. The data can then be downloaded from a dedicated website.

The 24 nodes were co-located at the reference AQM station of Kirkeveien rd., from April to June 2015. Then, between July and September 2015 some of the nodes were relocated to 3 AQM stations in Oslo, Åkerbergveien (5 pods), Manglerud (4 pods) and Alnabru (4 pods). The latter, unfortunately, was not operative during most time and cannot be include in the analysis. The remaining 10 was kept in Kirkevein rd. providing a reference for performance assessment.

The AQM stations at Kirkeveien and Manglerud are close to streets with busy traffic, while the AQM station at Åkebergveien is in the intersection of two streets with low to medium traffic. Originally, the different distributions of the nodes of the AQM stations have allowed to evaluate the performance in different urban environments, while the 10 nodes co-located at the Kirkeveien AQM station from April to September 2015, have allowed to evaluate long-term performance.

The deployed AQM stations were equipped with CO, NO, NO$_2$, O$_3$ and PM analyzers (see Table 1).

In particular, the platforms located at Kirkeveien are equipped also with T, RH and Air Pressure (AP) stations, while for the nodes relocated at Manglerud and Åkebergveien meteorological parameters are not available. For this reason, the multivariate calibration here described has taken into account the values of T and RH provided by the meteorological station of Blindern (Oslo, Norway).

In this contribution we have analysed 12 of the 24 AQMesh pods, i.e. 4 of the 10 that remained in Kirkeveien, 4 of the 5 that have been relocated in Åkerbergveien and the 4 pods that have been relocated in Manglerud (see Table 1).

Table 1 List of 12 AQMesh platforms analysed and gas pollutant concentrations measured by each station

Location	Platform	Measured parameters
Kirkeveien	AQ715150	NO, NO$_2$, CO, O$_3$, PM10, PM2.5, T, RH, AP
	AQ764150	
	AQ849150	
	AQ785150	
Åkebergveien	AQ743150	NO, NO$_2$, PM10, PM2.5
	AQ850150	
	AQ828150	
	AQ712150	
Manglerud	AQ856150	NO, NO$_2$, PM10, PM2.5
	AQ751150	
	AQ737150	
	AQ718150	

They were calibrated against NO_2 during their localization in Kirkeveien road on the basis of NO, NO_2, T and RH sensors responses.

Calibration law was implemented by training a shallow neural network with 5 hidden layer neurons on a 1200 h training set (April, 13th to May, 31st). A set apart test set of 240 h (June, 1st to June, 10th, namely, period 1) provided the ground for the assessment of initial performances of the pods in terms of Mean Absolute Error (MAE) and Correlation Coefficient (CC). Afterwise, from the July, 1st to Sept. 22nd, the 8 of them, as above mentioned, were relocated, in Åkerbergveien road and Manglerud road. The above sites are respectively 4.5 and 9 km away from Kirkeveien road, where the remaining 4 continued to operate. During this period, their calibrated output were measured for providing a reference measure of the performance change with respect to the initial test set. The other eight, simultaneously, provided the measurements for the relocation performance assessment. Three ten day periods have been chosen for this assessment (July,1st–10th—August, 1st–10th—September, 1st–10th).

For Nonlinear Multivariate calibration, a Feed Forward Neural Network (FFNN) with 5 hidden layer were selected and then, its performance was compared with those of the classical linear univariate approach.

3 Performance Analysis and Results

Our preliminary results, including those of stable and relocated pods, show a complex picture that does not allow for defining an easy interpretation, as it can be seen in Figs. 1, 2 and Tables 2a, 3a, 4a.

The relocated nodes suffer from a worsening of the correlation index between device estimations and real concentrations of NO_2. However, a similar behaviour, is found in the static nodes. All the nodes have also shown a deterioration in the MAE performance indexes.

Afterwise, they all recover, on average, at the initial CC performance level (Fig. 2). This recovery is not generally confirmed for the MAE performance indicator since it is shown, on average, only for the Åkebergveien relocated nodes (Fig. 1).

More precisely, Tables 2, 3, and 4 report the values in a numerical format. They also show the general performances boost obtained by nonlinear multivariate calibration approach (b) with respect to the linear univariate one (a), when operating on AQMesh outputs.

Obviously, we can expect that the performance change as significantly depending on the variation of the statistical distribution of the forcers, that, in turn, influence the response of the sensors including the unobserved interferents.

These changes may cause problems to the learnt calibrations. In particular, the black lines reported in Fig. 1, and 2 reports the behaviour of average temperatures. It correlates significantly with the behaviour of the performance indexes suggesting

Fig. 1 Picture of MAEs behaviour in the four considered periods, normalized to the value obtained in period 1. For each location, the four pods MAE is shown together with the location wide average (*solid*)
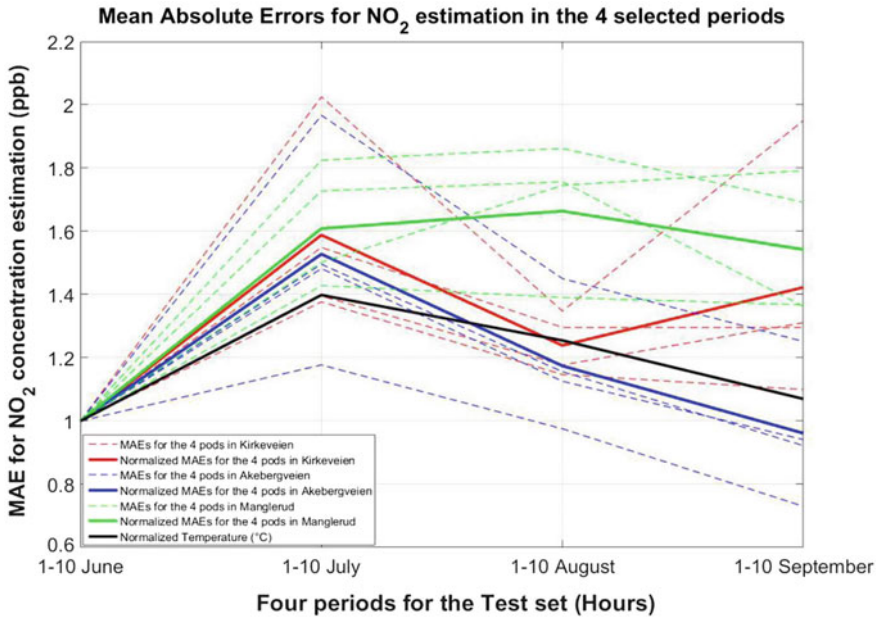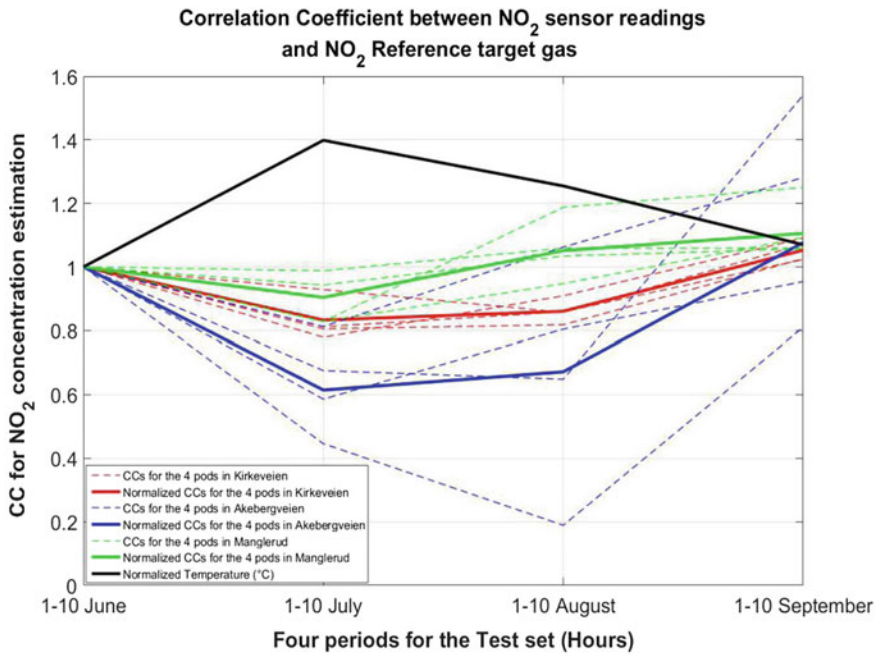

Fig. 2 Picture of CCs behaviour in the four considered periods, normalized to the value obtained in period 1. For each location, the four pods CC is shown together with the location wide average (*solid*)

Table 2 **a** Results obtained with Nonlinear multivariate calibration, for 4 stable pods located in Kirkeveien road. **b** Results obtained with Linear univariate calibration, for 4 stable pods located in Kirkeveien road

(a)				
Stable pods (Kirkeveien road)				
	MAE (STD)/CC			
POD	June, 1st–10th	July, 1st–10th	August, 1st–10th	September, 1st–10th
715150	4.40 (0.30)/ 0.84	8.91 (0.87)/ 0.78	5.93 (1.51)/ 0.72	8.58 (1.03)/0.90
764150	3.48 (0.10)/ 0.85	5.39 (1.25)/ 0.69	4.51 (0.54)/ 0.73	4.51 (0.49)/0.87
849150	4.63 (0.12)/ 0.77	6.46 (1.22)/ 0.62	5.45 (0.69)/ 0.63	6.07 (0.43)/0.79
785150	4.22 (0.25)/ 0.77	5.81 (0.99)/ 0.63	4.84 (0.58)/ 0.70	4.64 (0.47)/0.84
(b)				
Stable pods (Kirkeveien road)				
	MAE/CC			
POD	June, 1st–10th	July, 1st–10th	August, 1st–10th	September, 1st–10th
715150	7.40/0.12	7.29/0.26	7.13/0.29	9.48/0.54
764150	6.92/0.10	7.07/0.10	7.30/0.04	9.29/0.47
849150	6.62/0.44	5.88/0.54	5.69/0.57	6.56/0.70
785150	6.01/0.50	5.69/0.58	5.88/0.59	6.49/0.78

MAE values are in ppb

that temperature, a known interferent factors for the AQMesh electrochemical sensors, is one of the most relevant driver in determining final performances.

Furthermore, Fig. 3 (right) show a significant performance worsening in terms of bias and std, that is especially localized at highest and lowest concentrations that were not represented in the calibration set. Actually, changes in distribution of the target pollutant cause the calibrated sensors to operate outside the calibration envelope determining significant errors at the lower and higher edges of the concentration ranges. Note that given the actual distribution of NO_2, errors on the lower edges are more frequent and are consequently more relevant in affecting overall performances.

Regarding the target gas, we can also see, by Fig. 4, how Åkebergveien and Kirkeveien road stations have been exposed to very similar concentrations. With respect to the training phase, they show a preeminence of lower concentration values causing the joint performance worsening. Manglerud road nodes, instead, experienced a more significant distribution change experimenting more extreme

Table 3 **a** Results obtained with Nonlinear multivariate calibration, for 4 relocated pods in Åkebergveien road. **b** Results obtained with Linear univariate calibration, for 4 relocated in Åkebergveien road

(a)				
Relocated pods (Åkebergveien road)				
	MAE (STD)/CC			
POD	June, 1st–10th	July, 1st–10th	August, 1st–10th	September, 1st–10th
743150	3.59 (0.19)/ 0.87	5.37 (1.30)/ 0.51	4.15 (0.49)/ 0.70	3.31 (0.44)/ 0.83
850150	5.30 (0.10)/ 0.64	6.24 (1.98)/ 0.52	5.17 (0.73)/ 0.68	3.87 (0.14)/ 0.82
828150	5.13 (0.23)/ 0.74	10.09 (2.42)/0.33	7.44 (0.90)/ 0.14	6.42 (0.78)/ 0.60
712150	6.12 (0.24)/ 0.37	9.07 (5.65)/ 0.25	6.89 (2.84)/ 0.24	5.76 (1.04)/ 0.57
(b)				
Relocated pods (Åkebergveien road)				
	MAE/CC			
POD	June, 1st–10th	July, 1st–10th	August, 1st–10th	September, 1st–10th
743150	7.32/0.17	5.61/0.28	5.15/0.57	4.73/0.69
850150	6.26/0.54	5.14/0.55	4.25/0.68	4.32/0.80
828150	6.80/0.16	5.50/0.06	6.17/0.33	6.83/0.59
712150	6.49/0.01	6.04/0.03	6.33/0.52	6.65/0.68

MAE values are in ppb

values at both end of the distribution. Given the nodes error distribution and the relative high standard deviation this can be identified as a primary cause of the MAE worsening.

4 Conclusions

Our investigations shows that regardless of the location of the pods, a similar behaviour is observed in all the three colocation sites, with a collective deterioration of the performances in mid-summer time. Surprisingly, stable pods do not account for best relative performances showing median among the relocated ones. We observed that, during the Oslo short summer weeks, average temperatures were significantly higher than those observed during training phase and car traffic decreases determining a change in pollutant concentrations. We reported the effects

Table 4 a Results obtained with Nonlinear multivariate calibration, for 4 relocated pods in Manglerud road. **b** Results obtained with Linear univariate calibration, for 4 relocated pods in Manglerud road

(a)				
Relocated pods (Manglerud road)				
	MAE (STD)/CC			
POD	June, 1st–10th	July, 1st–10th	August, 1st–10th	September, 1st–10th
856150	5.58 (0.15)/ 0.64	7.97 (0.99)/ 0.53	7.76 (0.52)/ 0.76	7.63 (0.31)/ 0.80
751150	4.57 (0.17)/ 0.76	8.34 (1.39)/ 0.63	8.51 (0.62)/ 0.72	7.73 (1.28)/ 0.83
737150	3.45 (0.14)/ 0.88	5.96 (0.93)/ 0.83	6.06 (1.43)/ 0.91	4.70 (0.45)/ 0.93
718150	3.65 (0.16)/ 0.85	5.48 (1.12)/ 0.84	6.37 (1.35)/ 0.90	6.54 (0.67)/ 0.90
(b)				
Relocated pods (Manglerud road)				
	MAE/CC			
POD	June, 1st–10th	July, 1st–10th	August, 1st–10th	September, 1st–10th
856150	6.43/0.53	7.48/0.53	8.45/0.69	9.34/0.77
751150	7.17/0.37	8.87/0.30	8.74/0.66	7.51/0.79
737150	7.17/0.24	9.67/0.12	9.13/0.60	10.26/0.65
718150	7.09/0.17	8.74/0.30	8.77/0.62	10.38/0.65

MAE values are in ppb

of both the changes in the observed performances showing an interesting correlation among performance worsening and temperature increase as well as the increase of bias and standard deviation of MAE at both ends of the target gas concentration range at calibration time.

This study highlights the role of seasonal forcers distribution changes with respect to simple nodes relocation, within the herein considered distance range, in determining the on field calibrated nodes overall relative performance.
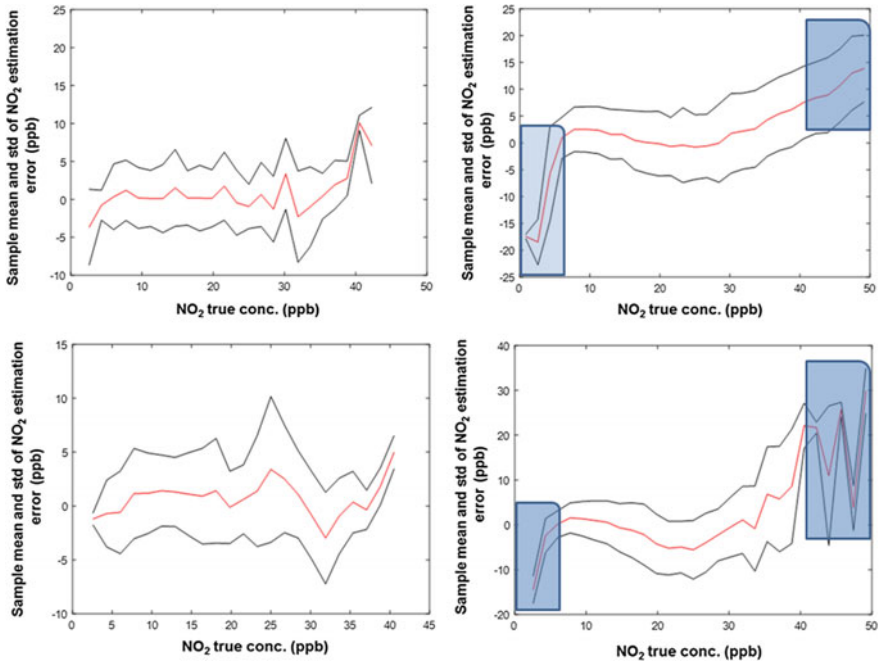
Fig. 3 Estimation mean bias (*red*) and uncertainty (*black*) versus actual NO_2 concentration in the calibrated nodes during their first test period (*left*) and after relocation event (*right*) for Kirkeveien stable nodes (*above*) and Akeberg relocated nodes (*below*) (Color figure online)
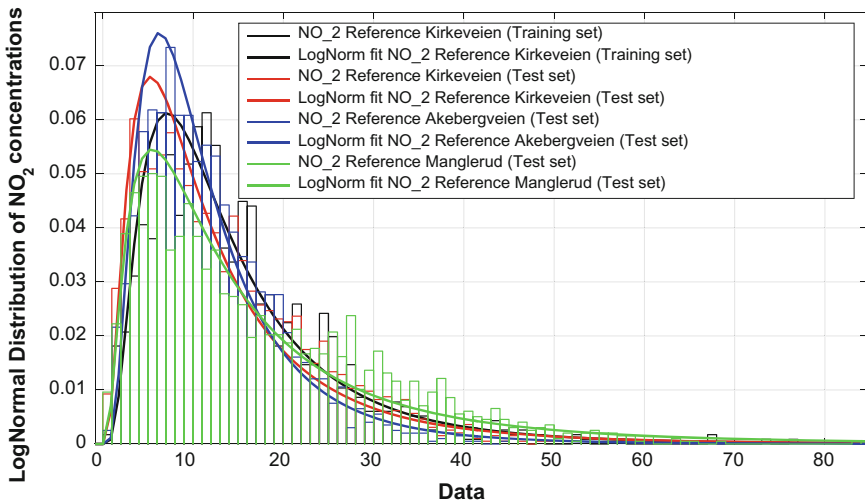
Fig. 4 Differences in the distribution of NO_2 concentrations (ppb) during training and test period for all pods (stable and relocated)

References

1. Spinelle, L., Gerboles, M., Villani, M.G., Aleixandre, M., Bonavitacola, F.: Field calibration of a cluster of low-cost available sensors for air quality monitoring. part A: ozone and nitrogen dioxide. Sens. Actuators, B **215**, 249–257 (2015)
2. Al Barakeh, Z., Breuil, P., Redon, N., Pijolat, C., Locoge, N., Viricelle, J.P.: Development of a normalized multi-sensors system for low cost on-line atmospheric pollution detection. Sens. Actuators, B **241**, 235–1243 (2017)
3. Castell, N., Dauge, F.R., Schneider, P., Vogt, M., Lerner, U., Fishbain, B., Broday, D., Bartonova, A.: Can commercial low-cost sensor platforms contribute to air quality monitoring and exposure estimates? Environ. Int. **99**, 293–302 (2017)

RGB-D Sensor for Facial Expression Recognition in AAL Context

Andrea Caroppo, Alessandro Leone and Pietro Siciliano

Abstract This paper investigates the use of a commercial and low-cost RGB-D sensor for real-time facial expression recognition in Ambient Assisted Living Context. Since head poses and light conditions could be very different in domestic environments, the methodology used was designed to handle such situations. The implemented framework is able to classify four different categories of facial expressions: (1) happy, (2) sad, (3) fear/surprise, and (4) disgust/anger. The classification is obtained through an hybrid-based approach, by combining appearance and geometric features. The HOG feature descriptor and a group of Action Units compose the feature vector that is given as input, in the classification step, to a group of Support Vector Machines. The robustness of the approach is highlighted by the results obtained: the average accuracy for fear/surprise is the lowest with 85.2%, while happy is the facial expression better recognized (93.6%). Sad and disgust/anger are the facial expression confused the most.

1 Introduction

Facial Expression Recognition (FER) plays an important role in several different areas, such as computer graphics and human-machine interaction. A large number of publications on this research area analysed multi-view facial expressions in 2D

A. Caroppo (✉) · A. Leone · P. Siciliano
National Research Council of Italy, Institute for Microelectronics and Microsystems,
Lecce, Italy
e-mail: andrea.caroppo@le.imm.cnr.it

A. Leone
e-mail: alessandro.leone@le.imm.cnr.it

P. Siciliano
e-mail: pietro.siciliano@le.imm.cnr.it

images and videos by tracking facial features and measuring the amount of facial movements [1–4]. Recently, the use of 3D depth sensors for FER [5, 6], such as the Microsoft Kinect, are gaining more popularity in the scientific community since human faces are 3D objects, and consequently the process representing 3D faces with 2D images is deficient in essential geometrical features. Moreover, If the human face does not face vision sensors directly, using 2D images could led some limitations on capturing relevant visual information like appearance-based features which are widely used in this application field.

In Ambient Assisted Living (AAL) context [7], such as a typical domestic environment, the input face images are often at low resolutions, very different light conditions and poses. The combined colour and depth information provided by Kinect can instead capture the meaningful appearance and geometrical features extracted from a face image, and enable higher preservation of facial details insensitive to different image resolution, pose and light conditions.

Generally a FER system is structured into three main stages, that are (1) pre-processing, (2) feature extraction, and (3) classification. The most important stage in FER pipeline is related to the extraction of the facial features from the acquired image. Generally existing approaches for facial feature extraction can be divided into three categories: geometric-based, appearance-based, and hybrid-based (both geometric and appearance features).

Geometric features present the shape and locations of facial components (including mouth, eyes, brows, and nose). The facial components or facial feature points are extracted to form a feature vector that represents the face geometry. The most used geometric feature-based methods are: Active Shape Model (ASM) [8, 9], Active Appearance Models (AAM) [10, 11] and scale-invariant feature transform (SIFT) [12].

On the other hand, the appearance features present the appearance changes of the face such as wrinkles and furrows. The aforementioned features can be extracted on either the whole-face or specific regions in a face image. The most three representative appearance-based feature extraction methods widely used in the research community are: Gabor Filters [13], Local Binary Patterns (LBP) [14] and Histogram Of Oriented Gradients (HOG) [15].

It is known that geometric-based and appearance-based features have their respective special properties and limitations, e.g., geometric-based features have effectiveness in computation while they are sensitive to noise; in contrast, appearance-based features are robust to image misalignment but it takes much time in computation. Therefore, the fusion of these features has become recently an active research topic.

In this work, a FER framework designed specifically for low cost RGB-D sensor is proposed. The feature extraction step is approached by an hybrid-based feature extraction methodology, by combining appearance and geometric features. The framework is able to classify four different classes of facial expressions: (1) happy, (2) sad, (3) fear/surprise, and (4) disgust/anger. The number of classes to distinguish is suggested by a recent research work [16] within which the authors have questioned the widely accepted notion that emotion communication is comprised of six

basic categories [17], and instead suggesting four. To the best of our knowledge, no significant work has been done in the area of FER using RGB-D images acquired with currently available low cost 3D sensors.

The rest of this paper is organized as follows. Section 2 details the proposed framework. Section 3 presents the experimental results. The conclusion is presented in Sect. 4.

2 Proposed Framework

The framework designed and implemented in the present work requires an algorithmic pipeline that involves different operating blocks (Fig. 1). First, the RGB image provided by Kinect is subject to a pre-processing stage with the goal of identifying the facial region. At the same time, the RGB and depth image are used together in order to compute the 3D facial mesh. Next, an appropriate set of features is extracted from both facial images; in particular, the histogram of oriented gradient (HOG) feature descriptor is evaluated starting from RGB face image, whereas a group of Action Units (AUs) are extracted from the facial mesh computed by Microsoft Kinect Face Tracking SDK [18]. The HOG feature descriptor combined with the weight of six AUs composes the feature vector that is given as input, in the classification step, to a group of Support Vector Machines (SVMs). Each operating step is detailed in the following subsections.
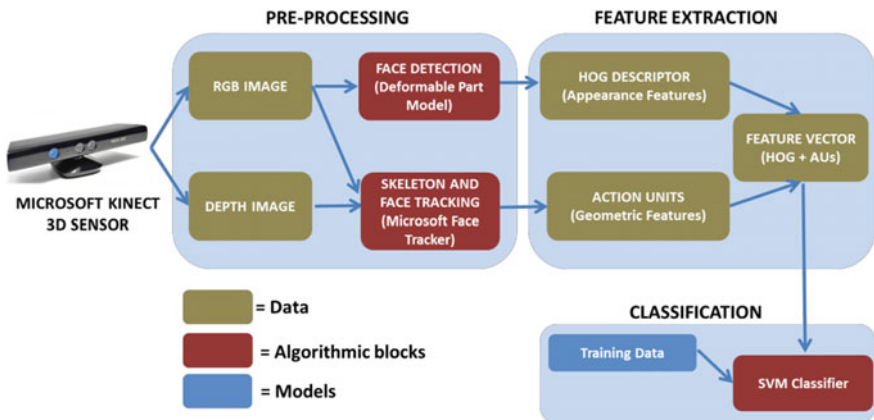

Fig. 1 Overview of the proposed FER framework

2.1 Pre-processing

The task of detecting a face in an image is not an easy problem because many difficulties arise and must be taken into account. Faces generally occupy very little area in most images and they are usually located arbitrarily. Moreover, in AAL context, faces acquired by a camera can look very different depending on orientation and pose. For example, a face seen from a profile perspective will have a completely different set of defining characteristics than a face seen head on.

Given that the original Viola-Jones face detector [19] has limitations for multi-view face detection (because it only detects frontal upright human faces with approximately up to 20 degree rotation around any axis), recently methodologies that have met much success have been proposed to tackle this problem, using Deformable Part Models (DPM). In this work, the approach used in [20] has been implemented, since it is based on a training step performed under fully supervised circumstances (Fig. 2).

At the same time, the Face Tracking SDK [18] is used to extract additional information from the face. The SDK is a part of the Kinect for Windows Developer Toolkit and contains a few sets of APIs that it is possible to use for obtaining useful information like for example 3D head pose. Face Tracking SDK requires colour and depth images from the RGB-D sensor as inputs, and returns the position data of the detected face, as well as some important recording points on the face, all of which can be retrieved and used for reconstructing the 3D face mesh that is a fundamental step for subsequent AUs evaluation.

2.2 Feature Extraction

In the proposed framework, appearance and geometric features are obtained from the detected face region independently. The appearance features are extracted by applying the HOG descriptor whereas a set of AUs are used to encode a geometry based feature.
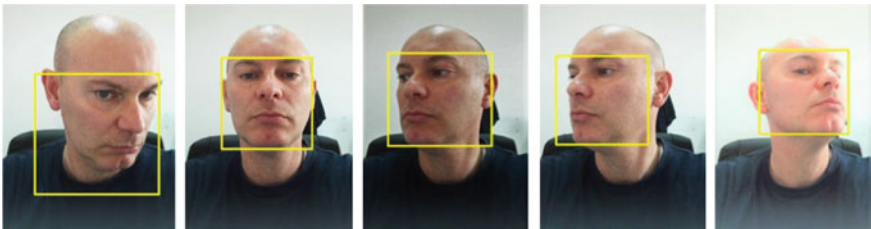

Fig. 2 Face detection results using the approach of Yu et al. [20]. The bounding box in *yellow* highlights the facial region identified by the algorithm with multi-view point of the face, different light conditions and various facial expression (Color figure online)

Appearance-based Features. The appearance and shape of the human face can be characterized in a very efficient way by the distribution of local intensity gradients or edge directions, even without precise knowledge of the corresponding gradient or edge positions. This statement leads to the definition of the Histogram of Oriented Gradient (HOG) technique [21].

HOG features are extracted from an image by a chain of normalizing local histograms of image gradient orientations in a dense grid. The method is based on evaluation of well normalized local histograms of image gradient orientations in a dense grid. So the image is divided into small regions called cells, where each cell collects a local 1-D histogram of gradient directions or edge orientations over the pixels of the cells and whole object is represented by combining these cell histograms. For better invariance to object illumination it is useful to contrast-normalize the local responses before using them, which can be accomplished by collecting a measure of local energy over a bit larger spatial regions termed as block in this work. Normalized descriptor blocks are referred as HOG descriptor and it is characterized by two main parameters, the cell size and the number of orientation bins. Cell size represents the dimension of the patch involved in the single histogram computation whereas the number of orientation bins refers to the quantization levels of the gradient information (Fig. 3a). In this work, the choice of these parameters has to be carefully carried out by taking into consideration the goal to be reached in the specific application context. After a qualitative and quantitative evaluation, based on various sets of facial images with different poses and pixel dimensions, the optimal parameters configuration was obtained with cell size of 7 pixels and 5 orientation bins.

Geometric-based Features. Information about characteristic points can be converted by libraries from Kinect for Windows SDK to Action Units (AUs), which represent important information in FER process. The AUs were described thanks to

(a)   **(b)**   **(c)**

AU0 – Upper Lip Raiser
AU1 – Jaw Lower
AU2 – Lip Stretcher
AU3 – Brow Lower
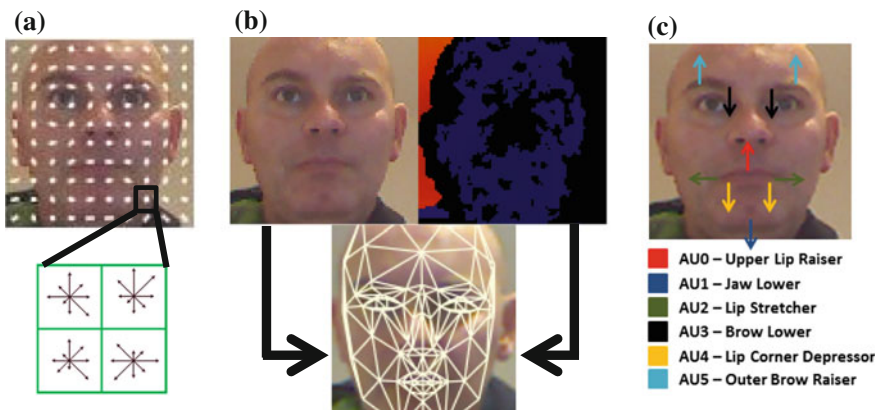AU4 – Lip Corner Depressor
AU5 – Outer Brow Raiser

Fig. 3 **a** HOG feature with an example of cell descriptor; **b** combination of RGB and depth image for 3D facial mesh computing process and subsequent AUs evaluation; **c** visualization of AUs (Color figure online)

research over FACS (Facial Action Coding System) which have been conducted by two, well known psychologists: Paul Ekman and Wallace V. Friesen [22].

The library from Kinect for Windows SDK shares only six AUs. Their values (which are between 1 and −1) describe position of face muscle groups. In this work, the value of six AUs are extracted for each frame. In particular, they describe movements and placement of the basic facial features such as eyes, eyebrows, and mouth. The AUs used are labelled as: AU0—Upper Lip Raiser, AU1—Jaw Lower, AU2—Lip Stretcher, AU3—Brow Lower, AU4—Lip Corner Depressor, AU5—Outer Brow Raiser (Fig. 3b, c).

2.3 Classification

After feature extraction, since the appearance feature's dimensionality turns out to be much larger than geometric feature's dimensionality, Principal Components Analysis (PCA) are applied to reduce the dimensionality of the appearance feature vector. Finally, the obtained feature vector (HOG+AUs) is given as input to a group of Support Vector Machine (SVM) that represent the learning model for each facial expression. SVM is a popular machine learning algorithm which maps the feature vector to a different plane, usually to a higher dimensional plane, by a non-linear mapping, and finds a linear decision hyper plane for classification of two classes. Since the classical SVM implementation is used only for a two classes problem and considering that the purpose of this work is to recognize four different classes of facial expression, the classification is addressed by the "one-against-one" method [23]. Consequently, SVMs are trained for each combination of classes and the final class label is decided using majority voting strategy. Here, Radial Basis Function (RBF) was used as kernel as suggested in [24] for non-linearly separable problems with penalty parameter $C = 1000$ and $\gamma = 0.05$.

3 Results

In this section, the performance of the proposed framework are discussed. For experiments, an embedded PC equipped with Intel Core i5-750 2.67 GHz, 8 GB RAM, 512 SSD was used.

A sufficiently large dataset containing facial expressions of 6 subjects (4 males and 2 females) has been created. The images were captured with different light conditions (measured in lx-luminous emittance) and with different head poses. The results of the proposed approach are depicted in the confusion matrix in Table 1: the average accuracy for fear/surprise is the lowest with 85.2%, while happy is the facial expression better recognized (93.6%). Sad and disgust/anger are the facial expression confused the most.

Table 1 Confusion matrix of 4-class facial expression recognition: Happy (Ha), Sad (Sa), Fear/Surprise (Fe/Su) and Disgust/Anger (Di/An)

		Predicition			
		Ha	Sa	Fe/Su	Di/An
Actual	Ha	**93.6**	2.4	3.1	0.9
	Sa	1.3	**91.1**	1.9	5.7
	Fe/Su	4.6	4.6	**85.2**	5.6
	Di/An	2.3	6.9	1.9	**88.9**

Bold values represent the correct predictions of the considered 4-class facial expression in terms of overall accuracy (calculated as the total number of correctly classified facial expression divided by the total number of test facial expression). In this way it is easy to visually inspect the table for prediction errors, as they will be represented by values outside the diagonal

On the other hand, the robustness of the approach is highlighted by the results reported in Tables 2 and 3, which report the percentage of correct facial expression class recognition at varying of head poses and light conditions. The user's head pose is captured by two angles: yaw and pitch. The angles are expressed in degrees, with values ranging from −60° to +60° for yaw angle and −30° and +30° for pitch angle.

The results reported in the previous tables show that the implemented approach enables effective classification of facial expressions even in the presence of significant changes in light conditions, that is a typical and unchecked event in domestic environments. Moreover, analysing the accuracy rates obtained at varying of yaw and pitch angle, the hybrid approach allows the recognition of facial expressions with a very low variance, confirming the choice of the used set of features.

Table 2 Accuracy rate (%) at varying of light conditions (15 lx and 80 lx) and yaw angle (between −60° and +60°)

Lx	15					80				
Head pose (yaw angle)	−60	−30	0	30	60	−60	−30	0	30	60
Happy	90.8	92.1	93.6	92.3	90.9	91.4	92.8	94.2	93	91.6
Sad	88.8	90.2	90.7	89.9	88.6	89.7	90.3	91.3	90.2	89.5
Fear/Surprise	81.9	83.2	84.8	83.5	81.7	83.6	84.6	85.6	84.4	83.9
Disgust/Anger	86.9	87.6	89	87.8	86.8	87.9	88.6	89.4	88.8	87.7

Table 3 Accuracy rate (%) at varying of light conditions (15 lx and 80 lx) and pitch angle (between −30° and +30°)

Lx	15					80				
Head pose (pitch angle)	−30°	−15°	0°	15°	30°	−30°	−15°	0	15°	30°
Happy	89.8	90.3	91.5	90.3	89.9	88.7	90.4	91.4	90.3	88.8
Sad	88	89.6	90.1	89.5	88.2	89.7	90.9	91.3	90.7	89.5
Fear/Surprise	81.1	81.6	83.7	81.5	80.9	83.4	84.2	85.6	84.1	83.3
Disgust/Anger	85.3	86.8	88.1	87	85.4	85.9	88.6	89.4	88.7	86

4 Conclusion

In this paper, we propose a novel approach for facial expression recognition in AAL context using both RGB and depth images captured by a low cost RGB-D sensor. The invariance of depth information to illumination variations and the ability of HOG descriptor in characterizing the appearance and shape of the human face, even if the face view is non-frontal, are exploited thanks to an hybrid approach. The results suggests that a promising recognition accuracy of facial expressions can be obtained even in situation of different light conditions and non-frontal face images, that are typical in uncontrolled image acquisition contexts. Moreover, another added value of this work lies in the fact that the suggested computational framework was optimized and validated for embedded processing in order to meet typical in-home application requirements such as low power consumption, noiselessness and compactness.

Future works will be addressed to study how the distance of the subject from the Kinect sensor influences the performance of the framework. Finally, a further development will be to analyse performance even in the presence of face part occlusion that are very common in domestic environments.

References

1. Hu, Y., Zeng, Z., Yin, L., Wei, X., Tu, J., Huang, T.S.: A study of non-frontal-view facial expressions recognition. In: 19th International Conference on Pattern Recognition, 2008 (ICPR 2008), IEEE, pp. 1–4 (2008)
2. Rudovic, O., Pantic, M., Patras, I.: Coupled Gaussian processes for pose-invariant facial expression recognition. IEEE Trans. Pattern Anal. Mach. Intell. **35**(6), 1357–1369 (2013)
3. Zheng, W.: Multi-view facial expression recognition based on group sparse reduced-rank regression. IEEE Trans. Affect. Comput. **5**(1), 71–85 (2014)
4. Cament, L.A., Galdames, F.J., Bowyer, K.W., Perez, C.A.: Face recognition under pose variation with local Gabor features enhanced by active shape and statistical models. Pattern Recogn. **48**(11), 3371–3384 (2015)
5. Sandbach, G., Zafeiriou, S., Pantic, M., Yin, L.: Static and dynamic 3D facial expression recognition: a comprehensive survey. Image Vis. Comput. **30**(10), 683–697 (2012)
6. Malawski, F., Kwolek, B., Sako, S.: Using kinect for facial expression recognition under varying poses and illumination. In: International Conference on Active Media Technology, pp. 395–406, Springer International Publishing (2014)
7. Andò, B., Siciliano, P., Marletta, V., Monteriù, A.: Ambient Assisted Living. (2015)
8. Chang, Y., Hu, C., Feris, R., Turk, M.: Manifold based analysis of facial expression. Image Vis. Comput. **24**(6), 605–614 (2006)
9. Shbib, R., Zhou, S.: Facial expression analysis using active shape model. Int J Signal Process., Image Process. Pattern Recognit. **8**(1), 9–22 (2015)
10. Cheon, Y., Kim, D.: Natural facial expression recognition using differential-AAM and manifold learning. Pattern Recognit. **42**(7), 1340–1350 (2009)
11. Chen, Y., Hua, C., Bai, R.: Regression-based active appearance model initialization for facial feature tracking with missing frames. Pattern Recognit. Lett. **38**, 113–119 (2014)

12. Soyel, H., Demirel, H.: Facial expression recognition based on discriminative scale invariant feature transform. Electron. Lett. **46**(5), 343–345 (2010)
13. Gu, W., Xiang, C., Venkatesh, Y.V., Huang, D., Lin, H.: Facial expression recognition using radial encoding of local Gabor features and classifier synthesis. Pattern Recognit. **45**(1), 80–91 (2012)
14. Zhao, G., Pietikainen, M.: Dynamic texture recognition using local binary patterns with an application to facial expressions. IEEE Trans. Pattern Anal. Mach. Intell. **29**(6): (2007)
15. Dahmane, M., Meunier, J.: Emotion recognition using dynamic grid-based HoG features. In: 2011 IEEE International Conference on Automatic Face & Gesture Recognition and Workshops (FG 2011), pp. 884–888, IEEE (2011)
16. Jack, R.E., Garrod, O.G., Schyns, P.G.: Dynamic facial expressions of emotion transmit an evolving hierarchy of signals over time. Curr. Biol. **24**(2), 187–192 (2014)
17. Ekman, P., Friesen, W.V.: Constants across cultures in the face and emotion. J. Pers. Soc. Psychol. **17**(2), 124 (1971)
18. Face Tracking: https://msdn.microsoft.com/en-us/library/jj130970.aspx
19. Viola, P., Jones, M.J.: Robust real-time face detection. Int. J. Comput. Vision **57**(2), 137–154 (2004)
20. Yu, X., Huang, J., Zhang, S., Yan, W., Metaxas, D.N.: Pose-free facial landmark fitting via optimized part mixtures and cascaded deformable shape model. In: Proceedings of the IEEE International Conference on Computer Vision, pp. 1944–1951 (2013)
21. Dalal, N., & Triggs, B.: Histograms of oriented gradients for human detection. In: IEEE Computer Society Conference on Computer Vision and Pattern Recognition, 2005 (CVPR 2005), vol. 1, pp. 886–893, IEEE (2005)
22. Ekman, P., Friesen, W.V., Hager, J.C.: Facial Action Coding System (FACS). A Technique for the Measurement of Facial Action. Consulting, Palo Alto, 22 (1978)
23. Knerr, S., Personnaz, L., Dreyfus, G.: Single-layer learning revisited: a stepwise procedure for building and training a neural network. In: Neurocomputing, pp. 41–50. Springer, Berlin (1990)
24. Hsu, C.W., Chang, C.C., Lin, C.J.: A Practical Guide to Support Vector Classification. (2003)
25. Aly, S., Trubanova, A., Abbott, L., White, S., Youssef, A.: VT-KFER: a Kinect-based RGBD + time dataset for spontaneous and non-spontaneous facial expression recognition. In: 2015 International Conference on Biometrics (ICB), pp. 90–97. IEEE (2015)

UV-Cured Composite Films Containing ZnO Nanostructures: Effect of Filler Shape on Piezoelectric Response

L. Francioso, G. Malucelli, A. Fioravanti, C. De Pascali, M.A. Signore, M.C. Carotta, A. Bonanno and D. Duraccio

Abstract In this work, a facile aqueous sol-gel approach was exploited for synthesizing different ZnO nanostructures; these latter were employed at 4 wt% loading in a UV-curable acrylic system. The piezoelectric behavior of the resulting UV-cured nanocomposite films (NCFs) at resonance and at low frequency (150 Hz, typical value of interest in energy harvesting applications) was thoroughly investigated and correlated to the structure and morphology of the utilized ZnO nanostructures. For this purpose, the NCFs were used as active material into cantilever-shaped energy harvesters obtained through standard microfabrication technology. Interesting piezoelectric behavior was found for all the prepared UV-cured nanostructured films; the piezoelectric response of the different nanofillers was compared in terms of RMS voltage measured as a function of the applied waveform and normalized to the maximum acceleration applied to the cantilever devices. The obtained results confirmed the promising energy harvesting capability of such ZnO nanostructured films. In particular, flower-like structures showed the best piezoelectric performance both at resonance and 150 Hz, gaining a maximum normalized RMS of 0.914 mV and a maximum peak-peak voltage of about 16.0 mVp-p corresponding to the application of 5.79 g acceleration.

L. Francioso (✉) · C. De Pascali · M.A. Signore
Institute for Microelectronics and Microsystems—CNR–IMM, Via Monteroni, Lecce, Italy
e-mail: Luca.Francioso@le.imm.cnr.it

G. Malucelli · M.C. Carotta · D. Duraccio
Department of Applied Science and Technology and Local INSTM Unit, Politecnico di Torino, Viale T. Michel 5, Alessandria, Italy

A. Fioravanti · A. Bonanno
CNR-IMAMOTER Ferrara, Via Canal Bianco 28, Ferrara, Italy

A. Fioravanti
Department of Chemistry, University of Parma, Parco Area delle Scienze 17A, 43124 Parma, Italy

D. Duraccio
CNR-IMAMOTER Torino, Strada Delle Cacce 73, 10135 Turin, Italy

1   Introduction

During the last years, several research groups proposed and thoroughly investigated the conversion of mechanical energy (e.g., pressure, bending, stretching and vibrational motions) into electricity, aiming at obtaining wireless self-powered systems by means of piezoelectric materials [1–11]. Different piezoelectric energy scavengers have been manufactured using both fully inorganic bulky materials (namely, ZnO nanowires [12–14], $PbZr_xTi_{12x}O_3$ [15–17], GaN [18] and $BaTiO_3$ [19–21]) and fully organic films (polyvinylidene fluoride—PVDF [22–28]), as well as a combination of these materials. Recently, the research on low-cost, mechanically stable, and high-output nanocomposite generators has been invented by using casting piezoelectric nanocomposites onto flexible plastic substrates at low temperature [29–34]. ZnO has several key advantages, being a biologically safe piezoelectric semiconductor occurring in a wide range of nanostructured morphologies. It is a potential candidate for commercial purposes, due to its inexpensiveness, relative abundance, and chemical stability in air. In the present work, different shaped ZnO nanoparticles, synthesized on purpose and embedded into a UV-curable acrylic polymer matrix, are considered; the effect of the different nanofiller shapes on the piezoelectric properties of the resulting polymer thin films is thoroughly investigated. The possibility to develop a novel flexible, efficient, versatile coating of easy fabrication and low environmental impact could lead to a real competition in the field of renewable/alternative energy technologies. In fact, the majority of the strategies described in literature involve complicated material processing and device fabrication (using precise manipulators), which exhibit hurdles for scalability and cost. Although these reports have provided the scientific community with significant contributions and set benchmarks, it seems important to explore innovative, cheap, scalable technologies based on new materials. ZnO nanostructures were synthesized following a facile aqueous sol-gel route in four different morphologies, namely: nano-particles (ZNP), bipyramidal structures (ZBP), flower-like nanostructures (ZNF) and long needles (ZLN). A commercially available acrylic resin, namely bis-phenol A ethoxylate diacrylate (Ebecryl 150—EB), kindly supplied by Cytec Industries BV (Netherlands), was used as UV-curable reactive precursor of the polymer network. 4 wt% of photoinitiator (Irgacure 1173, 2,2-dimethyl-2-hydroxy acetophenone, from BASF, Italy) was added to the acrylic UV-curable resin; then, the different ZnO nanofillers were dispersed in the UV-curable mixture at 4 wt% and ultrasonicated for 30 min at RT. The obtained dispersions were coated on glass slides, using a wire wound applicator (film thickness: about 150 μm) and then exposed to the UV radiation provided by a F300 S apparatus (Heraeus Noblelight, USA) working in static conditions. The radiation intensity on the sample surface, measured with an UV-meter, was about 800 mW/cm^2.

2 Results and Discussion

The typical SEM micrographs of ZnO nanostructures are shown in Fig. 1. ZNP (Fig. 1a) is characterized by spherical nanoparticles (sizes ranging in between 50 and 60 nm) while ZBP and ZNF samples appear as nanoparticle aggregates in form of bipyramids (Fig. 1b) and flower-like structures (Fig. 1c), respectively. In particular, the bipyramidal structures show the z-axis of about 10 μm and a fine structure made of nanoparticles, the size of which is only slightly lower than that of ZNP nanoparticles. A similar hierarchical structure appears in ZNF powders, where particles of about 30 nm in size are assembled in 1 μm sized flower-like structure. Figure 1d shows the typical SEM image of ZLN particles consisting of bi-dimensional nanocrystals shaped as long needles (about 100 nm wide and 7–8 μm long). All the synthesized nanostructures exhibit a hexagonal wurtzite structure (space group P63mc), irrespective of both the synthesis process and the morphology. XRD spectra show the typical peaks (at 2θ values of 31.9, 34.5, 36.3, 56.7 and 62.9°) for the zinc oxide when deposited in a nanostructured form.
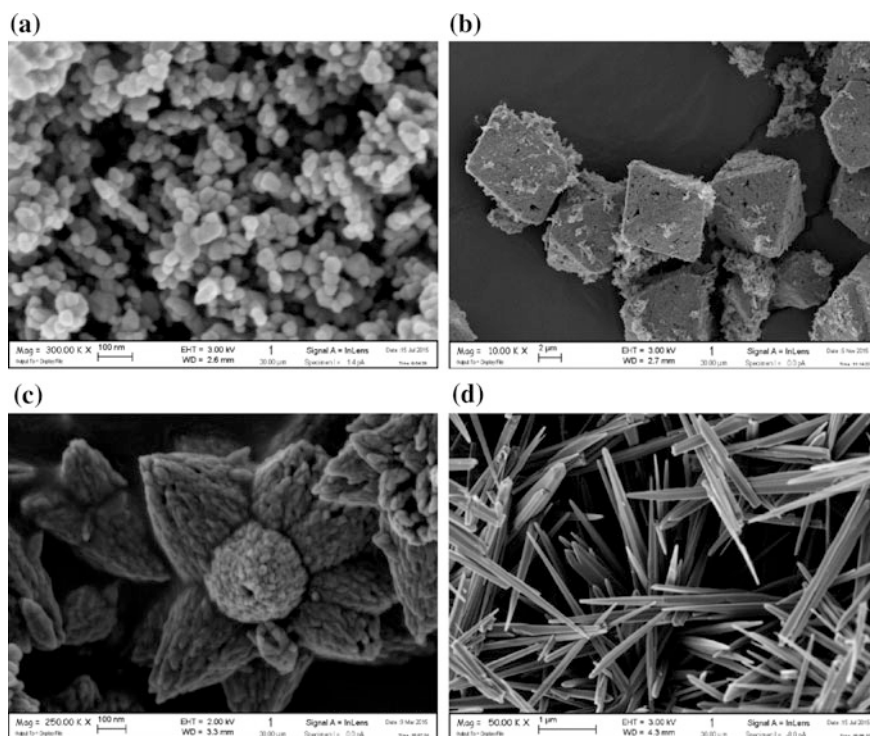

Fig. 1 SEM micrographs of ZnO nanostructures: **a** ZNP, **b** ZBP, **c** ZNF and **d** ZLN

The crystallite sizes, evaluated by the Scherrer formula, are listed in Table 1.

The responses, both in time and frequency domain, of the beams fabricated by using the nanocomposite films were evaluated as a preliminary step for experimentally assessing their behavior in terms of energy harvesting capability. The effective piezoelectric features of nanofiller-loaded devices have been demonstrated by comparing their piezoelectric response with that of cantilevers made of unfilled UV-cured resin. The generated voltages vs. excitation frequency were normalized to maximum acceleration.

Figures 2 shows the generated output voltages by ZNF nanofiller at the frequency of 150 Hz and at the resonance frequencies, respectively, at about 5.4 g of maximum acceleration. The generated voltage and current signals show a regular and stable time response with a constant amplitude output due to the homogeneous distribution of the nanofillers within the host polymer network, as already proven by SEM analyses. In order to compare the performance of the nanofillers in terms of generated power, the acquired sinusoidal spectra were normalized to the maximum acceleration applied to the cantilever devices; then, the obtained values were elaborated as root mean square (RMS), as shown in Fig. 3 for both the selected frequencies (i.e. 150 Hz and resonance frequency).

Table 1 Average dimensions and crystallite sizes of different ZnO morphologies

Morphologies	Dimensions[a]	Cristallite size[b] (nm)
Nanoparticles (ZNP)	50–60 nm	26
Bipyramidal structures (ZBP)	10 μm (z-axis)	24
Flower-like structures (ZNF)	1 μm (diameter)	30
Long needles (ZLN)	100 nm (width) 7–8 μm (length)	39

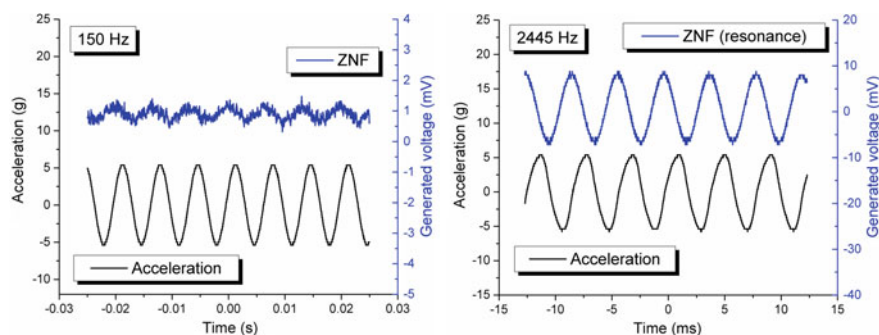[a]Calculated from SEM micrographs
[b]From WAXD analyses

Fig. 2 Output voltage measured at resonance and 150 Hz signal frequency, for flower-like nanostructured films
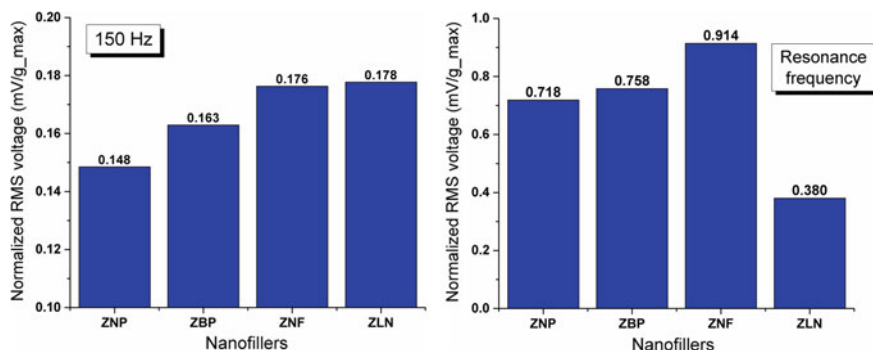
Fig. 3 Normalized voltage RMS values, for the four different nanofillers, at resonance and 150 Hz signal frequency

The highest RMS voltage at 150 Hz (about 0.177 ± 0.001 mV) was registered for EB-ZNF and EB-ZLN films; for the ZNF and ZLN devices, the peak-peak voltage was about 1.80 ± 0.01 mVp-p for a maximum applied acceleration of 5.38 g. Therefore, at this frequency, it is noteworthy that the ZnO particle shape does not significantly affect the piezoelectric response of the composite systems.

At variance, at the resonance frequency, the highest RMS voltage was measured on the UV-cured films containing ZNF (flower-like structures) with a maximum normalized RMS voltage of 0.914 ± 0.001 mV and a maximum peak-peak voltage of about 16.0 ± 0.1 mVp-p, corresponding to the application of 5.79 g acceleration; in addition, the lowest RMS voltage was measured for the UV-cured films containing ZLN filler (0.380 ± 0.001 mV).

It is important to consider that the piezoelectric effect of ZnO depends on the orientation of the 0002 crystallographic planes. In particular, piezoelectricity occurs when these planes are oriented perpendicularly to the applied mechanical stress [35]: though, in our systems, ZnO particles have random orientations, a small portion of (0002) crystals can be oriented in the desired direction, hence giving rise to voltage generation upon the application of the mechanical stress. The probability that the flower-like particles, in EB-ZFL films, possess a higher number of 0002 planes oriented perpendicularly to the measured solicitation is higher with respect to the other nanostructures. Thus, the particular shape of ZFL nanostructures justifies the highest measured voltage in their nanocomposite films; conversely, the z direction of ZLN particles (see Fig. 1) is mainly laid in the plane of the film. In fact, in the needle-like morphology, the planes 0002 are perpendicular to their z direction: this means that they are parallel to the stress application direction, hence providing the lowest RMS voltage recorded.

3 Conclusion

The present work aimed at investigating ZnO nanostructures with different morphologies (namely: nanoparticles, bipyramidal structures, flower-like nanostructures and long needles) that were synthesized through a facile aqueous sol-gel approach and used as fillers at 4 wt% loading in a UV-curable acrylic system. A good distribution of the different nanofillers, regardless of their specific morphology, was achieved in the UV-cured films. The piezoelectric behavior of the obtained nanocomposite films was investigated by integrating them into cantilever generator devices: unlike unfilled UV-cured films, which showed negligible generated voltage near to instrumental noise background, the responses, both in time and frequency domain, of the beams fabricated by using the synthesized composites were evaluated as a preliminary step for experimentally assessing their piezoelectric behavior all the systems. In particular, the different fabricated cantilever showed a good response in terms of RMS voltage measured as a function of the applied waveform, both at low and resonance frequency. The flower-like structures (ZNF) displayed the best piezoelectric performance both at 150 Hz and at the resonance frequency, with a maximum normalized RMS of 0.914 mV and a maximum peak-peak voltage of about 16.0 mVp-p, with the application of 5.79 g acceleration.

The experimental results clearly indicate that the fabrication of piezoelectric UV-cured coatings containing very low nanofiller loadings (below 5 wt%) and the possibility of tuning the flexibility of the obtained piezoelectric films on the basis of the selected UV-curable systems, opens the pathway towards the design of tunable, cost effective, low environmental impact thin coating devices for energy harvesting purposes.

References

1. Di Salvo, F.J.: Thermoelectric cooling and power generation. Science **285**, 703 (1999)
2. Chapin, D., Fuller, C., Pearson, G.: A new silicon p-n junction photocell for converting solar radiation into electrical power. J. Appl. Phys. **25**, 676–677 (1954)
3. Wang, Z.L., Song, J.H.: Piezoelectric nanogenerators based on zinc oxide nanowire arrays. Science **312**, 242–246 (2006)
4. Wang, X.D., Song, J.H., Liu, J., Wang, Z.L.: Growth of self-assembled ZnO nanowire arrays. Science **316**, 102–105 (2007)
5. Bowen, C.R., Kim, H.A., Weaver, P.M., Dunn, S.: Piezoelectric and ferroelectric materials and structures for energy harvesting applications. Energ. Environ. Sci. **7**, 25–44 (2014)
6. Briscoe, J., Dunn, S.: Piezoelectric nanogenerators—a review of nanostructured piezoelectric energy harvesters. Nano. Energ. **14**, 15–29 (2015)

7. Wang, X.: Piezoelectric nanogenerators-harvesting ambient mechanical energy at the nanometer scale. Nano. Energ. **1**, 13–24 (2012)
8. Wang, Z.L., Wu, W.: Nanotechnology-enabled energy harvesting for self powered micro-/nanosystems. Angew. Chem. Int. Ed. **51**, 11700–11721 (2012)
9. Chang, C., Tran, V.H., Wang, J., Fuh, Y.-K., Lin, L.: Direct-write piezoelectric polymeric nanogenerator with high energy conversion efficiency. Nano Lett. **10**, 726–731 (2010)
10. Beeby, S.P., Tudor, M.J., White, N.M.: Energy harvesting vibration sources for microsystems applications. Meas. Sci. Technol. **17**, R175–R195 (2006)
11. Wang, Z.Y., Hu, J., Suryavanshi, A.P., Yum, K., Yu, M.F.: Voltage generation from individual BaTiO3 nanowires under periodic tensile mechanical load. Nano Lett. **7**, 2966–2969 (2007)
12. Wang, Z.L., Song, J.: Piezoelectric nanogenerators based on zinc oxide nanowire arrays. Science **312**, 242–246 (2006)
13. Xu, S., Qin, Y., Xu, C., Wei, Y., Yang, R., Wang, Z.L.: Self powered nanowire devices. Nat. Nanotechnol. **5**, 366–373 (2010)
14. Yang, R., Qin, Y., Dai, L., Wang, Z.L.: Power generation with laterally packaged piezoelectric fine wires. Nat. Nanotechnol. **4**, 34–39 (2009)
15. Chen, X., Xu, S., Yao, N., Shi, Y.: 1.6 V nanogenerator for mechanical energy harvesting using PZT nanofibers. Nano Lett. **10**, 2133–2137 (2010)
16. Chen, X., Xu, S., Yao, N., Xu, W., Shi, Y.: Potential measurement from a single lead ziroconate titanate nanofiber using a nanomanipulator. Appl. Phys. Lett. **94**, 253113 (2009)
17. Zhang, G., Xu, S., Shi, Y.: Electromechanical coupling of lead zirconate titanate nanofibres. Micro Nano Lett. **6**, 59–61 (2011)
18. Huang, C.T., Song, J., Lee, W.-F., Ding, Y., Gao, Z., Hao, Y., Chen, L.-J., Wang, Z.L.: GaN nanowire arrays for high-output nanogenerators. J. Am. Chem. Soc. **132**, 4766–4771 (2010)
19. Ni, X., Wang, F., Lin, A., Xu, Q., Yang, Z., Qin, Y.: Flexible nanogenerator based on single BaTiO3 nanowire. Sci. Adv. Mater. **5**, 1781–1787 (2013)
20. Koka, A., Zhou, Z., Sodano, H.A.: Vertically aligned BaTiO3 nanowire arrays for energy harvesting. Energy Environ. Sci. **7**, 288–296 (2014)
21. Koka, A., Sodano, H.A.: A low-frequency energy harvester from ultralong, vertically aligned BaTiO3 nanowire arrays. Adv. Energy Mater. **4**, 1301660 (2014)
22. Crossley, S., Whiter, R.A., Kar-Narayan, S.: Polymer-based nanopiezoelectric generators for energy harvesting applications. Mater. Sci. Technol. **30**, 1613–1624 (2014)
23. Chang, C.E., Tran, V.H., Wang, J.B., Fuh, Y.K., Lin, L.W.: Direct-write piezoelectric polymeric nanogenerator with high energy conversion efficiency. Nano Lett. **10**, 726–731 (2010)
24. Chang, C.E., Fuh, Y.-K., Lin, L.: A direct-write piezoelectric PVDF nanogenerator, transducers 2009. In: Solid-state Sensors, Actuators and Microsystems Conference, pp. 1485–1488. Denver (2009)
25. Cha, S.N., Kim, S.M., Kim, H., Ku, J., Sohn, J.I., Park, Y.J., Song, B.G., Jung, M.H., Lee, E.K., Choi, B.L., Park, J.J., Wang, Z.L., Kim, J.M., Kim, K.: Porous PVDF as effective sonic wave driven nanogenerators. Nano Lett. **11**, 5142–5147 (2011)
26. Soin, N., Shah, T.H., Anand, S.C., Geng, J., Pornwannachai, W., Mandal, P., Reid, D., Sharma, S., Hadimani, R.L., Bayramol, D.V., Siores, E.: Novel "3-D spacer" all fibre piezoelectric textiles for energy harvesting applications. Energy Environ. Sci. **7**, 1670–1679 (2014)
27. Briscoe, J., Jalali, N., Woolliams, P., Stewart, M., Weaver, P.M., Cain, M., Dunn, S.: Measurement techniques for piezoelectric nanogenerators. Energy Environ. Sci. **6**, 3035–3045 (2013)
28. Granstrom, J., Feenstra, J., Sodano, H.A., Farinholt, K.: A review of power harvesting from vibration using piezoelectric materials. Smart Mater. Struct. **16**, 1810–1820 (2007)
29. Park, K.I., Lee, M., Liu, Y., Moon, S., Hwang, G.T., Zhu, G., Kim, J.E., Kim, S.O., Kim, D.K., Wang, Z.L., Lee, K.J.: Flexible nanocomposite generator made of BaTiO3 nanoparticles and graphitic carbons. Adv. Mater. **24**, 2999–3004 (2012)

30. Jung, J.H., Lee, M., Hong, J.I., Ding, Y., Chen, C.Y., Chou, L.J., Wang, Z.L.: Leadfree NaNbO3 nanowires for a high output piezoelectric nanogenerator. ACS Nano **5**, 10041–10046 (2011)
31. Jung, J.H., Chen, C.Y., Yun, B.K., Lee, N., Zhou, Y., Jo, W., Chou, L.J., Wang, Z.L.: Lead-free KNbO3 ferroelectric nanorod based flexible nanogenerators and capacitors. Nanotechnology **23**, 375401 (2012)
32. Park, K.I., Jeong, C.K., Ryu, J., Hwang, G.T., Lee, K.J.: Flexible and large-area nanocomposite generators based on lead zirconate titanate particles and carbon nanotubes. Adv. Energ. Mater. **3**, 1539–1544 (2013)
33. Jeong, C.K., Park, K.I., Ryu, J., Hwang, G.T., Lee, K.J.: Large-area and flexible lead-free nanocomposite generator using alkaline niobate particles and metal nanorod filler. Adv. Funct. Mater. **24**, 2620–2629 (2014)
34. Park, K.I., Jeong, C.K., Kim, N.K., Lee, K.J.: Stretchable piezoelectric nanocomposite generator. Nano Convergence **3**, 12 (2016)
35. Wang, Z.L.: Zinc oxide nanostructures: growth, properties and applications. J. Phys.: Condens. Matter **16**, R829 (2004)